NNT/NL : 2021AIXM0440/058ED352

THÈSE DE DOCTORAT

Soutenue à Aix-Marseille Université

le 18 novembre 2021 par

Jorge Andrés VILLA VÉLEZ

Spectrophotometric Analysis Around Cosmic Noon : Emission-Lines, Dust Attenuation, and Star Formation

Discipline
Physique et Sciences de la Matière

Spécialité
Astrophysique et Cosmologie

École doctorale
ED 352 PHYSIQUE ET SCIENCES DE LA MATIERE

Laboratoire/Partenaires de recherche
Laboratoire d'Astrophysique de Marseille - LAM

Composition du jury

Vivienne WILD University of St Andrews, Écosse	Rapporteure
Thierry CONTINI IRAP, Toulouse	Rapporteur
Olivier ILBERT LAM, Aix-Marseille Université	Examinateur
Lucia POZZETTI INAF OAS, Bologne	Examinatrice
Roser PELLO LAM, Aix-Marseille Université	Présidente du jury
Véronique BUAT LAM, Aix-Marseille Université	Directrice de thèse
Patrice THEULE LAM, Aix-Marseille Université	Invité

Je soussigné, Jorge Andrés Villa Vélez, déclare par la présente que le travail présenté dans ce manuscrit est mon propre travail, réalisé sous la direction scientifique de Dr. Véronique Buat, dans le respect des principes d'honnêteté, d'intégrité et de responsabilité inhérents à la mission de recherche. Les travaux de recherche et la rédaction de ce manuscrit ont été réalisés dans le respect à la fois de la charte nationale de déontologie des métiers de la recherche et de la charte d'Aix-Marseille Université relative à la lutte contre le plagiat.

Ce travail n'a pas été précédemment soumis en France ou à l'étranger dans une version identique ou similaire à un organisme examinateur.

Fait à Marseille le 18 novembre 2021

I, undersigned, Jorge Andrés Villa Vélez, hereby declare that the work presented in this manuscript is my own work, carried out under the scientific direction of Véronique Buat, in accordance with the principles of honesty, integrity and responsibility inherent to the research mission. The research work and the writing of this manuscript have been carried out in compliance with both the french national charter for Research Integrity and the Aix-Marseille University charter on the fight against plagiarism.

This work has not been submitted previously either in this country or in another country in the same or in a similar version to any other examination body.

Marseilles, November 18th 2021

Résumé

Dans ce travail de thèse, je présente les résultats de deux projets différents dont j'ai travaillé au sein du LAM dans le cadre de mes études doctorales. Un premier travail concernant l'ajustement spectro-photométrique des SEDs de galaxies en étudiant les raies d'émission, l'atténuation par la poussière et les taux de formation stellaire. Un second travail sur un projet de simulation en utilisant CIGALE pour créer des catalogues de spectres fictifs dans le cadre de la collaboration MOONS.

Pour le travail d'ajustement spectro-photométrique des SEDs dans la partie II, j'ai ajusté simultanément des données photométriques et spectroscopiques avec CIGALE dans le champ Cosmic Evolution Survey (COSMOS) en utilisant la photométrie de LAIGLE et al. (2016) et les flux de raies d'émission du survey FMOS-COSMOS (Fiber Multi-Object Spectrograph) (KASHINO et al., 2013; SILVERMAN et al., 2015). Un échantillon de 183 objets a été sélectionné pour avoir des mesures de flux de Hα et de [OIII]λ5007 à S/N > 3 dans le relevé FMOS-COSMOS à $1,40 < z < 1,68$. Dans un premier temps, j'ai effectué un ajustement de la SED sur cet échantillon couvrant l'émission continue de l'ultra-violet jusqu'au infrarouge lointain avec 21 fluxes à large bande et les flux des raies d'émission Hα. La conservation du bilan énergétique implementé dans CIGALE nous permet d'obtenir des estimations robustes de la quantité d'atténuation des poussières ainsi que de la masse stellaire et du taux de formation stellaire. Dans le cadre de cette étude, je propose dans la partie II de cette thèse une relation pour obtenir l'atténuation par la poussière de la raie d'émission [OIII]λ5007 en fonction de la masse stellaire de la galaxie. Ceci a été motivé par le fait qu'une corrélation positive a été trouvée entre les deux paramètres et qu'une approche similaire existe déjà pour la raie d'émission Hα. J'ai verifié que la consistence entre l'attenuation par la poussière de la raie Hα et la masse stellaire comment presenté par GARN et BEST (2010a). Il faut noter que la relation proposé peut-être utilisé pour faire des estimations de l'attenuation par la poussière de façon statistique mais pas individuelment. Les valeurs médianes de l'atténuation de la raie d'émission $A_{H\alpha} = 1,16 \pm 0,19$ mag et $A_{[OIII]} = 1,41 \pm 0,22$ mag sont rapportées. L'atténuation relative affectant les différentes populations est caractérisée par le paramètre μ dans la loi d'atténuation proposé par CHARLOT et FALL (2000). Je rapporte une valeur de $\mu = 0,57 \pm 0,14$ cohérente avec différents travaux dans la littérature et deux fois plus grande que la valeur originale proposée par CHARLOT et FALL (2000). Les résultats sont cohérents avec l'émission nebulaire étant plus atténuée que le continuum stellaire.

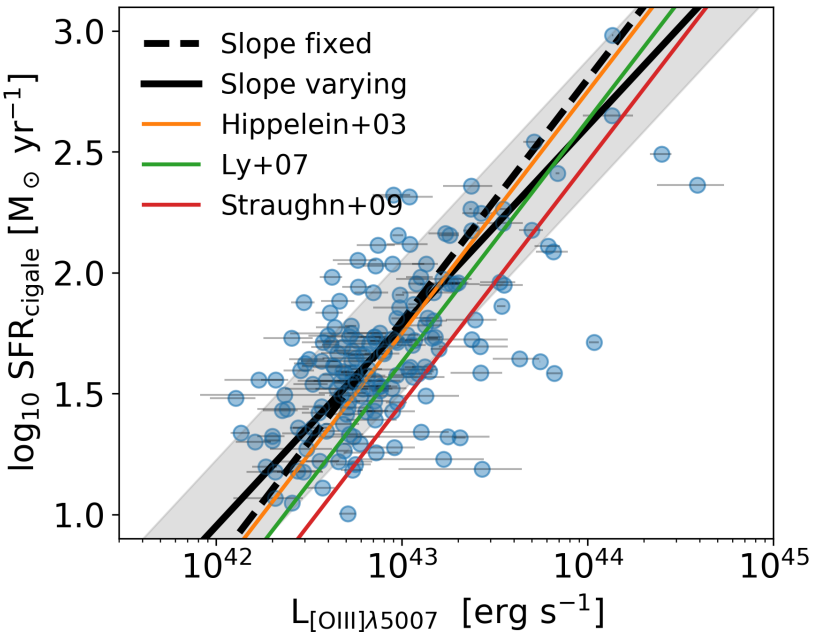

FIGURE 0.1. – Relation entre la luminosité corrigée de [OIII]λ5007 et le SFR. Les lignes noires pointillées et continues correspondent à l'ajustement linéaire utilisant une méthode de régression par distance orthogonale bootstrapped avec un coefficient de régression de Spearman $\rho_s = 0,57$. La dispersion de 0,32 dex est représentée par une zone grise ombrée. La relation montre une corrélation positive avec une dispersion significativement plus élevée par rapport à la relation KENNICUTT (1998) Hα. Les relations proposées par HIPPELEIN et al. (2003), et LY et al. (2007) sont représentées en orange et en vert, respectivement. STRAUGHN et al. (2009) est également présenté en rouge à titre de comparaison. Les relations sont converties de Salpeter en FMI de Chabrier.

D'autre part, je confirme une corrélation positive entre le SFR et la luminosité [OIII]λ5007 corrigée par les effets de la poussière. Je propose deux relations, une relation avec une pente fixe et une avec une pente libre. Les résultats sont présentés dans la Sec. 3.3. Le choix entre la pente fixée et libre est fait car certains point au-delà $L_{[OIII]} > 10^{44}$ erg s^{-1} pourrons avoir un impact large sur les résultats de la régression linéaire. Nous mesurons une pente cohérente avec l'unité dans la dispersion de 2σ de la relation. Nous estimons un rapport [OIII]λ5007/[OIII] 88 μm de 1,90 pour notre échantillon de galaxies et déduisons une relation SFR-[OIII] 88 μm en accord avec les relations précédentes qui ont été trouvées à la fois à des décalages vers le rouge faibles et élevés, bien que [OIII]λ5007/[OIII] 88 μm dépende fortement de la densité électronique et de la métallicité de la phase gazeuse. La comparasion faite avec la raie d'émission [OIII] 88 μm est motivée dans le cadre de nouveaux relevés spectroscopique qui auront lieu dans le prochaines années par example MOONS, MOSAIC, et PFS. Pour tester la consistenence de l'analyse de la photometrie et les flux de plusieurs

raies d'émission avec CIGALE j'ai fait un autre ajustement. Cet ajustement de la SED, incluant la photométrie, les flux de Hα, Hβ et [OIII]λ5007, est également effectué avec une grille raffinée de modèles de photoionisation et de métallicités estimées à partir de la relation masse-métallicité de CURTI et al. (2020). La métallicité est obtenu en fonction de la masse stellaire et le taux de formation stellaire derivés dans l'ajustement de la photometrie et la raie de Hα. Avec la métallicité er le paramètre d'ionisation calculé par CIGALE j'ai étudié la dispersion dans les rélations mentionées ci-dessus. Les variations de la métallicité en phase gazeuse et du paramètre d'ionisation induisent une dispersion dans la relation SFR-$L_{[OIII]\lambda5007}$ de 0,24 dex et 1,1 dex, respectivement. L'impact plus faible de la métallicité en phase gazeuse est probablement dû à la gamme limitée de notre échantillon (0,006< Z_{gas} < 0,016) et notre relation SFR-$L_{[OIII]\lambda5007}$ ne devrait être valable que pour les galaxies présentant des métallicités en phase gazeuse similaires à celles étudiées dans ce travail. Dans la Fig. 0.1 les résultats de cette partie sont résumés.

Dans la partie III de cette thèse, la création d'un échantillon de spectres fictifs avec CIGALE dans le cadre de la collaboration MOONS a été abordée. Dans un premier temps, j'ai créé un échantillon de galaxies basé sur des hypothèses simples de leurs histoires de formation stellaire pour reproduire des galaxies de type starburst, de type tardif et de type précoce. L'idée principale était d'utiliser cet échantillon pour tester les outils de simulation de MOONS et de fournir aux équipes scientifiques des spectres modélisés pour tester la performance de leurs codes sur différents ensembles de données. Avec l'équipe, nous avons décidé de créer un échantillon de données fictives mais cette fois basé sur des observations réelles. J'ai choisi de travailler sur le champ COSMOS car dans la partie II, j'ai déjà travaillé sur l'échantillon spectro-photométrique mais aussi parce que c'est l'un des trois principaux champs qui seront observés par MOONS. Je réalise un ajustement SED de l'ultra-violet jusqu'à l'infrarouge moyen sur un sous-échantillon de ~ 2000 de galaxies COSMOS2015. Cette première tentative de produire des échantillons fictifs réalistes n'est pas effectuée sur l'ensemble du demi-million de sources, car j'ai effectué une correspondance croisée avec les données FMOS afin de pouvoir comparer les résultats de la SED avec les observations réelles des lignes d'émission. L'idée est de créer une premier échantillon et fixer les paramètres pour extrapoler à l'ensemble du COSMOS2015.

Des hypothèses importantes doivent être faites sur les paramètres de le milieu interstellaire si l'on veut simuler des spectres réalistes par l'ajustement SED uniquement avec des données photométriques. Le paramètre d'ionisation ne peut pas être contraint en utilisant seulement l'émission à large bande, donc certaines relations dans la littérature ont été testées afin d'estimer ce paramètre basé sur la métallicité de la phase gazeuse (voir, Sect. 7.1). La métallicité en phase gazeuse est également un paramètre principal qui doit être affiné. Pour cela, j'ai mis en œuvre la même approche que dans la partie II en utilisant la relation CURTI et al. (2020) qui permet d'obtenir la métallicité en phase gazeuse en fonction de la masse stellaire et du taux de formation stellaire estimés avec CIGALE. La création de données de spectres fictifs est un proces-

sus complexe dans lequel il faut être prudent sur les hypothèses faites pour être aussi proche que possible de la réalité. De plus, à des décalages vers le rouge intermédiaires et élevés, il existe des divergences bien connues sur la reproduction des flux de raies d'émission par la modélisation de la région HII. Cependant le paramètre d'ionisation et la metallicité en phase gazeuse sont très importantes pour la modelization fidele de l'émission nebulaire. Dans la Fig. 0.2 un example des spectra obtenu par l'ajustement SED des galaxies dans le champ du COSMOS est presenté.

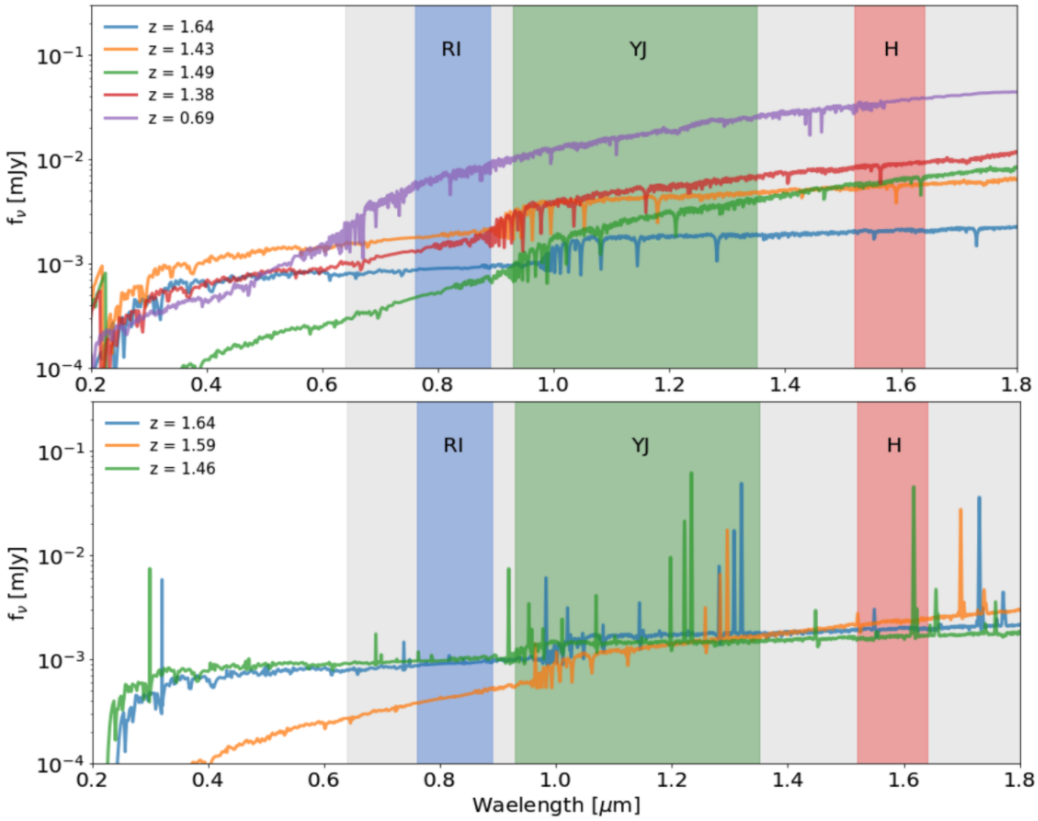

FIGURE 0.2. – Spectres fictifs modélisés avec CIGALE sur la base des observations réelles du champ COSMOS. Le panneau supérieur montre le modèle de continuum stellaire pour cinq sources différentes entre 0,69≤ z ≤ 1.64. Le volet inférieur montre le continuum et les raies d'émission pour trois objets entre 1.46 ≤ z ≤ 1.64. Dans ce cas, les flux ne sont pas normalisés par rapport à la masse totale comme dans la Fig. 6.1. Les zones ombrées en bleu, vert et rouge correspondent aux bandes *RI, YJ* et *H* de MOONS en mode haute résolution tandis que la zone ombrée en gris correspond au modèle basse résolution.

Pour conclure, ce travail propose de nouvelles relations entre les paramètres physiques des galaxies à décalage vers le rouge intermédiaire et la raie d'émission [OIII]λ5007. La combinaison des données photométriques et spectroscopiques dans les futures

analyses SED est primordiale pour établir des contraintes sur les paramètres liés au SFH et à l'atténuation. Les informations spectroscopiques aident à briser les dégénérescences et permettent d'étudier les galaxies de manière plus homogène en utilisant l'ajustement SED. La nécessité de mettre à jour les logiciels d'ajustement SED en termes de modèles d'émission nébulaire est essentielle pour préparer les futurs ensembles de données provenant de grandes études spectroscopiques. La compréhension des divergences dans les diagrammes d'excitation à un décalage vers le rouge intermédiaire reste cruciale pour modéliser correctement l'émission des régions HII. Cette thèse est une première tentative pour tester les performances de CIGALE en tant qu'ajusteur spectro-photométrique de SED mais aussi en tant que modélisateur de spectres. L'avenir de l'ajustement SED incluant les lignes d'émission est vraiment prometteur.

Mots clés : catalogues, galaxies : à haute redshift, galaxies : ISM, infrarouge : galaxies, ISM : poussières, extinction

Abstract

Galaxies are the building blocks of the Universe. Understanding their role in the cosmos translates into studying their emitted light from a multi-wavelength perspective as a large variety of physical processes inside galaxies are responsible for the radiation we observe.

This thesis is divided into three main parts. Part I takes the reader through a brief introduction to the state of the art of galaxies from a panchromatic point of view. A journey from the Big Bang through the evolution of galaxies across the Universe using a multi-wavelength construction to understand the different processes ongoing inside galaxies that give rise to what we observe. Galaxies are discussed in the context of spectral energy distribution (SED) fitting giving particular importance to the stellar and dust emission, as well as the dust attenuation effects. The importance of current SED fitting and the Bayesian estimation of the physical parameters is highlighted. Common derived properties such as stellar-mass, star-formation rate (SFR), gas, and dust properties are discussed at the end.

In part II, I present a SED fitting analysis carried out with CIGALE on a spectro-photometric sample. In chapter 2, the photometric sample covering from the ultra-violet (UV) to the far-infrared (FIR) using the Laigle et al. (2016) COSMOS2015 catalog along with the HELP database is described as well as the emission-line fluxes from the FMOS-COSMOS survey of Kashino et al. (2013) and Silverman et al. (2015). In this work, I characterized a sample of 182 objects with Hα and [OIII]λ5007 emission line measurements lying in a redshift range of $1.40 < z < 1.68$. The assumptions and tests on star-formation history (SFH), nebular emission, dust attenuation, and emission are thoroughly addressed in chapter 3. In this chapter, I discuss in particular the [OIII]λ5007, Hα, and SFR estimation through SED fitting using photometry and Hα fluxes, and the importance of the nebular parameters such as gas-phase metallicity and ionization parameter when studying emission lines. The sample covers a range of $10^{9.5} - 10^{11.5}$ $M_\odot$ and $10^{1} - 10^{3}$ $M_\odot$ yr^{-1}, with emission line attenuation of $A_{H\alpha} = 1.16 \pm 0.19$ mag and $A_{[OIII]} = 1.41 \pm 0.22$ mag. A difference of 57% in the attenuation experienced by emission lines and continuum is found in agreement with the emission lines being more attenuated than the continuum emission. SFR and [OIII]λ5007 are found to be correlated after dust-correction and two relations are proposed using a free and fixed slope lineal fits. In chapter 4, a test including Hα, Hβ, and [OIII]λ5007 emission line fluxes in the SED fitting is used to understand the dispersion in the SFR-[OIII]λ5007 relation proposed in chapter 3. The spread in the relation is driven by differences in the gas-phase metallicity and ionization parameter

accounting for a 0.24 dex and 1.1 dex of the dispersion, respectively. We report an average value of $\log U \approx -2.85$ for this sample of galaxies. Current discrepancies in the locus of galaxies in the excitation diagrams at intermediate redshift are discussed and the current state of HII-region modeling.

Finally, in Part III, I present the Multi-Object Optical and Near-IR spectrograph (MOONS) instrument in the context of extra-galactic Astronomy. An introduction to the relevant characteristic of the instrument in terms of spectroscopy is described in chapter 5 and its relation to the work presented in Part II. I address the ongoing work using CIGALE as a simulator to create galaxy spectra to test the calculators and exposure software of the instrument in chapter 6. A work base on a simple mock sample (i.e., models not necessarily related to observed galaxies) is described in this chapter. I created a set of objects which were later passed through the MOONS ETC and distributed to different working groups to test photometric redshift estimation software as well as to put constraints on expected magnitude limits. Different assumptions and the way CIGALE works are thoroughly described in this part of the thesis. In chapter 7, the current mock catalog generation procedure based on the UV-to-MIR data of the COSMOS field is developed focusing on the importance of nebular emission modeling. I show how as part of the collaboration we use a sub-sample of the COSMOS2015 catalog cross-matched to the FMOS-COSMOS survey to restrict parameters related to the nebular emission such as the ionization parameters and the gas-phase metallicity to model galaxies. This modeling strategy is still ongoing and we are in a trial stage as part of the scientific working groups of MOONS. A first mock catalog was distributed in the consortium to test outflows on the continuum. Conclusions and perspectives of this work are presented at the end, in particular, giving importance to the future of SED fitting using spectro-photometric samples but also on machine-learning techniques implementation to improve the executing time in future SED fitting software.

Keywords: catalogs, galaxies: high-redshift, galaxies: ISM, infrared: galaxies, ISM: dust, extinction

Acknowledgments

First and foremost I would like to thank my supervisor Dr. Véronique Buat, who encouraged me to do research in a completely different fashion, in a branch of Astronomy which encapsulates the beauty of the effects of dust in galaxies. I am extremely grateful for all the new things she taught me in order to be a good researcher and to pave my way as a scientist. I learned so many things, quite important for my future both as a person and as a researcher. To the thesis committee, Vivienne Wild, Thierry Contini, Olivier Ilbert, Lucia Pozzetti, Roser Pelló, and Patrice Theulé for helping me achieve this goal.

I dedicate this step in my career to my parents, Jorge Mario Villa Marín and Gladys Vélez Muñoz who have trusted in me along these years, always supporting my dream of becoming an Astronomer. They have always been an important shoulder I can rely on to take every step forward on my way to be a good scientist. Who I am right now, it is thanks to them, just because of being good parents and teaching me how to be a good person and accepting myself as I am. To all my family in Colombia (Yanet Zuluaga, Jonatan Zuluaga, Aida Vélez, Juan José Alzate, Ana Sofía Alzate, María Isabel Alzate) and in the USA (Yomaira Estrada, Víctor Estrada, Jeniffer Estrada, Esteban Estrada, Bryan Estrada, Jaime Muñoz-Lundquist, William Muñoz-Lundquist and Margaret Muñoz-Lundquist) because this dream would not have become real without their enormous help and trust. Last but not least, to the ones who now live among the stardust in the cosmos which I will reunite with at some point of this journey called life (Joaquín Zuluaga Betancur, María Egarlina Muñoz, Marta Rocío Muñoz, Rodrigo Vélez Jaramillo).

When I arrived in France after living in the Netherlands for two years I was in a shock. I left Amsterdam during a cold morning at −5C and arrived in Marseille with 30C. Everyone speaking French around me, not able to communicate, new culture, new world, my brain collapsed. The first days at LAM were crucial for me to settle down and progress in my new life which I knew if was going to last at least for three years by the Mediterranean sea. Three years after I see how lucky I was to meet Jana Bogdanoska my friend, office-mate and confident during all this time. I dedicate this to our funniest moments and beautiful memories we built in this city. To my closest friends Alessia Longobardi, Elena Sarpa, Arturo Núñez, Junais Madathodika, Gayathri Gururajan, Ambra Nanni, Simona Lombardo, Davide Punzo, Segio Hoyer, Valentina Abril, Romain Fétick, Mandy and Sean Morrison, and Abhishek Maniyar who were always there to share good times watching movies, partying, enjoying beach days, having apéros, hiking and beautiful moments that make life rich and valuable. Also to

Iva Laginja, Kelly Joaquina, Mona El Morsy, Olivier Kauffmann, Emily Bourne, Grégoire Aufort, Jana Kushanova, and Jesús López. To the new Ph.D. students I had the pleasure to meet during my last year Athanasia Gkogkou, Mathilde van Cuyck, Lucie Khlat (Ce n'est chocolatine ;)) and Diana Ismail. To my Spanish speaking gang at LAM Steven Rendón, Pía Cortés, and Lorena Acuña. Special thanks to Françoise Maxant for helping me from day one to get through the French administration and make all the process as completely smooth but primarily for her unconditional charm and love shared with me making me feel extremely welcomed to LAM. I will never have enough words to thank all you did for me. To my Colombian friends Carol Ann, Katherine Santa, Jeniffer Arboleda, Mónica Villa, Yeniffer Angarita, César Uribe, Malory Agudelo, who I always have in my mind even if we are oceans apart. To my friends in Netherlands Marta Figueiredo, Kathy Fourment, Lina Bayona, Guadalupe Cañas, Felipe Ramos and in Australia Juan Espejo. To the chachos in Marseille Rafael Arango, Juliana, Juan, Beatriz, Daniel, Dorian, Andrea and Eduardo who made Marseille warmer with their presence and make it feel like home. To my flatmates and ex-flatmates Maria Filannino, Hippolyte Reignier, Daisuke Kaku, Solène Miral, Constantin Baltès and Jérémy Richier who were always there interested on my research, unforgettable summers and good dinners together. I was lucky to meet other PhD students, postdocs and friends who made this step in my life bearable even during COVID times which was and is a really tough period of our lives.

Sometimes we are busy making others happy and we do not think about us. In February 2019 after watching some gay movies as 'called me by your name' and 'Mario' I realized than hiding and not living a proper life, free and happy as other human beings is not worth it. I told my parents I was gay and it was one of the best decisions I have ever taken in my life. After that I felt free to live my life as free human, a free person with a free spirit, and show my true self to the world. This decision took me to meet a beautiful person who not only helped to improve my French but also who showed me the good side of living in this beautiful country, who taught me how to enjoy life, and be who I am. Special thanks to Gaëtan Escudero my boyfriend because he gave me enormous support during my worst days, cheering me up, giving me force to continue, encouraging me to not back down and to look always forward. It is not easy to stay next to a person stressing our while writing a Ph.D. thesis in Astronomy but he definitely made everything worth it. To his family Véronique Escudero, Thierry Escudero, Karine Escudero, la petite Anna Rabillé, and Fabian Rabillé, and of course Mémé (Juliana Gueguen) for making me feel part of their family and showing me kindness. To Marion Di Majo, Hugo Vicat, Emily, Paul Pagnier, Marius Blondel, Elizabeth, and all the amazing architects I got to meet during this time Caro and Baptiste Vassy, Yohan, Marylou, Clémentine, Maëva, Léa and Jules. I never taught I was gonna learn so much about buildings and construction laws in my life :P.

Of course, the best of all this adventure is that I ate a lot of cheese and had good wines in the beautiful region of Haute-Savoie and in France in general. Muchas gracias a todos. Estaré eternamente agrecido con cada uno de ustedes :)!

Fables should be taught as fables, myths as myths, and miracles as poetic fancies. To teach superstitions as truths is a most terrible thing. The child mind accepts and believes them, and only through great pain and perhaps tragedy can he be in after years relieved of them. In fact, men will fight for a superstition quite as quickly as for a living truth—often more so, since a superstition is so intangible you cannot get at it to refute it, but truth is a point of view, and so is changeable.
—Hypatia of Alexandria (born c. 350–370; died 415 AD) Hellenistic Neoplatonist philosopher, astronomer, and mathematician.

L'Astronomie est peut-être la science où le plus petit nombre de découvertes est dû au hasard la science où l'esprit humain apparaît dans toute sa grandeur et par laquelle l'homme peut le mieux s'instruire de son néant.
—Le Miroir de l'âme (1773-1796) de Georg Christoph Lichtenberg.

L'algèbre est dans l'astronomie, et l'astronomie touche à la poésie ; l'algèbre est dans la musique, et la musique louche à la poésie. L'esprit de l'homme a trois clefs qui ouvrent tout : le chiffre, la lettre, la note. Savoir, penser, rêver. Tout est là.
—Les Rayons et les Ombres (1840), Préface de Victor Hugo.

Wat mij betreft weet ik niets zeker, maar naar de sterren kijken zet me aan het dromen.
—Vincent Willem van Gogh (1853 —1890) Dutch Post-Impressionist painter.

It is sometimes said that scientists are unromantic, that their passion to figure out robs the world of beauty and mystery. But is it not stirring to understand how the world actually works —that white light is made of colors, that color is the way we perceive the wavelengths of light, that transparent air reflects light, that in so doing it discriminates among the waves, and that the sky is blue for the same reason that the sunset is red? It does no harm to the romance of the sunset to know a little bit about it.
—Carl Sagan, Pale Blue Dot: A Vision of the Human Future in Space (1935 - 1996) American astronomer, cosmologist, astrophysicist, astrobiologist, author, science popularizer, and science communicator in astronomy and other natural sciences.

In third Dialogue there is first denied that base illusion of the shape of the heavens, of their spheres and diversity. For the heaven is declared to be a single general space, embracing the infinity of worlds, though we do not deny that there are other infinite 'heavens' using that word in another sense. For just as this earth hath her own heaven (which is her own region), through which she moveth and hath her course, so the same may be said of each of the innumerable other worlds.
—Giordano Bruno (1548 —1600) Italian Dominican friar, philosopher, mathematician, poet, and cosmological theorist.

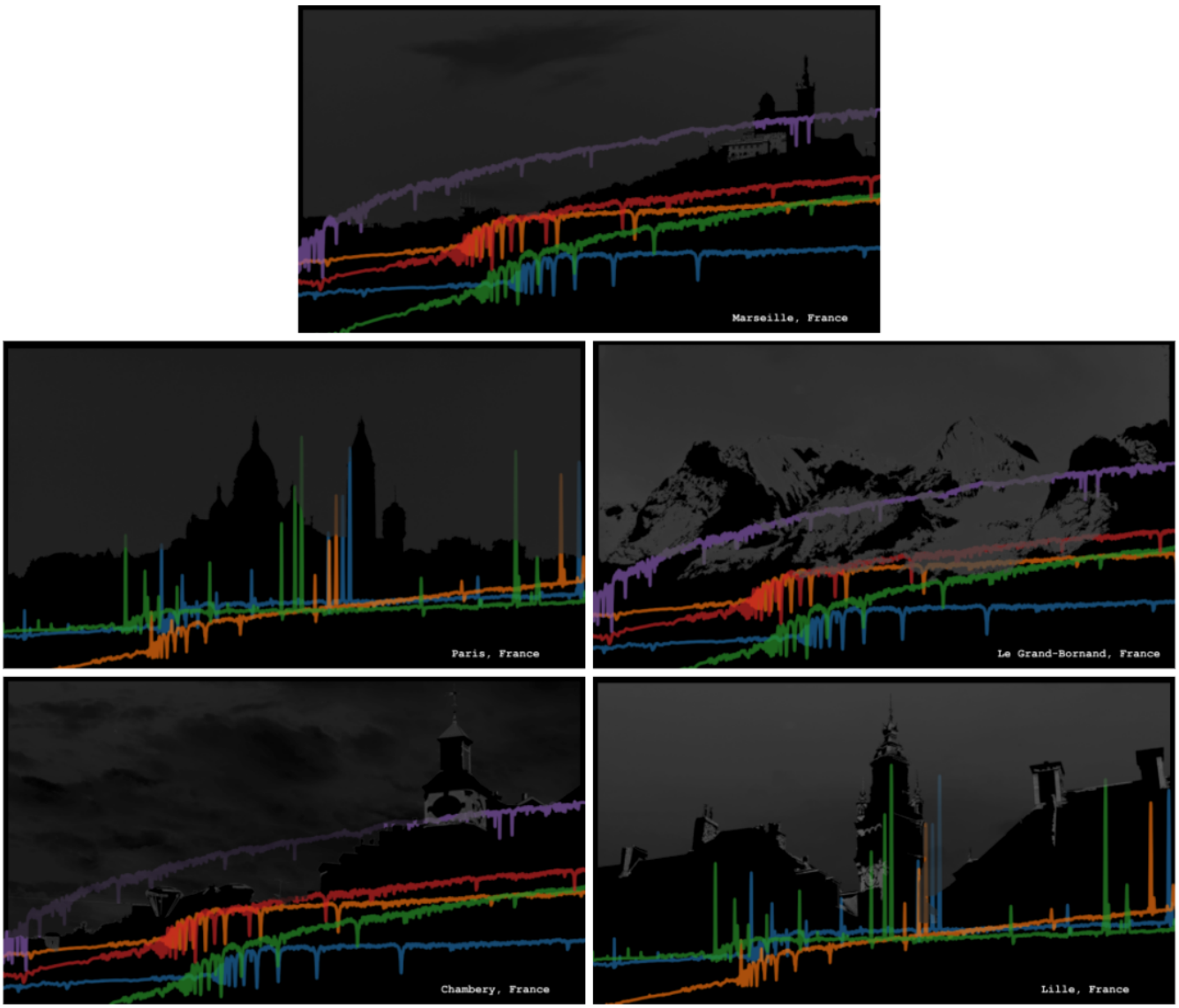

À la cité phocéenne qui m'a accueilli comment un de ses marins. À la ville lumière qui m'a redonné la force pour aller jusqu'au bout. À la Haute-Savoie qui m'a apporté le plus beau cadeau de la vie, l'amour. À la cité des ducs qui m'a enroulé dans ses bras alpins. À la capitale des Flandres qui m'a montré la diversité de la république.

Contents

List of Figures

List of Tables

List of Acronyms

AGN - Active Galactic Nucleus/Nuclei
ALFALFA - Arecibo Legacy Fast ALFA Survey
ALMA - Atacama Large Millimeter/submillimeter Array
Bagpipes - Bayesian Analysis of Galaxies for Physical Inference and Parameter EStimation
BC - Birth Cloud
BD - Balmer Decrement
BEAGLE - BayEsian Analysis of GaLaxy sEds
BPASS - Binary Population and Spectral Synthesis code
BPT - Baldwin, Phillips, and Terlevich diagram
CIGALE - Code Investigating GALaxy Emission
CITEVA - Centro de Astronomía de la Universidad de Antofagasta
CFHT - Canada France Hawai'i Telescope
CF00 - Charlot and Fall
CMB - Cosmic Background Radiation
COSMOS - Cosmic Evolution Survey
CXO - Chandra X-ray Observatory
C00 - Calzetti
DEIMOS - DEep Imaging Multi-Object Spectrograph
2dF Galaxy Redshift Survey - 2-degree-Field Galaxy redshift survey
ETC - Exposure Time Calculator
ELT - Extremely Large Telescope
FIR - Far-infrared
FIRST - Faint Images of the Radio Sky at Twenty cm
FMOS - Fiber-Multi Object Spectrograph
FMR - Fundamental metallicity relation
FPU - Fiber Positioning Units
FSPS - Flexible Stellar Population Synthesis
GALEX - Galaxy Evolution Explorer
GOODS - Great Observatories Origins Deep Survey
HELP - Herschel Extragalactic Legacy Project
HIJASS - HI Jodrell All-Sky Survey
HIPASS - HI Parkes All Sky Survey
HR - High-resolution
HSC - Hyper Suprime-Cam
IGM - Intergalactic Medium
IMF - Initial Mass Function
IR - Infrared
IRAC - Spitzer Infrared Array Camera
IRAS - Infrared Astronomical Satellite
IRX - Infrared excess
IP - Ionization potential
ISM - Interstellar Medium
JWST - James Webb Space Telescope [1] [2]
KBSS - Keck Baryonic Structure Survey
LAM - Laboratoire d'astrophysique de Marseille
lePHARE - PHotometric Analysis for Redshift Estimations
LMC - Large Magellanic Cloud
LoTSS - LOFAR Two-metre Sky Survey
Λ-CDM - Lambda-Cold Dark Matter Model
MAGPHYS - Multi-wavelength Analysis

1. https://www.nature.com/articles/d41586-021-02010-x
2. https://www.nature.com/articles/d41586-021-02678-1

of Galaxy Physical Properties
MCMC - Monte– Carlo Markov Chain
MIPS - SpitzerMulti-Band Imaging Photometer
MIR - Mid-infrared
MOONRISE - MOONS Redshift-Intensive Survey Experiment
MOONS - Multi Object Optical and Near-infrared Spectrograph
MOSAIC - Multi-Object Spectrograph for Astrophysics, Intergalactic-medium studies and Cosmology
MOS - Multi-Object Spectrometers
MOSDEF - MOSFIRE Deep Evolution Field
MSE - Maunakea Spectroscopic Explorer
MUSE - Multi Unit Spectroscopic Explorer
MZR - Mass-metallicity relation
2MASS - Two Micron All Sky Survey
NIR - Near-infrared
NUV - Near ultra-violet
NVSS - NRAO VLA Radio Survey
OB - Observing Blocks
OPS - Observation Preparation Software
PACS - HerschelPhotodetector Array Camera and Spectrometer
PAH - Polycyclic Aromatic Hydrocarbon
PDF - Probability distribution function
PDR - Photodissociation region
PFS - Subaru Prime Focus Spectrograph
Prospector - Python code for Stellar Population Inference from Spectra and SEDs
REDWAY - MOONS REDdened Milky WAY
RMF - Returned Mass Fraction
SCUBA-2 - Submillimetre Common-User Bolometer Array 2
SED - Spectral energy distribution
SDSS - Sloan Digital Sky Survey
SFH - Star Formation History
SMBH - Suppermassive Black Hole
SMC - Small Magellanic Cloud
SNR - Signal-to-noise ratio
SPIRE - Herschel Spectral and Photometric Imaging REceiver
SPLASH - Spitzer Large Area Survey with Hyper-Suprime-Cam
SSP - Single Stellar Population
Sub(mm) - Submillimeter
Suprime-Cam - SUBARU Prime Focus Camera
UKIRT - United Kingdom Infra-Red Telescope
UV - Ultra-violet
VANDELS - Deep VIMOS survey of the CANDELS CDFS and UDS fields
VLT - Very Large Telescope
WIRCam - MegaCam and Wide-field InfraRed Camera
WFC - Wide Field Infrared Camera
XMM-Newton - X-ray Multi-Mirror Mission

Part I.

Galaxies in a panchromatic context

1. Multi-wavelength background: Spectral energy distribution fitting

Contents

1.1. A brief story of the Universe

In the beginning, there was nothing, or there was, but all compacted in a singularity, a point of infinite density and gravity where all we see nowadays in the cosmos (Ancient Greek: κόσμος) was contained. Space and time did not exist per se in the form we see them today meaning that the origin of the Universe takes place at no place and no time. It all starts 13.8 billion years ago with the Big Bang, a great explosion that gave birth to the Universe as a result of the expansion of the singularity proposed in 1931 by Georges Lemaître (Lemaître, 1931a; Lemaître, 1931b). This is the most widely accepted and popular theory at the moment to understand how the Universe came into being although not the only one (e.g., Bondi and Gold, 1948; Frampton, 2006, Steady State Theory or the Oscillating Universe Theory). I will briefly address the most important transition epochs of the Big Bang theory below but a good summary can be found in Coles and Lucchin (2002).

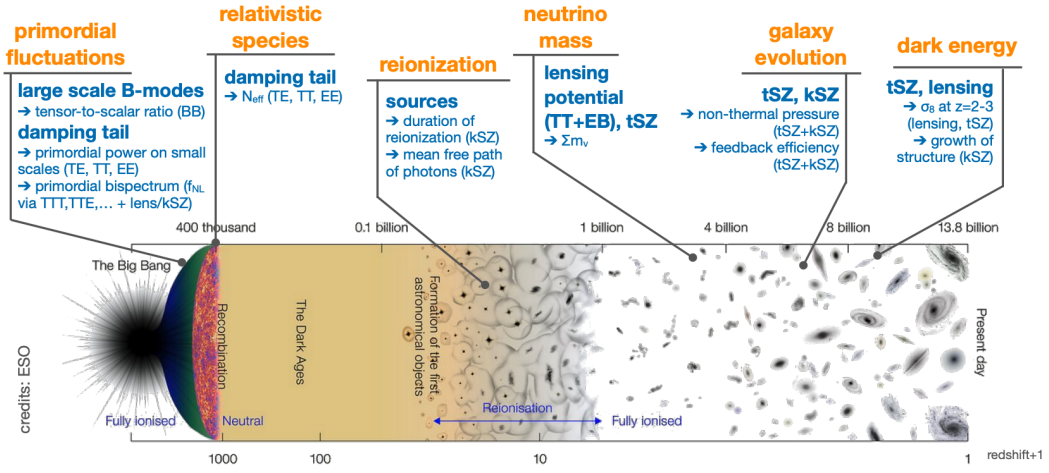

Figure 1.1. – Universe evolution. A diagram of the Universe evolution is presented covering the most relevant epochs from the Big Bang to the present day. Image credits: European Southern Observatory (ESO).

Chronologically, all starts with a singularity at a time known as the Planck Epoch (or Planck Era). This period expands from time zero to approximately 10^{-43} seconds. All the fundamental forces of physics (i.e., gravity, weak and strong interaction and electromagnetism) are immersed in the infinite dense singularity. The state of the Universe at this epoch is quite unstable crossing a transition temperature of 10^{32} K at a time between 10^{-43} and 10^{-36} leading to the separation of the gravitational force from the other forces (see, Coles and Lucchin, 2002, and references therein). At a temperature of roughly 10^{28} K, the electroweak and strong forces separate after 10^{-36} to 10^{-32} seconds of the Big Bang's creation. The separation of the fundamental forces leads to a period in which the Universe starts to rapidly expand known as the Inflation

Epoch (Linde, 1982; Albrecht and Steinhardt, 1982) characterized by high temperatures and pressure allowing the Universe to grow exponentially and cool down. In this period the random motions of the particles reach relativistic speeds as a result of the high temperatures. Particle and antiparticles are created and destroyed as a result of the collisions in a physical process called Baryogenesis in which an imbalance of matter and antimatter led to the present predominance of matter in our Universe. Once the inflation epoch stops around 10^{-12} seconds, the electroweak force separates into the electromagnetic and weak nuclear forces and the Universe has a reached a temperature of 10^{16} K (Weinberg, 1967; Salam, 1968; Georgi and Glashow, 1974). From this time, the Universe is not anymore a hot soup of matter and photons in equilibrium but a soup of elementary particles built of photons, quarks, electrons, and neutrinos in a period known as the Quark Epoch. At 10^{-6} seconds, in the Hadron Epoch, the temperature falls to 10^{13} K allowing the combination of quarks into hadrons (protons and neutrons) and the emergence of matter as we see it today after the annihilation of proton/anti-proton pairs (Coles and Lucchin, 2002). We have entered the Lepton Epoch where the production of lepton/anti-lepton pairs is still possible due to the high temperature producing the Leptogenesis resulting in both the creation of the same number of electrons and protons between 10^{-1} and 10 seconds and the decoupling of neutrinos around 1 second (Weinberg, 1967). Temperature drops to 10^{9} K after three minutes of the Big Bang giving raise to the nucleosynthesis, a process in which protons and free neutrons merge together to form H^2 (Deuterium) and He^4 (Helium) resulting in a primordial abundance of ~ 75% and ~ 25% for the Hydrogen and Helium atoms (Alpher, Bethe, and Gamow, 1948; Gamow, 1948b). Some traces of stable isotopes like H^2, He^3, and atomic elements like Li (Lithium), Be (Beryllium), and B (Boron) are also formed (Alpher, Bethe, and Gamow, 1948; Alpher and Herman, 1948; Gamow, 1948b; Gamow, 1948a).

The turmoil of the first minutes in the creation of the Universe is in the past and the Epoch of Recombination can take place after 300000 years and a temperature of 3000 K (Coles and Lucchin, 2002). Previous to this epoch the Universe is opaque to photons and it is here when the Universe starts becoming transparent as photons are liberated, and electrons and nuclei can combine to form neutral atoms. This epoch left an observable imprint known as the Cosmic Background Radiations (CMB), a relic of its origins. CMB expands losing energy reaching today a temperature of ~ 2.7 K placing its emission peak in the microwave wavelength range (Fixsen, 2009). At this epoch, the Universe is mostly built of neutral hydrogen and helium atoms that can absorb ultra-violet (UV) photons. As the primordial stars are not formed yet there exists no visible or infrared radiation. The Universe is at an epoch known as the Dark Ages. However, the Universe is still rapidly evolving and temperatures keep on cooling down reaching 30 K (Coles and Lucchin, 2002). Matter can start collapsing into the gravitational wells organizing itself into large-scale structures which after 500 Myr to 1 Gyr of the Big Bang will start forming the first objects in the universe (i.e., the first generation of stars) giving end to the Dark Ages and rise to light. The first galaxies and quasars are also formed and stellar evolution starts taking place enriching the

medium with new generated heavy metals from supernova explosions. The UV radiation created from these new objects starts creating ionized regions around them and after a high number of sources are formed, the hydrogen outside them that is spread in the Universe becomes fully ionized entering the Reionization Epoch which marks the gas transition from neutral to ionized. Galaxy evolution takes place after this epoch enriching the intergalactic medium with metals product of massive stars dying inside the galaxies via supernovae. Mergers of galaxies occur increasing the total mass of the galaxies creating massive objects that we observe today at ~ 14 Gyr after the Big Bang with a global Universe's temperature of ~ 2.7 K. This evolution leads to the matter being distributed on structures covering different sizes from planets and stars, to galaxies and galaxy clusters. The most accepted cosmological paradigm corresponds to the Lambda-Cold Dark Matter model (Λ-CDM), in which Dark Energy constitutes about 68.3% of the Universe with the matter distributed in a 26.8% of Dark Matter and 4.9% of Baryonic Matter (Planck Collaboration et al., 2020). Dark energy and Dark Matter are nowadays a hot topic and they are still not entirely understood. This scenario predicts an accelerated expansion of the Universe caused by the repulsive effects of the Dark Energy that overpowers gravity and pushes the Universe apart.

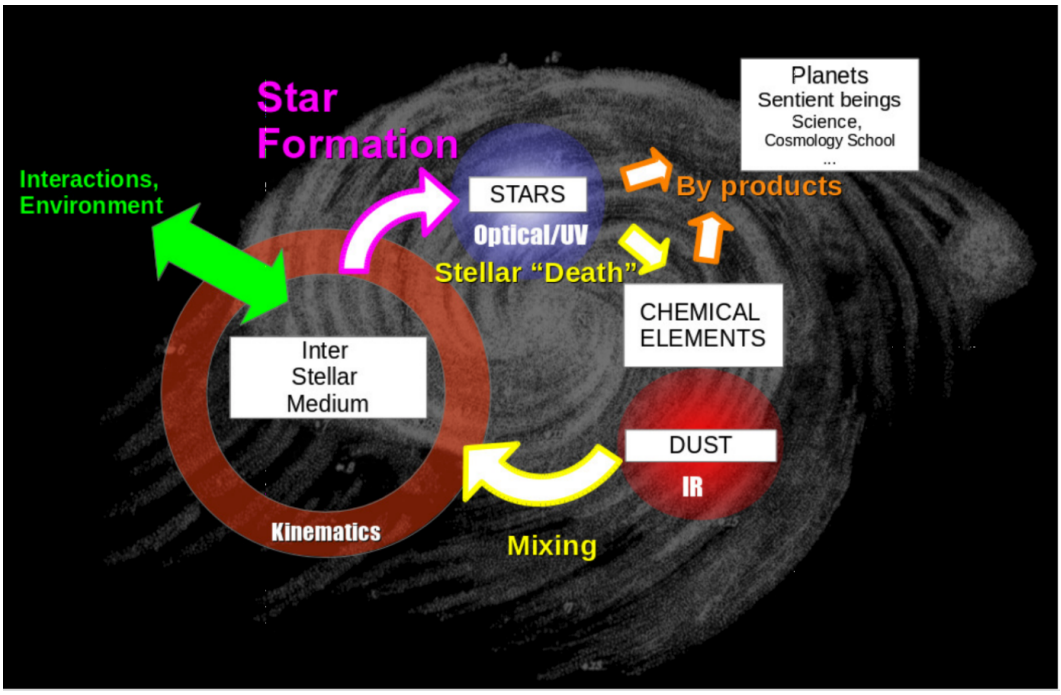

Figure 1.2. – Chemical evolution cycle in a galaxy. The figure shows how the interstellar medium of a galaxy is enriched by the evolution of stars and the environment interactions. Different contributions at specific wavelength ranges are shown. The figure is taken from Boissier (2017) where the background is a Messier 51 drawing of Lord Rosse drawn in 1845.

In this cosmological context, galaxies interact with the large-scale structure through-

out their formation and evolution. Thus, understanding the formation and evolution of galaxies is paramount to know more about how the Universe used to look like in the past and how that evolution turned into what we observe today. Let's focus on galaxies as the final result of the Baryonic matter that fell into the gravitational potential wells forming an agglomerate of gas and stars. Stars in the galaxy will evolve enriching the surrounding primordial interstellar medium (ISM), regulating the chemical evolution cycle (see, Fig. 1.2). Evidence on the past history of galaxies, their inside-out formation, the evolution of abundance gradients among others can be studied through chemical evolution models which are strongly related to important concepts as the initial mass function (IMF), the star formation rate (SFR), the returned mass fraction (RMF), among others (Boissier, 2017). From a general point of view as presented in Fig. 1.2, the first population of stars will transform the primordial gas in their cores during their lifetime enriching the ISM. These new chemical elements will be released once the star dies and a large fraction can be found in the form of dust grains. Star formation can be triggered by gravitation interactions with other galaxies, galaxy-mergers, and supernovae winds, producing the collapse of the enriched gas clouds and forming new stars with a heavy element abundance composition. It is important to note here that primordial stars emit light covering the UV-optical wavelength range (younger/bluer). The UV photons will heat the dust produced by the stellar evolution process and will re-emit this energy to the far-infrared (FIR) range. Old stars have also a contribution to the near-infrared (NIR) part of the electromagnetic spectrum. In this evolutionary process, some byproducts are produced such as the formation of planets around the stars, and the stellar winds which will blow away material out of low-mass galaxies (Boissier, 2017). All these interactions occur in a cosmological scenario in which the galaxies are immersed inside the cosmic web and they will interact with each other.

Two of the most common and well-known derived parameters in extragalactic astrophysics are the stellar mass and SFR. These two parameters help us to study galaxies and understand their evolution across the Universe. They are the basis of the stellar mass and SFR plane (see, Fig. 1.3) of galaxies in which a tight correlation is observed (e.g., Noeske et al., 2007; Elbaz et al., 2011; Pannella et al., 2015; Whitaker et al., 2012; Schreiber et al., 2015; Tomczak et al., 2016) for the majority of the objects known as the main sequence. Galaxies above the main sequence ($\sim 4\times$) are called starburst galaxies. They are characterized by a high star formation rate and prominent emission lines. Below the main sequence in the so-called green valley populated with disk-like and bulge-dominated transient systems, and the red sequence conformed by spheroidal-like shaped galaxies with low SFR and quiescent galaxies, respectively (Lee et al., 2018). Time evolution of SFR is generally measured from the main sequence (Rodighiero et al., 2011; Sargent et al., 2012; Renzini and Peng, 2015).

Figure 1.3. – Stellar mass and star formation rate plane. The popular classification of galaxy types based on their SFR and stellar mass are shown. Credits CANDELS collaboration.

In general, Astronomers use the emitted light from galaxies to extract valuable information and physically characterize galaxies. At some level, we can call ourselves "*photon torturers*", as we take the incoming light (i.e., photons) at different wavelengths and we extract precise information that tells us a story of what's occurring in these objects. Based on the cosmological evolution context of galaxies and on how they change through cosmic time as their stars evolve, a complete understanding of the evolution requires an analysis of all different components through a multi-wavelength analysis (Boselli, 2011). A more detailed panchromatic view of galaxies is presented in the following chapters. Their multi-wavelength study is put into context to understand the internal ongoing physical processes of these amazing inhabitants of our Universe.

1.1.1. Galaxies in a multi-wavelength context

A coherent picture of galaxies is achieved by studying galaxies through a multi-wavelength analysis. Different components in a galaxy will emit light in a particular wavelength range leaving their imprint. For example, as presented before, stars will emit energy covering from the UV-to-NIR wavelengths depending on their age. Evolved stars will dominate the NIR emission while the massive young stars will emit mostly at short wavelengths. The dust produced at the end of the life-cycle of stars, grain growth, and by other complex processes gets heated by energetic photons re-processing this energy and re-emitting it in the MIR, FIR, and millimeter domains. Contrastingly, the ionized gas in the galaxies can be observed and studied using emission lines, for example, through the HI line at 21 cm for the atomic gas or the carbon monoxide lines for the molecular component. Supernovae remnants accelerate elec-

Table 1.1. – Emission processes and their respective emitting sources at different wavelength ranges of the electromagnetic spectrum. The table is reproduced from (Boselli, 2011).

Domain	**X-ray**	**UV**	**Optical**	**NIR**	**MIR**	**FIR-sub(mm)**	**Radio**
λ	0.1 – 10 keV (1-100) Å	912-3500 Å	3500-7500 Å	0.75-5 μm	5-20 μm	20 μm-1 mm	1 mm-1 m
			Continuum				
Process	Black body Thermal bremsstrahlung	Black body	Black body	Black body	Thermal emission	Modified black body	Synchrotron
Emitting source	Accretion disk in binary systems Hot gas	Young stars	Intermediate age stars	Old stars	PAH, hot dust grains	Cold dust grains	Relativistic electrons in weak magnetic fields HII-regions
			Main emission lines				
Emission lines		Atomic hydrogen, metals	Atomic hidrogen, metals	Atomic and molecular hydrogen, molecules	PAH	[CII], CO, molecules	HI(21 cm)
Origin		HII-regions	HII-regions	HII-regions	PDR	Giant molecular clouds	Diffuse ISM
Absorption lines		Hydrogen metals	Hydrogen metals	Hydrogen			HI(21 cm)
Origin		Stellar atmosphere, ISM, IGM	Stellar atmosphere	Stellar atmosphere			Diffuse ISM

Note: PAH: Polycyclic Aromatic Hydrocarbons; PDR: photodissociation region; ISM: interstellar medium; IGM: intergalactic medium.

trons through their magnetic fields producing synchrotron radiation which dominates at wavelengths larger than 10^4 μm. The production of unbound electrons in HII regions by young and massive stars creates free-free emission in the millimeter radio and centimeter wavelengths. Recent star formation processes are strongly related to these emissions (Boselli, 2011). In the X-rays domain, we observe different components such as the diffuse ISM of gas-rich systems, the hot gas component of massive elliptical galaxies, and the accretion in binary systems. From this perspective, it is clear that each part of the electromagnetic spectrum shares valuable information on its origin and the physical process producing a given emission. The most relevant physical processes, as well as the sources responsible for radiation at a given wavelength range, are presented in Table 1.1.

A variety of physical processes are responsible for the different emissions at specific wavelength ranges. Then, to understand and study galaxies, we need a panchromatic framework that can only be achieved by observations at different regimes of the electromagnetic spectrum. In the past years, spectroscopic and photometric surveys have observed the nearby Universe (i.e., z ~ 0) mapping the UV to the far-infrared (UV-to-FIR) range. Regarding the photometry, at short wavelengths observations of the ROSAT (Röntgensatellite; Voges et al., 1999) satellite, the High Throughput X-ray Spectroscopy Mission and the X-ray Multi-Mirror Mission (XMM-Newton; Jansen et al., 2001), and the Chandra X-ray Observatory (CXO; Weisskopf et al., 2000) led to valuable observations of the X-rays as well as the Galaxy Evolution Explorer (GALEX; Martin et al., 2005) in the UV. In the optical, NIR, and IR regime, we have observa-

tions from the Sloan Digital Sky Survey (SDSS; York et al., 2000), and Two Micron All Sky Survey (2MASS; Skrutskie et al., 2006), and the Infrared Astronomical Satellite (IRAS; Neugebauer et al., 1984) and AKARI MIR and FIR surveys (Murakami et al., 2007). At longer wavelengths, centimeter and radio surveys like the Faint Images of the Radio Sky at Twenty cm (FIRST; Becker, White, and Helfand, 1995), and NRAO VLA Radio Survey (NVSS; Condon et al., 1998) and The LOFAR Two-metre Sky Survey (LoTSS; Shimwell et al., 2017), respectively. An example of two galaxies observed at different wavelengths covering from the UV to the radio domain is presented in Fig. 1.4. Spectroscopic information is also available covering from the 21 cm emission line in surveys like the HI Parkes All-Sky Survey (HIPASS; Barnes et al., 2001), HI Jodrell All-Sky Survey (HIJASS; Lang et al., 2003), and Arecibo Legacy Fast ALFA Survey (ALFALFA; Giovanelli et al., 2005), and The SDSS and the 2dF Galaxy Redshift Survey (2-degree-Field Galaxy redshift survey; Colless et al., 2001) for emission lines in the optical.

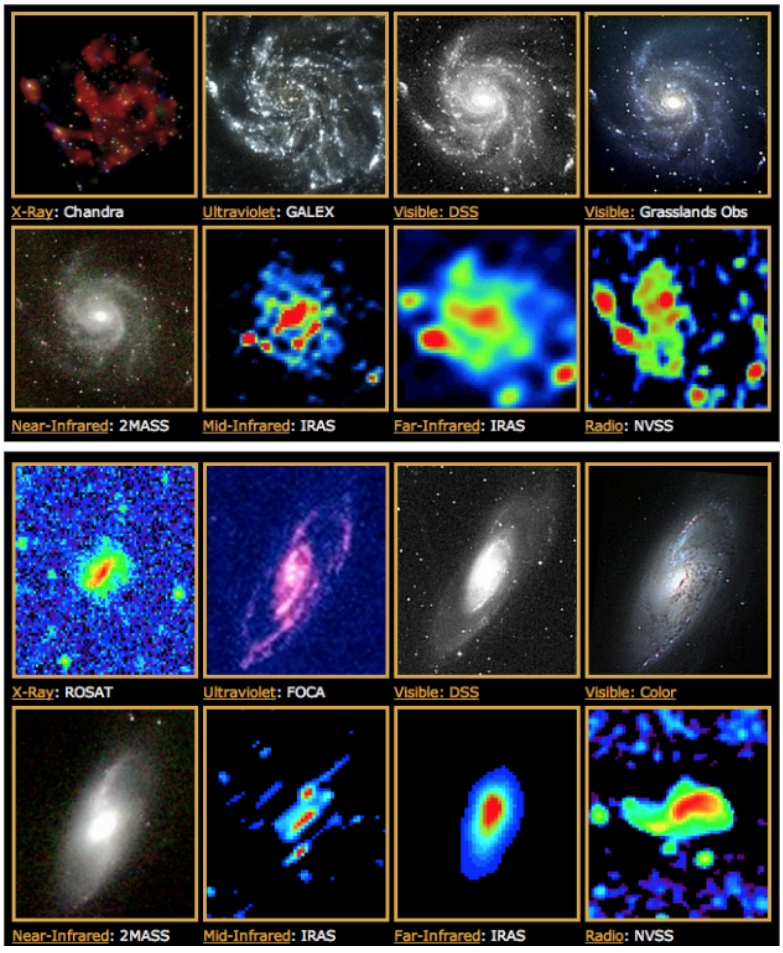

Figure 1.4. – A multi-wavelength view of M101 (upper image) and M106 (lower image). Credits: ROSAT, FOCA, DSS, 2MASS, IRAS, and NVSS, via NASA/CoolCosmos/IPAC.

At intermediate and higher redshifts (i.e., $z > 1$), observations are more complicated (except for the UV range) as the integration time required to obtain a good signal-to-noise ratio (SNR) is longer. Also, most of the interesting emission lines used for science are shifted to the IR domain that is not entirely accessible for current instruments. Spectroscopic surveys as the MOSFIRE Deep Evolution Field (MOSDEF; Kriek et al., 2015) at $1.37 < z < 3.80$, FMOS-COSMOS (Silverman et al., 2015; Kashino et al., 2013) $1.4 < z < 1.7$, the deep VIMOS survey of the CANDELS CDFS and UDS fields (VANDELS; Pentericci et al., 2018) at $1.0 < z < 5.5$, among others provides high-quality samples to study the distant universe using spectral energy distribution (SED) fitting. Deep exposures of small regions of the sky for the Great Observatories Origins Deep Survey (GOODS; Giavalisco et al., 2004) and the Cosmic Evolution Survey (COSMOS; Scoville et al., 2007) fields are available with multi-wavelength photometric and spectroscopic observations. Generally, these observations are performed in regions uncontaminated by the Galactic emission (Boselli, 2011). Same for Hubble Space Telescope legacy fields such as the UDS-HST and CDFS-HST.

1.1.2. Panchromatic view of galaxies

The radiation emitted can be understood as the combination of continuum and emission lines at different frequencies. We can divide the electromagnetic spectrum into three main regimes: X-ray, UV-optical-NIR, and IR+radio, which can help us have a broad panchromatic view of galaxies and understand their properties. Let's revise each one of these regimes.

X-ray: this type of emission is produced by hot plasma, supernovae remnant, and compact sources as the X-ray binaries. Properties such as star-formation can be traced by the massive binary population giving insights into the evolution of the stellar component. This emission allows studying active galactic nuclei (AGN) and the evolution of the parent black hole and feedback processes using the emission lines as well as outflow processes and metal abundance (Fabbiano, 2008). A wide range of X-ray luminosities is seen in galaxies depending on their type and the source of origin. For example, spiral galaxies have $\sim 10^{38} - 10^{42}$ erg s^{-1} in the spectral range $0.2 - 3.5$ keV (Fabbiano, 2008), while starburst spans over a range of $\geq 10^{41}$ erg s^{-1} in the band $0.5 - 10$ keV, and for the ellipticals of $10^{40} \leq L_X \leq 10^{43}$ erg s^{-1} (Mathews and Brighenti, 2003). Elliptical galaxies are dominated by low-mass X-ray binaries due to their past star-forming activity (Zezas, 2021). Hot gas, thermal Bremsstrahlung, and recombination emission (i.e., free-free and free-bound) surrounding the object, product of stellar mass loss can also produce this radiation. In the case of starburst galaxies, hot gas in the central regions, the disk, and the halo can also produce it, and it is related to star-forming regions, AGN activity, and high-mass X-ray binaries (Yang et al., 2020; Zezas, 2021). In spiral galaxies, the emission is dominated by supernovae remnants and X-ray binaries. Characterization of the hot gas properties such as its temperature and the total dynamical mass of the galaxy can be obtained by studying this radiation.

UV-to-NIR: in a galaxy, the UV-to-NIR emission (≥ 912 Å to ≤ 3 μm) is dominated by the underlying stellar population Boselli (2011). In the HII-regions, the starlight can be absorbed and scattered, and in particular, the Lyman continuum radiation (below 912 Å) is absorbed. The effects of dust are visible above $\lambda \gtrsim 3$ μm. Dust absorption and emission changes the observed colors of galaxies, reddening the observations. Thus, a galaxy that should look bluer as the underlying stellar population is young, will appear reddened by the dust. However, an elliptical galaxy can also look reddened just because the underlying stellar population is old. This is known as the age-dust degeneracy and disentangling these effects is paramount to interpret the physical properties of galaxies (Chisholm et al., 2019). Active Galactic Nuclei (AGN) emission coming from the accretion disk also contributes to the global emission in these wavelengths. Briefly, AGN are objects with a powerful central emission not related to stellar origin, at least not from fusion, but from a supermassive ($> 10^6 M_\odot$) black hole (SMBH). They can have high luminosities ($L_{bol} \sim 10^{48}$ erg s^{-1}), and produce intense emission lines (see, Padovani et al., 2017, review for further information on AGN). I will not center the discussion on these objects but on features related to stellar origins.

Stellar emission: the underlying stellar populations and gas give rise to the observed continuum and emission-line features at these wavelengths. The physical processes happening inside stars are well-studied, leading to a good understanding of the evolution of stars. Accurate reproduction of synthetic stellar spectra and stellar evolutionary models by Astronomers covering a wide parameter space range including metallicity, temperature, and gravity (Lejeune, Cuisinier, and Buser, 1997) is nowadays possible. The combination of UV-to-NIR emission with IMF and star formation history (SFH) allows building population synthesis models to study galaxies. The stellar population and the ISM are responsible for emission line and absorption features present in galaxy spectra in this wavelength range (see, Fig. 1.5). Emission lines, in particular, can be produced in HII-regions (a dominant component in normal galaxies), planetary nebulae, supernovae remnants, AGN accretion disk, and outflows (Harrison et al., 2018).

ISM component: the ISM can be divided into the HII-region where ionized species co-exist, the photodissociation region (PDR) that is predominantly neutral followed by cold molecular gas, and the HI region which contains warm/cold atomic gas. HII-regions with densities of $\sim 10 - 10^4$ cm^{-3} are photo-ionized by UV radiation coming from OB young and hot stars recently formed. Forbidden optical lines (see, Osterbrock and Ferland, 2006) such as [NII], [OII], [OIII], [NeIII], [SII], [ArIII], produced by collisions with electrons or ions helping to gas cooling as well as HI hydrogen recombination lines are characteristic of these regions (Boselli, 2011). Hydrogen recombination lines are produced by UV photons below 912 Å with enough energy to ionize diffuse atomic hydrogen (HI). A cascade produced by recombination is responsible for series produced in the UV (Lyman series), in the optical (Balmer), and the NIR (Paschen, Brackett, Pfund, and Humphreys series). The hydrogen recombination

lines' intensity depends marginally on density and weakly on temperature, and they are proportional to the ionization rate. One can use them to measure extinction by comparing observed ratio values to intrinsic ones. In the case of metals (i.e., elements heavier than He), the intensity depends on their abundance, making them difficult to be observed. However, forbidden lines produced by O, N, and S are observed in the UV-to-NIR range. Forbidden lines are very intense in low-density environments (Pagel, 1997; Lejeune, Cuisinier, and Buser, 1997; Lequeux, 2005) as collisionally excited ions have enough time to decay before being excited by another collision.

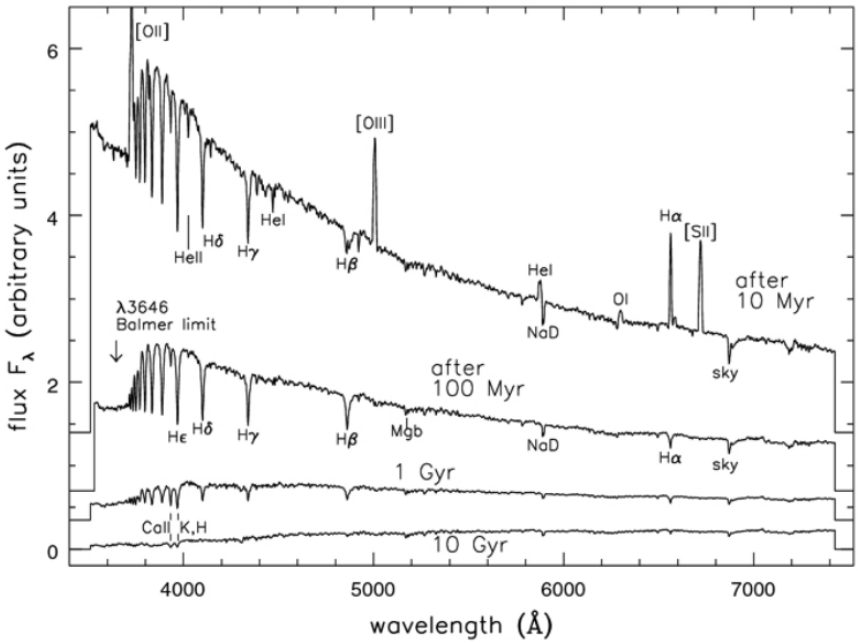

Figure 1.5. – Early-type and late-type galaxy spectra. Spectra for a 10 and 100 Myr, and 1 and 10 Gyr populations is presented. Emission lines are characteristic of the young systems, while absorption features are remarkable in old systems. The image is taken from B. Poggianti as reported in 'Galaxies in the Universe' Sparke/Gallagher CUP [1] 2007.

1. http://www.astro.wisc.edu/~sparke/book/webfigs.html

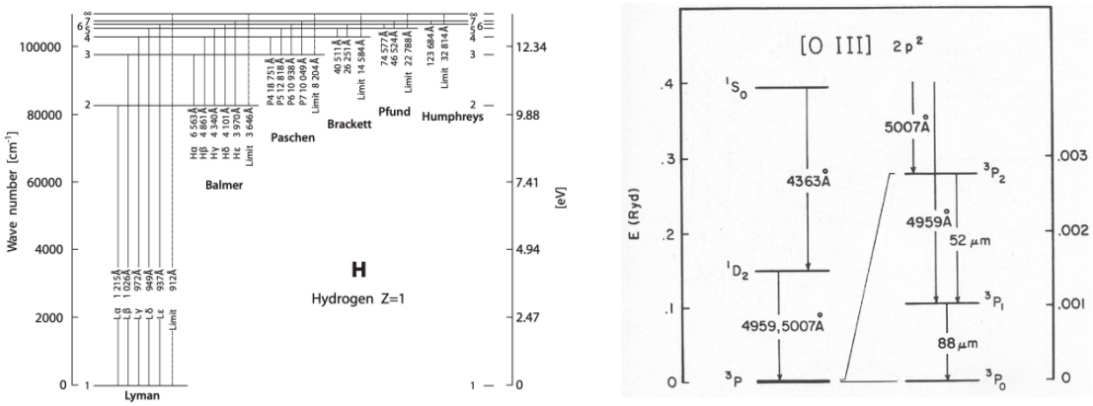

Figure 1.6. – Grotrian diagrams. The Grotrian diagram for the hydrogen atom and [OIII] are presented. Image composed from Boselli (2011) and Dinerstein (1983).

The ISM can be characterized and studied using emission lines. For example, the gas-phase density is usually measured through emission line ratios coming from emission lines of the same ion with similar level excitation energy while the temperature is derived using pairs of the same ion with different excitation energies (see, Sanders et al., 2021, and references therein). Usually [OII]λ3726/λ3729 and [SII]λ6716/λ6731 are used to obtain the gas-phase density while [OIII]λ4959 + λ5007/[OIII]λ4363] for temperature. Emission lines in this range are affected by dust attenuation and need to be corrected. The Grotrian diagrams for hydrogen and [OIII] are shown in Fig. 1.6. These diagrams show common transitions in both elements. Contrarily, absorption features are sensitive to temperature, velocity, magnetic fields, element abundance, among others with the advantage of being relatively insensitive to dust attenuation. Galaxy spectra reveal, in general, ISM absorption features due to hydrogen in the optical and UV, or by other elements, and emission and absorption caused by molecules.

MIR-to-FIR: dust grains dominate the MIR wavelengths of the electromagnetic spectrum. As a star evolves, dust produced in its atmosphere is released to the ISM by the stellar winds. Supernovae shocks can also lead to the creation of dust grains. However, the formation of grains is very complex in general (see, Galliano, Galametz, and Jones, 2018, review). These aggregates of metals have different sizes and distributions and are present in galaxies leaving an imprint in the IR and radio wavelengths. Several features are present in this domain such as those produced by Polycyclic Aromatic Hydrocarbons (PAHs; see Fig. 1.7) to fine-structure atomic lines from gas, as well as molecular transitions of CO. They are observable from the FIR to the submillimeter (sub(mm)), and H_2 in the MIR. Cooling emission lines are produced in the PDR between the HII-region and the molecular cloud. Their emission is present in the FIR and sub(mm) regimes. The most common coolants in PDRs are the CII ($\lambda \sim 157.7$ μm) and OI ($\lambda \sim 63.2$ μm) elements (Bernard-Salas et al., 2015).

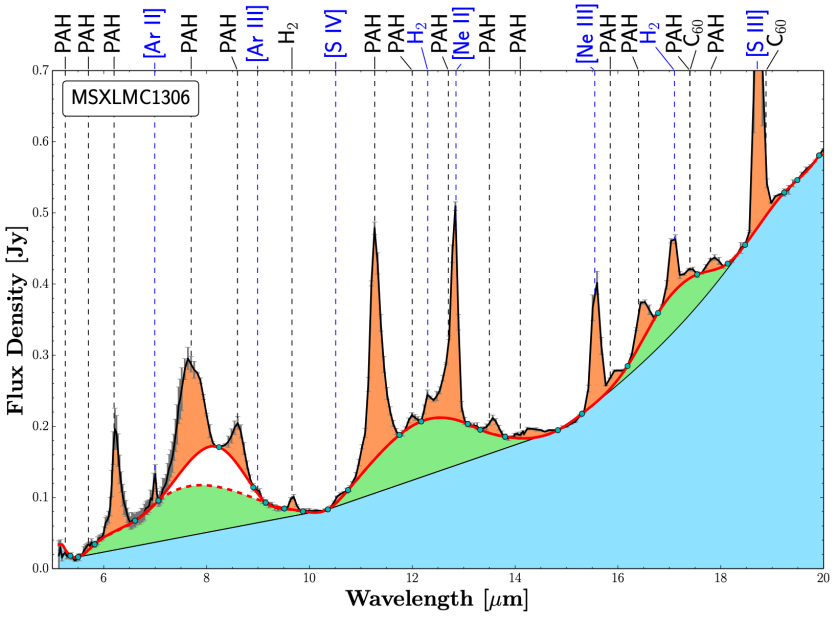

Figure 1.7. – Polycyclic Aromatic Hydrocarbons features. The image shows some PAH features, along with atomic and molecular emission lines for a typical *Spitzer*/IRS low-resolution spectrum. The image is taken from Shannon, Stock, and Peeters (2015).

The UV/optical photons can be absorbed by dust and re-emitted in the IR, controlling the gas heating and working as an important gas coolant, playing an important role in star-formation. Dust leaves its imprints between 5 μm to $\sim$ 1 mm with an emission characterized by a continuum with prominent emission lines. These lines have been attributed to the PAHs. Grains have different sizes and dominate different ranges of the continuum. Generally, grains with sizes larger than 200 Å dominate the IR emission for $\lambda > 60$ μm and are composed of graphite a silicate. On the contrary, smaller grains ranging from 10 Å to 200 Å emit in the range from 10 μm to 60 μm and are made up of silicates. At lower wavelengths (i.e., 3 μm $\leq \lambda \leq$ 15 μm) PAHs are assumed to dominate (see, Boselli, 2011, and references therein). Above $\lambda > 60$ μm in the FIR regime, large and cold (e.g., T 20 K) dust grains reprocess the absorbed energy and re-emit as a modified blackbody (i.e., greybody) because they are poor radiators. This means that their emissivity is less than 1 and decreases as a function of wavelength (Elia and Pezzuto, 2016).

Then, a galaxy is a mixture of all different processes related to each one of its components such as gas, dust grains of several sizes, and its composition. Also due to young and old stars and their luminosities and temperatures. AGN contribution, and intergalactic medium (IGM) absorption (Burgarella et al., 2017; Burgarella, 2021; Thorne et al., 2021) also play an important role. These components are summarized in Fig. 1.8. All this information is available in the spectral energy distribution (SED) of a particular object.

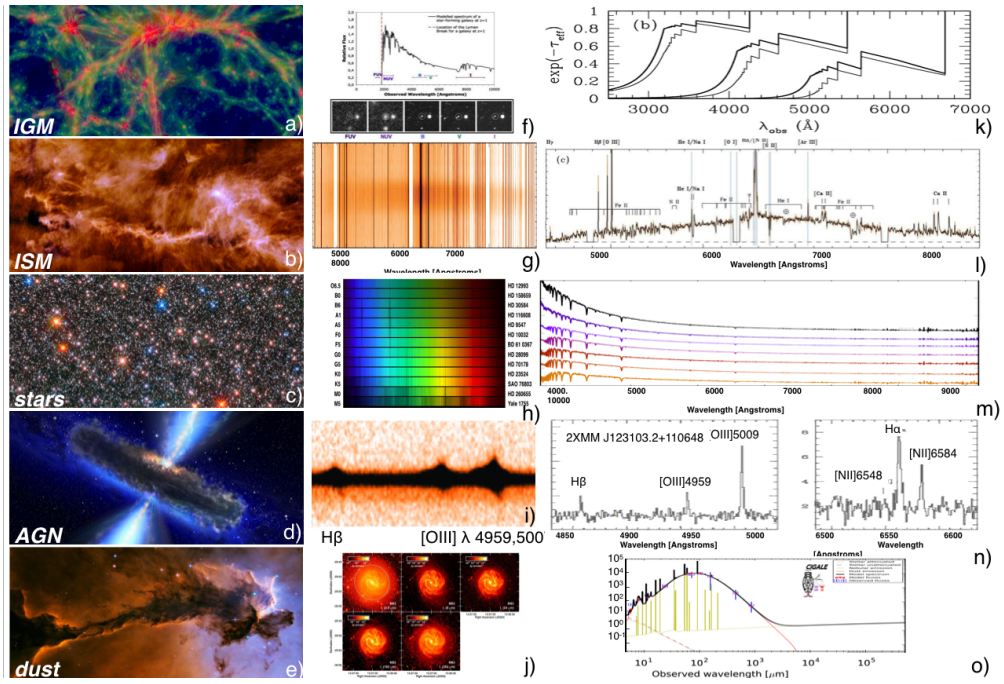

Figure 1.8. – SED components. Different components that contribute to the total SED of a galaxy are shown along with the characteristic spectra in the last column. The image is taken from Burgarella (2021).

1.2. Spectral Energy Distribution

SEDs give access to crucial quantities such as current SFR, and stellar mass, SFH over different timescales, dust attenuation, dust content, and/or stellar and gas metallicities over a large range of wavelengths when combining photometric data and emission lines. The coupling of stars, gas, and dust in a galaxy complicates the information extraction for each component. The comparison of models predicting the full SED to observed fluxes from the continuum and line emission has been proved to be very powerful to infer these physical parameters in star-forming galaxy populations (Fossati et al., 2018; Buat et al., 2018; Corre et al., 2018; Yuan et al., 2019). The estimation of physical parameters will strongly depend on the data coverage. For example, UV and FIR are needed to estimate SFR as dust absorbs UV light and re-emits in the IR. This is also important to estimate dust mass and temperature or to break degeneracies between the parameters as the age-metallicity-dust (Burgarella, 2021; Thorne et al., 2021). Limitations in measuring SFR from photometry are quite difficult when no information is available on emission lines like Hα or Hβ.

Multi-wavelength samples imply having more information in terms of data (e.g., several photometric measurements). Handling these data sets requires powerful com-

puters and a code able to deal statistically with the data and models (Burgarella et al., 2017). Two popular types of codes to conduct SED fitting are commonly implemented: i) radiation transfer modeling and ii) physically motivated modeling. Radiation transfer modeling is centered on solving the radiation equation including gas and dust in complex geometrical configurations. It makes assumptions on the SFH, the chemical composition, and dust/star geometry (Burgarella et al., 2017) but provides an accurate representation of the dust-heating processes in galaxies (Nersesian et al., 2019). Integrating over all the positions in the galaxy leads to its SED (Baes et al., 2011; Efstathiou et al., 2013; Nersesian et al., 2020). However, dealing with multi-wavelength information is computationally expensive with this method.

SED fitting is based on physical models (da Cunha, Charlot, and Elbaz, 2008; Boquien et al., 2019) and implements energy balance where the radiation absorbed by dust is re-emitted in the IR wavelengths. Here, templates are used to target each component contributing to the total SED of the galaxy. The luminosity is re-distributed following the attenuation law to obtain the IR SED. The reproducibility of observations depends on the models. Results are subject to inherent characteristics of the models due to the unknown evolution of the IMF (Kroupa, 2001), the stellar isochrones mapping (Bertelli et al., 1994; Girardi et al., 2000, e.g.,) and production of atmospheres on metallicity and temperature grids (Kurucz, 1992; Pickles, 1998; Le Borgne et al., 2003; Ivanov et al., 2019). Also to stellar binary evolution (Eldridge and Stanway, 2009) and the dust treatment (Charlot and Fall, 2000; Trayford et al., 2020). SED fitting can treat data at the same time in a homogeneous fashion saving computational time. In the next section, some codes are discussed. The general SED fitting process explained from a physically motivated code point of view is presented.

1.2.1. Spectral energy distribution fitters and code structure

The physically motivated SED fitting as presented before needs input models/templates to compare with observations. Different categories of models are used. The SFH is either modeled with simple analytical functions or non-parametric forms or comes from numerical simulations (semi-analytical or hydrodynamical). The interplay between dust and stars is described either with a radiation transfer modeling with more or less complex configurations or with simpler, phenomenological laws sometimes combined with an energy budget (Silva et al., 1998; Popescu et al., 2000; da Cunha, Charlot, and Elbaz, 2008; Boquien et al., 2019). The nebular component is added either using physical modeling with codes like CLOUDY or MAPPINGS (Ferland et al., 2017; Allen et al., 2008) as in Code Investigating GALaxy Emission (CIGALE [2]) (Boquien et al., 2019), BayEsian Analysis of GaLaxy sEds (BEAGLE) (Chevallard and Charlot, 2016), *ProSpect* package (Robotham et al., 2020), Python code for Stellar Population Inference from Spectra and SEDs (Prospector) (Leja et al., 2017; Johnson et al., 2021), Bayesian Analysis of Galaxies for Physical Inference and Parameter

2. https://cigale.lam.fr/

EStimation (Bagpipes) (Carnall et al., 2018), *MCSED* (Bowman et al., 2020), or with empirical relations relating different emissions as in PHotometric Analysis for Redshift Estimations (lePHARE) (Arnouts et al., 1999; Ilbert et al., 2006). Some SED fitting codes can combine continuum and emission-line fluxes (see Fig. 1.9). It will be important when the analysis of data obtained with new facilities will require handling large data sets and modeling very different galaxy populations (Ellis et al., 2017; Thorne et al., 2021).

IR emission is crucial to put constraints on stellar obscuration (Buat et al., 2018) and to estimate physical quantities such as the SFR of galaxies from the energy budget (Smith et al., 2012; Małek et al., 2018; Nersesian et al., 2019; Dobbels et al., 2020). Modeling of the infrared (IR) dust emission is not included in all the SED fitting codes. CIGALE includes three different sets of models from Draine and Li (2007) with updates of Draine et al. (2014), Casey (2012), and Dale et al. (2014) while Prospector, Bagpipes, ProSpect and BEAGLE only include one of the aforementioned sets. Moreover, Active Galactic Nuclei (AGN) templates from Casey (2012), Dale et al. (2014), and SKIRTOR (Stalevski et al., 2012; Stalevski et al., 2016) are implemented in CIGALE and X-CIGALE (Yang et al., 2020). ProSpect also includes Andrews et al. (2018) templates. Nevertheless, emission line models are still not available to be used along with the AGN templates. This information is summarized in Fig. 1.9 produced by Thorne et al. (2021) showing model/templates currently implemented in SED fitters. The isochrones, stellar templates, atmospheres, and IMF used to build stellar population synthesis (SSP) are also summarized in Fig. 1.10.

The final result of a typical SED is presented in Fig. 1.11 where the components contributing to the total SED are colored for the stars, gas, and dust contributions. As explained before, the stars in blue dominate the UV-to-NIR emission and suffer absorption from dust grains in the UV and re-emitted in the IR by dust in red color. Emission lines are visible at all wavelengths, and both nebular continuum and line emission contribution are shown green. Important radiation processes are presented such as the absorption and scattering in the UV, the free-free, and synchrotron emission in the sub(mm) and FIR.

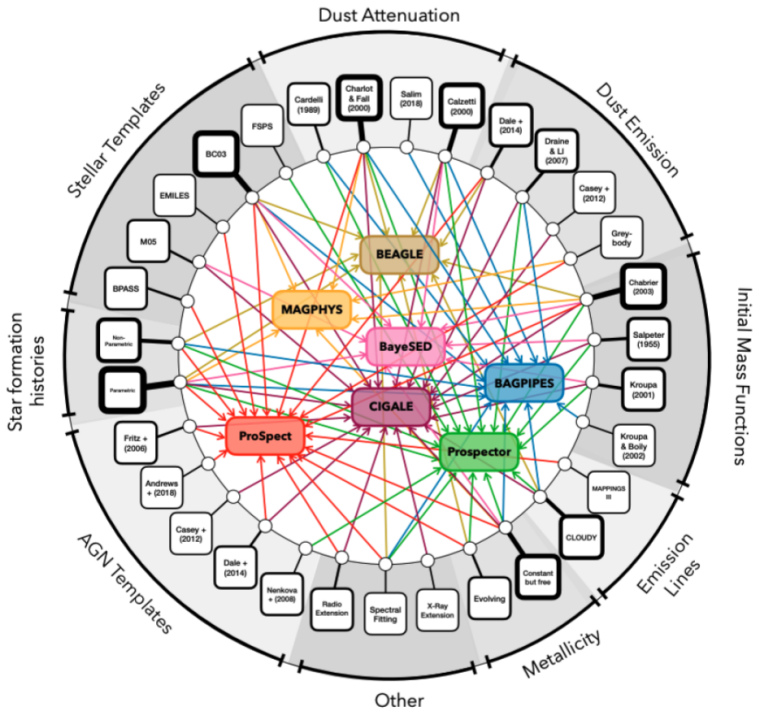

Template Type	Template	SED Fitting Code					
		ProSpect	MAGPHYS	BEAGLE	PROSPECTOR	BAGPIPES	CIGALE	BayeSED
Stellar Templates	BPASS	■						
	M05						■	■
	E-MILES	■	■	■		■	■	■
	BC03				■			
	FSPS							
Dust Attenuation	Cardelli et al. (1989)	■	■	■	■	■	■	
	Charlot & Fall (2000)							
	Salim et al. (2018)			■	■	■	■	■
	Calzetti et al. (2000)				■	■	■	■
Dust Emission	Dale et al. (2014)	■		■	■	■	■	
	Draine & Li (2007)							
	Casey (2012)				■	■	■	
	Grey-body		■					
Initial Mass Function	Chabrier (2003)	■	■	■	■		■	■
	Salpeter (1955)							
	Kroupa (2001)				■			
	Kroupa & Boily (2002)					■		
Emission Lines	MAPPINGS-III	■						
	CLOUDY						■	
Star Formation Histories	Parametric	■	■	■	■	■	■	■
	Non-parametric							
Metallicity	Constant but free	■	■	■	■	■	■	■
	Evolving							
AGN Templates	Fritz et al. (2006)	■					■	
	Andrews et al. (2018)							
	Casey (2012)							
	Dale et al. (2014)	■					■	
	Nenkova et al. (2008)				■			
Other	Radio Extension	■					■	
	Spectral Fitting			■	■	■		
	X-ray Extension						■	

Figure 1.9. – Typical models and templates implemented in SED fitting codes. The figure created by Thorne et al. (2021) shows the input model/templates used to fit photometry and emission-line fluxes to reproduce the total SED of the object. The figure below is a tabular form of the scheme for better reading and comparison between the SED fitters.

Large spectro-photometric surveys on 8-meter telescopes like the Multi-Object Optical and Near-infrared Spectrograph (MOONS) for the Very Large Telescope, and the Subaru Prime Focus Spectrograph (PFS), and further on larger facilities (e.g., Extremely Large Telescope) as the Multi-Object Spectrograph for Astrophysics, Intergalactic-medium studies, and Cosmology (MOSAIC) will provide thousands to millions of

spectra in the deepest photometric fields. The James Webb Space Telescope (JWST) will push the observations of both rest-frame UV-optical continuum and emission lines to a very high redshift. In particular the Hα and [OIII]λ5007 emission lines for which different physical conditions and configurations will need to be taken into account in their modeling (Schaerer and de Barros, 2009; Wright et al., 2015; Wells et al., 2015; Álvarez-Márquez et al., 2019; Chevallard et al., 2019). Treating both photometric and emission-line information simultaneously is important to account for the potential contribution of emission lines in photometric bands. This can substantially modify the observed fluxes increasing the uncertainties in the parameter estimations (Schaerer and de Barros, 2010; Stark et al., 2013; Tang et al., 2021). The coupling of multi-wavelength data sets in the SED fitting including emission lines and good treatment of the IR emission remains paramount to characterize, derive and measure properties of galaxies accurately. In the next sections, I will discuss the relevant modules and templates used to estimate the SED of galaxies with an emphasis on CIGALE.

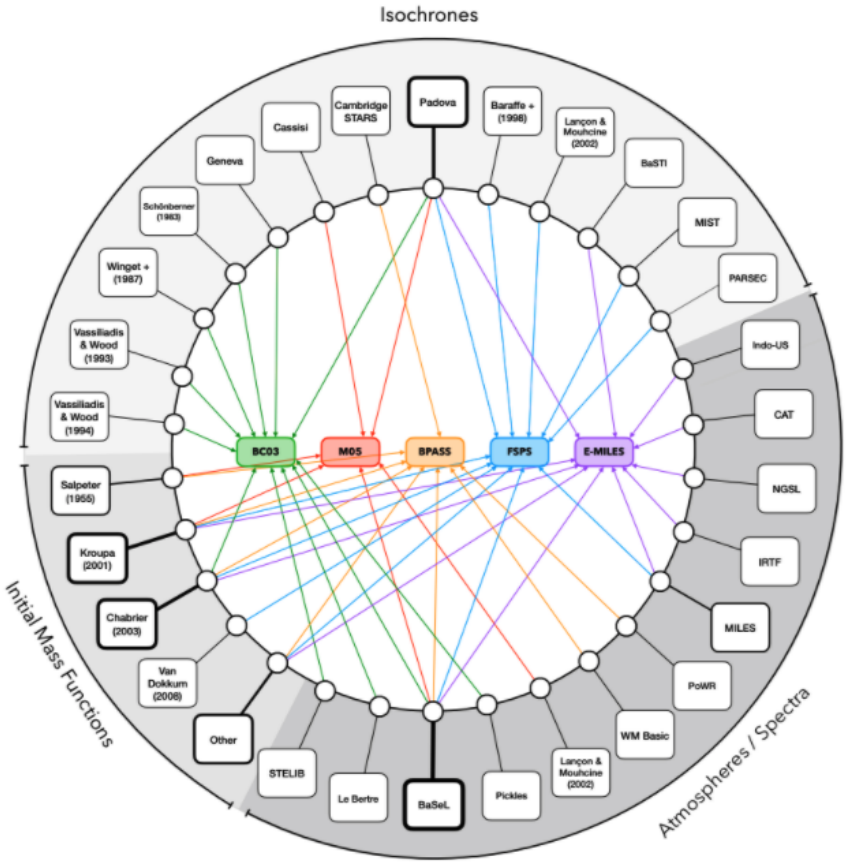

Figure 1.10. – Isochrones, stellar templates, atmospheres, and IMF implemented in SED fitters. The figure created by Thorne et al. (2021) summarizes common libraries used to build the stellar synthesis population (SSP) used in SED fitting.

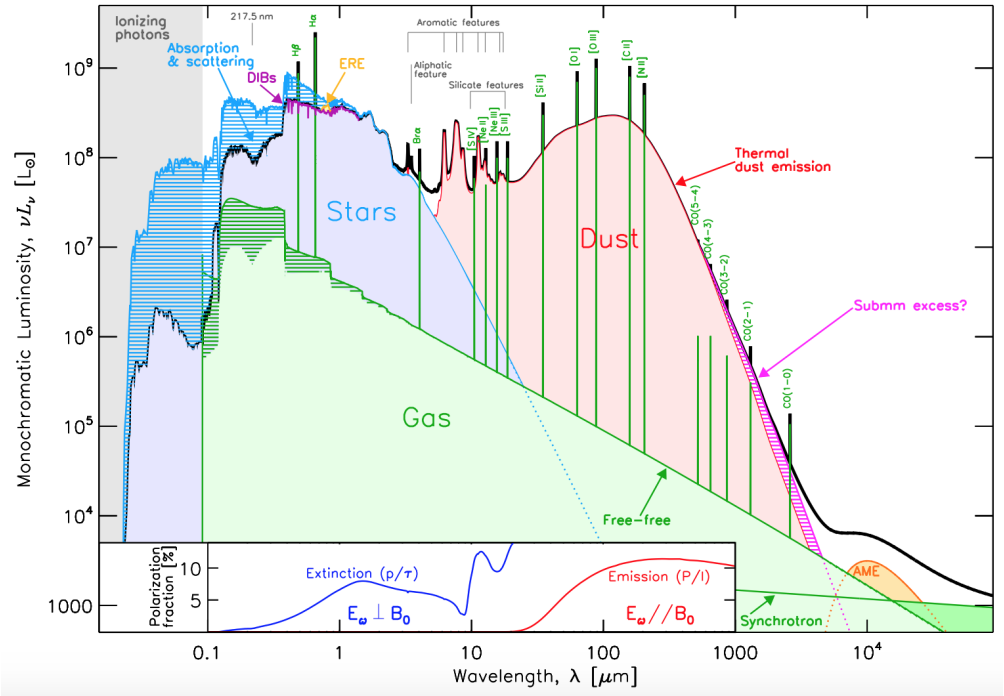

Figure 1.11. – Late-type galaxy typical SED. The figure summarizes the contribution of stars, gas, and dust as many other radiative processes that lead to the total shape of a SED of a galaxy. Each component is shown in different colors, and the most important features are highlighted. The figure is taken from Galliano, Galametz, and Jones (2018).

1.2.2. Star formation history and star formation rate

The stellar emission shares information from the stars present in a galaxy. Therefore, this emission must be related to the formation of stars (i.e., SFR). To build the global stellar emission (i.e., unreddened emission) for the SED modeling, Single Stellar Population (SSP, Bruzual and Charlot, 2003; Maraston, 2005; Maraston and Strömbäck, 2011) models needs to be implemented. An SSP as stated in Conroy (2013): "*...describes the evolution in time of the SED of a single, coeval stellar population at a single metallicity and abundance pattern*". SSP models are construct with a stellar mass distribution function (IMF), isochrones, and stellar spectral library (see, Fig. 1.12). In general, the SSP models are difficult to create because either the libraries and theoretical isochrones could be incomplete or due to poorly calibrated physics (Conroy, 2013).

Several isochrones need to be put together to have good completeness and coverage regarding the stellar ages, metallicities, and evolutionary phases. Some of them are the Padova models (Bertelli et al., 1994; Girardi et al., 2000; Marigo et al., 2008), the BaSTI models (Pietrinferni et al., 2004; Cordier et al., 2007) and the Geneva models (Schaller et al., 1992; Meynet and Maeder, 2000). Differences between the models rise from the treatment of stellar evolutionary phases and the assumptions to approximate

3D-physics inside the stars. Stellar libraries can be theoretical or empirical, and they are used to convert a model output into an observable SED. Some of them are optical/NIR libraries including those of Pickles (1998), ELODIE (Prugniel and Soubiran, 2001), STELIB (Le Borgne et al., 2003), MILES (Sánchez-Blázquez et al., 2006), and the X-shooter library (Chen et al., 2011). Finally, the IMF (e.g., Salpeter, 1955; Scalo, 1986; Kroupa, 2001; Chabrier, 2003) controls the rate of luminosity evolution and normalization of the mass-to-light ratio. Generally, they take a power-law shape to describe different stellar mass regimes.

All these ingredients, as in a recipe, are key to studying galaxy formation and evolution because we want to know the SFR as a function of redshift to understand the mass assembly of galaxies. As presented in Buat (2017), using the stellar evolutionary tracks $F_\lambda(m,\theta)$, an IMF given by $\psi(m)$, and the SFR as a function of time SFR(t), one can define the luminosity emitted by the stars as a function of time and wavelength as:

$$L(\lambda,t) = \int_0^t \int_{M_{low}}^{M_{high}} F_\lambda(m,\theta) SFR(t-\theta)\psi(m) dm d\theta. \tag{1.1}$$

Then, a solution for the SFR can be obtained from this equation leading to:

$$SFR = \left(\int_0^t \int_{M_{low}}^{M_{high}} F_\lambda(m,\theta) SFR(t-\theta)\psi(m) dm d\theta \right)^{-1} \times L(\lambda). \tag{1.2}$$

Adding UV-to-IR emission is necessary to get all the recent star formation activity as UV suffers from dust attenuation and the absorbed light is re-emitted in the IR (see, Fig. 1.13). The timescale traced by UV is shorter than that of the IR, ~ 100 Myr and 1 Gyr, respectively. Including recombination lines can reduce this timescale to a few Myr (Kennicutt and Evans, 2012; Conroy, 2013; Boquien, Buat, and Perret, 2014; Buat, 2017). Boquien, Buat, and Perret (2014) proved that using a constant SFR through a timescale of ~ 100 Myr overestimates the actual SFR due to contamination of long-lived stars. Emission lines such as Lyα, Hα, and Pα are commonly used to trace star-formation with a preference of Pα as the effects of dust at longer wavelengths are negligible. SED fitting provides a way to overcome these difficulties by combining UV-to-FIR and recombination lines using a robust method to account for obscured and unobscured star formation and obtain robust estimates of the SFR. Thus, SFR can then be derived in a self-consistent way using information from the whole range of the electromagnetic spectrum, from the UV to the FIR/sub(mm). In Fig. 1.13 a comparison of the different SFR tracers to the true one using simulations is presented as reported in Boquien, Buat, and Perret (2014). Also, the UV, IR, and UV+IR SFR density measurements are presented as in Madau and Dickinson (2014).

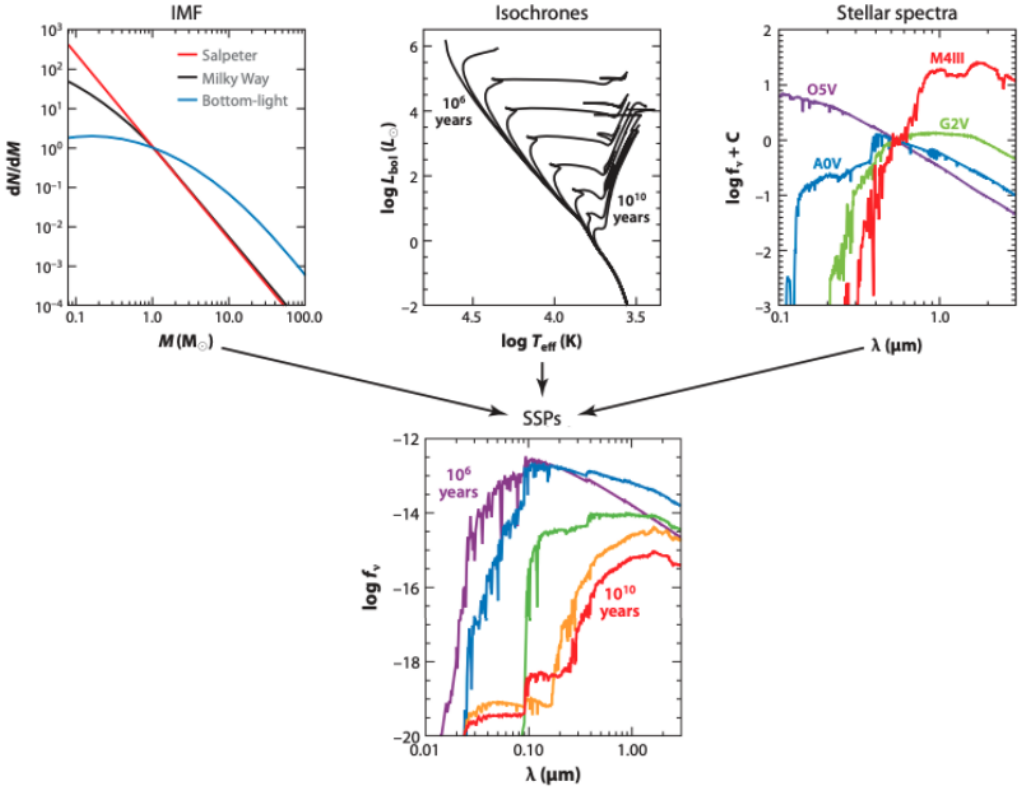

Figure 1.12. – Scheme showing SSP construction. The IMF, isochrones, and stellar spectral libraries are necessary to build the SSPs. They are the main components of SED fitting software. The figure is modified from the original shown in Conroy (2013).

A strength of SED fitting is the capability to explore different SFHs allowing to constrain the SFR of an object as accurately as possible. SFH implemented in SED fitting software are either parametric or non-parametric as shown in Fig. 1.9. The only condition of the parametrization is to be as general as possible to include several SFH to match observations/simulations (Conroy, 2013). As stated in Thorne et al. (2021), the parametric and non-parametric name is a bit misleading as both forms need parameters to be modeled. In the parametric forms, one can find various functional forms such as exponentially declining, delayed-exponentially declining, double power laws, lognormal, and exponentially increasing. For the non-parametric, piecewise functions are needed to describe the SFR as a function of time (Conroy, 2013; Thorne et al., 2021). Some studies (Boquien, Buat, and Perret, 2014; Ciesla et al., 2015) using CIGALE have proven that using simple modeling is not sufficient to reconstruct the whole SFH of galaxies and that stellar ages are underestimated. Therefore, non-parametric are preferred over parametric although more flexibility implies more parameters and probably more nonphysical solutions and its high dependence on the parametric SFH assumed (Carnall et al., 2019; Leja et al., 2019; Lower

et al., 2020). Recent works of Carnall et al. (2019) and Leja et al. (2019) comparing parametric versus non-parametric SFH using BAGPIPES and Prospector reinforce the idea that non-parametric recover input SFH and with fewer errors as compared to parametric. However, Lagos et al. (2018) and Robotham et al. (2020) using parametric SFH in ProSpect and semi-analytical models found that a well-selected parametric SFH leads to similar results as non-parametric step functions.

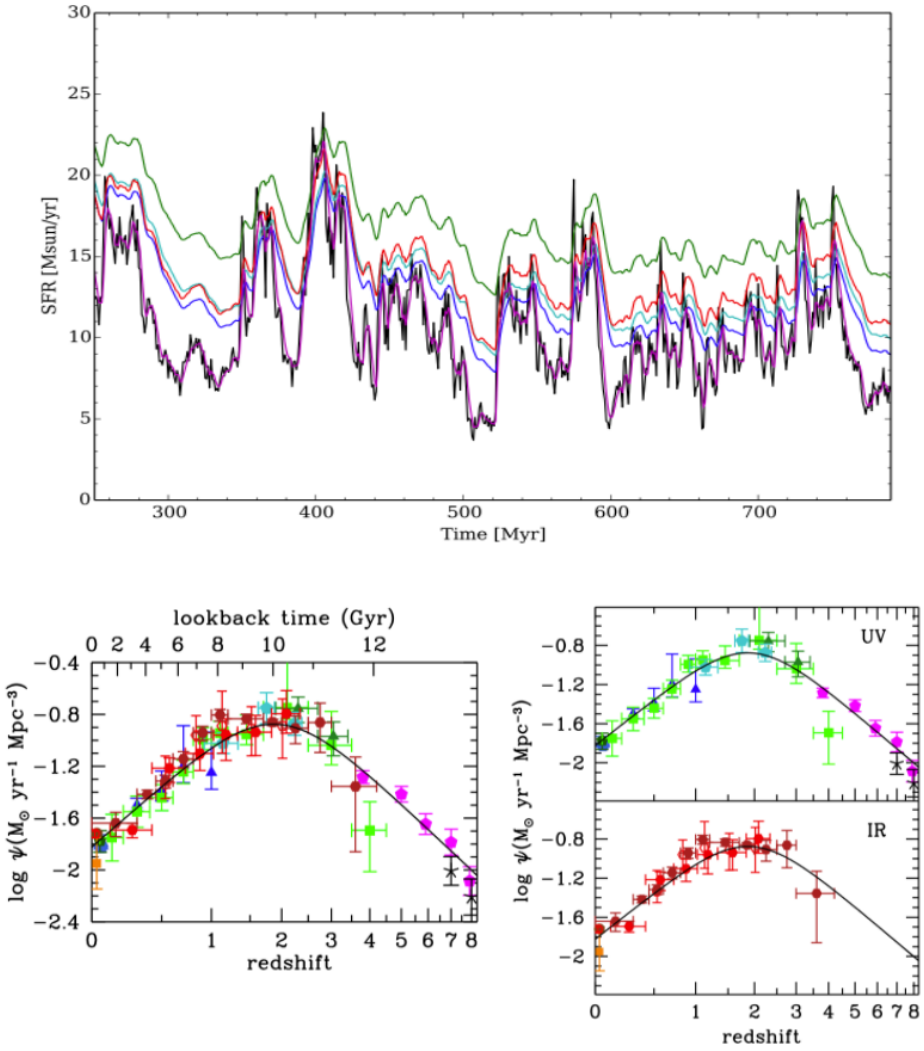

Figure 1.13. – SFR tracers. The upper panel figure shows a good match between the truly simulated SFR (black) and Lyman continuum in magenta. The FUV (blue), NUV(cyan), U band (green), and total IR (red) are also presented. The lower panel shows the SFR density as a function of redshift for UV, IR, and UV+IR. The figures are a composite taken from Boquien, Buat, and Perret (2014) and Madau and Dickinson (2014).

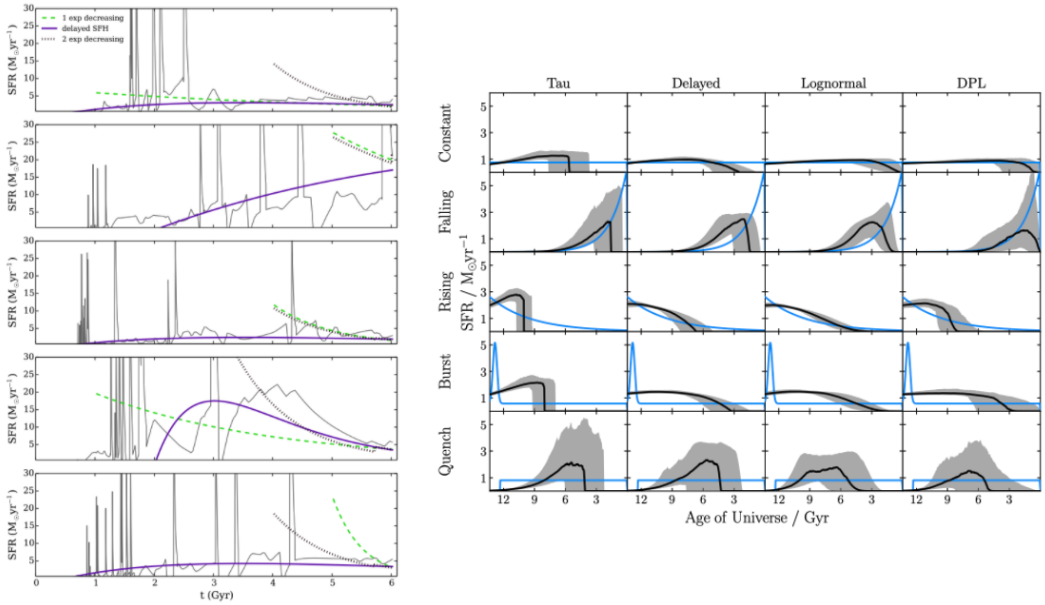

Figure 1.14. – Semi-analytical comparison of SFHs. In the left panel, the SFH models are shown in black together with CIGALE fits for three different models. The mock galaxy photometry SEDs are created with the semi-analytical code galform. In the right panel, each row represents a mock object (with input SFH as a blue line) and each column a parametric SFH fitted with Bagpipes. Here, the mock photometry SEDs are created with Bagpipes covering GALEX FUV to *Spitzer* IRAC bands.. The figure is composite of Ciesla et al. (2015) and Carnall et al. (2019).

One thing is clear in terms of obtaining robust estimations of the SFR from SED fitting, dust attenuation needs to be carefully and well-constrained using UV-to-IR data, and if possible, recombination lines need to be included to break degeneracies (Buat, 2017; Buat et al., 2018). In this way, uncertainties are just governed by differences in the SFH as they are directly obtained from the stellar emission instead of traditional observational methods. For example, those based on recombination line calibrations or continuum emission as UV, MIR, and FIR, radio, or even X-ray.

1.2.3. Dust and IR emission

Dust produces obscuration of the stellar light in the UV-to-NIR range that depends on the star-dust geometry (Charlot and Fall, 2000). The IR SED of an object is characterized by the global emission of the absorbed UV and the re-emission in the IR (i.e., energy budget principle; Fig.1.17). The SED can be also modified by the extinction/attenuation processes which depend on wavelength and local conditions. The effects of dust are studied through the extinction and attenuation that is addressed in Sect. 1.3. Briefly, the main difference between extinction and attenuation relies on the fact that extinction accounts for the total loss of light along a single line of sight as a conse-

quence of optical properties of the grains, their size, and distribution (Weingartner and Draine, 2001). Additionally, attenuation accounts for the same effects, including the light that is scattered out and into the sight-line, and star-dust geometry (Conroy, 2013; Salim and Narayanan, 2020).

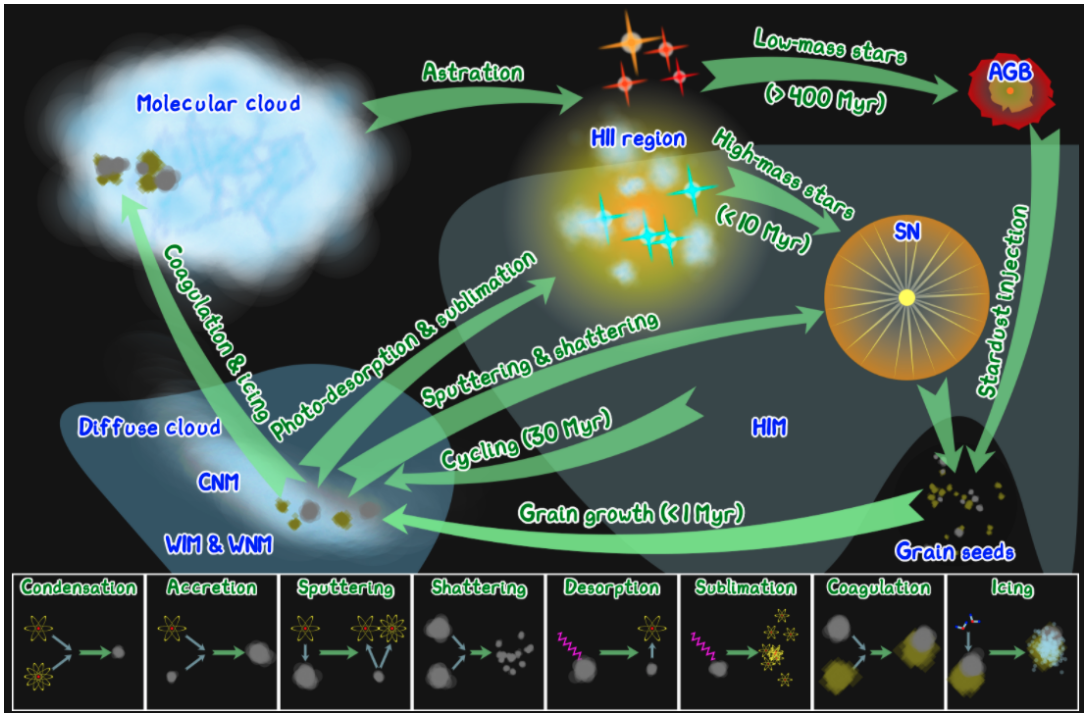

Figure 1.15. – Lifecycle of the interstellar dust. This scheme shows how the dust created in the Asymptotic Giant Branch (AGB) and Supernovae (SN) is reprocessed in the different mediums (HIM: Hot Ionized Medium; WIM: Warm Ionized Medium; WNM: Warm Neutral Medium; CNM: Cold Neutral Medium) transforming the grain seed. Image credits: Frédéric Galliano [3].

From a SED point of view, as presented in Fig. 1.17, dust emission dominates beyond $\lambda \sim 5$ μm. In current models, dust grains are treated as silicates (e.g., graphite) if they are large, or carbonaceous (e.g., PAHs) if they are small (Draine, 2003). A variety of models couple the grain optical properties and its distribution with stellar emission to predict the IR emission as in Draine and Li (2007), Casey (2012), Draine et al. (2014) or Dale et al. (2014). They include modeling of the PAHs which dominate IR emission at $\lambda < 12$ μm. At $\lambda \sim 50$ μm, the dust contributes to $\sim 2/3$ of the IR luminosity while the 1/3 left is accounted for by single-photon heating of dust grains including PAHs (Conroy, 2013). IR emission can also be modeled as a modified blackbody for the thermal emission along with stochastic heating of dust grains as presented in

3. http://irfu.cea.fr/Pisp/frederic.galliano/

da Cunha, Charlot, and Elbaz (2008). In Fig. 1.9 the current status of IR emission models/templates used in different SED fitting software is presented. In Fig. 1.16 some common templates/models implemented in SED fitting software, especially in CIGALE, are presented for different configurations of the parameters. These templates are in charge of constraining the total IR emission using the energy balance principle (Burgarella, 2021).

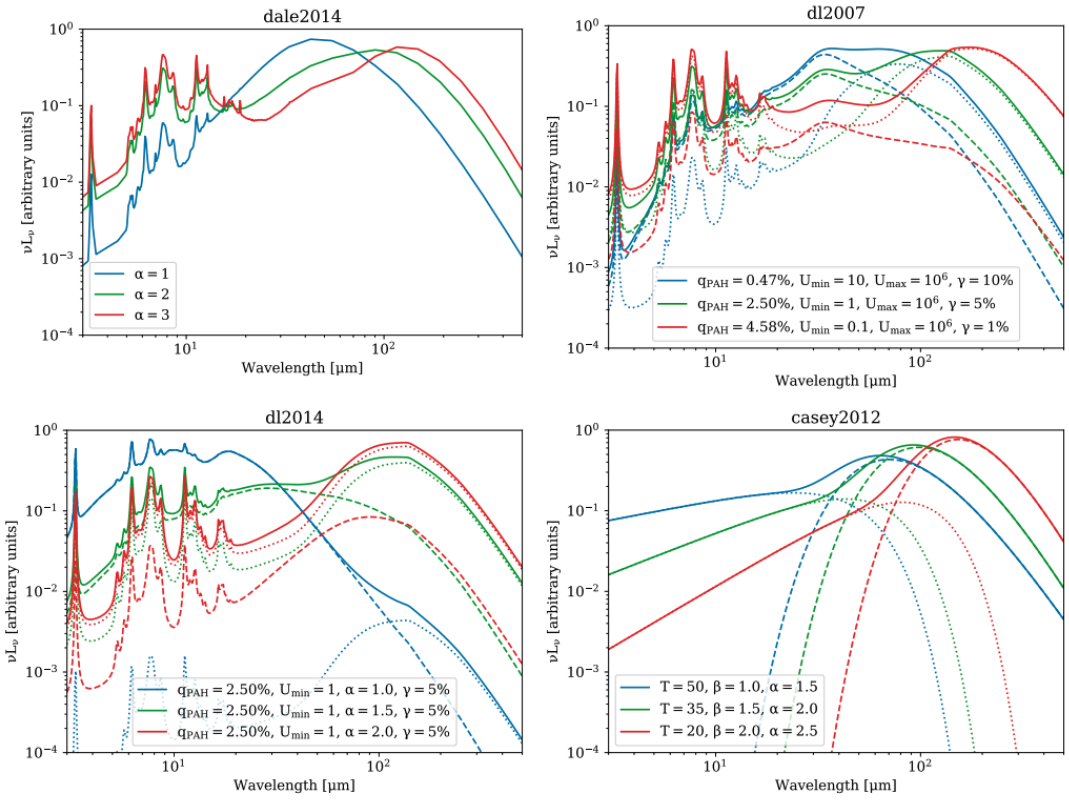

Figure 1.16. – IR model/templates from Dale et al. (2014), Draine and Li (2007), Draine and Li (2007) updated with Draine et al. (2014), and Casey (2012). The models are shown as a function of wavelengths for a different set of parameters shown in the legend as presented in Boquien et al. (2019) and implemented in CIGALE.

To measure dust properties and its effects using SED analysis IR data is paramount. Photometry-only covering UV-to-NIR photometry showed to poorly constrained the dust properties (e.g., Papovich, Dickinson, and Ferguson, 2001; Shapley et al., 2006; Kriek et al., 2008; Taylor et al., 2011) as a consequence of the dust-age degeneracy (Papovich, Dickinson, and Ferguson, 2001). The degeneracy can be broken including spectroscopy (see, Fossati et al., 2018; Buat et al., 2018; Corre et al., 2018; Yuan et al., 2019) as this puts constraints on the mean stellar age (Conroy, 2013) or including UV-to-FIR photometry as robust measurements of the dust content can be inferred (e.g., Burgarella, Buat, and Iglesias-Páramo, 2005; Noll et al., 2009; Bouwens et al.,

2012; Finkelstein et al., 2012; Buat et al., 2018).

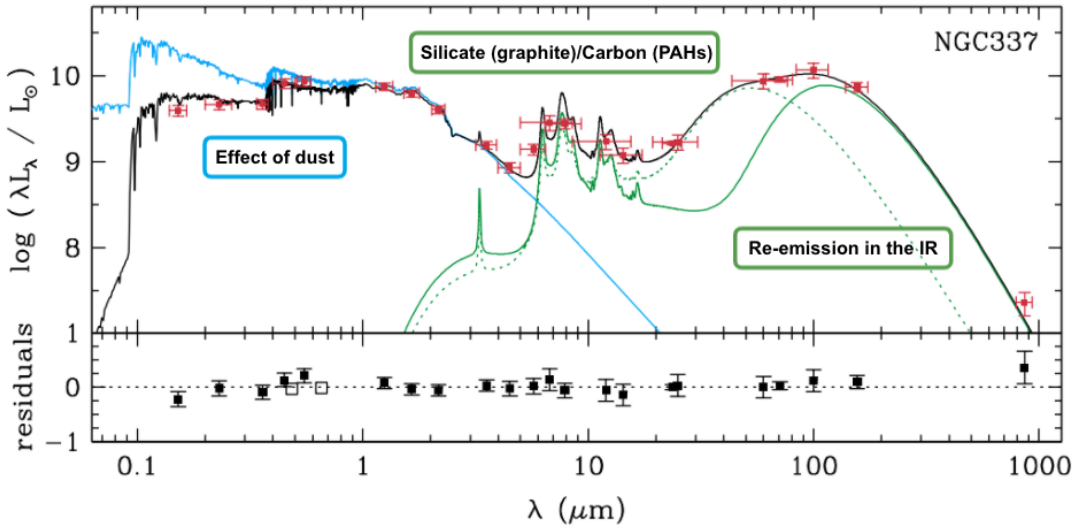

Figure 1.17. – SED model of NGC 337 as presented in da Cunha, Charlot, and Elbaz (2008). The unattenuated starlight is shown in blue, while the dust emission of the ISM and the birth cloud are presented as green continuous and dotted lines, respectively.

Constraints on dust mass and temperature, abundances of PAHs, as well as the bolometric luminosity, are provided by dust IR information. This helps us to understand the nature of dust in galaxies and its relation with stars and gas (see, Draine et al., 2007; Dale et al., 2012; da Cunha, Charlot, and Elbaz, 2008; Galliano, Dwek, and Chanial, 2008). Extracting parameters from the global SED of a galaxy such as dust mass fraction in PAHs, diffuse ISM, and photo-dissociation region emission fraction, temperature, and strength of the radiation field are possible thanks to the implementation of physical dust models (Conroy, 2013). For example, those of Draine and Li (2007) (updated with Draine et al., 2014) and Dale et al. (2014).

In the next sections, I describe the main differences between extinction and attenuation, and the way they are coupled to perform SED fitting analysis. This is crucial to understand the choices and measurements I report in Part II and Part III of this thesis.

1.3. Dust effects on the Spectral Energy Distribution

In order to study dust effects (e.g., the redistribution of the energy from absorbed UV and re-emitted IR), the amount of obscuration need to be computed. As stated before, dust comes from the atmospheres of evolved stars and/or supernovae explosions, as

well as from complex grain growth and other processes in the ISM. The grains sizes and masses are diverse and if they are compared to regular dust at a household they are two orders of magnitude smaller (Weingartner and Draine, 2001; Salim et al., 2007). To quantify the effects of dust, Astronomers use two physical concepts known as extinction and attenuation which are related to each other but are not conceptually the same.

Concepts used to understand extinction curves can be applied to those of attenuation as the extinction curves are the building blocks of the attenuation curves (Salim and Narayanan, 2020). Extinction accounts for the loss of light along the line of sight via absorption or scattering. However, attenuation includes the same effects of extinction but also accounts for both the contribution of obscure stars and scattering back into the line of sight. Attenuation is sensitive to the geometrical configuration of stars and dust in a galaxy. A schematic view of these concepts is presented in Fig. 1.18.

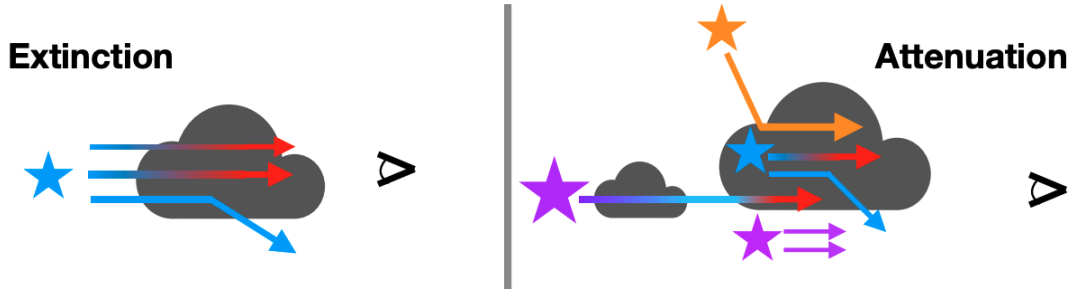

Figure 1.18. – Extinction versus attenuation. In the left panel, the starlight is absorbed and scattered by the column density before reaching the observer. On the right side, light suffers the same effects mentioned before but different star-dust configurations give rise to a more complex result as viewed by the observer and to an additional scattering into the line of sight. The image is taken from Salim and Narayanan (2020).

The wavelength-dependent extinction/attenuation in magnitudes can be seen as a difference of an intrinsic, unattenuated SED and the observed one (i.e., $A_\lambda = m_\lambda - m_{\lambda,0}$). In the literature, the shape of the attenuation is taken as A_λ/A_V where the normalization is arbitrary. Usually, it is normalized by the reddening $A_B - A_V \equiv E(B-V)$, with the curve given by κ_λ meaning that $\kappa_\lambda = A(\lambda)/E(B-V)$, since $R_V = A_V/(A_B - A_V)$.

The extinction and attenuation curves can be divided in five different regions in which slopes are define to facilitate comparison among galaxies (Salim and Narayanan, 2020). These regions and slopes are: the overall UV-optical slope (A_{1500}/A_V), UV slope (A_{1500}/A_{3000}), optical slope (A_B/A_V), near-IR slope ($\lambda^{-\beta_{NIR}}$) and the UV 2175 Å absorption bump strength (A_{bump}) independent of the A_λ normalization (see, Fig. 1.19). The UV bump location lies between 1700 and 2700 Å (Salim and Narayanan, 2020). A range of 1950 and 2400 Å for the bump is reported in Shivaei et al. (2020).

In general, the physical properties inferred from SED fitting can vary dramatically depending on the assumed dust extinction/attenuation curve (Kriek and Conroy, 2013; Shivaei et al., 2015; Reddy et al., 2015; Salim et al., 2016). Extinction curves are measured on only a few galaxies, gamma-ray bursts, and quasars. They are the basis for attenuation curves. They exhibit a wide range of slopes as compared to the Milky Way and the Small Magellanic Cloud extinction curve (Salim and Narayanan, 2020). When a curve is less steep than another it is usually referred to as grayer. Attenuation curves in galaxies also show different types of slopes from steeper ones generally associated with low dust columns and shallow ones associated with opaque galaxies (Chevallard et al., 2013). A diverse range of UV bump strengths is also observed at low and high redshift but not so strong as Milky Way on average (Conroy, Schiminovich, and Blanton, 2010; Hagen et al., 2017; Salim et al., 2007). This will be addressed in the next sections, in which I discuss separately the current status of extinction and attenuation and their implementation in SED fitting software like CIGALE.

1.3.1. Extinction

The majority of our knowledge on extinction curves comes from observations in the Milky Way and the Magellanic Clouds. To get these measurements one needs to observe a point source (e.g., star, gamma-ray burst, and/or quasars) which is obscured by dust and compare it to a similar object (i.e., similar luminosity or spectral type in the case of stars) unaffected by the dust. More specifically, compare their spectra or SEDs (Conroy, 2013; Salim and Narayanan, 2020). This is known as the pair-pair method (Stebbins, Huffer, and Whitford, 1939) and is widely used, although some extra correction for extinction is needed when comparing stars, for example. Other methods to measure extinction curves include using dust-free references as theoretical stellar atmosphere models or a large survey statistical approach.

An extinction curve measured for the same galaxy using different lines of sight can show large variations, as well as the average of extinction curves when compared between galaxies. This is illustrated in Fig. 1.19 where the Milky Way and, Large and Small Magellanic Clouds (LMC, SMC) average extinction curves are presented. LMC and SMC curves are steeper on average, and the bump is less prominent as compared to the Milky Way (e.g., Sabbi et al., 2013; De Marchi et al., 2016; Yanchulova Merica-Jones et al., 2017; Roman-Duval et al., 2019).

The emerging picture of extinction curves shows a large variety ranging from steep slopes and weak bumps for $A_V < 0.8$ mag to relatively shallow and bumpy curved for higher A_V and higher metallicity (Salim and Narayanan, 2020). Confirmation of the UV bump at $z \sim 1.0 - 2.2$ (Ma et al., 2015; Ma et al., 2017; Corre et al., 2018) with different strengths and sometimes as large as the Galactic mean are confirmed. The SMC curve is preferred in high-redshift studies due to its sub-solar metallicity as in the distant Universe due to galaxy evolution the expected grains' size, distribution, and composition are not the same as in the local Universe. Therefore, obtaining an

extinction curve translates into knowing the physics of the dust grains. Based on emission and absorption features, two different ways of modeling have emerged like the synthesis models and direct numerical simulation where grain size distribution and dust composition, taking into account depletion, IR emission, polarization, and the response of the local environment (i.e., ISM densities/radiation field) are taken into account (Draine and Li, 2007; Jones et al., 2017).

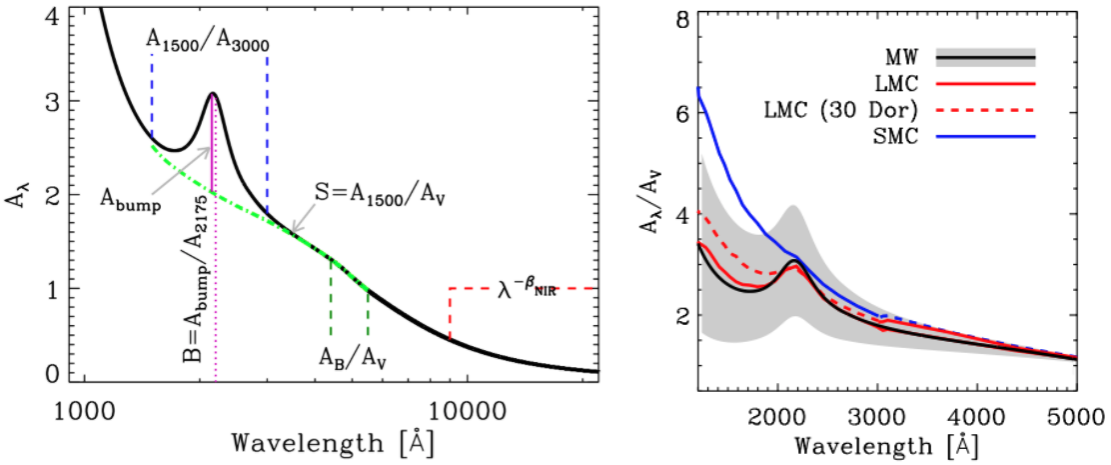

Figure 1.19. – Extinction curves state-of-art. On the left, the common regimes in which slopes are measured to study extinction/attenuation curves are shown as explained in Sect. 1.3. On the right, the Milky Way, Large and Small Magellanic Clouds extinction curves are reported. The image is taken from Salim and Narayanan (2020).

A direct translation from an extinction curve into an effective attenuation curve is not easy. Both curves differ in many ways that are difficult to constraint observationally (Hagen et al., 2017; Corre et al., 2018), or from simulations as a wide range of attenuation curves can be obtained with a fixed extinction curve varying the dust content and the star-dust geometry (see, Narayanan et al., 2018; Trayford et al., 2020).

1.3.2. Attenuation

The important concept for SED fitting is attenuation as this includes some complex configuration of the star-dust geometry which can be found in galaxies. As presented in Conroy (2013), four popular techniques are used to measure dust attenuation: *(i)* using UV-to-NIR and moderate-resolution spectra in SED analysis (e.g., Conroy, Schiminovich, and Blanton, 2010; Buat et al., 2012; Wild et al., 2011; Salmon et al., 2016; Lo Faro et al., 2017) to constrain dust effects as its effect is dominant in the UV, line emission are age-sensitive (Buat et al., 2018) and SED fitting allows an analysis on large samples (Lo Faro et al., 2017). *(ii)* measuring the Balmer decrement (i.e., Hα/Hβ,

Calzetti, 2001) to compare it to the intrinsic ratio providing measurements of attenuation towards HII-regions, *(iii)* measuring of the total absorption through the infrared excess (IRX; Salmon et al., 2016; Narayanan et al., 2018) from energy conservation as UV/optical photons absorbed by dust will re-emit in the IR wavelengths, and *(iv)* constraining attenuation of a foreground galaxy using a background luminous source with known spectrum. Deriving attenuation curves can be done either observationally or by implementing physical models.

To observationally derive an attenuation curve, an unattenuated SED is needed to get a normalization. This can be built either using stellar population synthesis models or inferring it empirically. Empirical templates producing the attenuation curve for starburst galaxies were implemented by Calzetti, Kinney, and Storchi-Bergmann (1994) which were calibrated using IR data in Calzetti et al. (2000) and led to the well-known Calzetti attenuation curve. The pair-pair comparison, as in the case of extinction, is applicable for attenuation comparing galaxies which are assumed to be intrinsically similar but both having different obscuration (Kinney et al., 1994; Wild et al., 2011). Empirical methods do not depend on parametrization. However, they are subject to assumptions on the homogeneity of the templates.

Analytical (e.g., Granato et al., 2000; Fontanot et al., 2009; Fontanot and Somerville, 2011; Wilkins et al., 2012; Gonzalez-Perez et al., 2013; Popping, Somerville, and Galametz, 2017) and hydrodynamical models (e.g., Jonsson et al., 2006; Rocha et al., 2008; Natale et al., 2015) coupled to cosmological simulations are also used to derive attenuation curves. One important difference between models relies on the star-dust geometry implementation (Salim and Narayanan, 2020) as generally all of them account for the structure of the galaxy that includes stars and ISM, dust grain properties assumptions, and a model of radiative transfer for the stellar light. To investigate attenuation curves, models for the formation and evolution of galaxies are created using cosmological simulations (Narayanan et al., 2018; Trayford et al., 2020). The stellar emission is added coupling stellar population synthesis models (Narayanan et al., 2018). As attenuation is a complex process that depends on the star-dust geometry, but also the scattering of light and the dust grain properties (Trayford et al., 2020) radiative transferring simulations and fitting the formalism of Calzetti et al. (2000) and/or Charlot and Fall (2000) to the resulting SED to obtain the dust attenuation is implemented. Let's focus on the foreground and birth cloud analytical models. In Fig. 1.20, a schematic view of the models is shown. The foreground models consist of adding the attenuation as a screen which obscures the light. This follows an extinction curve such as that of the Milky Way, LMC, SMC. However, when more complex configurations of the ISM are needed, for example, to explain the differences in nebular emission and continuum attenuation (see, Buat et al., 2018; Shivaei et al., 2020), a different model is required. Charlot and Fall (2000), inspired by results of Fanelli, O'Connell, and Thuan (1988) and Calzetti, Kinney, and Storchi-Bergmann (1994), separated the ISM diffuse medium where old stars are located from the birth cloud where young stars locate. The old/young separation relies on the dispersal time

of the birth cloud (e.g., young < 10 Myr while old > 10 Myr). Stars in the birth cloud suffer attenuation from the diffuse ISM and the birth cloud while stars in the ISM are only affected by the birth cloud (see, Fig. 1.20).

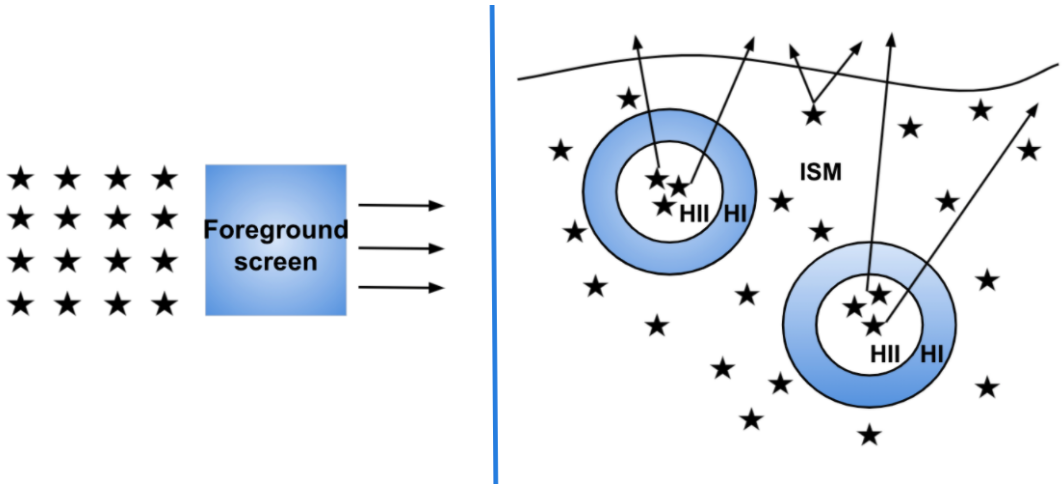

Figure 1.20. – Attenuation models. On the left, the foreground scheme is presented in which stars are attenuated by a screen which could be any known extinction/attenuation curve. In the right, a more complex star-dust configuration as developed by Charlot and Fall (2000) is shown in which stars are divided into two environments (i.e., birth cloud and diffuse ISM) according to the dispersal time of the birth cloud.

In the birth cloud scenario, the two components are assumed to follow a power-law relation normalized to the amount of attenuation in the V-band ($\lambda_V = 0.55\mu$m),

$$A_\lambda^{BC} = A_V^{BC}(\lambda/\lambda_V)^{n^{BC}}, \tag{1.3}$$

$$A_\lambda^{ISM} = A_V^{ISM}(\lambda/\lambda_V)^{n^{ISM}}, \tag{1.4}$$

where the total attenuation is given by the combination of both the birthcloud and ISM attenuations (see, Sect. 3.1.3 for more details). In the original study of Charlot and Fall (2000), the slopes were found to satisfy $n^{BC} = n^{ISM} = -0.7$. However, in da Cunha, Charlot, and Elbaz (2008) a value of $n^{BC} = -1.3$ was used. This value is implemented in the MAGPHYS code while in CIGALE the two component can be modified by the user.

1.3.3. Variations in the attenuation curves

Grayer (flatter) attenuation curves are the result of inhomogeneities in the ISM and more complex geometries (e.g., clumpy) as UV photons from massive stars can escape

easily, reducing the net measured optical depths at short wavelengths (Salim and Narayanan, 2020). On the contrary, steeper attenuation curves are related to simple, not clumpy star-dust distributions (Witt and Gordon, 1996; Gordon, Calzetti, and Witt, 1997; Witt and Gordon, 2000). Metallicity and age also lead to steeper curves (Corre et al., 2018; Shivaei et al., 2020). An attenuation curves comparison from simulations and observations as well as a function of the galaxy inclination is presented in Fig. 1.21. Also, a comparison of attenuation curves for galaxies at z > 0.5 is shown in Fig. 1.22.

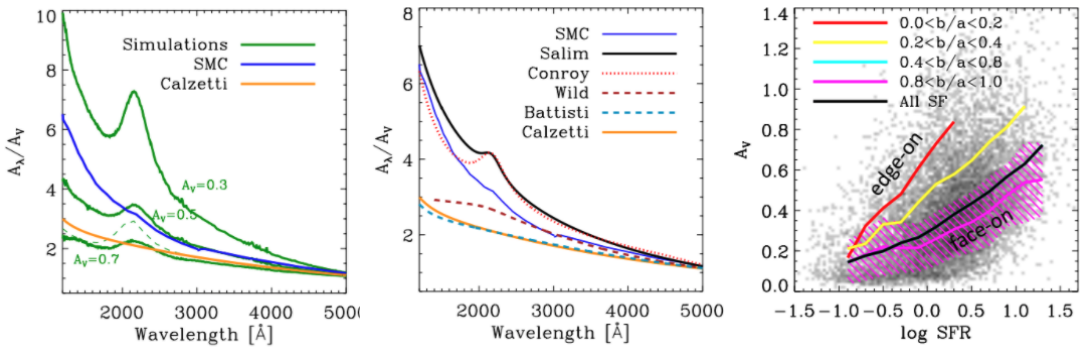

Figure 1.21. – Attenuation curve comparison. Left panel, a comparison of simulated curves for different optical depths are shown alongside the Calzetti et al. (2000) and SMC curves. In the middle panel, various curves (e.g., Calzetti et al., 2000; Conroy, Schiminovich, and Blanton, 2010; Wild et al., 2011; Battisti, Calzetti, and Chary, 2016; Salim, Boquien, and Lee, 2018) are compared to the SMC average extinction curve. The right panel shows the change of A_V as a function of SFR and the inclination. Image taken from Salim and Narayanan (2020).

In recent SED fitting packages, attenuation curves can be better estimated in a parametric form (see, Boquien et al., 2019, CIGALE) and prospector (Leja et al., 2019; Johnson et al., 2021), implementing Bayesian fitting techniques (Kauffmann et al., 2003a; Salim et al., 2005; Salim et al., 2007; Noll et al., 2009; Leja et al., 2017; Boquien et al., 2019; Johnson et al., 2021) and energy-balance methods (da Cunha, Charlot, and Elbaz, 2008; Boquien et al., 2019). This helps to put constraints on the IR luminosity based on templates and/or photometry (Salim and Narayanan, 2020). One can assume that the luminosity is reduced just by absorption without specifying the star-dust configuration. Then, as scattering in the ISM can also affect the photons, the final absorption curve (i.e., effective curve) will differ from a curve derived directly from the optical properties of dust grains (Charlot and Fall, 2000). The dust attenuation curve can be implemented as an effective curve or using the two-component model of (Charlot and Fall, 2000) in the SED fitting. To reduce the number of parameters, a parametrization of the attenuation curve is needed when implemented in SED fitting. Usually in terms of the slope and the UV bump (Salim and Narayanan, 2020). Some

of this parametrizations are the Cardelli, Clayton, and Mathis (1989) parametrization of the Milky Way extinction curve, the single-family parametrization of Fitzpatrick (1999) also for the Milky Way, a parametrization of the Calzetti et al. (2000) attenuation curve in Noll et al. (2009), modified Calzetti curve parameterization in Salim, Boquien, and Lee (2018), Boquien et al. (2019), and Leja et al. (2019) implemented in CIGALE and PROSPECTOR. All these parametrizations produce shapes based on empirical extinction or attenuation curves.

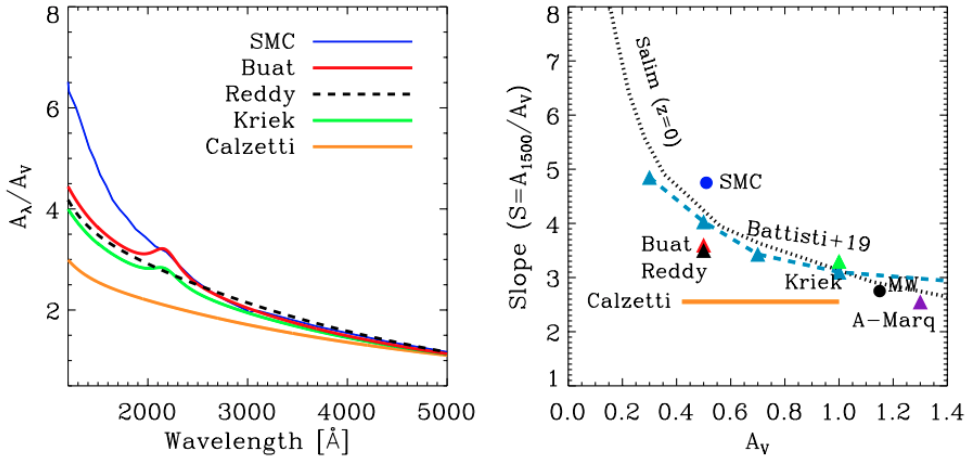

Figure 1.22. – High-redshift (z > 0.5) attenuation curves state of the art. In the left, the SED fitting derived curved of Buat et al. (2012) and Kriek and Conroy (2013), and empirical-template based by Reddy et al. (2015) are shown along with the Calzetti et al. (2000) and SMC curves. In the right, the slope as a function of the sample-averaged A_V. Image taken from Salim and Narayanan (2020).

In Fig. 1.23, a summary of the slope and dust dependence of the attenuation curve is presented. In general, at high redshift (e.g., z > 0.5), gas properties are affected by the large amounts of its content, low metallicities, and high SFR. All this changes the attenuation curve leading to a vast family of curves (Corre et al., 2018; Narayanan et al., 2018; Shivaei et al., 2020). Similar trends are observed for the nearby Universe. The dominant parameter that influences the determination of the slope of attenuation is A_V (Salim and Narayanan, 2020). On average, curves derived via empirical methods tend to be shallower than the SMC extinction curve. The evidence for UV bumps is mixed, but on average, they do not seem to be as strong as the MW bump. Most SED fitting studies find slopes on average steeper than the Calzetti curve.

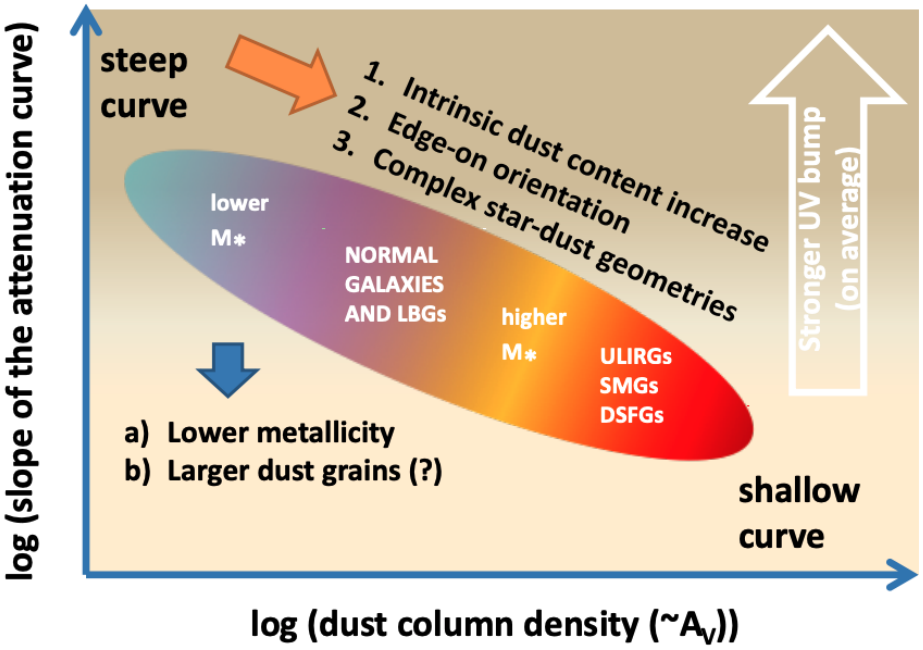

Figure 1.23. – Dust attenuation slope as a function of the dust column density. The most important physical parameters leading to the steep and shallow differences are summarized in this scheme. Image taken from Salim and Narayanan (2020).

1.4. Photoionization models

Astronomers obtain physical information from astrophysical objects by analyzing their light either using photometric and/or spectroscopic data. The gas around young and hot stars can be ionized, producing emission lines. This nebular emission is a tracer of star-formation and shares information on the physical properties of the gas like the chemical abundances, densities, temperatures, among others. This emission also needs to be corrected for dust effects and in some broadbands, they can have a large contribution to the flux (Burgarella, 2021). Including spectroscopic data in the multi-wavelength analysis allows putting constraints on stellar and ISM parameters such as the stellar age and gas-phase metallicity. It breaks degeneracies that cannot be disentangled using only photometry (see, Fossati et al., 2018; Buat et al., 2018; Corre et al., 2018; Yuan et al., 2019).

Using spectroscopic information along with photometry is not new. Kennicutt (1998) proposed a method to obtain SFR in terms of calibrated Hα and [OII] emission lines combining the stellar ionizing radiation with population synthesis models of Kennicutt (1983). Modeling and matching emission-line luminosities to stars, gas, and dust parameters was needed to avoid uncertainties caused by calibrations using empirical line ratios in terms of Hα to calibrate other emission lines (Gallagher,

Bushouse, and Hunter, 1989; Kennicutt, 1992; Barbaro and Poggianti, 1997). In works of Lehnert and Heckman (1994) and Kobulnicky, Kennicutt, and Pizagno (1999), nearby star-forming galaxies showed similarities in the optical-line ratios as those present in HII-regions. Emission-line information proved to be essential when interpreting stellar and gas parameters (Evans and Dopita, 1985). A common problem with the majority of the models was that they were calibrated for the nearby universe and they showed to be inappropriate to study star formation and ISM physics of young galaxies (Charlot and Longhetti, 2001), meaning that new suitable models were needed to be implemented. One of the first models (i.e., Charlot and Fall (2000)) that includes a simple prescription to treat dust effects for line and continuum was implemented by Charlot and Longhetti (2001) to interpret galaxy spectra in terms of stars, gas, and dust at the same time. They calibrated the nebular properties of their model using observed ratios of a nearby spiral and irregular, starburst and HII galaxies, including (Charlot and Fall, 2000) model to account for dust absorption in the lines and continuum and compute the SEDs. Calzetti et al. (2000) includes natively, dust extinction for lines in their recipe.

Emission lines global diagnostics are nowadays used to obtain information of SFR, dust content, gas-phase metallicity, and nuclear activity in galaxies (e.g., Izotov and Thuan, 1999; Kobulnicky, Kennicutt, and Pizagno, 1999; Kauffmann et al., 2003b; Nagao, Maiolino, and Marconi, 2006; Kewley and Ellison, 2008). Also, NIR spectroscopy opened a door to study optical rest-frame galaxies (e.g., Pettini and Pagel, 2004; Hainline et al., 2009; Richard et al., 2011; Guaita et al., 2013; Kashino et al., 2013; Steidel et al., 2014; Shapley et al., 2015; Silverman et al., 2015) and faint emission lines in the rest-frame UV (e.g., Shapley et al., 2003; Erb et al., 2010; Stark et al., 2014; Stark et al., 2015b; Stark et al., 2015a; Stark et al., 2017; Sobral et al., 2015) are popular in the extragalactic field. To have an overall picture, a coupling of stellar population synthesis models and photoionization codes is paramount (e.g., Garcia-Vargas, Bressan, and Diaz, 1995; Stasińska and Leitherer, 1996; Charlot and Longhetti, 2001; Zackrisson et al., 2001; Kewley and Dopita, 2002; Panuzzo et al., 2003; Dopita et al., 2013; Dopita et al., 2016; Nicholls et al., 2017). Uncertainties can be reduced by including more emission lines (e.g., Hβ, [OII], and [OIII]) in the SED fitting process to obtain better estimations of the physical parameters. Nevertheless, Hα plays an important role in constraining the gas-phase metallicity and the dust content Charlot and Longhetti (2001).

Photoionization models are implemented in current SED fitting software (e.g., Chevallard and Charlot, 2016; Boquien et al., 2019; Carnall et al., 2019; Robotham et al., 2020). (Chevallard and Charlot, 2016) implemented Gutkin, Charlot, and Bruzual (2016) prescription along with CLOUDY modeling in BEAGLE. Boquien et al. (2019) and Carnall et al. (2019) also include photoionization modeling from CLOUDY for CIGALE and Bagpipes, respectively. MAPPINGS is used to create the nebular emission models for ProSpect (Robotham et al., 2020). In general CLOUDY and MAPPINGS codes are the preferred software to model HII-regions and PDRs as they include novel

treatments for the dust composition, element abundances, attenuation, stellar evolution, among others (see, Ferland et al., 2017; Sutherland et al., 2018). The main parameters describing the HII-regions emission are the gas-phase metallicity, ionization parameter, dust-to-metal mass ratio, and electron density.

Metallicity is defined, in general, as the mass fraction of metals (i.e., all the elements different from Hydrogen and Helium). Globally, $X + Y + Z = 1$, where X, Y, and Z correspond to the mass fraction of Hydrogen, Helium, and the metal, respectively. The solar metallicity was commonly set to $Z_\odot = 0.02$ but Asplund et al. (2009) reported new values of $X_\odot = 0.7154$, $Y_\odot = 0.2703$, and $Z_\odot = 0.0142$ (Boissier, 2017). A common notation for atoms is given in terms of the oxygen abundance $12 + \log(O/H)$ where O/H stands for the ratio of oxygen and hydrogen atoms. On the other hand, the dust-to-metal mass ratio provides a way to account for the metals trapped in dust grains through the depletion factors. This is an important parameter when modeling emission lines and some common values are reported in the literature (see, Dopita et al., 2016; Byler et al., 2017; Nicholls et al., 2017). Some tension exists on the metallicity scale as it highly depends on the nitrogen and oxygen abundance (Nicholls et al., 2017). Oxygen is mostly created in the core collapse of a supernova while nitrogen has primary and secondary abundances (Vila-Costas and Edmunds, 1993). This has led to discrepancies in trying to interpret the locus of galaxies in the excitation diagrams at intermediate redshift (see. Sect. 4.1) in Part II of this thesis). The electron density controls the intensity of the emission lines and values around 100 cm^{-3} are commonly reported at $z \sim 2$ (Kashino et al., 2019). A parameter as important as the gas-phase metallicity is the ionization parameter. CLOUDY/MAPPINGS modeling can be seen as an ionizing point-like source at the center of a spherical distribution of gas of concentric layers. As presented in Charlot and Longhetti (2001), the ionizing profile of the gas and the geometry are fixed by the ratio of innermost layer radius r_{in} and the Strömgren radius R_S (i.e., the radius of a sphere where all the hydrogen is ionized),

$$R_S^3 = 3Q/(4\pi {n_H}^2 \epsilon \alpha_B),$$

where Q is the rate of ionizing photons, n_H and ϵ the hydrogen density and the volume filled by the gas, and α_B the case-B recombination coefficient for hydrogen. Then, the ionization parameter can be defined as the ratio of the rate of ionizing photons to gas densities at a distance "r" from the ionizing source,

$$U(r) = Q/(4\pi r^2 n_H c),$$

where c is the speed of light. Then, the ionization parameter can be seen as an ionization wave traveling across the HII-region at light speed. This parameter characterizes the overall level of ionization in the cloud. Modeling emission lines implies specifying the ionizing spectrum (e.g., created with any synthesis population model) and a range of metallicities (i.e., abundances) and ionization parameter to cover all the possible configurations of the ISM of HII-regions in galaxies.

Using Dopita et al. (2013) models with a constant SFH, Byler et al. (2017) showed that CLOUDY and MAPPINGS codes lead to similar coverage in terms of emission-line ratios with some disagreement between points with equal metallicity and ionization parameter. However, the discrepancy arises from differences at the high-metallicity end and also from different stellar population synthesis models applied as in CLOUDY the Flexible Stellar Population Synthesis (FSPS; Conroy, Gunn, and White, 2009), was used whereas Dopita et al. (2013) models implement Starburst99 D'Agostino et al. (2019). To faithfully compare intrinsic differences between both codes D'Agostino et al. (2019) produced models using the same fiducial parameters (i.e., ionizing spectrum, ionization parameters, abundances, depletion factors, and gas-phase density). They obtained a variation of ~ 0.1 dex as presented in Fig. 1.24 related to the input physics, model assumptions, and atomic datasets differences in both software.

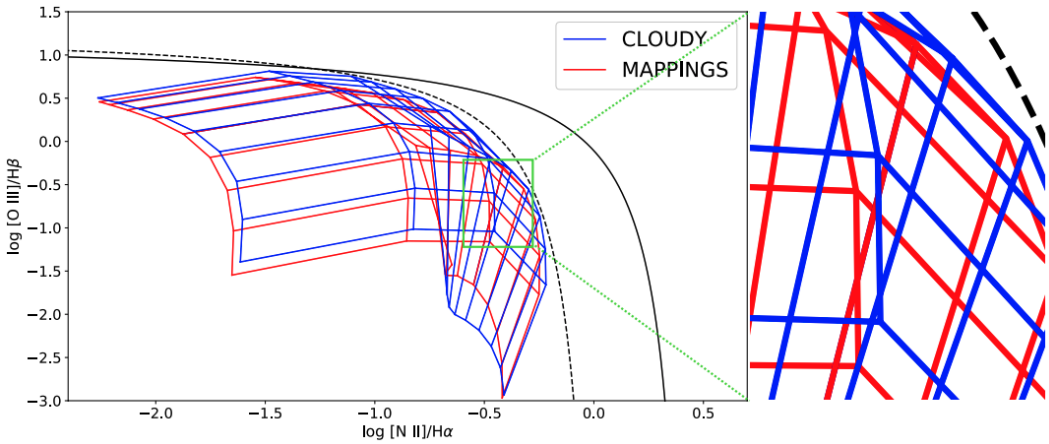

Figure 1.24. – CLOUDY and MAPPINGS excitation diagram grids. A comparison as presented by D'Agostino et al. (2019) is shown using the same fiducial input parameters. The figure on the right is a zoomed-in portion of a region of interest in the diagram done as given in D'Agostino et al. (2019).

1.4.1. Excitation diagrams

Emission lines are important because we can use them to know more about the physics of the ISM and stars such as the gas-phase metallicity, stellar ages, quantify the amount of attenuation for the lines only, or measure redshifts of galaxies. The gas is ionized by the massive and hot stars inside the HII-regions. Therefore, star-forming galaxies present the same emission lines in their spectra Boselli (2011) as HII-regions. However, AGN also produce intense emission lines as a consequence of the in-falling matter onto a supermassive black hole of mass $10^6 - 10^{10}$ $M_\odot$, and generated in a torus disk of ions (La Mura et al., 2017). Emission line allows us to classify star-forming and separate them from possible AGN contaminants as Seyfert or LINERS (i.e., galaxies which emission lines come from highly or low ionized gas, respectively). The most

common way to classify galaxies is through the excitation diagrams constructed from optical emission-line ratios, close enough in wavelength to avoid dust attenuation effects.

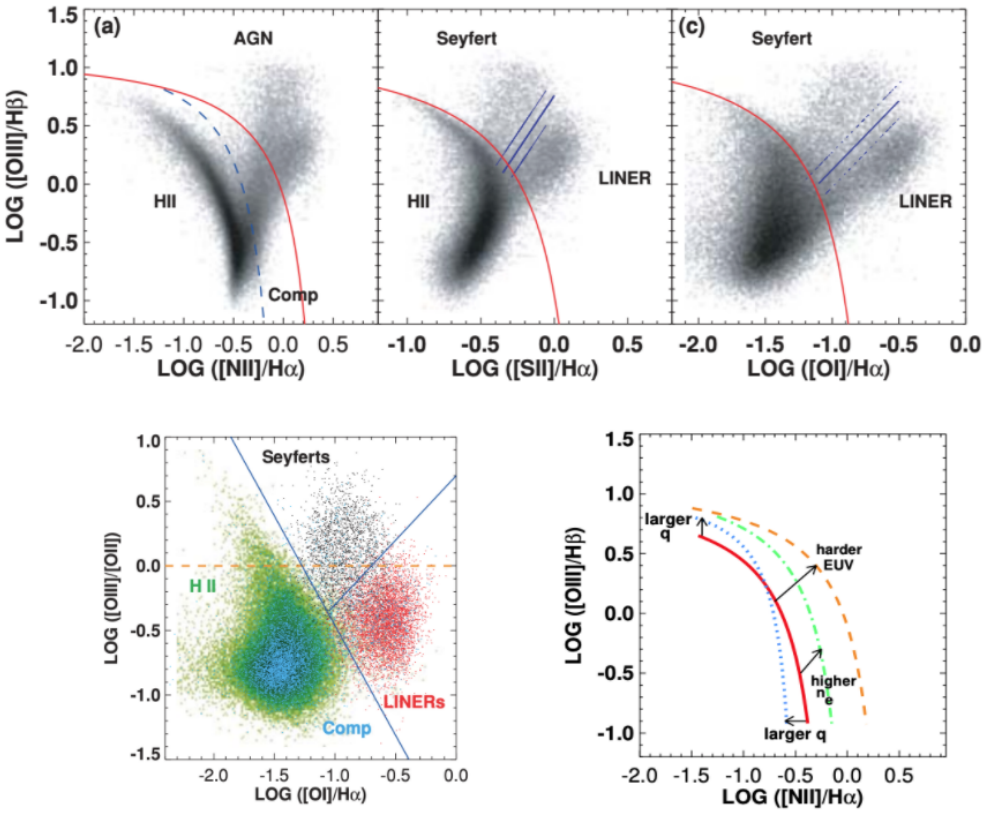

Figure 1.25. – Excitation diagrams. Some of the popular excitation diagrams based on recombination lines are presented. These diagrams are useful to understand discrepancies based on the different ISM physics (e.g., electron density, ionization parameter, ionizing spectrum hardness) governing different types of galaxies. The images are taken from Kewley et al. (2006) and Kewley, Nicholls, and Sutherland (2019).

Various line diagnostics were proposed in the past based on observations and models (e.g., Heckman, 1980; Baldwin, Phillips, and Terlevich, 1981; Veilleux and Osterbrock, 1987; Ho, Filippenko, and Sargent, 1997) which have been widely tested using observational data and comparing with photoionization models (e.g., Kauffmann et al., 2003b; Brinchmann et al., 2004; Kewley et al., 2006; Dopita et al., 2013; Kewley et al., 2013b; Shapley et al., 2015; Dopita et al., 2016; Kashino et al., 2017; Strom et al., 2017; Nicholls et al., 2017). The common emission line diagrams based on nearby Universe galaxies (i.e., $z \sim 0$) as presented in Kewley et al. (2006) are shown

in Fig. 1.25. These diagrams are used to divide galaxies into star-forming, generally below the dashed line (see, Kauffmann et al. (2003b)), composite between the dashed and solid line (see, Kewley et al. (2006) and Kewley et al. (2013a)), and AGN divided into Seyfert and LINER.

Each line ratio is sensitive to a particular parameter of the ISM. For example, [OIII]/Hβ and [OIII]/[OII] are sensitive to the ionization parameter, while [NII]/Hα, and [SII]/Hα are more sensitive to the metallicity. [OI]/Hα on the contrary, is sensitive to the hardness of the ionization field. Variations on the ratios can be attributed to different physical parameters helping us to classify and understand the ongoing physical and chemical processes in galaxies.

It is well-known that the locus of galaxies in these diagrams shows an offset for galaxies at intermediate and high redshift (e.g., z > 1) without a clear consensus (e.g., Maiolino and Mannucci, 2019) of the direct cause. Usually studied in terms of different values of the ionization parameter, discrepancies in the ionization spectrum and gas-phase metallicity variations (e.g., Steidel et al., 2014; Shapley et al., 2015; Steidel et al., 2016; Dopita et al., 2016; Strom et al., 2017; Kashino et al., 2017; Bian et al., 2020; Sanders et al., 2021). This is still a hot topic, and future spectroscopic surveys will help to have a better understanding of the high-redshift galaxies classification in terms of emission-line ratios. MOONS, PFS, and MOSAIC will provide excellent high-resolution spectra in which multiple lines will be observed, helping us to constrain important ISM parameters like temperature, electron density, and metallicity (Puech et al., 2018; Cirasuolo et al., 2020; Maiolino et al., 2020).

IR and FIR emission lines are also important to classify galaxies mainly because they do not suffer from strong dust attenuation giving us a way to derive physical properties without worrying about dust. Although I do not go deeper into this topic several lines coming from elements like oxygen, and nitrogen, or molecules such as CO, and H_2, among others, are used to derive densities, temperatures, abundances, and even study the dynamics of the gas in distant galaxies (see, Kewley, Nicholls, and Sutherland (2019) review for more details on emission line diagnostics). In Sect. 3.3.3, I present a comparison between the optical emission of [OIII] at 5000 Å to the IR line at 88 μm in an attempt to understand the underlying physics of [OIII] at intermediate and high-redshift.

1.4.2. Gas and dust properties

As presented before, we can derive properties of the gas and dust in galaxies combining emission lines and UV-to-FIR continuum information. The gas-phase metallicities can be obtained using emission lines if the electron temperature and density are known. It is common to use [OII]λ3727,29 or [SII]λ6716,31 doublets to derive the electron density, while for the electron temperature [OIII]λ4959+λ5007/[OIII]λ4363, [OII]λ3726+λ3729/[OII]λ7320 + λ7330, and [NII]λ5755/[NII]λ6584 are preferred.

Direct methods to calibrate metallicity are based on the former emission lines although sometimes these auroral lines are difficult to observe (see, Boselli, 2011, and references therein). Therefore, the indirect method using emission line ratios like [OIII]λ3727/λ3729, [OIII]λ4959 + λ5007, and [NII]λ6548 + λ6584 are implemented (Sanders et al., 2020).

On the other hand, dust is a crucial component of the ISM controlling the cooling of atomic and molecular gas absorbing energy coming from massive stars (Boselli, 2011). Dust also plays a role in the star formation process. Generally, as dust grains emit in the IR and sub(mm) wavelengths, this emission is used to measure the dust grain mass and its temperature. Studying dust allows us to understand attenuation as well as the contribution of the well-known PAHs to the overall SEDs of observed galaxies

1.5. Parameter estimation: Bayesian analysis and mock catalogs

Providing robust estimates of the physical parameters derived using SED fitting and their uncertainties, as well as a precise way to check their reliability is paramount when analyzing multi-wavelength data. These data sets contain a large number of data points and parameters involved in the fitting invoking the necessity of statistical treatment. A popular method, firstly used by Kauffmann et al. (2003a) and widely used in other works (see, Brinchmann et al., 2004; Salim et al., 2007; Walcher et al., 2008; da Cunha, Charlot, and Elbaz, 2008; Boquien et al., 2019) relies on the implementation of Bayesian statistics to estimate the parameters, uncertainties and deal with degeneracies inherent to the fitting process.

Bayesian fitting is useful when non-linearities due to dust attenuation, line emission, and dust emission need to be taken into account (Walcher et al., 2011). Broadly, when performing SED fitting, one constructs a family of models **M** that will be compared to the observations. The number of parameters can be larger than the number of data points **N** that will be fitted (Walcher et al., 2008). A likelihood or probability function can then be created on the space of all possible models to derive the best estimate and uncertainty related to a modeled parameter making use of this distribution (Kauffmann et al., 2003a). In a formal mathematical way of speaking, this translates in using Bayes' theorem, where a posterior probability density function will give the likelihood of a particular value of **M** given the data set **D**. This leads to,

$$P(M|D)dM = A \times f_D(M) Pr\{D|M\}dM, \tag{1.5}$$

where A is a normalization constant and Pr{D|M} is the probability of data set **D** as-

suming that its distribution can be described by **M**. Equation 1.5 can be approximated to,

$$P(M|D) \propto P(M) \times P(D|M), \tag{1.6}$$

with P(M) being the prior knowledge we have in the form of a model probability, P(D|M) as the probability of the data set given a model which is the information we have, and finally P(M|D) as the probability of the model given the data which is what we want to obtain (Walcher et al., 2008). The prior knowledge is included when selecting a given set of models based on the characteristics of the objects to be fitted. For example, one can neglect the chemical evolution of galaxies in the models as this is not constrained using only broadband photometry, but also simplify the SFH to estimate SFR based on the type of object (Walcher et al., 2011). We assume that the uncertainties are Gaussian distributed (see, Kauffmann et al., 2003a; Walcher et al., 2008) reducing $P(D|M) = \exp(-\chi^2/2)$.Integrating Eq. 1.6 over all the model space (all the parameters except the one to be derived), and minimizing χ^2 (Boquien et al., 2019; Burgarella, 2021) one obtains the probability distribution function (PDF) which median and width correspond to the best estimate and uncertainty of the estimated parameter. This method is Bayesian, as prior knowledge or at least a belief about the functional forms needs to be assumed. The advantage of this method relies on the fact that all measurements and their uncertainties contribute to the fit. The models account for the non-linear effects, and the derived uncertainties include measurement uncertainties as well as degeneracies. Also, the effects of degeneracies can be spotted as non-Gaussian PDFs or if the confidence regions are large for a given parameter (Walcher et al., 2008). However, as a caveat, the results can be dependent on the realistic input physical models and the sensitivity to the prior distribution of libraries or models (Walcher et al., 2011).

A principal difference in SED fitting codes relies on the implemented algorithm that samples the priors (Boquien et al., 2019). Some use Monte– Carlo Markov Chain (MCMC) method, grid-based codes, or parametric SFH (see, Kauffmann et al., 2003a; Brinchmann et al., 2004) when the dimension of the problem is large. This sampling can be sparse, missing some high-likelihood regions, and very computationally demanding. Others, such as in the case of CIGALE, perform the analysis on a fixed grid of models (needs to be reasonably well sampled) computed only once for all the objects and analyzing the physical properties from the likelihood–weighted parameters. I will focus on how CIGALE estimates, in a Bayesian fashion, the physical parameters and their uncertainties as this is relevant for future sections.

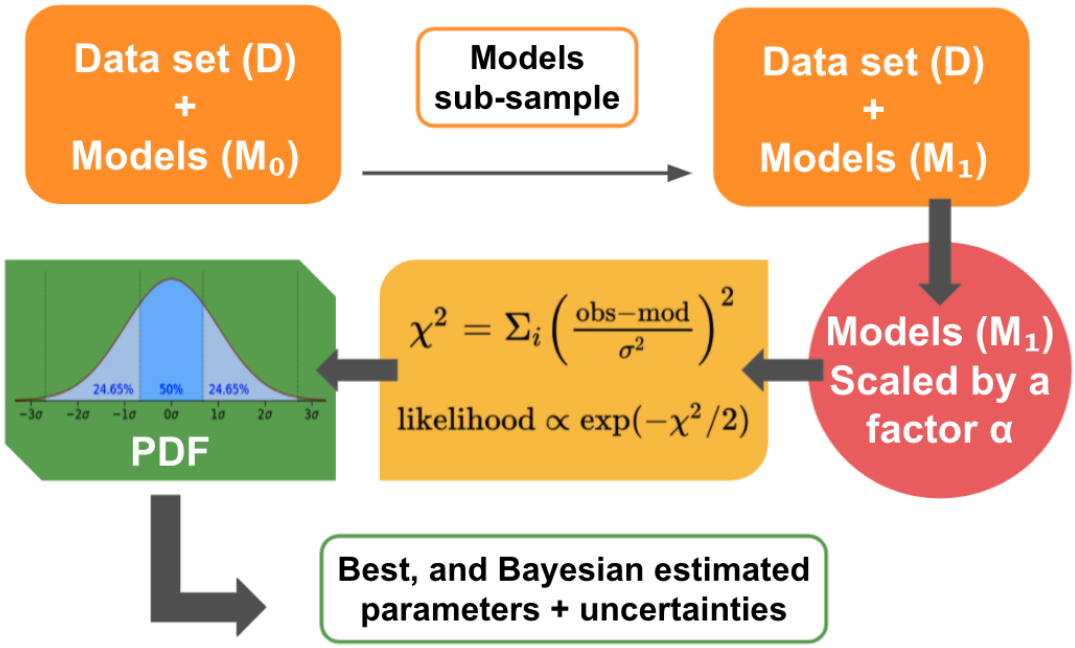

Figure 1.26. – Bayesian estimation process in CIGALE. The workflow scheme of the Bayesian estimation of the physical parameters and their uncertainties is shown in this figure. The intermediate step when the χ^2 and the likelihood are computed is shown in a general fashion because the functional form changes when using upper limits for the fluxes.

CIGALE creates a set of models M_0 and takes a sub-sample based on the redshift of the object to be consistent (i.e., M_1). This is a flat prior distribution. The models need to be scaled up by a factor α, as presented in Eq. 1.7, to match the observations (i.e., data set **D**). Once this is done, the χ^2 (see Eq. 1.8) is computed using the sub-sample of models and the observations as well as the likelihood $\exp(-\chi^2/2)$ for the sub-sample M_1. Finally, a likelihood–weighted mean and standard deviation computed from the probabilistic distribution is obtained for each physical parameter involved in the fitting. This process is summarized in Fig. 1.26. The scaling factor and χ^2 are given by,

$$\alpha = \frac{\Sigma_i f_i \times m_i/\sigma_i^2}{\Sigma_i m_i^2/\sigma_i^2} \tag{1.7}$$

$$\chi^2 = \Sigma_i \left(\frac{f_i - \alpha \times m_i}{\sigma_i} \right)^2, \tag{1.8}$$

where f_i stands for the observed and m_i for the modeled fluxes. The observational uncertainties are denoted by σ. CIGALE can also deal with upper limits in which

the same process described above is valid, but the way of computing the χ^2 and the scaling factor α is more complicated (see Sect. 4.3 of Boquien et al., 2019, for a more detail description).

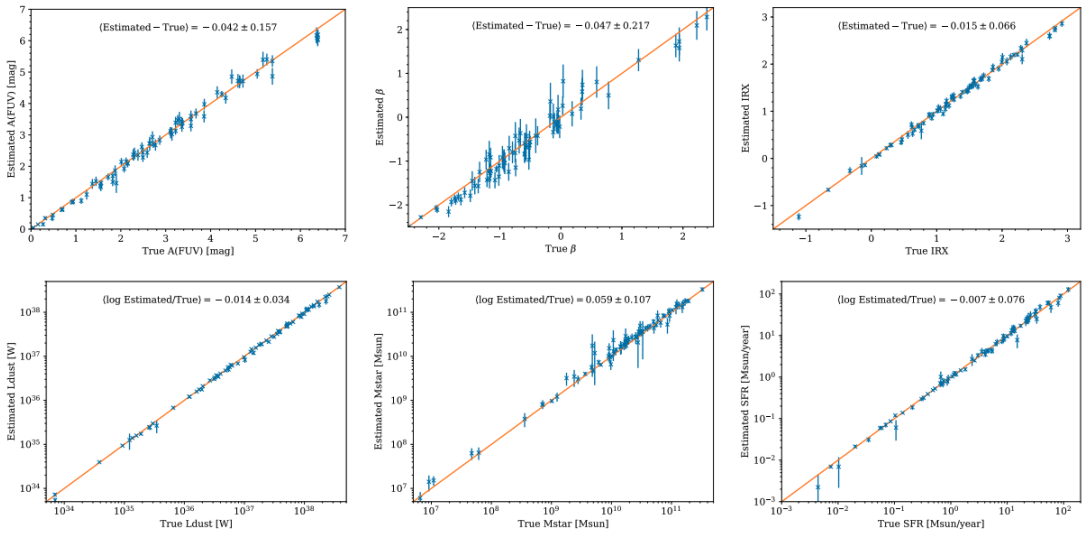

Figure 1.27. – Mock catalogs. The figure shows mock catalogs for the attenuation in the FUV, slope β, IRX, dust luminosity, stellar mass, and star formation. All the parameters are well-estimated. Figure taken from Boquien et al. (2019).

Checking the reliability of the physical parameters can be assessed using mock catalogs. The properties of the mock catalog are known, and one can compare them to the estimates from the analysis of the likelihood distribution. In CIGALE, to build the mock catalog, the best fit that is obtained from the analysis is taken for each object. A value from a Gaussian distribution with the same standard deviation as the observation is added to the best value. This new data set is analyzed in the same way as the observations. If the exact and estimated values are very similar, one can say that the physical property is reliable (Boquien et al., 2019; Burgarella, 2021). This is a way to control degeneracies. A check on the reliability of parameters using mock catalogs is presented in Fig. 1.27. Here all the parameters are well-estimated as can be inferred from the one-to-one relation followed by the objects. On the other hand, for example in Fig. 1.28, we see various cases (e.g., the parameters related to the SFH in the middle row and those related to the attenuation in the last row) where the agreement is not so evident. It tells us that the reliability of these parameters based on the SED fitting of the observations is not secure.

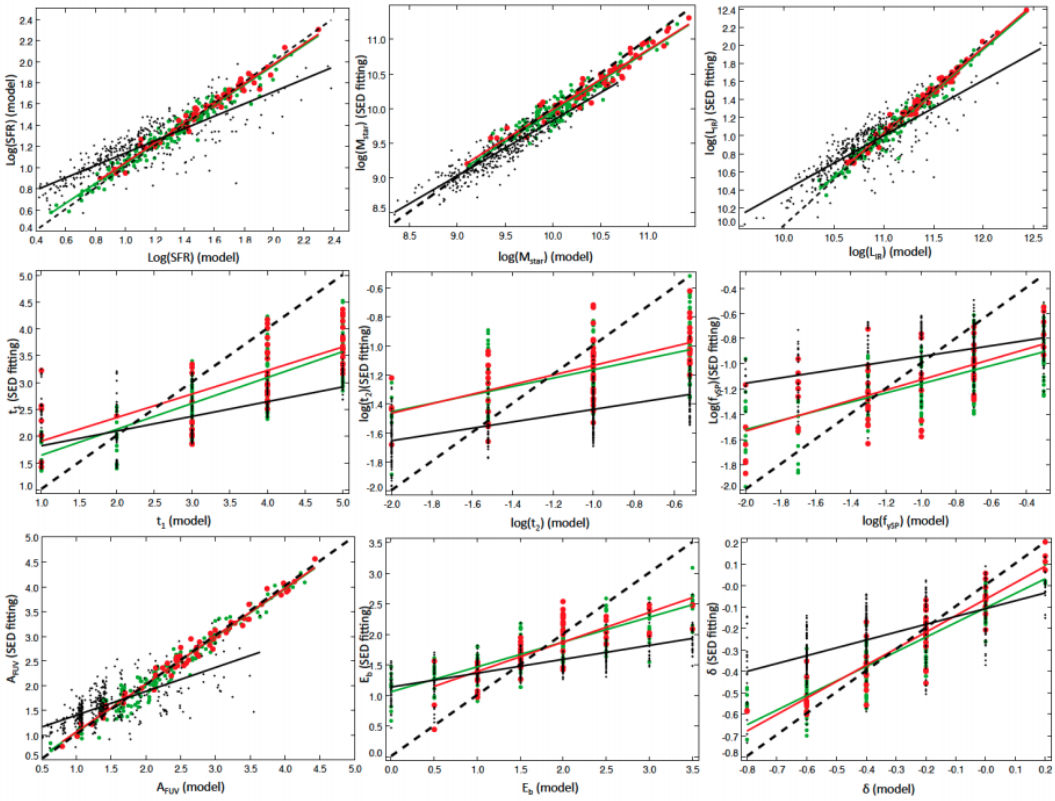

Figure 1.28. – Mock catalogs. The figure shows mock catalogs for the SFR, stellar mass, IR luminosity, parameters of the SFH, and the attenuation recipes. Not all the parameters are reliably estimated. The image is taken from Burgarella et al. (2017).

1.6. Outline of the thesis work

In the next chapters, I will synthesize two studies I worked on, closely related to diagnostics (e.g., emission lines and photometry) and scientific topics (i.e., spectro-photometric SED fitting). A first work analyzing a spectro-photometric dataset of galaxies in the COSMOS field using FMOS emission line fluxes to estimate emission lines attenuation, SFR, and stellar masses. A second project on using CIGALE as a simulator to create mock spectra catalogs either using empirical parameters or based on photometric fitting of COSMOS galaxies. I will briefly summarize the two main parts of this thesis work below.

The FMOS-COSMOS work was carried out with members of the CIGALE team at the laboratoire d'astrophysique de Marseille (LAM) and the centro de Astronomía (CITEVA) at the University of Antofagasta in Chile. In this work presented in Part II, I selected galaxies in the COSMOS field to have UV-to-FIR good coverage as well as emission lines from the FMOS-COSMOS surveys (Kashino et al., 2013; Silverman et al.,

2015). I modified CIGALE nebular module to include new models of HII-regions developed by Patrice Theulé to reproduce more accurately the emission lines of galaxies at redshift ~ 1.6. First, I performed SED fitting including continuum and Hα emission line fluxes to obtain robust estimates of the SFR, stellar masses, and dust attenuation to correct the emission lines. I propose a relation to obtain the attenuation of [OIII]λ5007 in terms of the stellar mass and an SFR-[OIII]λ5007 relation. The dispersion in the SFR-[OIII]λ5007 relation is studied in terms of physical parameters governing the ISM of these galaxies as the ionization parameter and the gas-phase metallicity. To address this, in a second step, I included more emission lines in the SED fitting (e.g., Hβ and [OIII]λ5007) to study the difficulties in simultaneously fitting continuum photometry and emission lines with SED fitting software. I address the main results from this end of the section.

As part of this project and a big part of the work is the modification of CIGALE's nebular module to include new nebular models separating the stellar metallicity from the SSPs and the gas-phase metallicity. This was motivated by the work in common I have with the MOONS spectrograph consortium. More specifically, for the extragalactic team in which I am involved for the galaxy mock sample modeling. The MOONS work is presented in Part III of this thesis. In the first place, I created mock spectra catalogs for the MOONS working groups using CIGALE as a simulator instead of a SED fitter. I built a sample of galaxies based on common physical parameters describing these objects. In other words, the parameters were just set to reproduce classical galaxies as early-type and late-type. These models were passed through the MOONS ETC, and different groups used them to derive physical parameters and estimate sensitivity for the expected results with MOONS. In a work, still in a preliminary phase, I fitted a sub-sample of galaxies of the COSMOS field for which we have FMOS-COSMOS emission lines creating new mock catalogs this time based on real photometric data. It covers the UV-to-MIR to guarantee that the SFHs are more realistic and representative of galaxies that will be observed with MOONS. In the future, I plan to expand this process to the entire COSMOS catalog and possibly include emission lines (i.e., Hα) to put better constraints on parameters as the ionization parameter and gas-phase metallicity and create robust mock catalogs. The main results are presented at the end with the general conclusions and perspectives of this thesis work.

Part II.

Multi-wavelength analysis of FMOS-COSMOS galaxies

2. Multi-wavelength and spectroscopic data

Contents

2.1. Introduction

In this part of the thesis, I will address a spectro-photometric SED fitting analysis carried out using CIGALE on a sample selected in the COSMOS field. For this purpose, I first disconnected the stellar metallicity from the gas-phase metallicity inside the SED fitting software changing the structure of the nebular module. With the help of Dr. Patrice Theulé, we created a new sample of HII-region models using Bruzual and Charlot (2003) as the ionizing spectrum varying the ionization parameter in a range of $-4.0 < \log U < -1.0$, covering 25 gas-phase metallicities spanning over $0.0001 < Z_{gas} < 0.05$, and computing emission lined for three electron densities $n_e = 10, 100, 1000$ cm^{-3}. This version of CIGALE is not public yet however, updates will be included in a coming release. This work is done to analyze the UV-to-IR continuum emission along with emission line fluxes such as Hα in a first run, and Hα, Hβ, and [OIII]λ5007 for a second run. We derived robust SFR and dust attenuation for the emission lines. We performed a comparison between the estimated dust attenuation correction from the Bayesian analysis carried out with CIGALE and the traditional Balmer decrement method for a sample with Hα and Hβ fluxes and using the Milky Way attenuation and Calzetti et al. (2000) attenuation curves.

Emission lines are corrected using the attenuation estimated with CIGALE and compared to SFR. We found a positive correlation with the [OIII]λ5007 emission line although more dispersed than the classical relation reported for Hα in Kennicutt (1998). Linear relations with a fixed and free slope are reported. Oxygen is sensitive to the physics of ISM (e.g., density, ionization field, abundances) then we studied the dispersion in the SFR-[OIII]λ5007 relation as a function of crucial parameters like the gas-phase metallicity and the ionization parameter. We fit the continuum emission and Hα, Hβ, and [OIII]λ5007 emission fluxes fixing the gas-phase metallicity to that inferred from Curti et al. (2020) relation and letting the ionization parameter vary in a known confident range for galaxies at redshift $z \sim 1.6$. We showed that the dispersion on the relation is mostly driven by the ionization parameter. Nonetheless, a contribution of gas-phase metallicity is expected. However, our metallicity range covered by the sample is not large enough to precisely attribute variation to this parameter. We comment on current difficulties in the locus of intermediate and high redshift galaxies in the excitation diagrams and we also compare our relation to well-known literature relations for emission at 88μm. The future perspective using spectro-photometric samples from large spectroscopic surveys like MOONS and PFS is discussed.

2.2. Spectro-photometric samples: the need for the far-UV and the far-IR, and emission lines

The need for data samples covering the UV-to-IR wavelength domain was justified in Part I of this thesis based on observations and SED fitting software structure. One

direct justification is linked to the energy-budget principle as photons are absorbed by dust particles at UV wavelengths re-processing this energy and emitting it in the IR range. Then, full coverage is necessary to properly model the SED of an object and to securely constrain the physical parameters. Including IR emission is important to robustly estimate stellar obscuration (Buat et al., 2018) but also to properly derive SFR in galaxies (Smith et al., 2012; Małek et al., 2018; Nersesian et al., 2019; Dobbels et al., 2020) as this can be largely affected by the dust-age degeneracy. A way to break this degeneracy is to include emission lines as they trace shorter timescales (see, Conroy, 2013, review for complementary information) as compared to the UV continuum emission, for example, leading to better estimation of the stellar ages and the dust content. As SED fitters deal with a wide range of parameters it is necessary to have a good sampling in terms of photometry and emission-line fluxes to break possible degeneracies and to obtain secure information from the SED. IR missions like *Herschel* and *Spitzer* are not currently operating. Therefore, we count on new telescopes like the JWST, and future facilities like the ELT to obtain better samples in this regime along with large spectroscopic surveys like MOONS and PFS which will enrich our knowledge of galaxies. We need to prepare current SED fitting codes to deal with future spectroscopic data because, at the moment, good knowledge dealing with photometry is done but not entirely with spectro-photometric samples. The future of SED fitting relies on a homogeneous treatment of these kinds of samples. This is a strong motivation that led us to modify CIGALE nebular module, thinking in the future, and how we need to prepare the code to analyze thousands of data that will be available in the coming years.

For this work, we had specific aims like deriving robust Bayesian estimates of the SFR which is one important parameter widely used in Astronomy to understand galaxy evolution and formation. We also aimed to constrain the dust amount of attenuation in galaxies, more precisely, for the emission lines. In the dusty universe, a large fraction of the star-formation is obscured with FIR accounting for 90% of the star-formation flux density at redshifts below $z < 3-4$ (see, Burgarella, 2021, and references therein), then is paramount to properly correct our datasets accounting for dust. Of course, this has a large impact on the physical properties we derive, and it has been an active topic during the past decades. In the light of what has been presented before, the need for spectro-photometric samples and their treatment as a whole to derive the physical parameters is paramount. the main two pillars of this work and SED fitting, in general, are the good estimation of physical parameters and the correction of datasets by dust effects which gives us the spectro-photometric samples as good allies to start paving this road.

In the next section, I explain the current knowledge we have about the COSMOS field. Also, the main choices that led us to create a sample in this particular region of the sky for our work.

2.3. The Cosmic Evolution Survey

The Cosmic Evolution Survey (COSMOS) is one of the best known multi-wavelength observed fields used in Astronomy to study galaxy formation and evolution as a function of redshift. This field has observations of around two million sources, covering 2 deg^2 of X-ray to radio image information as well as spectroscopic data. The multi-wavelength coverage in this field is the result of different observations using ground-base and space telescopes such as *Chandra*, GALEX, *Spitzer*, *Herschel*, Hubble, Subaru, CFHT, among others (see, Laigle et al., 2016, and references therein). A recent compilation improving that of Scoville et al. (2007) was reported in Laigle et al. (2016) known as the COSMOS2015 catalog. The major improvement of this catalog is the addition of NIR and IR data from the UltraVISTA (McCracken et al., 2012) and *Spitzer* Large Area Survey with Hyper-Suprime-Cam (SPLASH) projects.

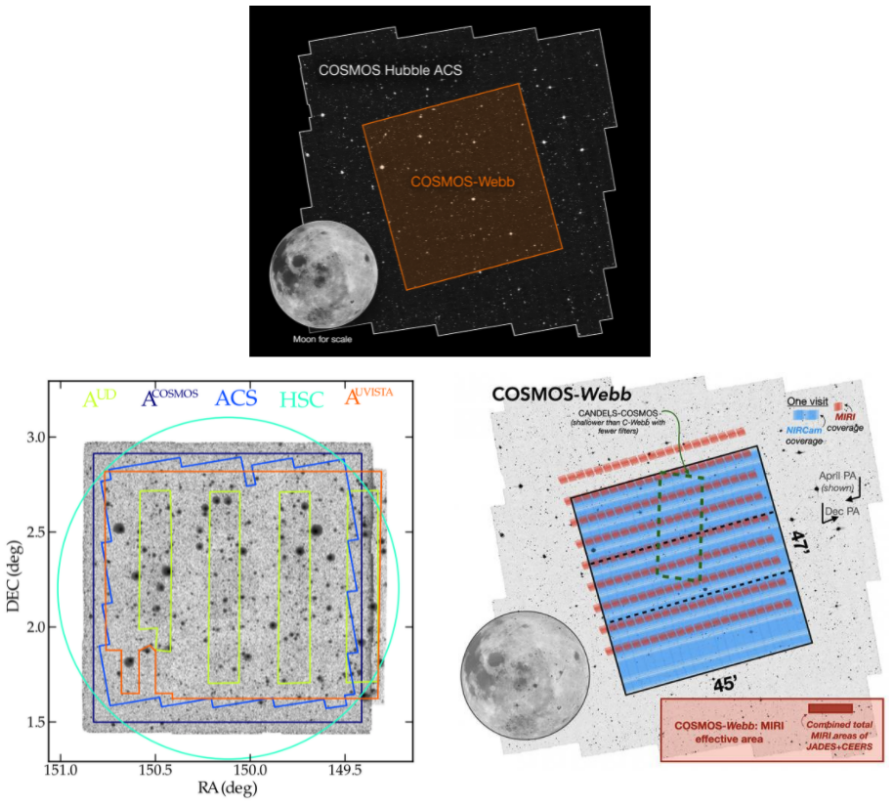

Figure 2.1. – COSMOS field. The image shows the COSMOS Hubble ACS footprint and the main components of the COSMOS2015 catalog, along with the future COSMOS-Webb footprint. Image is a composite from the COSMOS2015 catalog of Laigle et al. (2016), and future COSMOS-Webb Jeyhan Kartaltepe (RIT); Caitlin Casey (UT Austin); and Anton Koekemoer (STScI) Graphic Design Credit: Alyssa Pagan (STScI).

A new version of the COSMOS field catalog is presented in Weaver et al. (2021) in

which new data available for this field was processed and analyzed using 39 bands. This new COSMOS2020 catalog provides one magnitude deeper sensitivity when compared to the COSMOS2015 catalog, and better astrometric measurements using Gaia DR1 data. During the time we performed this work, the new catalog was not available, so we used the available information from the COSMOS2015 catalog.

In the future, more observations will be available for this field as part of the new observations that will be carried out by the JWST. A project called COSMOS-Webb led by scientists at Rochester Institute of Technology and the University of Texas at Austin will be in charge of mapping with the Near Infrared Camera (NIRCam) an area of 0.6 deg^2 and simultaneously with the Mid Infrared Instrument (MIRI) an area of 0.2 deg^2. The goal is to study galaxies at high-redshift, explore the epoch of re-ionization, and study primary objects through weak lensing. This will bring new unprecedented data changing the perspective we have of the Universe, in particular, that of the COSMOS field galaxies. A representative image of the COSMOS2015 catalog, COSMOS Hubble ACS, and COSMOS-Webb is presented in Fig. 2.1.

The choice of this field and the COSMOS2015 catalog is the well-known multi-wavelength coverage to maximize the number of objects we can use. In this work, we also used emission line fluxes as several spectroscopic surveys have been carried out in this field. This increases our chance of obtaining good quality data to build a good spectro-photometric sample. Also to test the capabilities of CIGALE when fitting all this information simultaneously.

2.4. COSMOS field sample selection

In the next sections I present the COSMOS field photometric and spectroscopic datasets used in this work. I address the different selection criteria applied in terms of data quality, AGN contamination, as well as a comparison of two different datatsets for the IR wavelengths. At the end, the final selection is presented and used in the next chapter to perform SED fitting on a spectro-photometric sample with the CIGALE software.

UV (Galex) to mid-IR (IRAC) photometry

The COSMOS field covers 2 deg^2 and is centered at α(J2000) = $10^h0^m27.9^s$ and δ(J2000) = $0^h8^m50.3^s$ (Scoville et al., 2007). We adopt the multi-wavelength catalog of Laigle et al., 2016, COSMOS2015, containing photometry from Galaxy Evolution Explorer near ultra-violet (GALEX NUV) as well as U, B, V, r, i, z, y, J, H, and K_s, and the *Spitzer* Infrared Array Camera (IRAC) 3.6, 4.5, 5.8, and 8.0 μm photometry from Canada France Hawaii Telescope (CFHT) MegaCam and Wide-field InfraRed Camera (WIRCam), SUBARU Prime Focus Camera (Suprime-Cam) and Hyper Suprime-Cam (HSC), and United Kingdom Infra-Red Telescope (UKIRT) Wide Field Infrared Camera

(WFC), and *Spitzer*, respectively. The NUV fluxes overlapping the Lyman break are discarded in the fits to avoid the break being inside the filter's bandwidth. NUV fluxes for sources with spectroscopic z > 1.5 at the GALEX NUV filter's effective wavelength of $\lambda_{\rm eff}$ = 2304.74 Å are not use in the SED fitting analysis.

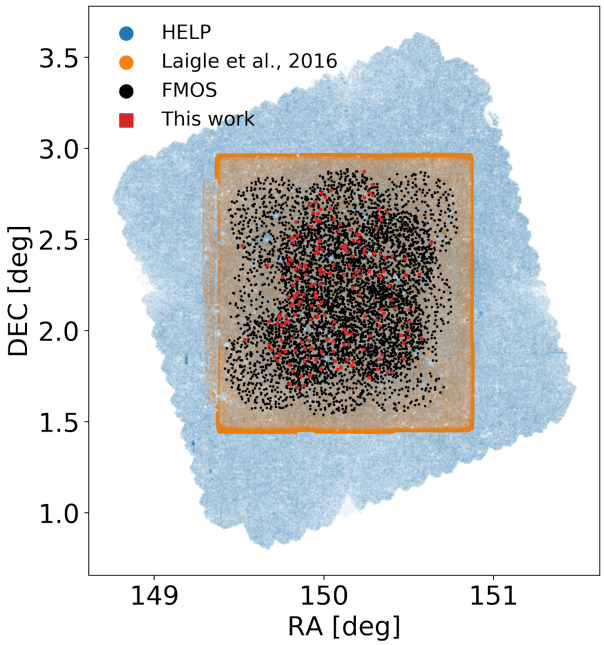

Figure 2.2. – Spectro-photometric sample. In blue, we show the position for objects in the HELP-project catalog. In orange, the main bulk of photometry from the COSMOS2015 catalog (Laigle et al., 2016). In black, the FMOS-COSMOS emission line targets. In red, the final selection for this work.

2.5. Mid-IR (MIPS) to Sub-mm (SPIRE) photometric data catalog comparison

The COSMOS field is a well-studied region of the sky with a good panchromatic covering of its sources. At IR wavelengths, we have data from the *Herschel* Extragalactic Legacy Project (HELP [1]) database and a recent work from Jin et al. (2018) with super-deblended data covering the *Spitzer* Multi-Band Imaging Photometer (MIPS) 24 μm, and both *Herschel* Photodetector Array Camera and Spectrometer (PACS) and *Herschel* Spectral and Photometric Imaging REceiver (SPIRE) bands. In Jin et al. (2018), prior positions are obtained for a total of 589713 sources in K_s and radio bands. Nevertheless, due to the large number of sources the authors only includes 88008 MIPS 24 μm and/or radio bands prior catalog for FIR/(sub)mm as well as 106420 K_s sources which are selected in stellar mass. The final prior catalog has 194428 MIPS

1. https://herschellegacyproject.wordpress.com/

24 μm+radio+mass-selected sources. Using redshift information and a SED fitting analysis, non-relevant prior information at the FIR/(sub)mm bands are ruled out in their analysis. Their uncertainties are calibrated using Monte Carlo simulations. They report a complete sample of 194428 obtained from the FIR/(sub)mm deblended images. The HELP survey provides measurements for galaxies on the same photometric bands. *Spitzer* MIPS, and *Herschel* PACS and SPIRE fluxes are the result of the HELP XID+ extraction based on priors position. XID+ uses a Bayesian probabilistic framework including priors to measure fluxes and their uncertainties (Hurley et al., 2017). Therefore, we can compare both datasets before defining our final sample in the IR wavelengths.

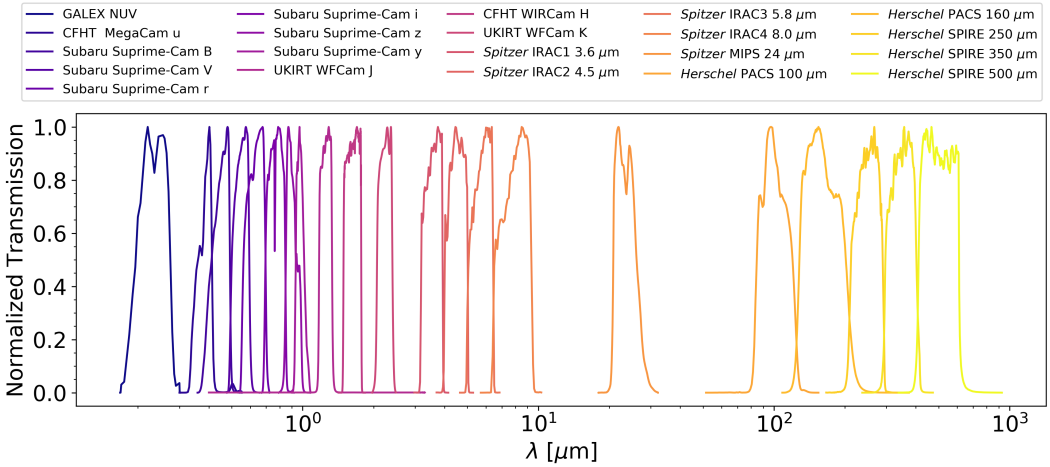

Figure 2.3. – Normalized transmission curves of photometric filters used in CIGALE to estimate the modeled flux densities in each band for the FMOS-COSMOS sample. The list of the filters is shown on the top.

We crossmatched both catalogs using a tolerance of 1 arcsec in coordinates to have a good compromise between the different IR datasets prior assumptions. We obtain a total matched-sample of 191743 sources between the HELP and Jin et al. (2018) catalogs. In Fig. 2.4, the SNR computed as the flux over the reported uncertainty for each band is presented as a function of the fluxes. Also, the flux difference in each band between both catalogs. In particular, the shape of the curves is similar for both data sets although Jin et al. (2018) 24 μm flux distribution saturates to an SNR of ~ 10 above 0.1 mJy. HELP data has a better SNR as compared to Jin et al. (2018) probably caused by the smaller uncertainties reported in HELP as can be noticed in Fig. 2.7. The same features presented in figures 2.4, 2.5, and 2.6 are presented in Jin et al. (2018) work when comparing to the PEP catalog of Lutz et al. (2011) and the XID+ catalog of Hurley et al. (2017) in which discrepancies especially towards the faint sources is attributed to crowded regions in which the deblending process is complicated to achieve. The comparison between fluxes from each catalog is presented in Fig. 2.5 while in Fig. 2.6 only sources with SNR > 3 in each catalog are shown. At 24 μm both

catalogs agree except at the faint end. Discrepancies in the fluxes are notorious at *Herschel* PACS with the agreement breaking below ~ 4 mJy at 100 μm, and below 10 mJy at 160 μm. This is less prominent at *Herschel* SPIRE bands although at 250 μm and 350 μm the agreement breaks below ~ 4 mJy, and is not so clear at 500 μm. At *Herschel* PACS bands Jin et al. (2018) reports a tail of low fluxes as compared to the PEP catalog primarily attributed to blended sources in the latter catalog as Jin et al. (2018) fits 5× more priors. In our comparison, we see that a tail of low fluxes below 0.1 mJy in Jin et al. (2018) for sources with SNR > 3 and fluxes above 0.4 mJy in HELP (see the two last rows of Fig. 2.4 and Fig. 2.6). According to Jin et al. (2018), XID+ results underestimate the uncertainties and overestimate the fluxes as the deblending process is performed statistically. However, this does not explain why sources with good SNR and high fluxes are dramatically underestimated in the new deblended catalog of Jin et al. (2018).

The agreement for sources with SNR > 3 in both cases is good. As the purpose of this work is to include spectroscopic information and good IR data we matched the HELP and Jin et al. (2018) catalog to the FMOS-COSMOS survey from Kashino et al. (2013) which has 5484 objects. We finished with a subsample of 2143 objects in total. We fit the SED of our objects using separately HELP and Jin et al. (2018) data. We inspected the SEDs produced by CIGALE using the two different sets and realized that unreliable configurations (e.g., *Herschel* PACS fluxes at 100 μm being larger than 160 μm) were in agreement in most of the cases in both catalogs. In Fig. 2.8 an example of the best SED for an object fitted using the two different IR data sets is shown. The *Herschel* SPIRE bands 350 μm and 500 μm are consistent within the errors with the rest of the photometry in the Jin et al. (2018) catalog. The χ^2 when comparing individual objects was in general underestimated (i.e., median reduced χ^2 of 0.82, see Fig. 2.7) when using Jin et al. (2018) dataset. Based on the flux discrepancies at the faint flux end, the uncertainties distribution, and the preliminary SED fitting results we decided to use the HELP dataset in our analysis. Good quality data in the IR is necessary to guarantee a robust estimation of the physical parameters from the SED fitting (i.e., SFR). This is the first comparison of both data sets performed on a small sample useful for our particular case. More quantitative analysis in a larger sample comparing all the sources and possible differences is needed.

Based on this comparison, we decided to use for the IR wavelengths the data from the HELP database. We use the *Spitzer* 24 μm, *Herschel* PACS 100, and 160 μm, and SPIRE 250, 350, 500 μm data products. Both *Spitzer* MIPS 24 μm and *Herschel* PACS 100, and 160 μm were obtained using *Spitzer* IRAC sources from the Spitzer Large Area Survey with Hyper-Suprime-Cam (SPLASH; Capak et al., 2012) as positional priors. In the case of *Herschel* SPIRE 250, 350, 500 μm, XID+ was run using 24 μm priors from Le Floc'h et al. (2009) catalog with addition of Submillimetre Common-User Bolometer Array 2 (SCUBA-2), radio and Atacama Large Millimeter/submillimeter Array (ALMA) data. The products corresponds to *Spitzer* MIPS 'dmu26_XID+MIPS_COSMOS', *Herschel* PACS 'dmu26_XID+PACS_COSMOS', and *Herschel* SPIRE 'dmu26_XID+SPIRE_-

COSMOS' available in the merged version 'dmu32_COSMOS' at the HELP-repository[2]. For further information: https://github.com/H-E-L-P/dmu_products.

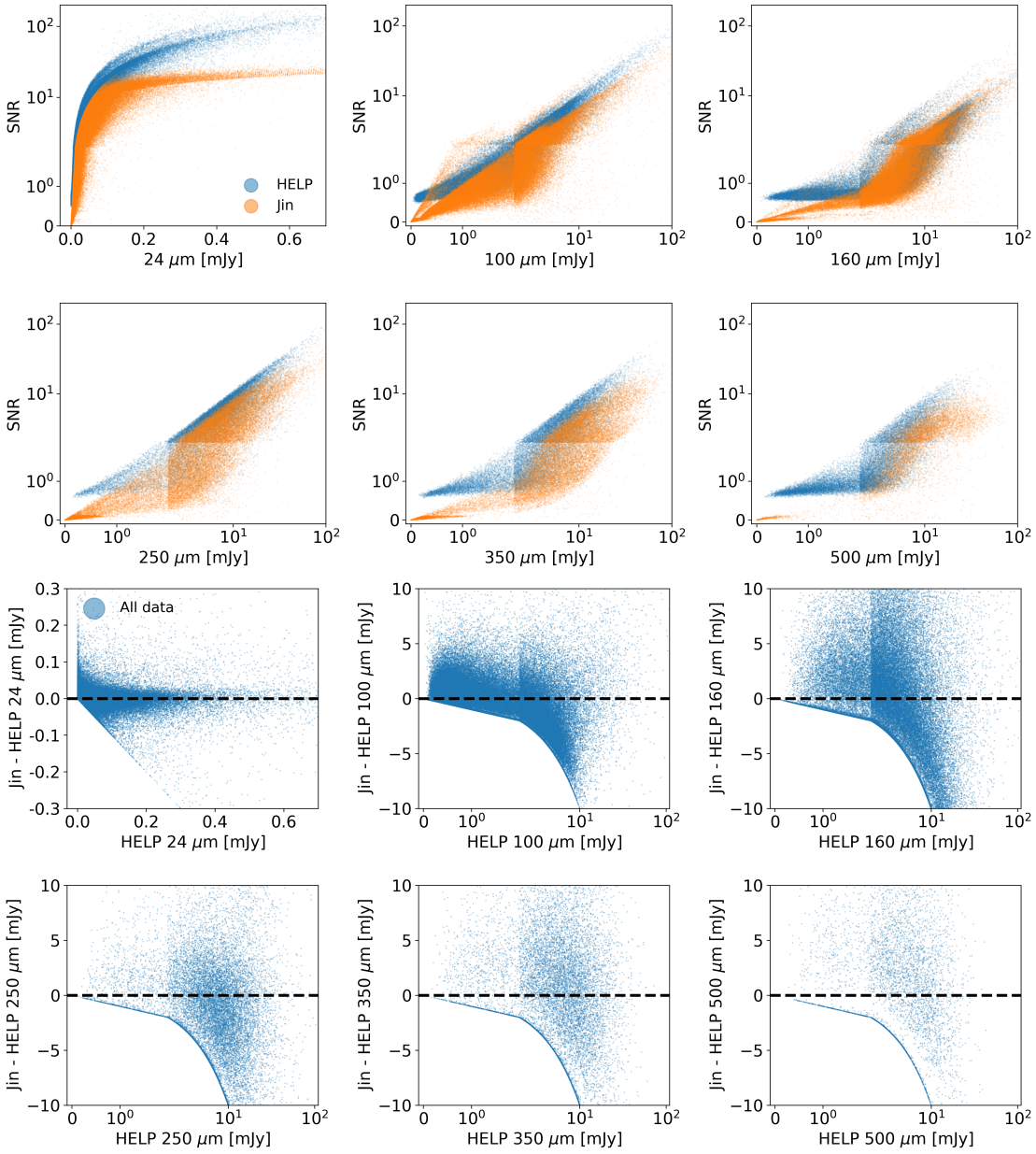

Figure 2.4. – Signal-to-noise ratio and flux difference. The SNR versus the HELP and Jin flux for the 24 μm, and *Herschel* PACS and *Herschel* SPIRE bands are shown in blue and orange, respectively, in the two first rows. The last two rows correspond to the flux difference (i.e., Jin et al. (2018) - HELP) versus the HELP fluxes. The horizontal black line is centered at zero. The fluxes and flux differences are in mJy.

2. http://hedam.lam.fr/HELP/dataproducts/dmu32/dmu32_COSMOS/

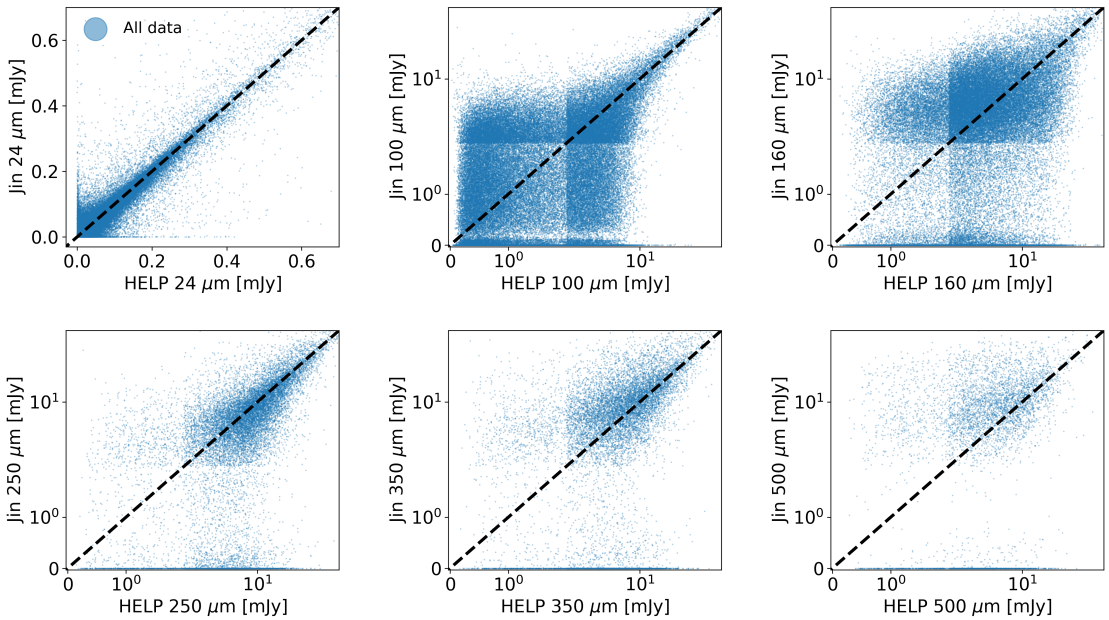

Figure 2.5. – IR bands comparison. A flux comparison for a sample of 1487 objects is presented for the 24 μm, and *Herschel* PACS and *Herschel* SPIRE bands. The black line represents the 1:1 relation.

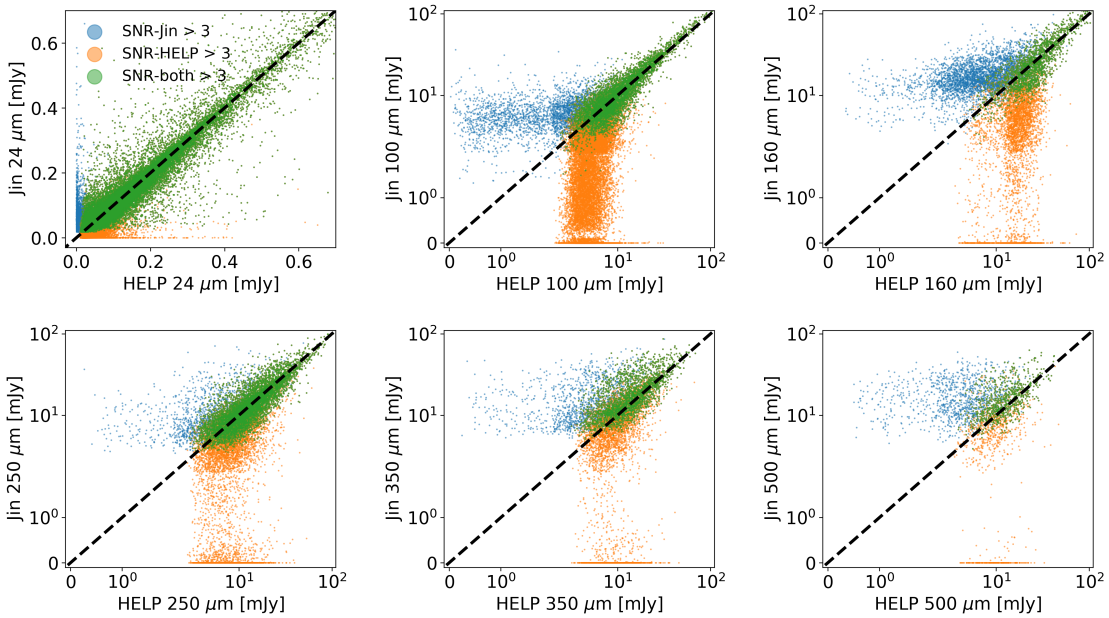

Figure 2.6. – IR bands comparison. A flux comparison for objects with SNR > 3 is presented for the 24 μm, and *Herschel* PACS and *Herschel* SPIRE bands. The blue dots correspond to objects with SNR > 3 in the Jin catalog. In orange for the HELP catalog, and in green in both catalogs. The black line represents the 1:1 relation.

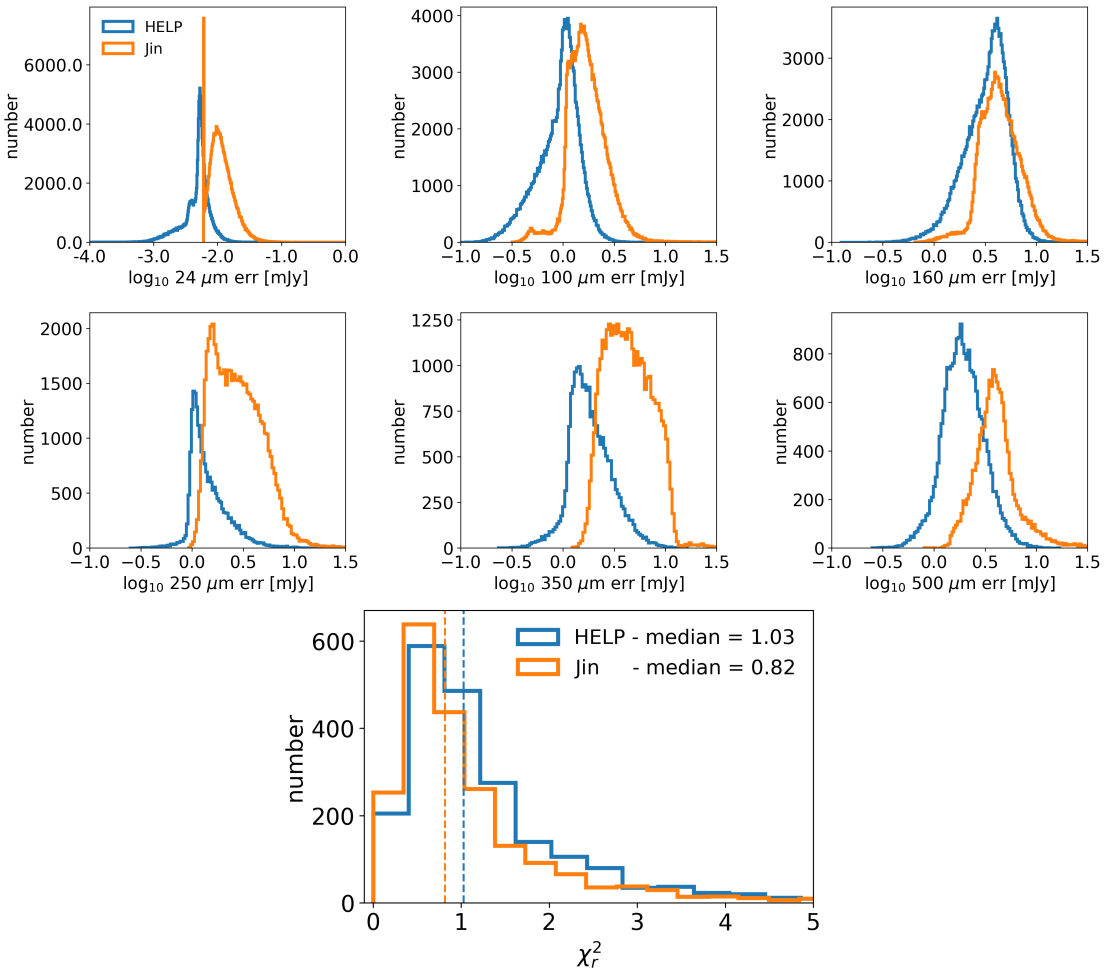

Figure 2.7. – Uncertainty distributions and χ^2 results. In the first two rows, the distribution of the reported uncertainties in the HELP and Jin et al. (2018) catalog are presented in blue and orange, respectively, for the IR bands. The last row shows the histogram distribution for the reduced χ^2 computed with CIGALE while using each dataset to calculate the SEDs of the objects in a sub-sample of FMOS-COSMOS galaxies.

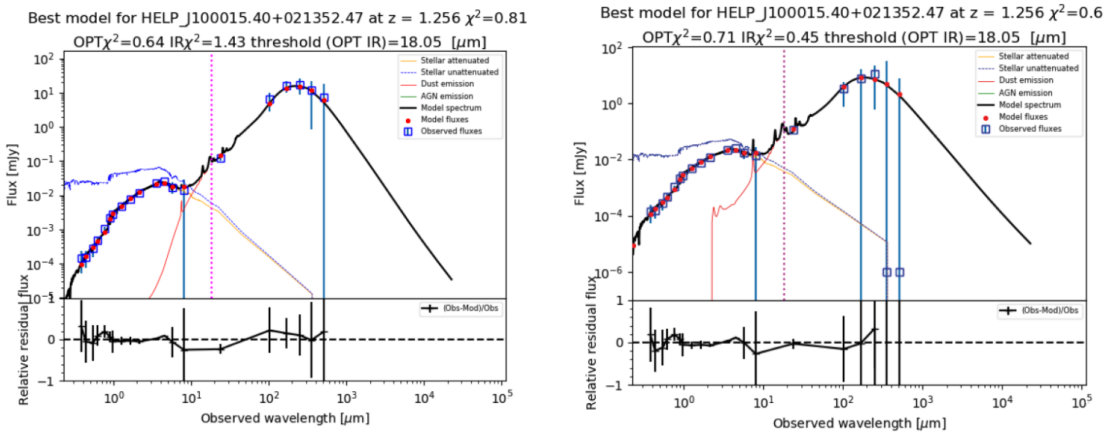

Figure 2.8. – SED using different IR sets. The best SED is presented for an object fitted using the photometry from the HELP survey in the left and from Jin et al. (2018) in the right. The blue boxes correspond to the photometric data while the red dots are the modeled fluxes. The black line corresponds to the best SED and each component is shown in color and described in the legend.

Spectroscopy

The Fiber Multi-Object Spectrograph (FMOS) is an instrument located at the Subaru telescope at the Mauna Kea Observatory in Hawaii. The instrument is a fiber-fed system allowing wide-field spectroscopy and enabling NIR spectroscopy. We use data from the FMOS-COSMOS survey as described in Kashino et al. (2013) and Silverman et al. (2015) for the emission line fluxes. These observations were performed using FMOS in high-resolution (HR) mode. It contains Hα, Hβ, [NII]λ6584, [OIII]λ5007, [SII]λ6717 and [SII]λ6731 [3] emission line fluxes. From the 5484 sources catalog, we select objects with at least Hα and [OIII]λ5007 flux measurements limiting the redshift range to $1.38 < z < 2.6$ in which both lines are observable by FMOS leading to a sample of 1557 objects. Aperture corrections are applied following prescriptions of Kashino et al. (2019). To guarantee good quality for the Hα, [NII]λ6584, Hβ, and [OIII]λ5007 spectral lines we select from the catalog sources with spectral fits obtained using a single Gaussian model (Silverman et al., 2015). We only consider emission lines detected with SNR larger than 3 leading to a sub-sample of 328 sources.

The measurement error in the emission line corresponds to the formal error provided by the line fitting process. The aperture correction value provided for each object is the best value derived from three different methods (see Kashino et al., 2019) and is used to correct in-fiber measurements. We keep only objects for which the flux loss is lower than 70%. To calculate the full uncertainty (i.e., fitting process and aperture

3. The [SII]λ6717 and [SII]λ6731 data are a private communication of the authors (Kashino & Silverman)

correction), the formal errors on the observed emission-line need to be added up in quadrature with a suggested factor of 1.5 by Kashino et al. (2019) to account for the uncertainty introduced by the aperture correction.

2.6. Final sample

The 328 sample of sources with emission lines was crossmatched to the COSMOS2015 catalog and to the available IR data from the HELP-project. We finished with a sample of 183 objects with UV-to-FIR photometry and Hα and [OIII]λ5007 emission line fluxes. The different data sets used in this work are represented in Fig. 2.2. In Fig. 2.3 the normalized transmission curves of each photometric filter used to estimate the modeled flux densities are presented (see Sect. 2.4 and Sect. 2.5).

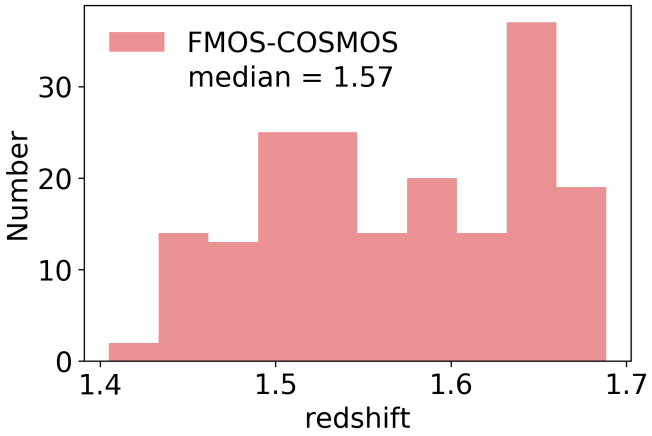

Figure 2.9. – Final redshift distribution of the 182 FMOS-COSMOS selected sources. The sample has a median of 1.57 in redshift.

In Fig. 2.9, the final sample redshift distribution covering $1.4 < z < 1.68$ is presented. This selection is shown in Fig. 2.2 as red dots over imposed on the FMOS-COSMOS sample (black dots), the COSMOS2015 catalog from Laigle et al. (2016), and the HELP-project data. The number of objects per band is shown in Table 2.1. SNR drops for *Herschel* PACS and *Herschel* SPIRE bands leading to 43 and 15 objects with SNR > 3 at 100 μm, and 160 μm, and 50, 35, and 0 objects for the *Herschel* SPIRE bands 250, 350, and 500 μm, respectively. All our sample has SNR > 3 in the *Spitzer* MIPS 24 μm, *Spitzer* IRAC1 3.6 μm, and *Spitzer* IRAC2 4.5 μm bands, but drops for *Spitzer* IRAC3 5.8 μm and *Spitzer* IRAC4 8.0 μm with 95 and 44 objects, respectively. Individual poorly measured photometric data does not affect the SED fitting result because the weight of these bands in the overall fit is small due to their large measurement error.

Most of the sample includes UV-to-MIR photometry and Hβ, [NII]λ6584, [SII]λ6717, and [SII]λ6731 emission line fluxes. The quality of the flux measurements is assessed

Table 2.1. – Final sample. The number of objects per band and SNR > 3. Emission lines marked with a star are provided by the authors Kashino & Silverman in private communication.

Bands	Data	$> 3\sigma$
GALEX NUV	51	13
CFHT MegaCam u	182	181
Subaru Suprime-Cam B	183	183
Subaru Suprime-Cam V	183	183
Subaru Suprime-Cam r	183	183
Subaru Suprime-Cam i	183	183
Subaru Suprime-Cam z	183	183
Subaru Suprime-Cam y	183	182
UKIRT WFCam J	182	182
CFHT WIRCam H	182	182
UKIRT WFCam K	182	182
Spitzer IRAC1 3.6 μm	183	183
Spitzer IRAC2 4.5 μm	183	183
Spitzer IRAC3 5.8 μm	173	95
Spitzer IRAC4 8.0 μm	128	44
Spitzer MIPS 24 μm	183	183
Herschel PACS 100 μm	183	43
Herschel PACS 160 μm	183	15
Herschel SPIRE 250 μm	81	50
Herschel SPIRE 350 μm	81	35
Herschel SPIRE 500 μm	81	0
Emission line		
FMOS Hα	183	182
FMOS Hβ	139	114
FMOS [NII]λ6584	139	112
FMOS [OIII]λ5007	183	182
FMOS [SII]λ6717*	40	22
FMOS [SII]λ6731*	35	15

by the SNR. Of the 139 objects that have data for the Hβ and [NII]λ6584 emission lines, 114 and 112 sources have an SNR > 3, respectively. [SII]λ6717 and [SII]λ6731 emission line measurements are of very poor quality leading only to 22 and 15 objects with SNR > 3. The quality of the Hβ measurements in terms of the Balmer Decrement (BD) will be addressed in Sect. 3.2. In Sect. 4.1 a more detailed study of the emission lines is presented.

We need to avoid any possible contamination due to an AGN contribution. Kashino et al. (2017) flagged AGN in the FMOS-COSMOS sample as point sources with an associated X-ray emission provided by the *Chandra*-COSMOS Legacy survey catalog (Elvis et al., 2009; Civano et al., 2016) with $L_{X-ray} \gtrsim 10^{42}$erg s^{-1} at 0.5 – 0.7 keV. Any source flagged to be associated with X-ray emission was discarded from our main sample. Obscured AGN contamination is still possible even if X-ray detected sources are excluded. Kashino et al. (2017) identified 39 objects consistent with obscured (type-II) AGN based on narrow line ratios with only 4 of those objects having an X-ray counterpart. Nevertheless, we did not exclude these objects from our analysis because our results are robust enough even if these objects are included probably because they are not extreme cases. We use the color criteria of Donley et al. (2012) to separate AGN from star-forming galaxies and verify that none of our objects lie inside the AGN region.

3. Star formation rate and dust attenuation

Contents

3.1. SED fitting with CIGALE

In this section, we present the SED fitting process carried out with the code CIGALE (Boquien et al., 2019). We describe the modules that we use and their direct impact on the analysis of our data set. The structure of the code is addressed by different authors in the literature (e.g., Ciesla, Elbaz, and Fensch, 2017; Małek et al., 2018; Buat et al., 2018; Boquien et al., 2019). CIGALE is based on the energy balance principle in which dust partially absorbs emission of all origins in the UV-optical wavelength range and re-emits this energy in the IR. The code creates millions of models to be compared with the observations and estimates physical parameters of galaxies (such as SFR, stellar mass, dust luminosity, dust attenuation, AGN fraction) applying a Bayesian statistical analysis approach.

Different modules are chosen from the CIGALE library to model the star-formation history (SFH), the nebular emission, dust attenuation, and re-emission. The parameters and their uncertainties are computed using the goodness of fit of all the models from a likelihood-weighted mean and likelihood-weighted standard deviation, respectively. A global indicator of the quality of the fits is given by the reduced χ^2 (χ^2_r). In general, the χ^2_r must account for the degrees of freedom, however, the non-linearity of the equations (Chevallard and Charlot, 2016) linking the parameters and their non-trivial dependence on each other, makes it difficult to include them. Therefore, the χ^2_r corresponds to the χ^2 divided by the total number of input fluxes.

The combination of Hα fluxes with UV-to-IR data with preservation of energy budget allows us to get reliable estimates of dust attenuation (see Sect. 3.2) without recurring to other methods such as the Balmer Decrement (BD). It also allows secure estimations of the SFRs. Although we have Hβ, [NII]λ6584, [OIII]λ5007, [SII]λ6717 and [SII]λ6731 information we do not fit these lines because of current discrepancies concerning the HII-region models (see Sect. 4.1) and/or poor quality of the data as presented in Sect. 2.6 and Table 2.1. In particular Hβ fluxes are discarded either because of their low SNR or a Hα/Hβ ratio below the canonical value of 2.86 (see Sect. 3.2). [NII]λ6584, [SII]λ6717, and [SII]λ6731 only satisfy the SNR criterion for 112, and 22 and 15 objects, respectively.

3.1.1. Star-formation history

We use a delayed SFH with the functional form presented in Eq. 3.1. This form depends on the time of the star-formation onset t_0, and the e-folding time of the stellar population $\tau_{\rm main}$. A recent burst of constant star formation that has been going for at most 70 Myr is superimposed to the delayed SFH. This form allows us to have a variation of the SFH where the SFR increases from the onset of star-formation until its peak at $\tau_{\rm main}$. After that point, the SFR declines.

$$\mathrm{SFR_{main}(t)} \propto \frac{\mathrm{t}}{\tau^2_{\mathrm{main}}} \times \exp(-\mathrm{t}/\tau_{main}) \text{ for } 0 \leq \mathrm{t} \leq \mathrm{t_0}. \quad (3.1)$$

The delayed component allows us to add a burst that we define with constant amplitude over the last years (Corre et al., 2018; Carnall et al., 2019; Leja et al., 2019; Chevallard et al., 2019; Buat et al., 2019). The amplitude of the burst is fixed by $\mathrm{f_{burst}}$. It is defined as a mass ratio between the stars formed during the burst and the total mass of stars. We selected objects with emission lines thus we expect the amplitude of the burst to have a direct impact on the derivation of SFR for at least some objects in our sample. SFR is averaged over 10 Myr compatible to the time-scale traced by Hα. The input parameters are described in Table 3.1 where the e-folding time and the age of the main stellar population are left as free parameters as well as the age and the mass fraction of the burst. We use a Chabrier (2003) IMF at solar metallicity 0.02 for the stellar population. Effects on the variation of the estimated parameters due to a fixed stellar metallicity are discussed in Sec. 4.1.2.

3.1.2. Nebular emission lines

CIGALE models the galaxy's emission of the ionized gas by stellar generations as an effective HII-region. It encompasses the ensemble of HII-regions and the diffuse ionized gas. The nebular emission lines are pre-computed in the nebular module of CIGALE and re-scaled with the number of Lyman continuum photons from the stellar emission of the model galaxy.

The radiation field intensity is given by the dimensionless ionization parameter $\log \mathrm{U} \equiv \log(\mathrm{n}_\gamma/\mathrm{n_H})$, where n_γ is the number density of photons capable of ionizing hydrogen and $\mathrm{n_H}$ the number density of hydrogen. The photo-ionizing field is generated with the single stellar population (SSP) model library of Bruzual and Charlot (2003), using a constant SFH over 10 Myr. In Sect. 4.1, we detail the major changes made in modeling nebular emission as compared to the previous version described in Boquien et al. (2019). The updated version of the HII-region models is used alongside this work to fit photometry and emission line fluxes. Our main purpose is to measure dust attenuation and SFR and to compare the latter to [OIII]λ5007 luminosities. The new photoionization models allow us to interpret the locus of our galaxies in the excitation diagrams in an attempt to understand the underlying physics of the ISM.

3.1.3. Dust attenuation recipe and dust emission

We adopt the recipe proposed by Charlot and Fall (2000) (CIGALE module called dustatt_modified_CF00; hereafter CF00) where two stellar populations are considered: young stars (age $< 10^7$ years) which are still located in a birth cloud (BC) while older stars (age $> 10^7$ years) already moved into the interstellar medium (ISM). Both populations experience a different dust attenuation: the emission of young stars goes through the BC and the ISM while the emission of older stars is only attenuated by

dust located in the ISM. The dust attenuation in the ISM and the BC are both modeled as power-laws normalized to the amount of attenuation in the V-band ($\lambda_V = 0.55\mu$m),

$$A_\lambda^{BC} = A_V^{BC}(\lambda/\lambda_V)^{n^{BC}}, \tag{3.2}$$

$$A_\lambda^{ISM} = A_V^{ISM}(\lambda/\lambda_V)^{n^{ISM}}. \tag{3.3}$$

The ratio of the attenuation in the V-band experienced by the young and old stars is given by,

$$\mu = A_V^{ISM}/(A_V^{ISM} + A_V^{BC}), \tag{3.4}$$

where μ is considered as a free parameter in our fitting process (da Cunha, Charlot, and Elbaz, 2008; Battisti et al., 2019). Nebular lines coming from the Lyman continuum photons due to very young stars are attenuated as young stars (BC+ISM). This recipe is used to correct both continuum and emission line fluxes in this thesis work. The values used in the CIGALE's attenuation module for each parameter are given in Table 3.1.

The slopes of the two power-laws (i.e., BC and ISM) are fixed to -0.7 following Charlot and Fall (2000). This value reproduces the observed mean relation between the IRX and UV spectral slope of nearby starburst galaxies. Lo Faro et al. (2017), Wild et al. (2007), da Cunha, Charlot, and Elbaz (2008), and Battisti et al. (2019) set $n^{BC} = -1.3$ to account for effects introduced in the absorption curve due to the optical properties of dust grains as those present in the Milky Way and the Large and Small Magellanic Clouds. However, it has been shown from HII-region studies (see Caplan and Deharveng, 1986; Liu et al., 2013) that grayer values closer to the one chosen in this work are more suitable to reproduce the effective attenuation in dusty galaxies. Letting n^{BC} free is not suitable because we use only one emission line and its value would be poorly constrained. In Sect. 3.2 we explore the effects of changing -0.7 to -1.3 for n^{BC}. The only free parameters in our recipe are the μ and A_v^{ISM}. The μ parameter relates the undergone attenuation in the V-band by the ISM (i.e., old stars, continuum) and the BC+ISM (i.e., young stars, emission lines). Letting μ free to vary allows some variations of the effective attenuation law (Battisti, Calzetti, and Chary, 2016; Buat et al., 2018; Małek et al., 2018; Chevallard et al., 2019). Moreover, introducing this flexibility in the SED fitting process allows for a better quality fit of the Hα emission. Variations of the attenuation law will be explored as further work.

The Dust emission is fitted with the Draine and Li (2007) models based on a set of parameters to constrain the starlight intensity and link dust to star-formation, including updates of Draine et al. (2014). We use these models because we have 24 μm information, making them better suited and more flexible for our purpose.

Table 3.1. – CIGALE modules and input parameters used for the SED fitting process as presented in Boquien et al. (2019)

Parameter	Symbol	Values
Delayed Star Formation History and Recent Burst		
e-folding time of main stellar population (Myr)	τ_{main}	1000.0, 3000.0, 4000.0
age of main stellar population (Myr)	age_{main}	2000.0, 2500.0, 3500.0, 4000.0
age of the late burst (Myr)	age_{burst}	10.0, 40.0, 70.0
mass fraction of the late burst population	f_{burst}	0.0, 0.001, 0.05, 0.1, 0.15
Stellar Populations		
Stellar population synthesis models from Bruzual and Charlot (2003)		
initial mass function	IMF	Chabrier
metallicity	Z_{star}	0.02
Nebular Emission		
ionization parameter	logU	-4.0, -3.5, -3.0, -2.5, -2.0, -1.5, -1.0
gas metallicity	Z_{gas}	0.008, 0.006, 0.01, 0.02, 0.03, 0.04, 0.05
Dust attenuation		
Templates based on values adopted by Charlot and Fall (2000); Buat et al. (2018)		
ISM attenuation in the V-band (mag)	A_V^{ISM}	0.0, 0.3, 0.5, 0.7, 0.9, 1.1, 1.3, 1.5, 1.7, 1.9
$A_V^{ISM}/(A_V^{ISM}+A_V^{BC})$	μ	0.1, 0.3, 0.5, 0.7, 1.0
slope of the attenuation in the ISM	n_{ISM}	-0.7
slope of the attenuation in the BC	n_{BC}	-0.7
Dust Emission		
Templates based on average values following Małek et al. (2018) and references therein		
mass fraction of PAH	qPAH	0.47, 1.12, 1.77, 2.5
minimum radiation field	U_{min}	5.0, 10.0, 25.0
powerlaw slope $dU/dM \propto U^{\alpha}$	α	2.0
fraction illuminated from U_{min} to U_{max}	γ	0.02

3.1.4. SED Fitting

We fit the SEDs of our sample using a set of parameters obtained from previous works and summarized in Table 3.1. We analyze the quality of the fits, using the global χ^2, and also comparing the Bayesian estimate of each flux with the observed values. In this work, Bayesian estimates stand for likelihood-weighted averages over all SED models to differentiate from best-fit values. In Fig. 3.1 the distribution of the obtained χ^2 and χ^2_r are shown. For each filter, we compute the median value of the difference between the Bayesian estimate from CIGALE and the observed values of fluxes with SNR > 3. Their distribution is presented in Fig. 3.2. SED modeled Hα fluxes are presented in Fig. 3.3 as a function of the observed flux as well as the flux difference (H$\alpha_{\rm CIGALE}$-H$\alpha_{\rm FMOS}$).

From Fig. 3.2, it is clear that the fluxes are well fitted by CIGALE with a flux difference smaller than 0.1 dex and dispersion smaller than 0.13 dex except for GALEX NUV for which the dispersion reaches 0.28 dex. *Herschel* PACS 100 μm and 160 μm are underestimated and exhibit a larger dispersion of 0.37 dex and 0.31 dex, respectively. ONLY 43 objects have SNR > 3 in *Herschel* PACS 100 μm. 23 objects have 100 μm fluxes larger than their respective flux at 160 μm. This is an unrealistic configuration at z ∼ 1.5 with rest-frame fluxes 40 and 60 μm, respectively. The dispersion of the results in *Herschel* PACS bands can be reduced (e.g., red squares in Fig. 3.2) if we consider the sample of 9 objects with SNR > 3 in both *Herschel* PACS 100 μm and *Herschel* PACS 160 μm. Therefore, the overall bad results at *Herschel* PACS bands can be explained as a combined effect of low SNR and non-realistic configuration at the IR bands. We used a deblended IR catalog in the COSMOS field provided by (Jin et al., 2018) to check if the situation for these bands improves. Both data sets (i.e., HELP and Jin et al., 2018) are consistent for our sample with the same trends in terms of unrealistic configuration of *Herschel* PACS 100 μm and *Herschel* PACS 160 μm. Jin et al. (2018) data have even lower SNR than our final sample selection described in Sect. 2.6. Using HELP data for our sample leads to better results for the fits. CIGALE weighs the data as the inverse square of the error which means that even if flux with a low SNR is ill-fitted, its impact on the overall SED fitting output is minimal. We also fit our sources without the *Herschel* PACS and SPIRE bands to check whether SFR, stellar mass, and attenuation estimations are affected when IR data are excluded. The retrieved estimates with and without IR information are consistent with each other within 1σ uncertainty. The impact of *Herschel* SPIRE data on the SFR as compared to the *Herschel* PACS bands is larger (i.e., 0.15 dex). In both cases, the difference in attenuation is larger (3×) for [OIII]λ5007 than for Hα. We kept the *Herschel* data for the whole sample in the overall fit. In Fig. 3.3 the Bayesian values of the Hα fluxes and the FMOS measurements follow the 1:1 relation indicating that we can fit very well the line flux within a 0.2 dex scatter as already found by Buat et al. (2018) on a smaller sample in the same field using spectroscopic information from the 3D-HST survey.

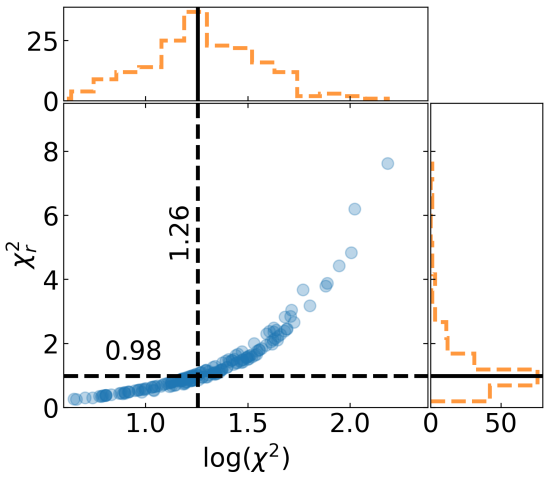

Figure 3.1. – Reduced χ^2_r versus the χ^2. The upper and right panels show the distribution of each parameter while the blue points correspond to objects in our sample selection. The black lines correspond to the mean value of 0.98 and 1.26 in each case.

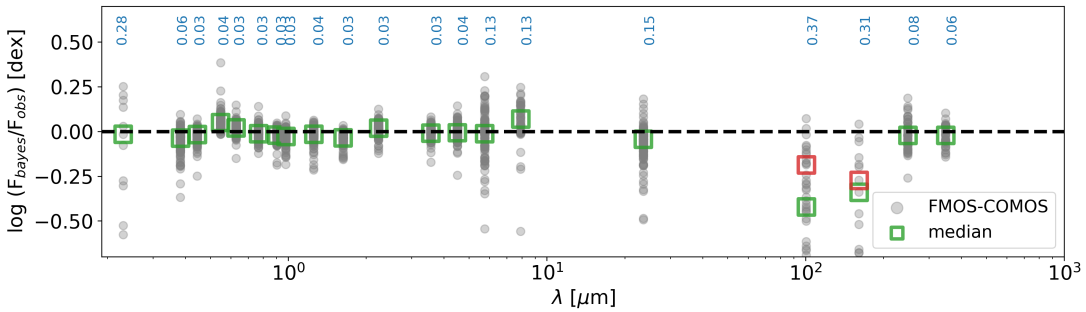

Figure 3.2. – Median distribution of the SED estimated and observed fluxes. On the x-axis, each wavelength corresponds to the photometric bands used in the SED fitting. The difference between the computed Bayesian flux with CIGALE and the observations is shown in the y-axis. Each object in our sample is drawn as a gray dot with a SNR > 3 in each band. Median values are shown as green squares. The median values for objects with SNR > 3 in both *Herschel* PACS 100 μm and *Herschel* PACS 160 μm are presented as red squares. Dispersion on the flux difference at each wavelength is reported on top.

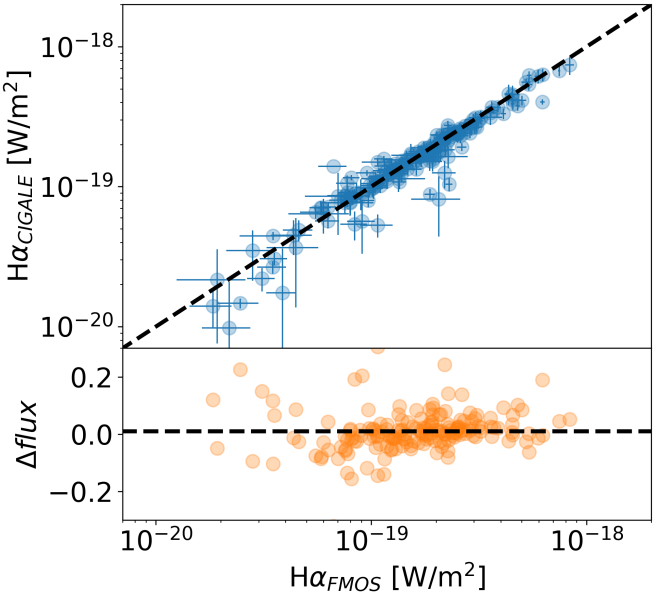

Figure 3.3. – Hα emission line fit quality. The upper panel shows the computed Bayesian flux using CIGALE on the y-axis vs the FMOS measured flux in the x-axis. The 1:1 relation is shown as a dashed line. The relative difference in flux is presented in the lower panel on a logarithmic scale. Bayesian and measured errors are shown for CIGALE and FMOS Hα fluxes, respectively. The differences between the computed flux with CIGALE and the observed data are not larger than 0.2 dex.

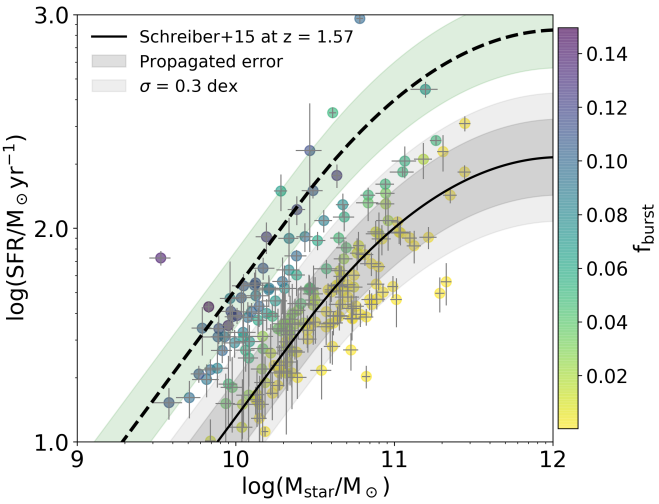

Figure 3.4. – Star-formation rate versus stellar mass diagram for our sample of 183 galaxies. The black continuous line corresponds to the Schreiber et al. (2015) curve evaluated at a median sample redshift of z = 1.5. The propagated error dispersion from the fitted errors of the function and a 0.3 dex scatter usually found for the relation in literature are shown as shades. Objects are color-coded by the mass fraction of the late burst population (f_{burst}). Galaxies four times above the main-sequence (black-dashed line) are consistent with a SED validated starburst population ($f_{burst} \sim 0.1$) within the 1σ dispersion shown as green shade area. Bayesian error for SFR and stellar mass are reported.

Accurate determination of SFRs is crucial as we want to compare them with the [OIII]λ5007 luminosities. Stellar masses and SFRs retrieved from the SED fitting cover a range of $10^{9.5} - 10^{11.5}$ $M_\odot$, and $10^1 - 10^3$ $M_\odot$ yr^{-1}, respectively. Current high SFRs can be expected for some objects since our sample is selected for the detection of recombination lines. To confirm the need to add a burst the delayed SFH we performed a fit with a burst amplitude set to 0. We compared both fits by calculating the Bayesian Information Criterion (BIC) of each of them as introduced by Schwarz (1978) and defined as

$$\mathrm{BIC} = -2 \times \ln(\mathrm{likelihood}) + \kappa \times \ln(\mathrm{N}),$$

where N stands for the number of observations i.e., number of bands fitted, κ the number of degrees of freedom and $\chi^2 = -2 \times \ln(\mathrm{likelihood})$ the non-reduced χ^2 obtained from CIGALE (Ciesla, Elbaz, and Fensch, 2017; Buat et al., 2018). A significant difference and evidence against a model is characterized by the higher BIC. We compute the difference of BIC values Δ(BIC). As the number of bands fitted is the same in both cases any difference arises from the number of degrees of freedom ($\kappa_{fix} = 14$ and $\kappa_{free} = 16$) and the χ^2. $\Delta(\mathrm{BIC}) > 2$ for 90 ($\Delta(\mathrm{BIC}) > 6$ for 69) objects meaning that for 1/3 to 1/2 of our sample the introduction of a burst improves the fit. In Fig.

3.4 our sample is presented in the SFR-mass diagram color-coded with f_{burst}. The Schreiber et al. (2015) main-sequence relation for a redshift of z = 1.5 is drawn with a 0.3 dex dispersion usually found for the relation in literature (Karim et al., 2011; Rodighiero et al., 2011, see,). The dispersion computed using error propagation from the originally fitted parameter errors proposed by Schreiber et al. (2015) is also shown as a darker shaded contour. The bulk of galaxies is found to lie within the 0.3 dex curves. Galaxies four times above the main sequence are usually considered starbursting (Sargent et al., 2012). A total of 31 objects in our sample are consistent to be starbursts with $f_{burst} > 0.06$ within a 1σ dispersion. The median value of f_{burst} for these objects is 0.10 ± 0.03. We fit the data using a stellar continuum metallicity of 0.008 and confirm that the results are consistent with the stellar continuum metallicity case of 0.02. Variations are within 1σ dispersion for the stellar mass, SFR, and attenuation estimates.

3.2. Dust attenuation

As mentioned above, we fit simultaneously photometric and spectroscopic data (i.e., Hα fluxes) using the Charlot and Fall (2000) modified recipe. Emission lines are produced by excited gas inside the BC as a result of the emitted radiation by young stars. Therefore, lines suffer from attenuation due to the BC but also the ISM surrounding the HII-region.

The energy budget principle of stellar photons being absorbed and re-emitted by dust in the Mid-and-far-IR combined with the attenuation recipe allows measuring the net effect of dust obscuration (i.e., the effective attenuation) in our galaxy sample. CIGALE calculates the resulting attenuation at any wavelength and for any emission line allowing us to obtain the amount of attenuation in the Hα and [OIII]λ5007 emission lines directly from the fits using photometry and Hα emission line fluxes. A comparison to the attenuations estimated with the BD method is addressed in Sect. 3.2.

The reliability of the estimation of the effective attenuation has to be checked carefully. We use a CIGALE option to create and analyze mock catalogs to verify if the main parameters involved in our derivation can be trusted and ensure that our analysis is robust enough to constrain the attenuation. Each flux in the mock catalog corresponds to the value of the best model which is modified by adding a value taken from a Gaussian distribution centered at 0 with the same standard deviation as the observations. The mock catalog of fluxes contains the same number of sources and is fitted in the same way as the original catalog. The estimated and exact values for the two free parameters in the Charlot and Fall (2000) recipe and the Hα attenuation are compared in Fig. 3.5. A_V^{ISM} is very well reproduced with a Spearman's correlation coefficient of $\rho_s = 0.95$. The μ parameter is more difficult to constrain even if a clear positive correlation is found between exact and estimated

values (Spearman's correlation coefficient of $\rho_s = 0.84$). The ratio of the attenuation in the V-band experienced by the young and old stars characterized by μ is difficult to constrain and as a consequence A_V^{BC} is also not very well constrained. $A_{H\alpha}$ is well-constrained with a Spearman's correlation coefficient of $\rho_s = 0.93$ reflecting the effects of the BC+ISM combination.

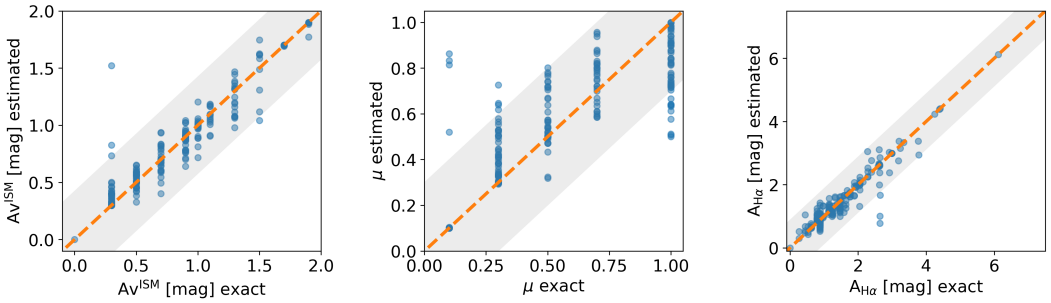

Figure 3.5. – Mock data sets comparison for the CF00 attenuation recipe intrinsic parameters (A_V^{ISM} and μ), and the Hα attenuation. On the y-axis the estimated values from the mock catalogs are shown. The x-axis corresponds to the exact value retrieved by CIGALE. The dashed line shows the 1:1 relation. The 1σ levels computed as the standard-deviation of the estimated parameters are drawn as gray shades.

Attenuation robustness: mocks, Balmer decrement and stellar mass trends

The retrieved attenuation for the Hα and [OIII]λ5007 emission lines is a crucial output of the SED fitting process for this work. We can use these values to correct line luminosities as the attenuation is constrained by the energy budget method through the UV-to-IR photometry coverage. Nevertheless, the measure of attenuation based on the BD method is widely used to compute the amount of attenuation when both Hα and Hβ are available. Attenuation in the Hα line can be obtained directly using the observed Hα and Hβ fluxes, and assuming a given extinction curve following,

$$A_{H\alpha} = \frac{-2.5\kappa_{H\alpha}}{\kappa_{H\beta} - \kappa_{H\alpha}} \log_{10}\left(\frac{2.86}{H\alpha/H\beta}\right), \tag{3.5}$$

where $\kappa_{H\alpha}$ and $\kappa_{H\beta}$ is a particular extinction curve evaluated at Hα and Hβ wavelengths, respectively. The attenuation for the hydrogen lines (i.e., Hα) can be translated into an attenuation of the [OIII]λ5007 emission using the same extinction curve at the respective wavelength.

In order to compare BD derived attenuations with CIGALE's attenuation estimates we select from a total of 139 objects with both Hα and Hβ measurements a sub-sample of 80 objects satisfying the $H\alpha/H\beta > 2.86$ [1] criterion. 23 of the excluded sources have

1. The intrinsic value 2.86 is assumed to be consistent with a temperature T= 10^4K and electron

Table 3.2. – Hα and [OIII]λ5007 attenuation comparison for a selected sample of 80 galaxies. The median values of attenuation and uncertainties are presented. The single-star value is computed using $n^{BC} = -1.3$ instead of -0.7. The dagger value is obtained including Hα, Hβ, and [OIII]λ5007 in the fit (see Sect. 4.1.2).

Method	A_{H_α} [mag]	$A_{[OIII]}$ [mag]	$A_{[OIII]}$-A_{H_α}
CIGALE fit	1.16±0.19	1.41±0.22	0.25
CIGALE fit*	1.17±0.14	1.53±0.20	0.36
CIGALE fit†	1.11±0.18	1.34±0.22	0.23
BD (MW)	0.82±0.19	1.14±0.26	0.31
BD (C00)	0.97±0.22	1.30±0.30	0.33

* **with** $n^{BC} = -1.3$
†**including Hα, Hβ, and [OIII]λ5007 in the fit**

a Balmer decrement consistent with 2.86 within 1σ uncertainty. The rest that are not consistent have overestimated Hβ fluxes as compared to Hα. We do not include any of these sources in the analysis to be consistent with the photoionization models implemented in CIGALE. Excluding values below the canonical value of the ratio allows us to exclude negative attenuation values inconsistent with the case B recombination assumption for the emission lines. We compute the attenuation applying Eq. 3.5 along with the the Milky Way curve ($\kappa_{H\alpha} = 2.52$; and $\kappa_{H\beta} = 3.66$; $\kappa_{[OIII]} = 3.52$) of Cardelli, Clayton, and Mathis (1989) updated by O'Donnell (1994). For comparison and to show the effects in the derived attenuation due to the choice of an extinction curve we also consider the Calzetti et al. (2000) (C00) curve ($\kappa_{H\alpha} = 3.33$; and $\kappa_{H\beta} = 4.59$; $\kappa_{[OIII]} = 4.46$) [2]. Attenuation using the Charlot and Fall (2000) recipe is directly obtained from the SED fitting.

In Table 3.2 we present median attenuation values for Hα and [OIII]λ5007, as well as the $A_{[OIII]}$-A_{H_α} ratio. All values are derived with a fixed BC slope $n^{BC} = -0.7$ except for the starred case in which $n^{BC} = -1.3$ was implemented. The fit with $n^{BC} = -1.3$ is as good as the $n^{BC} = -0.7$ case. In Fig. 3.6, the derived attenuations using the BD method are compared to CIGALE's estimates. The absence of correlations shows the intrinsic problems of using BD with extinction curves that could or not be appropriate for the objects and the emission lines in particular. We check the distribution of CIGALE's attenuation in the [OIII]λ5007 emission line as a function of stellar mass and fit a linear relation shown in orange in the lower panel of Fig. 3.7. We obtain,

$$A_{[OIII]} = (1.19 \pm 0.15) + (0.98 \pm 0.22) \log_{10}(M_*/10^{10} M_\odot)$$

density $n_e = 100 cm^{-3}$ for case B recombination Osterbrock (1989) and does not vary significantly with the physical conditions

2. This curve is only valid for stellar continuum and not appropriate to describe nebular emission line attenuation (Pannella et al., 2015; Reddy et al., 2015; Puglisi et al., 2016; Battisti, Calzetti, and Chary, 2016; Theios et al., 2019; Qin et al., 2019; Shivaei et al., 2020).

.

We will explore the effects of using this relation to correct [OIII]λ5007 luminosities in Sec. 3.3.2. Applying either the Milky Way or C00 reddening curve leads to lower median attenuations than those derived using Charlot and Fall (2000) recipe in CIGALE as shown in Fig. 3.7. CIGALE's attenuation estimates are globally in agreement with the $A_{H\alpha}$-mass relation of Garn and Best (2010a). BD derived attenuations (i.e., blue and red dots) are not entirely consistent with this relation placing the majority of the objects below the relation. Objects above Garn and Best (2010a) relation have SFR $> 10^{1.5}$ $M_\odot$ yr^{-1} but they are not classified as starbursting from our analysis. Hα attenuation increases with stellar mass in agreement with previous works (Garn and Best, 2010b; Garn and Best, 2010a; Ibar et al., 2013; Zahid et al., 2017; Shivaei et al., 2020) following the Garn and Best (2010a) relation and confirming that in more massive galaxies nebular regions have higher attenuation (Koyama et al., 2019). This also confirms that this relation is not just valid for the local universe but also at higher redshift. From the attenuation ratio between [OIII]λ5007 and Hα presented in Table 3.2 we see that our results using CF00 lead to a flatter effective attenuation curve (Chevallard and Charlot, 2016; Lo Faro et al., 2017; Buat et al., 2018) as compared to the Milky Way or C00 recipe. The difference arises from the choice in fixing both slopes in the CF00 to the same value of -0.7. We performed the same analysis using $n^{BC} = -1.3$ and verified that the effective curve is steeper than in the $n^{BC} = -0.7$ case and closer (and even slightly steeper) than the Milky Way and C00 case.

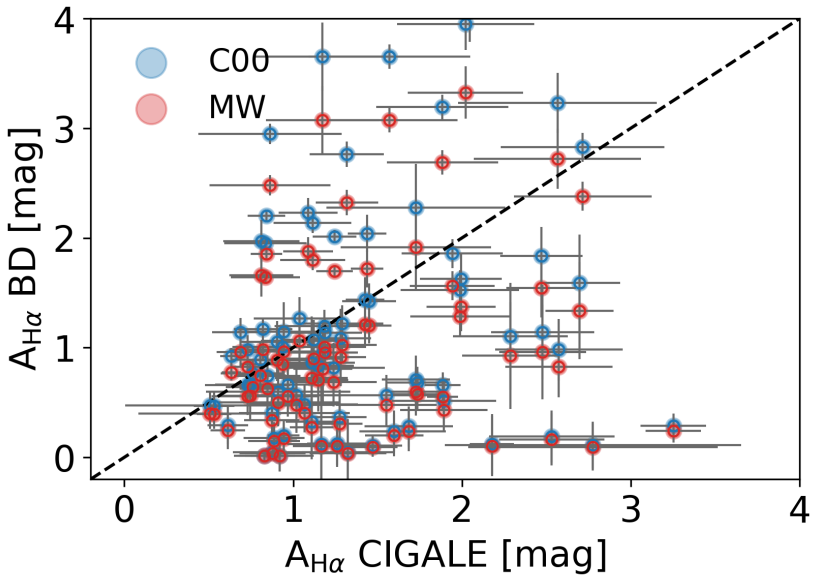

Figure 3.6. – Balmer Decrement and CIGALE $A_{H\alpha}$ comparison. Blue and red dots correspond to the BD derived attenuations computed using Eq. 3.5 and a Calzetti et al. (2000) and Milky Way extinction curve, respectively. The Hα attenuation obtained directly from CIGALE is shown in the x-axis. The 1:1 relation is shown as a dashed black line.

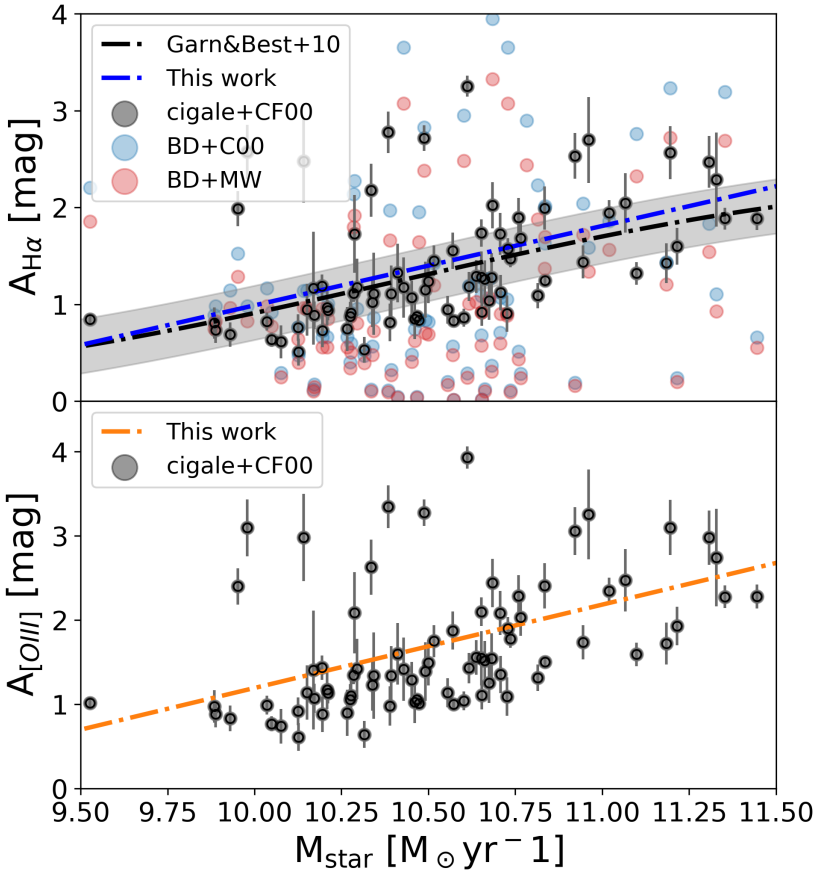

Figure 3.7. – Variation of the $A_{H\alpha}$, and $A_{[OIII]}$ attenuation with the stellar mass. The attenuation computed with CIGALE is presented as black dots with their respective uncertainties. Milky Way and C00 are shown in red and blue, respectively, without uncertainties for clarity on the upper panel. The dashed line corresponds to the $A_{H\alpha}$-M_{star} relation obtained by Garn and Best (2010a) in the local universe. The shaded area indicates the relation's $\pm 1\sigma$ distribution width. The blue line represents a linear fit to the black dots. The lower panel corresponds to the attenuation retrieved for the [OIII]5007 emission line. A linear fit is shown in orange.

The attenuation distributions obtained for the entire sample from the SED fitting are shown in Fig. 3.8 for the Hα and [OIII]λ5007 emission lines as well as for the V-band. The nebular line attenuation distribution follows in both cases a similar behavior as both lines are produced inside the HII-regions and they are attenuated in a similar way (inherent to CIGALE modeling). Stellar continuum attenuation as traced by A_v is lower. The differential attenuation suffered by young and old stars is measured by the μ parameter in the CF00 recipe as explained in Sect. 3.1.3. The original value proposed by Charlot and Fall (2000) corresponds to 0.3 for the nearby universe. We measure a larger value of $\mu = 0.57 \pm 0.14$. In general higher values are found at higher redshift (see Buat et al., 2018, and references therein). This is in agreement with nebular emission

being more attenuated than the stellar continuum.

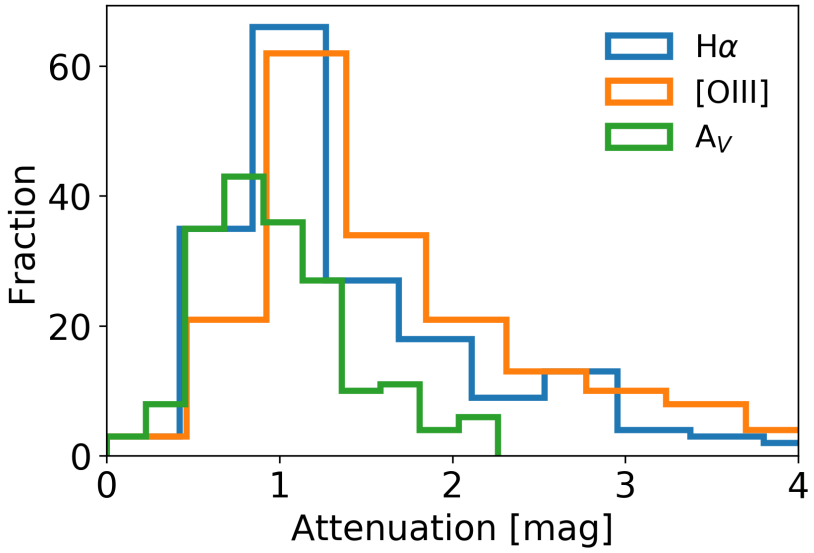

Figure 3.8. – Distribution of the total attenuation in the Hα and [OIII]λ5007 emission lines and the stellar continuum (i.e., V-band) are shown in blue, orange, and green, respectively. The distribution of the amount of attenuation obtained for the emission lines is very similar.

3.3. [OIII]λ5007, Hα fluxes and SFR measurements

In Sect. 3.2 we show that we constrain well the attenuation in our sample with the multi-wavelength plus IR bands coverage and the inclusion of the Hα emission line, and the CF00 recipe which introduces a differential attenuation between young and old stellar populations.

We compute [OIII]λ5007 line luminosities for our sample of galaxies using FMOS-COSMOS observed fluxes. These luminosities are corrected for dust effects using the Bayesian attenuation $A_{[OIII]}$ presented in Sect. 3.2. We find that the Hα and [OIII]λ5007 emission lines span over a similar range in luminosities and the amount of attenuation is found to increase with luminosity and SFR confirming previous works (e.g., Cortese et al., 2012; Bourne et al., 2012; Santini et al., 2014). In Fig. 3.9 the observed and dust corrected Hα and [OIII]λ5007 luminosities are shown in gray and color dots, respectively. In the dust-corrected data we measured a slope of 0.99 with a 0.39 dex dispersion. Emission lines are not strongly correlated before dust correction. After accounting for dust attenuation both quantities correlate (with a Spearman's coefficient of $\rho_s = 0.6$). In the next sub-sections we address the gas-phase metallicity influence on the [OIII]λ5007/Hα line ratio, the SFR measurements, and we compare both [OIII]λ5007 and [OIII] 88 μm line emissions.

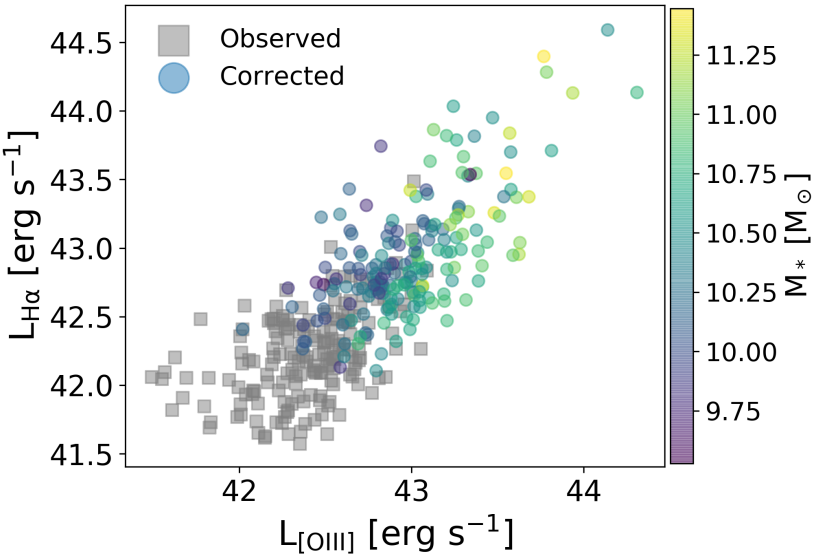

Figure 3.9. – Hα and [OIII]λ5007 luminosity. The observed luminosities uncorrected for dust are shown as gray dots. The color dots correspond to luminosities de-reddened using $A_{H\alpha}$ and $A_{[OIII]}$ as constrained by the SED fitting with CIGALE. The corrected data is color-coded by the stellar mass. A slope of 0.99 is measured in the dust corrected sample with a 0.39 dex dispersion.

3.3.1. Gas-phase metallicity

The oxygen abundance (O/H) and stellar mass are positively correlated giving rise to the well-known mass-metallicity relation (MZR) (e.g., Lequeux et al., 1979; Tremonti et al., 2004; Lee et al., 2006; Kewley and Ellison, 2008; Mannucci et al., 2010; Berg et al., 2012; Andrews and Martini, 2013; Blanc et al., 2019; Curti et al., 2020). At fix stellar mass the (O/H) ratio decreases with increasing redshift. It is usually described by a power law that flattens, reaching a metallicity value at high masses. This relation has a strong dependence on SFR leading to a fundamental metallicity relation (FMR) (e.g., Ellison et al., 2008; Lara-López et al., 2010; Mannucci et al., 2010; Yates, Kauffmann, and Guo, 2012; Cresci, Mannucci, and Curti, 2019; Curti et al., 2020) in which increasing SFR translates in a decreasing (O/H) ratio at fix stellar mass. The dependence on stellar mass and SFR arises from the interplay of in-fall of pristine gas causing the dependence on SFR being dominant at high redshift and the outflow of enriched material dominant at low redshift leading to a stellar mass dependence (Mannucci et al., 2010).

The shape of both MZR and FMR depends on the method used to derive the metallicity. Auroral emission and strong-emission lines are widely used to infer metallicities. The direct method consists of computing the ratio of weak auroral emission lines to strong emission of the same ionic species to compute the electron temperature of the ionized gas. Usually a ratio of weak emission lines as [OIII]λ4363 and [OIII]$\lambda\lambda$1661,66,

and strong emission lines as [OIII]λ5007 are used. Nevertheless, at redshift z > 1 observations of the auroral lines are extremely difficult (around ~ 100x fainter than strong lines) and not commonly detected in spectroscopic surveys (Sanders et al., 2020). As strong emission lines are easily detected some calibrations using HII regions measurements at z ~ 0 relating the strong-line ratios and direct-method are proposed (e.g., Pettini and Pagel, 2004; Pilyugin and Thuan, 2005; Marino et al., 2013; Curti et al., 2017) as well as implementing photoionization models (e.g., Kewley and Dopita, 2002; Kobulnicky and Kewley, 2004; Tremonti et al., 2004; Dopita et al., 2016). Parameters regulating the intensity of the lines like ionization parameter, hardness of the ionizing spectrum, N/O ratio, ISM density/pressure can vary with redshift making difficult the determination of metallicity from lines. To avoid this problem, the electron temperature method is preferred as it is independent of z ~ 0 calibrations based on strong-line emission.

Different MZR and FMR relations based on direct and strong-line methods are reported in literature sometimes including the effects of SFR (e.g., Pettini and Pagel, 2004; Mannucci et al., 2010; Andrews and Martini, 2013; Zahid et al., 2017; Sanders et al., 2021; Sanders et al., 2020; Curti et al., 2020). Using a sample of 137 extragalactic HII-regions and the electronic temperature method Pettini and Pagel (2004) determined the oxygen abundance proposing a polynomial relation in terms of the [NII]λ6584/Hα allowing to estimate metallicities within a factor of ~ 0.4 dex at 95 per cent confidence level. Similarly implementing the direct method (Sanders et al., 2020; Sanders et al., 2021) proposed MZR and FMR relations valid for $\log(M/M_\odot) = 7-10$ and $7.5 < \log(O/H) < 8.2$ using a sample of 18, 300 and 150 MOSFIRE Deep Evolution Field (MOSDEF) galaxies at z = 1.7 – 3.6, z ~ 2.3, and z ~ 3.3, respectively finding that variations were not larger than ~ 0.1 dex at fix stellar mass and SFR from z ~ 0 – 2.2. Mannucci et al. (2010) studied the evolution of the MZR studying Sloan Digital Sky Survey (SDSS) galaxies at z ~ 0 and different samples reported in literature up to z ~ 4 finding that the evolution of the relation is caused by a selection bias as high SFR (low metallicity) are selected at higher redshifts sampling different parts of the relation. They propose the FMR with a $\mu = \log(M/M_\odot) - a\log(SFR/M_\odot yr^{-1})$ with $a = 0.32$ as a projection of the FMR which reduced the scatter of local galaxies and cancels out the redshift evolution up to $z \sim 2.5$. Sanders et al. (2020) finds that the value is at least twice the value leading $a = 0.63$ in order to cancel the evolution. Andrews and Martini (2013) using also the strong-line ratio method on a 200000 SFGs SDSS galaxies spanning $\log(M/M_\odot) = 7.4-10.5$ found that μ is minimized with a value of $a = 0.66$. Recently Curti et al. (2020) using strong-line ratios on SDSS galaxies spanning $\log(M/M_\odot) = 7.95-11.85$ and $-1.5 < \log(SFR/M_\odot yr(^-1)) < 1.5$ obtained a FMR relation accounting for the variation of SFR leading to similar results confirmed by Sanders et al. (2021) using the direct method.

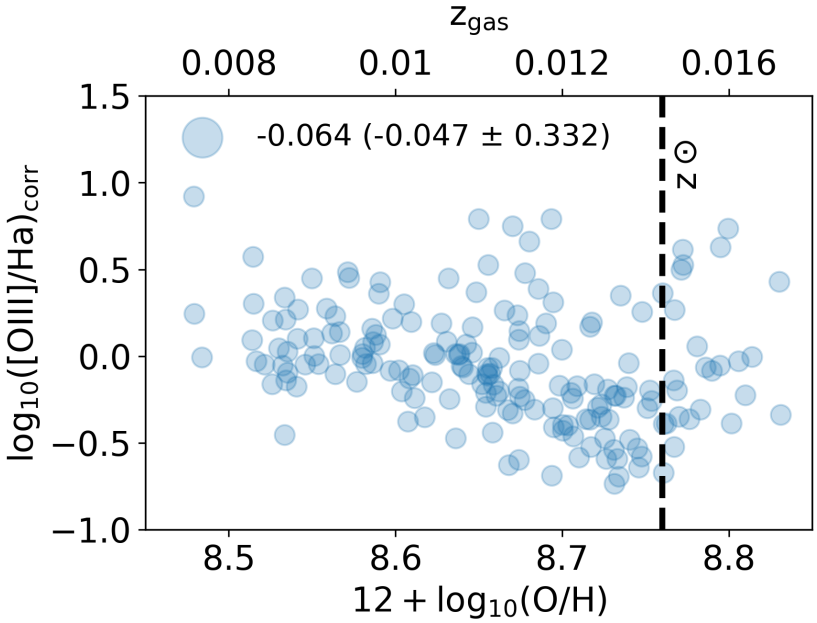

Figure 3.10. – [OIII]λ5007/Hα ratio corrected for dust attenuation. We present the logarithm of the ratio as a function of oxygen abundance computed using Curti et al. (2020) FMR relation on the x-axis. The secondary axis corresponds to the translation in terms of gas-phase metallicity where the solar values correspond to 0.0142 or 8.76. The ratio has been corrected using the attenuation for each line as computed with CIGALE. A linear and logarithmic median and mean ratio of 0.86 (−0.065) and 0.89 (−0.047) are found. The 0.332 dispersion corresponds to the standard deviation.

The [OIII]λ5007 emission line is sensitive to the ionization parameter (i.e., the ionizing field; Kewley et al., 2013a; Kewley et al., 2013b; Dopita et al., 2013; Dopita et al., 2016; Nicholls et al., 2017) but can be also affected by the gas-phase metallicity (Kennicutt, 1992; Kennicutt et al., 2000; Steidel et al., 2014; Gutkin, Charlot, and Bruzual, 2016; Byler et al., 2017). Different mass metallicity relations (MZR) based on direct and strong-line methods are reported in literature sometimes including the effects of SFR (e.g., Pettini and Pagel, 2004; Mannucci et al., 2010; Andrews and Martini, 2013; Zahid et al., 2017; Sanders et al., 2021; Sanders et al., 2020; Curti et al., 2020). We compute oxygen abundances using the fundamental metallicity relation (FMR) calibration of Curti et al. (2020) which is based on strong-line oxygen abundance measurements for SDSS galaxies. Their relation is fully consistent with a relation derived for a MOSDEF sample of individual and stacked galaxies at z ∼ 2.3 in Sanders et al. (2021). The dust corrected [OIII]λ5007/Hα ratio is presented in Fig. 3.10 as a function of oxygen abundance. Our galaxy sample covers a sub-solar abundance range of $8.4 < 12 + \log(O/H) < 8.8$ (i.e., gas-phase metallicity $0.006 < Z_{gas} < 0.016$) [3]. The ratio

3. The solar metallicity is $z_\odot = 0.0142$ as in Grevesse et al. (2010).

slightly decreases when metallicity increases. The median value of the ratio is 0.86 (or −0.065 dex) with a dispersion of 0.3 dex as measured by the standard deviation of the data set. The dispersion at a fixed metallicity can be produced by the sensitivity of the oxygen species to the ionizing field. The dependence on both metallicity and ionizing field is likely to produce effects on the ratio which we cannot easily disentangle. In Sect. 4.1.2 we will explore variations of the intensity of the radiation field fixing the metallicity in three bins with an equal number of galaxies and fitting simultaneously Hα, Hβ, and [OIII]λ5007 line fluxes.

3.3.2. SFR–[OIII]λ5007 calibration

Understanding SFR in terms of different physical parameters such as the IR and UV emission, Hα flux, and even in terms of colors of galaxies is vital in the extragalactic field. We have oxygen emission at 5007 Å which can be corrected by dust effects and compared to the SFR derived from our SED fitting process. In Fig. 3.11 the dust-corrected [OIII]λ5007 observed luminosities, and SED fitting derived SFR are presented. Both parameters are correlated with a non-negligible dispersion as compared to the well-known Kennicutt (1998) relation (i.e., SFR-Hα). However, it is of our interest to explore this line which could be useful for future spectroscopic surveys like MOONS and PFS that will observe the line at high-redshift, providing insights on the nature of these objects and the ongoing physics of the ISM.

Several authors in the past studied the link between the [OIII]λ5007 emission line and SFR based on a fixed [OIII]λ5007/Hα ratio and the calibration of the Hα emission line in terms of SFR. At z ∼ 0.1 on a sample of 196 SDSS narrow band emitters Moustakas, Kennicutt, and Tremonti (2006) measured a scatter in the [OIII]λ5007-SFR relation as large as a factor 3 – 4 when compared to other tracers like [OII], Hβ emission lines or U-band. Hippelein et al. (2003) derived from global emission densities an [OIII]λ5007/Hα ratio of 0.79, consistent with our median value, on 92 galaxies at 0.40 < z < 0.64 finding that although [OIII]λ5007 depends on the excitation and metallicity, the $SFR_{[OIII]}$ estimated median values were consistent for the sample. Ly et al. (2007) reported a [OIII]λ5007/Hα ratio of 1.05 at z = 0.07 – 1.47 for a Subaru Deep Field spectroscopic sample of 196 narrow-band emitters while Teplitz et al. (2000) fixed the ratio to unity at z > 3 for a sample of five galaxies observed with the near-IR camera on the Keck I telescope. Both works of Teplitz et al. (2000) and Ly et al. (2007) found similar results on the dependence of the line ratio with metallicity and ionization field. Maschietto et al. (2008) studied a sample of 13 [OIII] emitters at z ∼ 3.09 – 3.16 and derived a lower limit relation based on a [OIII]λ5007/Hα ratio of 2.4 from observed star-forming galaxies. Straughn et al. (2009) also explored the relation based on [OIII]λ5007/Hα ratios from galaxy knots in which both emission lines were observed for a sample of 136 galaxies at z ∼ 0.5. The reported relation implies a median [OIII]λ5007/Hα ratio of ∼ 1.23. Bowman et al. (2019) found a strong correlation but did not propose any relation for a set of 3D-HST galaxies at z ∼ 2 (see their figure 6).

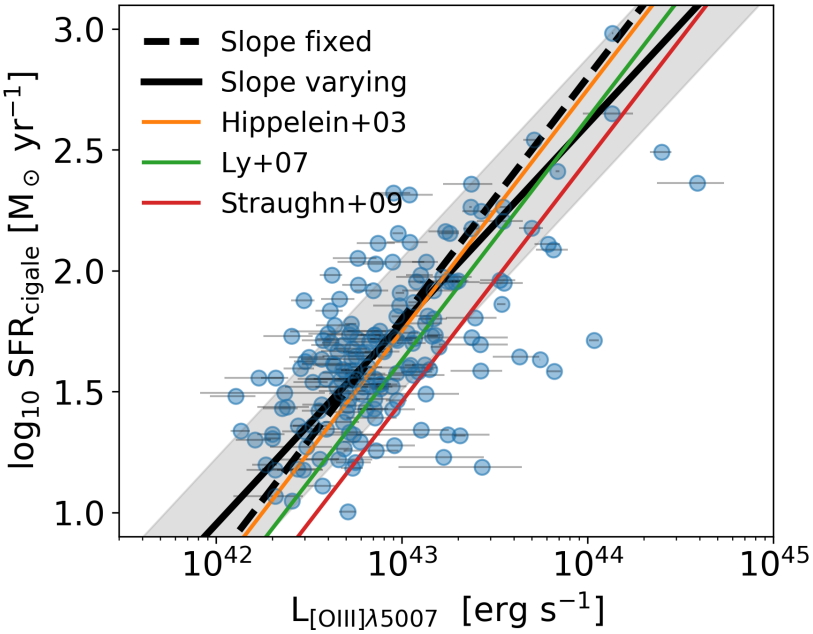

Figure 3.11. – [OIII]λ5007 corrected luminosity and SFR relation. The dashed and continuous black lines correspond to the linear fit using a bootstrapped orthogonal distance regression method with a spearman's regression coefficient $\rho_s = 0.57$. The 0.32 dex dispersion is presented as a gray shaded area. The relation shows a positive correlation with scatter significantly higher compared to Kennicutt (1998) Hα relation. Relations proposed by Hippelein et al. (2003), and Ly et al. (2007) are shown in orange and green, respectively. Straughn et al. (2009) is also presented in red for comparison. Relations are converted from Salpeter to Chabrier IMF.

To provide a relation we need to explore the effects of outliers present in the sample which could have a large impact on the fitting. First, we fit only the intercept using an orthogonal distance regression in the L$_{[\rm OIII]}$-SFR plane to be consistent with different works in the literature in which [OIII]λ5007/Hα ratio is left fix. The quality of the fit is measured by the non-parametric Spearman's and Kendall's correlation coefficients equal to $\rho_s = 0.57$ and $\rho_s = 0.40$, respectively. This first attempt results in,

$$\log_{10} \mathrm{SFR} = \log_{10} \mathrm{L}_{[\rm OIII]} - (41.27 \pm 0.03), \tag{3.6}$$

with the luminosity and SFR expressed in units of ergs s^{-1} and M$_\odot$ yr^{-1}, respectively. To trim our sample, we explore a couple of methods, for example, cutting in luminosity, or clipping using the geometrical distance of the data points to the linear fit in Eq. 3.6. In the luminosity case we use three different scenarios, one with the whole

sample, and two in which we clip objects with $L_{[OIII]} \geq 10^{43.5}$ergs s^{-1}, and objects with $L_{[OIII]} \geq 10^{44}$ergs s^{-1}. In the geometrical distance case, we compute the distance between each point to the linear fit presented in Eq. 3.6 and cut at a given radius from the distance distribution (i.e., distance ≥ 0.45, and distance ≥ 0.5). Then, we applied a bootstrapping method to check how robust the intercept's estimation is in the linear case. But also in the case when both the slope and the intercept are free to vary. The bootstrapping method with replacing consists of mimicking the sampling process by using random sampling with replacement. The properties of the estimator such as the mean, median, and variance can be obtained by sampling from an approximating distribution. Then, the idea is to create several trials of the approximated distribution and perform the orthogonal fit in this sample. As it is randomly replaced, it is quite unlikely that in several runs one gets the outliers altogether. This reduces the effects they could have in the orthogonal distance fit. The result is a Gaussian distribution of the intercept for the linear case and for both the slope and intercept in the varying scenario for which we can measure the mean value and the error as the standard deviation directly from the distribution.

We start with the linear method for which the slope is fixed to the unity. In Fig. 3.12, we present the results using the whole sample, objects with $L_{[OIII]} \leq 10^{43.5}$ergs s^{-1}, and objects with $L_{[OIII]} \leq 10^{44}$ergs s^{-1}. In Fig. 3.13 we show the results when clipping data using the distance method. After bootstrapping and analyzing the distribution for the intercept, we realized that the estimation of this parameter is robust within the 2σ error for the different cuts. The same conclusions are inferred from the distance clipping case.

Now, if we leave the slope and intercept free to vary simultaneously and perform the same analysis as before, we see that results can change drastically depending on the sample cuts we impose. We see in Fig. 3.15 the effect of using the whole sample with a free slope in which the slope tends to be shallower than the case with the cut $L_{[OIII]} \leq 10^{43.5}$ergs s^{-1}. Including $L_{[OIII]} \leq 10^{43.5}$ergs s^{-1} reduces the slope being comparable to the case in which we use the sample. To address this issue, as cutting in luminosity is not justified, we clip the data if the distance is larger than distance ≤ 0.45, and distance ≤ 0.5 respect the linear fit. In Fig. 3.14 the original sample, as well as the clipped sample, are shown. In this case, we present the $\log(L_{[OIII]}/\mathrm{SFR})$ for which we can guarantee that the new distribution represents the original one. We find 15 objects which are possible outliers. We later confirmed that these objects indeed have low SNR at GALEX NUV and *Herschel* bands which leads to a bad estimation of their attenuation, affecting the corrected luminosities and probably also retrieving a not so well-constrained SFR. Clipping the sample in this way and bootstrapping gives better results either for the fix-slope or varying-slope scenarios as presented in Fig 3.16. This guarantees that the SFR and $L_{[OIII]}$ distributions remain unchanged and representative of our original sample after the trimming process.

We decide to use the results after clipping the sample using distance ≤ 0.45 because

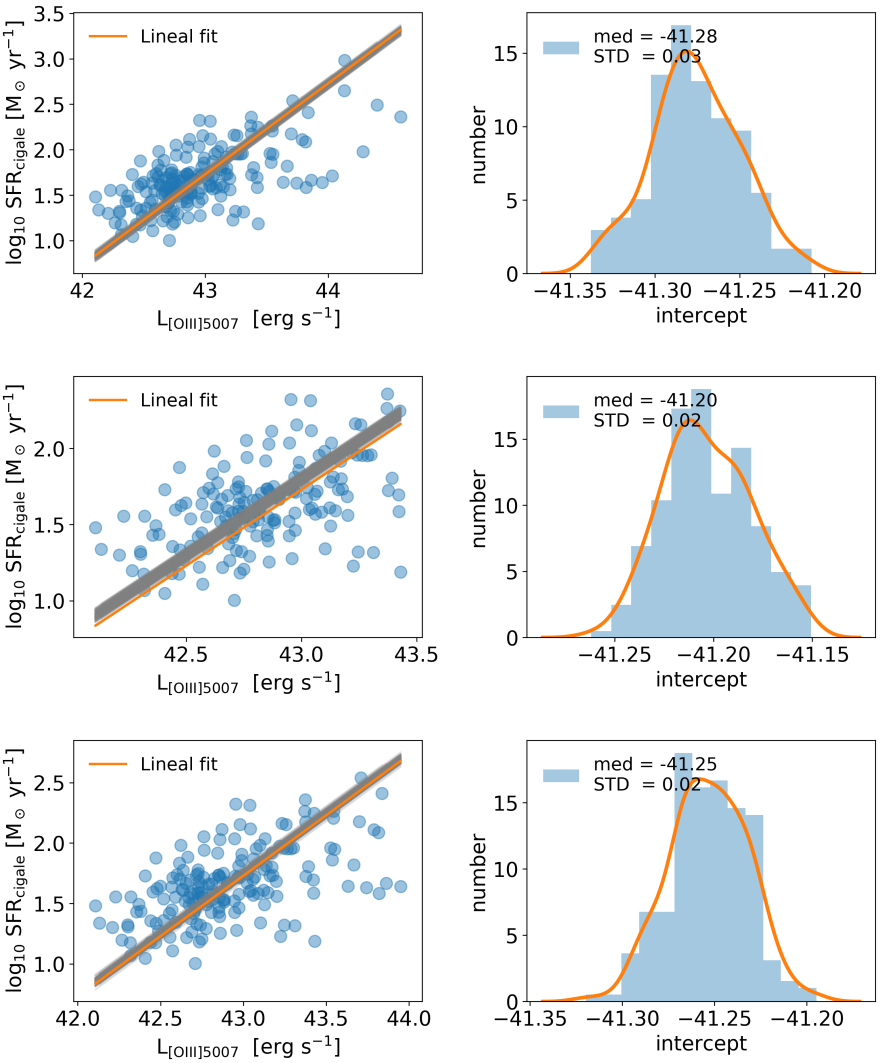

Figure 3.12. – Orthogonal distance fitting with slope fixed to unity. **top:** Entire sample; **center:** $L_{[OIII]} \leq 10^{43.5}$ergs s^{-1}; **bottom:** $L_{[OIII]} \leq 10^{44}$ergs s^{-1}. The orange line represents the linear fit from Eq. 3.6 while the gray lines correspond to 200 realizations of the bootstrapping process. The estimated distribution of the intercept after bootstrapping is presented in the right column. Clipping the sample in luminosity has no large impact on the results when leaving the slope fix.

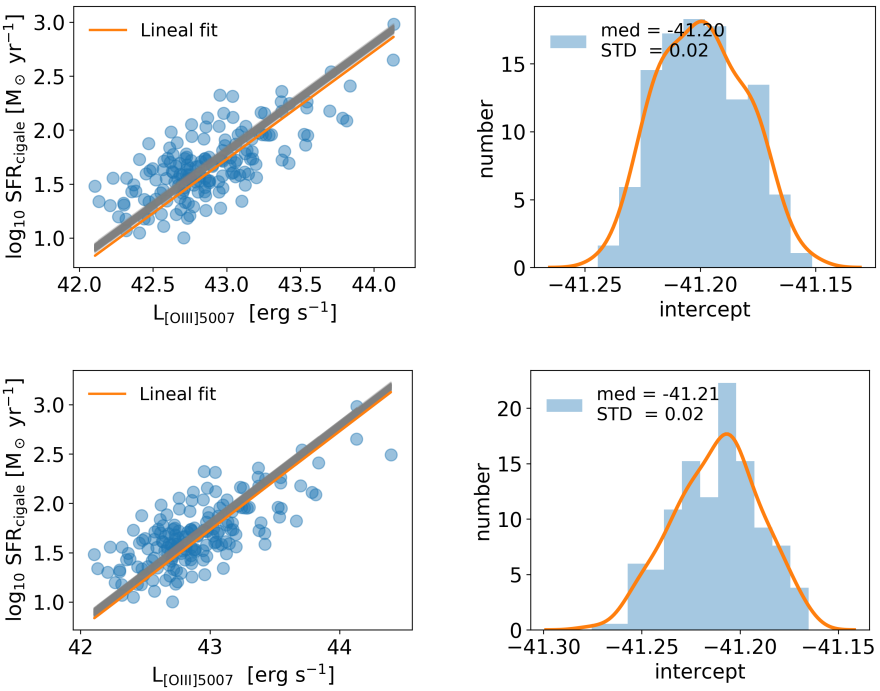

Figure 3.13. – Orthogonal distance fitting with slope fixed to unity. **top:** distance ≤ 0.45; **bottom:** distance ≤ 0.50. The orange line represents the linear fit from Eq. 3.6 while the gray lines correspond to 200 realizations of the bootstrapping process. The estimated distribution of the intercept after bootstrapping is presented in the right column. Clipping the sample using the distance of each point to the linear fit presented in Eq. 3.6 has no large impact on the results when leaving the slope fix.

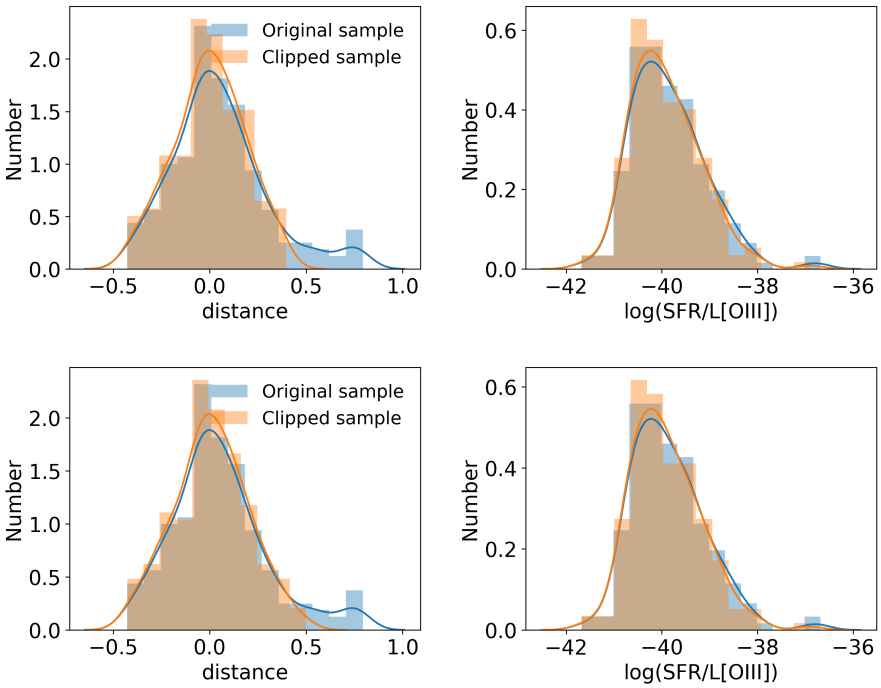

Figure 3.14. – Distribution of the $\log(L_{[OIII]}/SFR)$ for the original and clipped sample. **top:** distance ≥ 0.45; **bottom:** distance ≥ 0.50. In both cases the clipping is symmetric and the original distribution of $\log(L_{[OIII]}/SFR)$ is preserved being representative of our sample.

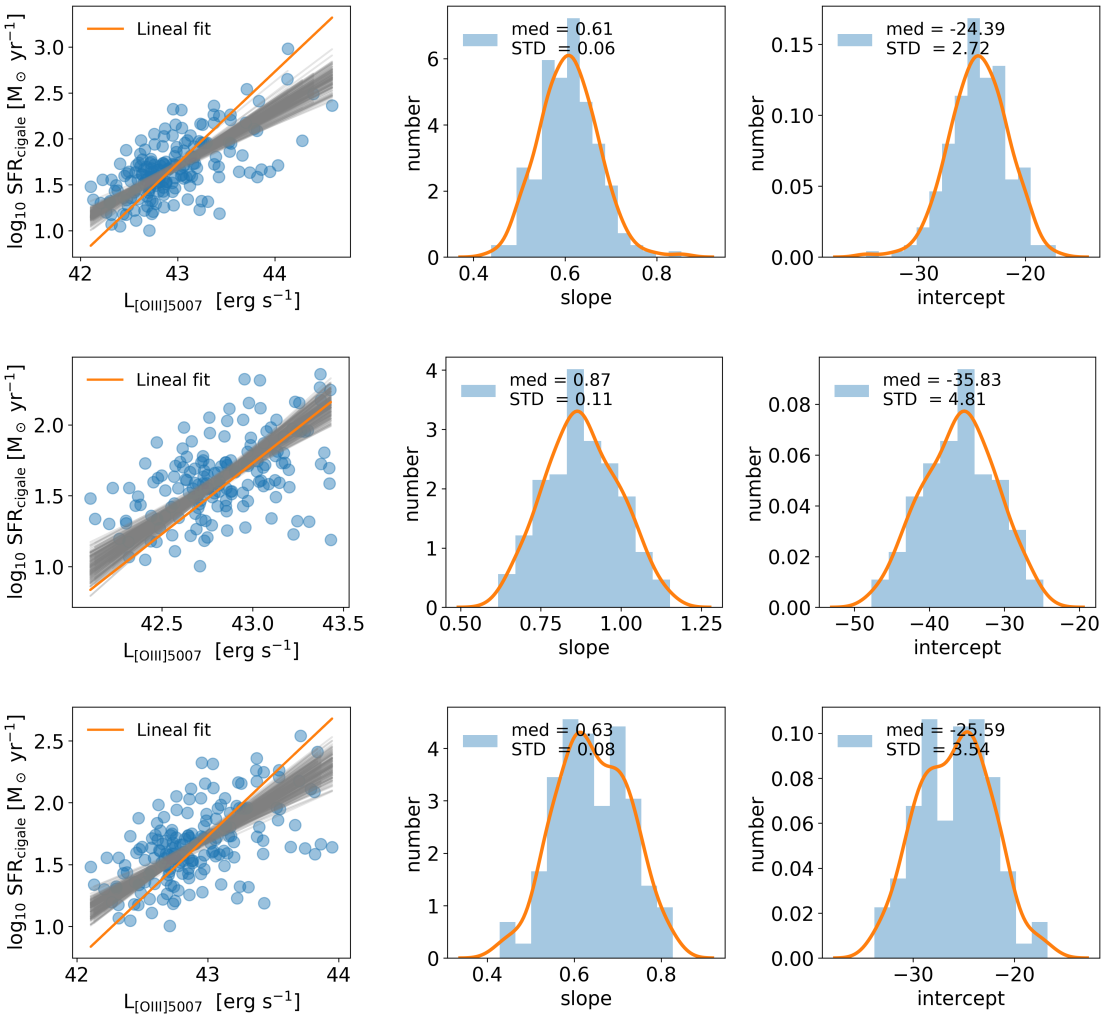

Figure 3.15. – Orthogonal distance fitting with both slope and intercept varying. **top:** Entire sample; **center:** $L_{[OIII]} \leq 10^{43.5}$ergs s^{-1}; **bottom:** $L_{[OIII]} \leq 10^{44}$ergs s^{-1}. The orange line represents the linear fit from Eq. 3.6 while the gray lines correspond to 200 realizations of the bootstrapping process. The estimated distribution after bootstrapping of the slope and intercept are presented in the middle column and the right column, respectively. Slope estimates vary strongly on the way luminosities are clipped as this changes the distribution of $L_{[OIII]}$ and SFR.

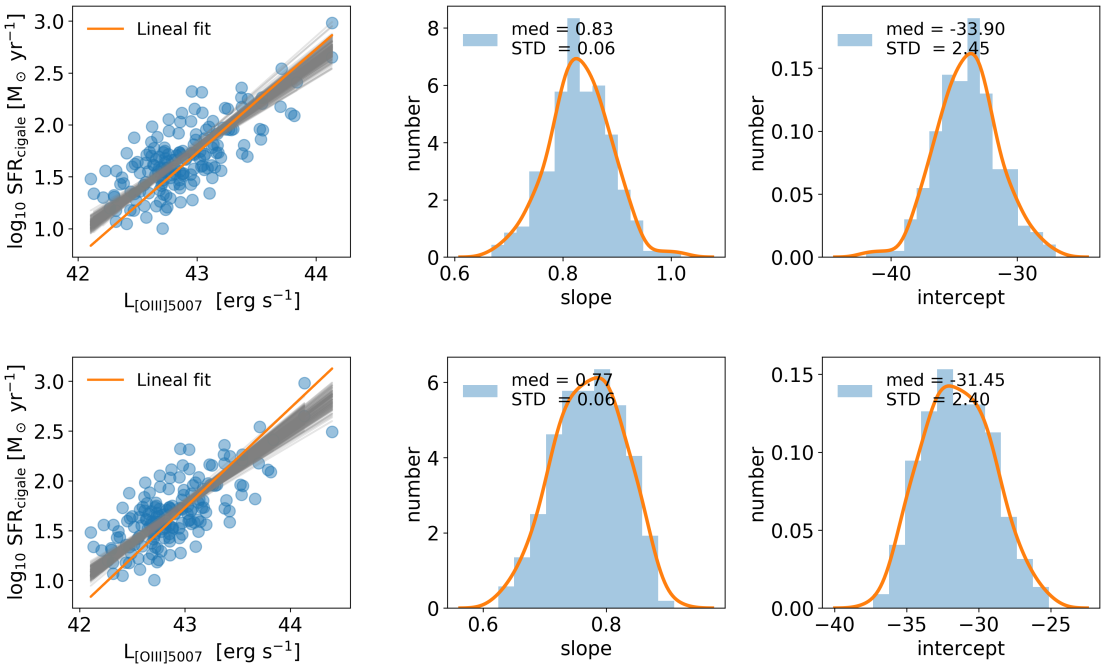

Figure 3.16. – Orthogonal distance fitting with both slope and intercept varying. **top:** distance ≥ 0.45; **bottom:** distance ≥ 0.50. The orange line represents the linear fit from Eq. 3.6 while the gray lines correspond to 200 realizations of the bootstrapping process. The estimated distribution after bootstrapping of the slope and intercept are presented in the middle column and the right column, respectively. Slope and intercept estimates are robust and well estimated as the original median distribution of $L_{[OIII]}$ and SFR are preserved.

they give the best compromise for our purposes. After bootstrapping with replacing we obtain new solutions for a fix and varying slope. This leads to,

$$\log_{10} \mathrm{SFR} = \log_{10} \mathrm{L}_{[\mathrm{OIII}]} - (41.20 \pm 0.02), \tag{3.7}$$

$$\log_{10} \mathrm{SFR} = (0.83 \pm 0.06) \log_{10} \mathrm{L}_{[\mathrm{OIII}]} - (33.90 \pm 2.45). \tag{3.8}$$

For comparison we fit the sample with all the objects and a varying slope obtaining $\log_{10} \mathrm{SFR} = (0.61 \pm 0.06) \log_{10} \mathrm{L}_{[\mathrm{OIII}]} - (24.39 \pm 2.72)$. The slope in Eq. 3.8 is different than the unity but consistent within the 2σ error. The relations presented in Eq. 3.7 and 3.8 are drawn in Fig. 3.11 as a black dashed and continuous line with a 0.32 dex dispersion as a gray shaded area. Since the Hα emission can be considered as proportional to the SFR, the dispersion of the [OIII]λ5007-SFR correlation is expected to have the same origin as the one affecting the [OIII]λ5007/Hα ratio: metallicity and radiation field.

Our calibration relies on quantities estimated for each galaxy (e.g., [OIII]λ5007 luminosity, SFR). It can be compared to relations obtained with individual [OIII]λ5007/Hα ratios as those obtained by Hippelein et al. (2003), and Ly et al. (2007) [4]. Their dust corrected relations are reported in Fig. 3.11 (orange and green lines) and are fully consistent with our result within the 1σ dispersion error, and our median reported [OIII]λ5007/Hα ratio of 0.86. This relation can be used to estimate the SFR of galaxies with corrected [OIII]λ5007 luminosity in the absence of any other information such as the Hα line.

3.3.3. [OIII]λ5007 and [OIII] 88 μm lines benchmark

[OIII] also produces a fine structure emission line at 88.33 μm from low excitation and highly ionized gas located in a low-density environment. This line is not affected by dust attenuation and is also used to trace SFR at both low and high redshifts (e.g., De Looze et al., 2014; Harikane et al., 2020). In this section, we aim at predicting a relation between [OIII] 88 μm and SFR from the relation we measured between [OIII]λ5007 and SFR and HII-region models. Dust effects are negligible for the [OIII] 88 μm emission line. Additionally, this line is targeted by different surveys at high-redshift which is a good candidate to study and to characterize the cooling budget of the ISM in distant objects.

The [OIII]λ5007-[OIII] 88 μm ratio is known to vary with gas-phase metallicity and density (Dinerstein, 1983; Stacey et al., 2010; Ferkinhoff et al., 2010; Moriwaki et al., 2018), but not to be very sensitive to the ionization parameter (Moriwaki et al., 2018). To select photoionization models relevant for our analysis we restrict the ionization parameter to $-3.0 < \log \mathrm{U} < -2.0$ in agreement with our results presented in Sect. 4.1.2. Kashino et al. (2017) derived an electron density of ~ 200 cm^{-3} for the FMOS-COSMOS

4. All relations are converted to Chabrier IMF

sample. Three different values of the electron density are available in CIGALE (i.e., n_e = 10, 100, and 1000 cm^{-3}) and we fix n_e to 100 cm^{-3}. From our estimations of the gas-phase metallicity (Sect. 3.3.1) we restrict models to $0.006 < Z_{gas} < 0.016$ (or $8.4 < 12 + \log(O/H) < 8.8$). With the selected models, we derived a mean [OIII]λ5007-[OIII] 88 μm ratio of ~ 1.90 (with a 1σ dispersion of 0.84). This mean is obtained over all the models as variations of the ratio are highly dependant on gas-phase metallicity and ionization parameter. We use this average value of the ratio to translate our SFR-[OIII]λ5007 linear relation presented in Eq. 3.7 into another linear relation between [OIII] 88 μm and SFR. This is presented in Fig. 3.17 as a black dotted line with a gray shaded area accounting for the dispersion with gas-phase metallicity.

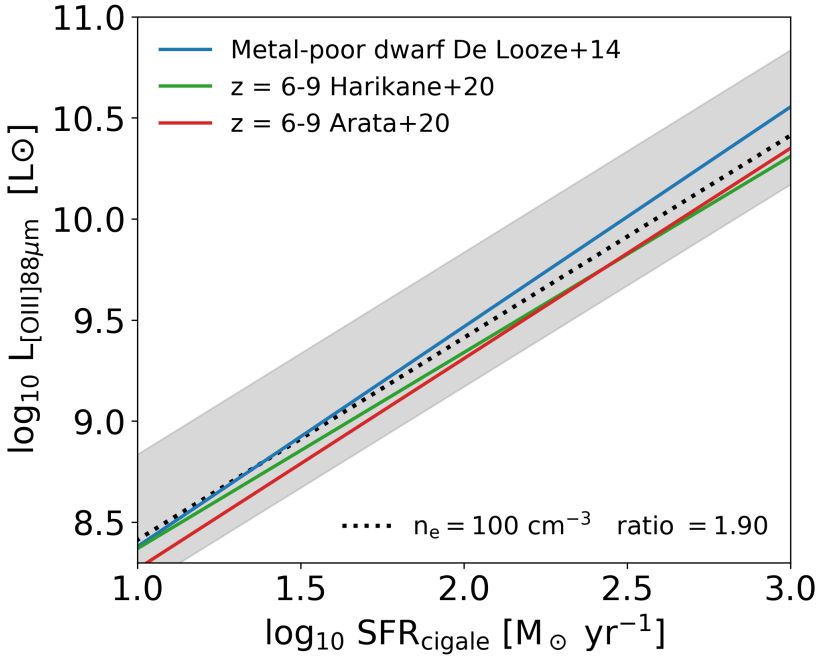

Figure 3.17. – [OIII] 88 μm-SFR relation. The blue line shows the metal-poor local dwarf galaxies relation from De Looze et al. (2014). The green line corresponds to the high-redshift observed relation proposed by Harikane et al. (2020) while the red line corresponds to simulation results from Arata et al. (2020) both at z = 6 – 9. We translate our [OIII]λ5007 luminosities into [OIII] 88 μm using a mean ratio of 1.9 derived from CLOUDY HII-region models at an electron density of n_e = 100 cm^{-3} shown as a black dotted line. The gray area is the dispersion in the translation with gas-phase metallicity.

Our relation is found consistent with the relations proposed by De Looze et al. (2014) for metal-poor local dwarf galaxies and by Harikane et al. (2020) for high redshift galaxies despite the different gas-phase metallicities of their samples. Arata et al. (2020) reports a $L_{[OIII]88\mu m}$ – SFR relation derived from simulations at z = 6 – 9

covering a gas-phase metallicity range of $6.6 < 12 + \log(O/H) < 8.9$ that matches our metallicity range and is also consistent with different predictions from the literature (De Looze et al., 2014; Moriwaki et al., 2018; Harikane et al., 2020). Both electron density and gas-phase metallicity are paramount to properly convert one emission into another as well as to compare different samples of galaxies. At intermediate and high densities [OIII]λ5007 line remains an important coolant for ionized gas as compared to [OIII] 88 μm. The [OIII]λ5007 emission line will be targeted in future surveys like MOONS, PFS, and JWST allowing synergies with observatories like the Atacama Large Millimeter/submillimeter Array (ALMA) that can perform observations of [OIII] 88 μm at high-redshift providing a direct method to characterize the overall cooling budget and the ISM physics of HII-regions in intermediate and high-redshift galaxies and to refine their calibration in SFR.

4. FMOS-COSMOS spectro-photometric SED fitting

Contents

4.1. Spectro-photometric modelling: HII-region and stellar continuum modelling

I used CIGALE to model the [OIII]λ5007/Hβ, [NII]λ6584/Hα emission line ratios and compared them with the FMOS observations in a so-called BPT diagram (Baldwin, Phillips, and Terlevich, 1981). The locus of the observations in the BPT diagram depends strongly on the relative abundances of nitrogen and oxygen, and thus on the choice of the standard metallicity scale (Nicholls et al., 2017). Because we do not know exactly how element abundances scale relative to another over cosmic times, from the early Universe to present days, abundances are often simply scaled by a multiplicative factor. This factor is either related to Z, the mass fractions of all elements heavier than H and He, such as $Z/Z_\odot$ (where $Z_\odot$ is the solar metallicity), or related to oxygen abundances for nebular modeling (Lodders, 2010). The nebular scaling of nitrogen with oxygen is problematic since while oxygen is principally produced in core-collapse supernovae, nitrogen has primary and secondary abundances (Vila-Costas and Edmunds, 1993). The primary abundances originate from enrichment by core-collapse supernovae in the native gas cloud from which the H II region formed, and the secondary abundances arise from delayed nucleosynthesis through hot-bottom burning and dredge-up in intermediate-mass stars as they evolve. The emission line modeling and of this work was carried out in collaboration with Patrice Theulé at LAM.

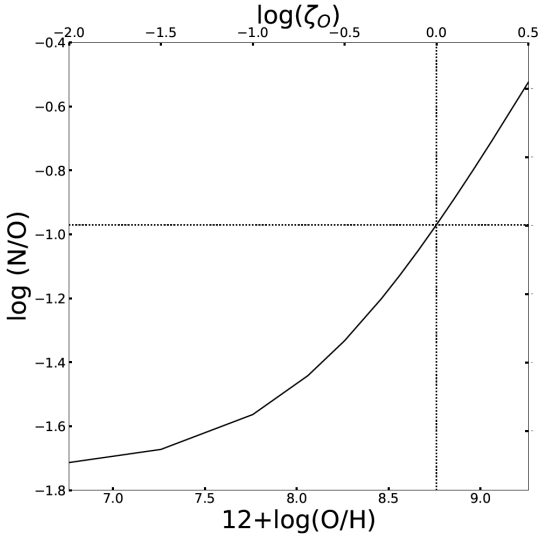

Figure 4.1. – N/O and O/H abundance comparison. The N/O abundance as a function of the 12+log(O/H) abundance is presented as a black thick line. The scaling parameter ζ_0 is shown on the top axis. The vertical and horizontal lines represent the galactic concordance values. The figure is provided by Patrice Theulé.

We use the standard, present-day scale, extended from the cosmic abundance stan-

Table 4.1. – Correspondence between the scaling parameter ζ_O, and the stellar and gas-phase metallicity. The solar metallicity corresponds to $Z_{gas} = 0.014$ (or $Z_{star} = 0.02$). The closest stellar metallicity to each gas-phase metallicity is used to produce the ionizing spectrum which is passed to CLOUDY to model the emission lines.

Z_{star}	Z_{gas}
	$\log(\zeta_O)$
0.05	0.051, 0.046, 0.041
	0.50, 0.45, 0.40
0.02	0.037, 0.033, 0.030, 0.025, 0.022, 0.019, 0.016, 0.014
	0.35, 0.30, 0.25, 0.20, 0.15, 0.10, 0.05, 0.0
0.008	0.012, 0.011, 0.009, 0.008 ,0.007
	-0.05, -0.10, -0.15, -0.20, -0.25
0.004	0.006, 0.005, 0.004, 0.003
	-0.30, -0.40, -0.50, -0.60
0.0004	0.0025, 0.002, 0.001, 0.0004
	-0.70, -0.80, -1.0, -1.5
0.0001	0.0001
	-2.0

dard and scaling developed by Nieva and Przybilla (2012), based on the observed metallicities of 29 early B-type stars in the local galactic region rather than the solar standard references. Indeed, solar abundances are uncertain and photospheric abundances do not reflect bulk or protosolar values (cf 5 Gyr ago Asplund et al., 2009; Grevesse et al., 2010; Lodders, 2010). The choice of the cosmic abundance standard proposed by Nieva and Przybilla (2012) and the derivation of element abundances is discussed in Nicholls et al. (2017). At the so-called local Galactic concordance, $12 + \log(O/H)_{GC} = 8.76$, which is close to the 8.73 estimated primordial solar abundance derived by Asplund et al. (2009) and Lodders (2010), and $(O/H)_{GC} = 5.76 \times 10^4$, $(N/H)_{GC} = 6.17 \times 10^5$ and $Z_{GC} = 0.0142$. Following Nicholls et al. (2017) we introduce the ζ_O scaling parameter related to to oxygen abundance: $\zeta_O = (O/H)/(O/H)_{GC}$, and thus $\log\zeta_O = 0$ at the fiducial point and $\log\zeta_O < 0$ for sub-metallic galaxies. Table 4.1 gives the correspondence between the scaling based on the oxygen abundance and on the Z mass fraction. Fig. 4.1, created by Patrice Theulé, gives the variation of the (N/O) abundance as a function of the oxygen abundance.

We disconnect the ISM gas-phase metallicity Z_{gas} from the stellar metallicity Z_{star}. The stars have fewer metals than the ISM because they formed from the previous surrounding ISM gas, which is later enriched by stellar evolution. The photoionizing radiation field was derived using Bruzual and Charlot (2003) single stellar population synthesis for six stellar metallicities (i.e., 0.0001, 0.0004, 0.004, 0.008, 0.02, 0.05).

To allow a finer grid, we considered 25 Z_{gas}, each one of them being related to its preceding closest Z_{star} BC03 stellar metallicities according to Table 4.1. The emission line spectrum for a given gas-phase metallicity is therefore calculated using the stellar radiation field of the corresponding stellar metallicity.

The photoionizing field shape and intensity define the number of photons that can ionize hydrogen (ionization potential (IP) of 13.6 eV), O^{2+} (IP 35.1 eV) and N^{+} (IP 14.5 eV), and are directly related to the Hα, Hβ, [OIII]λ5007 and [NII]λ6584 recombination line emissivity. We use a photoionization field shape derived from the SSP model library of Bruzual and Charlot (2003) along with the IMF of Chabrier (2003) in the range $0.1-100\,M_{\odot}$. The photoionizing radiation field is generated using a constant star formation history and taken at a 10 Myr age. The shape of the radiation field depends both on the stellar metallicity and age. The intensity of the photoionizing radiation field is given by the dimensionless ionization parameter U:

$$U \equiv \frac{\Phi(H)}{n_H c} = \frac{1}{n_H c} \int_{\nu_0}^{+\infty} \frac{F_\nu}{h\nu}, \tag{4.1}$$

where c is the speed of light in cms^{-1}, $\Phi(H)$ is the surface flux of ionizing photons in $cm^{-2}s^{-1}$, F_ν is the surface energy flux of the input radiation, and ν_0 is the frequency of the Lyman edge ($h\nu_0$ = 13.6 eV) for hydrogen. Because $\Phi(H)/n_H$ is the number density of photons capable of ionizing hydrogen, U represents the number density of H-ionizing photons to the number density of hydrogen. In that parameter, the number density of H-ionizing photons and the matter density are correlated. Note also that due to the difference in ionization potential the number densities of H^{-}, $O^{2+}-$ and $N^{+}-$ ionizing photons are not the same. Thus, both the shape and the intensity of the photoionization radiation field directly affect the [OIII]λ5007/Hβ, [NII]λ6584/Hα line emission ratios. The U ionization parameter is varied from 10^{-4} to 10^{-1} by decimal exponent of 0.1. CIGALE scales the emission lines on this ionization parameter U to the number of ionizing photons.

The updated version of the HII-region models is used to fit photometry and emission line fluxes. These models allow us to interpret the locus of our galaxies in the excitation diagrams in an attempt to understand the underlying physics of the ISM. A summary of the main parameters described in this section to create the photoionization models is presented in Table 4.2. Our FMOS-COSMOS sample has Hα, Hβ, [NII]λ6584, [OIII]λ5007, [SII]λ6717, and [SII]λ6731 fluxes (cf Sect. 2.4). In our initial SED fitting analysis, we only include the Hα emission line because of the current challenges in the production of photoionization models to reproduce observations. I will discuss these issues in this section and introduce more line intensities in the fits.

Table 4.2. – Summary of the main important parameters used to produce the HII-region models with CLOUDY.

Parameter	Value
Electron density (n_e)	10, 100, 1000 cm^{-3}
Gas-phase metallicity	See Table 4.1
Grains	No grains included
SSP	BC03 SSP models (Bruzual and Charlot, 2003)
IMF	Chabrier (0.1-100 $M_\odot$) (Chabrier, 2003)
SFH	Constant SFH
Stellar metallicity	0.0001, 0.0004, 0.004, 0.008, 0.02, 0.05 (Bruzual and Charlot, 2003)
Ionizing spectrum age	10 Myr
Ionization parameter	$-4.0 < \log U < -1.0$ with 0.1 dex steps

4.1.1. The Baldwin-Phillips-Terlevich and [SII]$\lambda\lambda$717,31 excitation diagrams

In Fig. 4.2, the [OIII]λ5007/Hβ, [NII]λ6584/Hα diagram (so-called Baldwin-Phillips-Terlevich (Baldwin, Phillips, and Terlevich, 1981); see also Veilleux and Osterbrock (1987)) and the [SII]$\lambda\lambda$6717,31 excitation diagrams (hereafter [NII]-BPT and [SII]-BPT) along with our photoionization models are presented color-coded by the ionization parameter and the gas-phase metallicity. In the left panel the demarcation between star-forming galaxies and systems hosting an AGN of Kauffmann et al. (2003b) from SDSS data at z = 0 is shown as a black-thick line and the extreme starburst separation line of Kewley et al. (2013a) at z = 1.6 as a dashed line.

The blue, green and orange lines correspond to best-fit relations for the loci of galaxies in the [NII]-BPT at z ~ 2.2, z ~ 2.3, and z ~ 1.6 from Strom et al. (2017), Shapley et al. (2015), and Kashino et al. (2017), respectively. Individual FMOS-COSMOS points show the well-known offset from the local sequence. Our FMOS-COSMOS sample with valid measurements in the four emission lines and their corresponding measured errors are represented by dots. For a smaller sample of 16 objects, we show in the right panel the [SII]-BPT diagram with the star-forming and AGN separation of Kewley et al. (2001) and the best-fit for the loci of galaxies of Strom et al. (2017).

The CLOUDY models cover well the star-forming region below the Kauffmann et al. (2003b) line in the [NII]-BPT diagram. However, only 61% of the flux ratios presented are covered pointing towards a difficulty related to the nitrogen-to-oxygen abundances more than the photoionizing field. In this diagram, 23% of the objects lie in the composite region where AGN/star-forming coexist at z = 0. For the [SII]-BPT diagram models agree with the locus of galaxies with valid measurements within the observational errors. HII-region models able to predict emission line ratios above the local star-forming relation are difficult to create because of *i.* nitrogen abundance underestimation, *ii.* ionizing field hardness choice, *iii.* gas-phase metallicity and density discrepancies, and/or single stellar population models. The models depend strongly

on the relative abundances of nitrogen and oxygen, and thus on the choice of the standard metallicity scale (e.g., Nicholls et al., 2017). The nebular scaling of nitrogen with oxygen is problematic: while oxygen is principally produced in core-collapse supernovae in the native gas cloud from which the HII-region formed, nitrogen has both primary and secondary abundances, which are caused by delayed nucleosynthesis through hot-bottom burning and dredge-up in intermediate-mass stars as they evolve (Vila-Costas and Edmunds, 1993). Increasing the nitrogen abundance has been suggested by many authors to match observations (e.g., Masters et al., 2014; Masters, Faisst, and Capak, 2016; Steidel et al., 2014; Shapley et al., 2015; Yabe et al., 2015; Cowie, Barger, and Songaila, 2016; Sanders et al., 2016). A shift by $0.2-0.4$ dex in the N/O fraction is proposed by Masters, Faisst, and Capak (2016) while Kojima et al. (2017) and Strom et al. (2017) require ~ 0.1 dex to cover the locus of galaxies in the BPT at $z \sim 2.3$. We find that to cover all the galaxy sample at $z \sim 1.6$ a shift by $0.2-0.3$ dex is necessary.

[OIII]λ5007 and [NII]λ6584 have an ionization potential (IP) of 35.12 and 14.53 eV and are ionized by both charge transfer with protons and photoionization. Thus, [OIII]λ5007 and [NII]λ6584 abundances are less sensitive to the photoionizing field, which are determined indirectly through the HII abundance, and the initial oxygen and nitrogen abundances. [SII]$\lambda\lambda$6717,37 has an IP of 10.36 eV making its abundance very sensitive to the hardness of the photoionizing field in the UV. Indeed, Steidel et al. (2014) and Steidel et al. (2016) applied harder radiation fields using the binary Population and Spectral Synthesis code (BPASS) being able to produce models covering larger values of $\log([\mathrm{OIII}]\lambda5007/\mathrm{H}\beta)$ but always below the Kauffmann et al. (2003b) line.

Other authors point to a higher ionization parameter and/or electron density as the main parameter producing the offset (e.g., Brinchmann, Pettini, and Charlot, 2008; Kewley et al., 2013a; Kewley et al., 2013b; Dopita et al., 2016; Kojima et al., 2017; Bian et al., 2020). Nevertheless, current stellar synthesis models are unable to produce such hard radiation fields (Levesque, Kewley, and Larson, 2010). The densities from models in high-redshift galaxies ($z \geq 1-2$) are higher than in low-redshift galaxies, on the order of several 10^2 to several 10^3 per cm^{-3} (Shimakawa et al., 2015; Kashino et al., 2017). Density (i.e., the pressure) has only secondary effects on the locus of the models in the [NII]-BPT diagram (Masters, Faisst, and Capak, 2016).

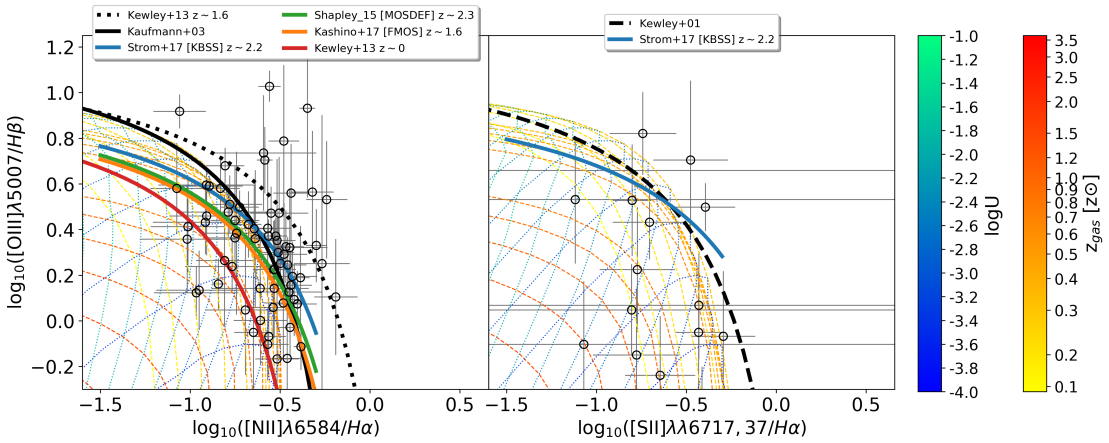

Figure 4.2. – **Left:** Baldwin–Phillips–Terlevich (BPT) diagram ([OIII]λ5007/Hβ versus [NII]λ6584/Hα). Thin lines show the new models implemented in CIGALE color-coded by gas-phase metallicity in solar units and ionization parameter log U. Only a few metallicities are shown for clarity. The FMOS-COSMOS sample is shown as gray dots with error bars. The solid black line corresponds to the Kauffmann et al. (2003b) relation and the dashed-black line corresponds to Kewley et al. (2013a) evaluated at z ~ 1.6. The curves of Shapley et al. (2015), Kashino et al. (2017), and Strom et al. (2017) are shown in green, orange, and blue, respectively. The red line represents the local-universe locus of galaxies as shown by Kewley et al. (2013a). **Right:** [SII]$\lambda\lambda$6717,31 excitation diagram ([OIII]λ5007/Hβ versus [SII]$\lambda\lambda$6717,31/Hα). The current models implemented in CIGALE are color-coded by gas-phase metallicity and ionization parameter log U to illustrate the coverage. Only a few metallicities are shown for clarity. The FMOS-COSMOS sample is shown as black circles with error bars. The dashed black line corresponds to that of Kewley et al. (2001) and the blue line to Strom et al. (2017).

4.1.2. Hα Hβ and [OIII]λ007 SED fitting

To test the performance of SED fitting including more emission lines, we fit simultaneously the photometry and the Hα, Hβ, and [OIII]λ5007 fluxes to explore the impact of the ionization parameter in the dispersion of the proposed SFR-$L_{[OIII]}$ relation. Our sample of galaxies spans over a gas-phase metallicity range of $0.006 < Z_{gas} < 0.016$ (see Sect. 3.3). We divide the sample in three different gas-phase metallicity bins with roughly equal number of sources and median metallicities given by $Z_{gas} = 0.009$, $Z_{gas} = 0.011$ and $Z_{gas} = 0.014$. We perform SED fitting including the UV-to-FIR photometry and the Hα, Hβ, and [OIII]λ5007 emission lines by fixing the gas-phase metallicity in each bin to its median value. Only two stellar metallicities of the BC03 models, 0.02 and 0.008 are included in the full range of gas-phase metallicity of our sample. We set the stellar metallicity to 0.02 after checking that using 0.008 does not affect our

parameter estimation. In the case of Hβ, we only include measurements of the lines for objects satisfying BD > 2.86 to be consistent with our models. We let the ionization parameter to vary between $-4.0 < \log U < -1.0$ and we use $n_e = 100$ cm^{-3} consistent with the electron density derived by Kashino et al. (2017) for the FMOS-COSMOS sample.

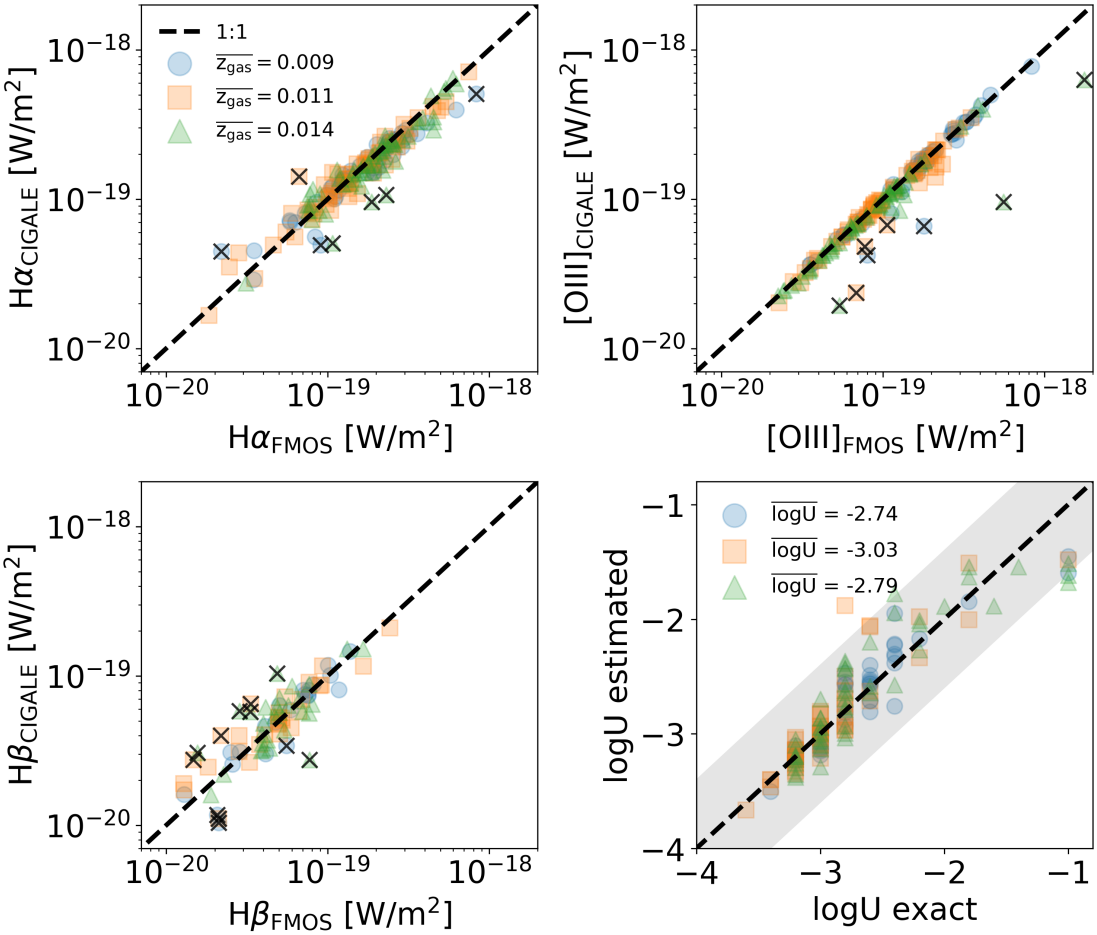

Figure 4.3. – Quality of the fits including Hα, Hβ, and [OIII]λ5007 emission lines, and ionization parameter estimation. From left to right, top to bottom, we show the CIGALE fit versus observed flux for the Hα, [OIII]λ5007, Hβ emission lines. The three different gas-phase metallicity bins are presented as blue circles, orange squares, and green triangles. The black crosses correspond to excluded data with flux differences larger than 0.2 dex. The black line corresponds to the 1:1 relation. The three emission lines are well fitted for the three different median gas-phase metallicity models. The last panel shows the estimated versus exact value for log U from mock samples created with CIGALE. Symbols are the same as the legend in the first panel and the median ionization parameter value is shown. The shaded area corresponds to the standard deviation.

4.1.3. Ionization parameter estimation

We exclude from the analysis 21 objects with a difference between observed and fitted fluxes larger than 0.2 dex for the three emission lines. In Fig. 4.3 the observed and estimated fluxes from the three emission lines are compared. In the case of the Hα line as compared to our previous fit in Fig. 3.1 similar results are obtained and the line fit is not improved by including more emission lines. The distribution of the estimated [OIII]λ5007 fluxes is not symmetric with an excess of overestimated fluxes. Hβ estimated fluxes have a standard deviation of ~ 0.13 dex which is twice as large as that of Hα and [OIII]λ5007 emission lines. We obtain a median attenuation from CIGALE of $A_{H\alpha} = 1.11 \pm 0.18$ mag and $A_{[OIII]} = 1.34 \pm 0.22$ mag († as reported in Table 3.2), consistent with values derived using photometry and the Hα emission only.

Stellar mass, SFR, and attenuation in the Hα and [OIII]λ5007 emission lines are not found to vary substantially by including more emission lines in the SED fitting process as shown in Fig. 4.4. Using mock catalogs created with CIGALE we investigate the robustness in the estimation of the ionization parameter $\log U$. The exact and estimated values of $\log U$ are compared in the bottom-right panel in Fig. 4.3 showing a good agreement within a 0.6 dex (1σ) dispersion for the three different gas-phase metallicity bins guaranteeing the reliability in the estimation of the ionization parameter.

From our fit, we estimate median values of $\log U_{0.009} \sim -2.74$, $\log U_{0.011} \sim -3.03$, and $\log U_{0.014} \sim -2.79$ while including the Hβ, and [OIII]λ5007 lines. The 16th and 84th percentiles in logU for each gas-phase metallicity bin are $\log U_{0.009} \sim -3.02, -2.35$, $\log U_{0.011} \sim -3.21, -2.60$, and $\log U_{0.014} \sim -3.14, -2.00$, respectively.

Kaasinen et al. (2018) measured $\log U \sim -2.72$ from an evolutionary analysis of the ionization parameter using a sample of 50 star-forming galaxies selected from the FMOS-COSMOS catalog with DEep Imaging Multi-Object Spectrograph (DEIMOS) observations. Sanders et al. (2020) constrain the ionization parameter using BPASS grids for a MOSDEF and Keck Baryonic Structure Survey (KBSS) samples at $z \sim 1-3$ to $\log U \sim -2.63$ and $\log U \sim -2.85$, respectively. Topping et al. (2020) found that the local $12 + \log(O/H)$-$\log U$ relationship of Pérez-Montero (2014) for low redshift galaxies is still applicable at $z \sim 2$. From this relation, the ionization parameter range for our sample should span over the range $-3.2 < \log U < -2.5$ in agreement with our estimations.

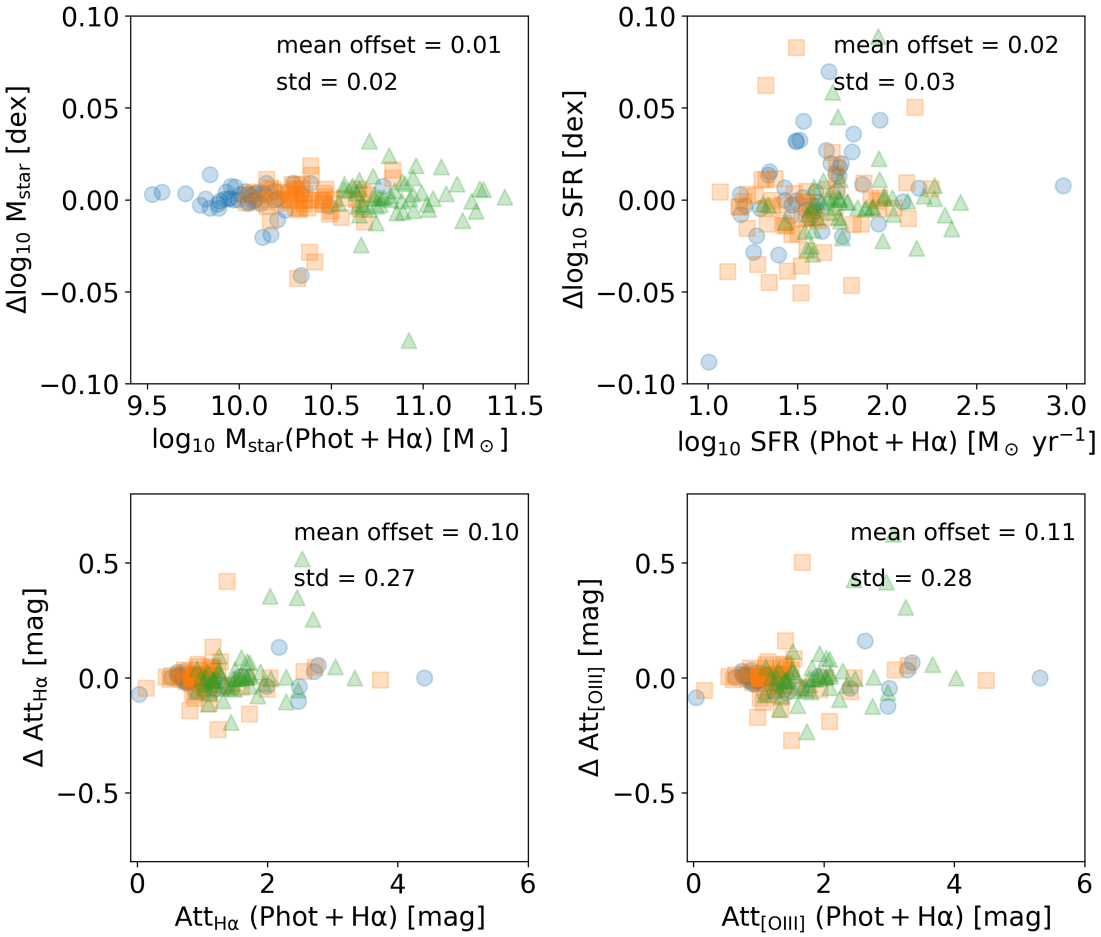

Figure 4.4. – Stellar mass, SFR, and Hα and [OIII]λ5007 attenuation. We compare the derived parameters using photometry and Hα flux in the SED fitting and adding Hβ and [OIII]λ5007 emission lines fluxes. The three different gas-phase metallicity bins are presented as blue circles, orange squares, and green triangles as in Fig. 4.3. The mean offset and dispersion of the are shown for each parameter.

4.1.4. SFR–[OIII]λ5007 dispersion

The SFR-L$_{[OIII]\lambda5007}$ ratio can be interpreted as the Hα-[OIII]λ5007 ratio because Hα is a tracer of SFR. The dispersion in the [OIII]λ5007/Hα dust corrected ratio (Fig. 3.10) depends on both ionization parameter and gas-phase metallicity. Now we explore the influence of the ionization parameter on our previous relation between SFR and [OIII]λ5007 (Sect. 3.3). In Fig. 4.5, we present SFR/L$_{[OIII]5007}$ from Eq. 3.7 as a function of the ionization parameter that we derived from the fit with emission lines and the three different median metallicities in each bin. In this figure, the error bar symbols represent the median values for each bin of gas-phase metallicity with the standard deviation as the error. We measured median ratios of ([OIII]λ5007/Hα)$_{0.009}$ =

1.12, $([\mathrm{OIII}]\lambda5007/\mathrm{H}\alpha)_{0.011} = 0.79$ and $([\mathrm{OIII}]\lambda5007/\mathrm{H}\alpha)_{0.014} = 0.54$ in each gas-phase metallicity bin. However, similar average log U values can lead to different [OIII]/Hα ratios due to variations with gas-phase metallicity. In Table 4.3 we show median values of the SFR-$L_{[\mathrm{OIII}]\lambda5007}$ ratio for each gas-phase metallicity in 0.5 dex log U bins for the $-3.5 < \log \mathrm{U} < -2.5$ range in which the ratio seems to be quite stable.

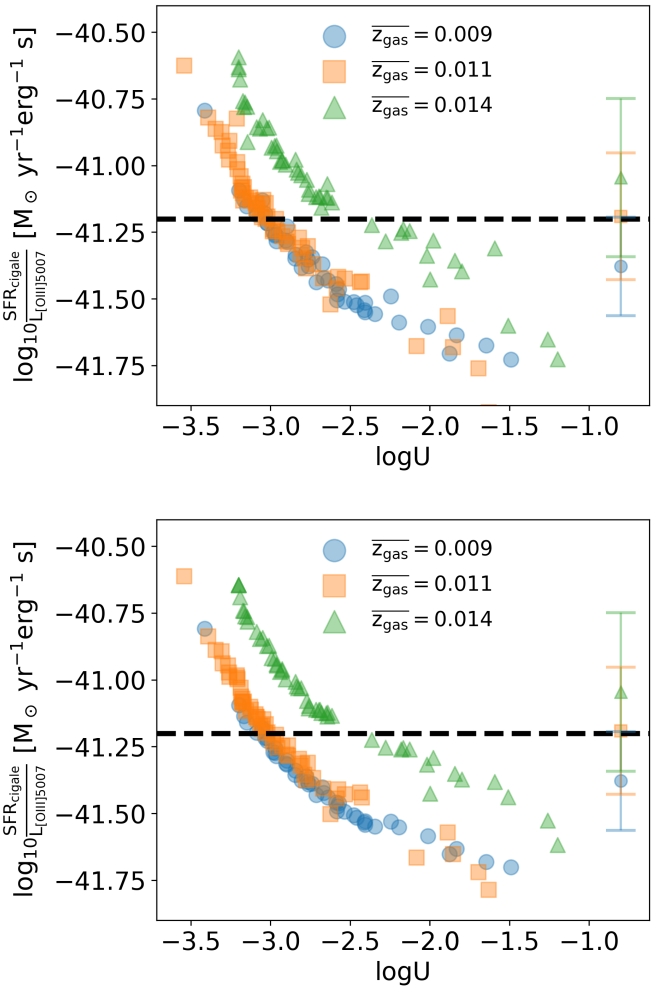

Figure 4.5. – SFR and $L_{[\mathrm{OIII}]5007}$ ratio versus the ionization parameter. Each metallicity bin is presented as blue dots, orange squares, and green triangles. The ionization parameter is computed with CIGALE for each fixed metallicity case. The black dashed line corresponds to the −41.20 [$M_\odot$ $yr^{-1}erg^{-1}$ s] intercept found in Eq. 3.7. The symbols with errors represent the median values of the SFR/$L_{[\mathrm{OIII}]5007}$ ratio for each metallicity. The ionization parameter has a larger impact on the dispersion than the gas-phase metallicity.

We measure a mean dispersion of 0.24 dex in gas-phase metallicity and 1.1 dex for the ionization parameter in the range $-3.5 < \log \mathrm{U} < -2.5$. The effects of the ionization

Table 4.3. – SFR-$L_{[OIII]\lambda5007}$ ratio mean values in 0.5 dex log U bins for the three different metallicities.

Z_{gas}	0.009	0.011	0.014
	$\log_{10}\left(\frac{SFR_{cigale}}{L_{[OIII]5007}}\right)$ $[M_\odot\ yr^{-1} erg^{-1}\ s]$		
log U			
-2.0 -2.5	-41.54	-41.44	-41.25
-2.5 -3.0	-41.35	-41.31	-41.04
-3.0 -3.5	-41.15	-41.10	-40.78

parameter on the SFR-$L_{[OIII]\lambda5007}$ dispersion are dominant, but our sample covers only a range of 0.4 dex in gas-phase metallicity. A sample spanning over a larger range of metallicity is needed to explore in detail the relative influence of both parameters. Our results are consistent with previous studies (e.g., Pérez-Montero, 2014; Kaasinen et al., 2018; Sanders et al., 2020; Topping et al., 2020).

In future work, we plan to explore the effects of using SED fitting with CIGALE implementing BPASS to explore how the locus of galaxies in the [NII]-BPT is affected. Leaving the abundance ratio of (N/O) as a free parameter to introduce flexibility in HII-region models, and checking also different ways of modeling the emission lines will be explored. The SED fitting and HII-region model coupling remain paramount to perform homogeneous analysis of a sample of galaxies and break degeneracies between the different parameters involved. Fully understanding of working with spectro-photometric samples and SED fitting is needed in preparation for new instruments like PFS and MOONS.

4.2. Summary and Conclusions

In this work, we perform SED fitting using CIGALE on an FMOS-COSMOS spectro-photometric sample covering UV-to-FIR continuum emission with 21 broad-band fluxes and emission lines at $z \sim 1.6$. A sample of 183 objects was selected to have flux measurements of both Hα and [OIII]λ5007 at SNR > 3 in the FMOS survey. From SED fitting of both photometric and Hα fluxes, we estimate SFR and stellar mass and constrain dust attenuation affecting the Hα and [OIII]λ5007 emission lines. We measure median values of the emission line attenuation of $A_{H\alpha} = 1.16 \pm 0.19$ mag and $A_{[OIII]} = 1.41 \pm 0.22$ mag, respectively. Both $A_{H\alpha}$ and $A_{[OIII]}$ increase with stellar mass with a larger attenuation correction for [OIII]λ5007 emission line as compared to Hα. We find a steeper effective attenuation curve than the Milky Way or C00 curves. A

relation to estimate the attenuation for the [OIII]λ5007 line as a function of the stellar mass is proposed in the same way as it exists for Hα. This relation could be useful to infer average values of the SFR of a sample but not for individual galaxies. The relative attenuation affecting different populations is characterized by the μ parameter in the attenuation law. We find a value of $\mu = 0.57 \pm 0.14$ consistent with different works in the literature and twice as large as compared to the original value proposed by Charlot and Fall (2000).

An SFR-$L_{[OIII]\lambda5007}$ dust-corrected relation is derived. We measure a slope consistent with unity within the 2σ dispersion of the relation. We estimate a [OIII]λ5007/[OIII] 88 μm ratio of 1.90 for our sample of galaxies and deduce A SFR-[OIII] 88 μm relation in agreement with previous relations found at both low and high redshifts, although [OIII]λ5007/[OIII] 88 μm is strongly dependent on electron density and gas-phase metallicity. SED fitting including photometry, Hα, Hβ, and [OIII]λ5007 fluxes is also performed with a refined grid of photoionization models and metallicities estimated from the mass-metallicity relation of Curti et al. (2020). The variations of gas-phase metallicity and ionization parameter induce a dispersion in the SFR-$L_{[OIII]\lambda5007}$ relation of 0.24 dex and 1.1 dex, respectively. The lower impact of gas-phase metallicity is likely to be due to the limited range of our sample ($0.006 < Z_{gas} < 0.016$) and our relation SFR-$L_{[OIII]\lambda5007}$ is expected to be only valid for galaxies of similar gas-phase metallicities as the ones studied in this work.

Part III.

MOONS: Multi-Object Optical and Near-infrared Spectrograph

5. MOONS project overview

Contents

5.1. Introduction

In the next sections, I will address the state-of-art of MOONS (Multi-Object Optical and Near-infrared Spectrograph). I will briefly discuss the instrument, the observational strategy, and the galactic and extragalactic survey planning.

I joined the consortium as part of the CIGALE team to work in the scientific working (TG-WG7) and the technical working group package (C-WG1). These groups are integrated by researchers from different institutions all around the world. With the C-WG1 I worked along with Myriam Rodrigues and Adam Carnall debugging the MOONS ETC and making decisions on how we should target the creation of models to be added to the different software packages used by the whole team. At the TG-WG7, I am in charge of producing mock spectra catalogs with CIGALE taking advantage of the different physical models, and the new nebular emission discussed in Part II of this thesis. In the beginning, I produced motivated models based on simple assumptions based on expected characteristics of three main different galaxy types (i.e., late and early type, and starburst) as the goal was to test the different MOONS modeling software. After discussion with the teams, based on the first analysis performed by different members of the consortium, we decided to start building mock spectra catalogs based on real data. For this, we chose the COSMOS field as it is part of my main work. Also because it has good spectro-photometric information and the team has vast experience working on this dataset. Fitting real SEDs in the COSMOS2015 catalog of Laigle et al. (2016) is addressed in these sections making a point on physical assumptions and relations used to model the nebular emission fitting only the UV-to-MIR photometry.

The production of spectra mocks samples is still an ongoing work in which I am involved with members of the CIGALE team like Véronique Buat and Denis Burgarella. The main goal is to provide a solid sample that can be used, in general, to test instrument outcomes based on SEDs coming from real observations.

5.2. MOONS: instrument, consortium

The Multi-Object Optical and Near-infrared Spectrograph (MOONS) is a powerful instrument currently being built for the VLT Nasmyth focus taking advantage of the telescope's full field of 500 arcmin^2. It will have 1001 optical fibers in total with 501 fibers dedicated for the objects and 500 fibers for the sky. The spectral resolution ranges from R ~ 5000 to R ~ 20000 providing observational power to develop science cases from galactic to extragalactic Astronomy, and cosmological scales. The instrument is designed to cover the NIR wavelength range spanning over 0.65μm – 1.8μm to study galaxy formation and evolution from the Milky Way to the epoch of re-ionization (Cirasuolo et al., 2012; Taylor et al., 2018; Cirasuolo et al., 2020).

This collaboration involves ten different institutions from six countries (e.g., Chile,

France, Germany, Italy, Norway, Portugal, Switzerland, the United Kingdom, and ESO) and it is coordinated by the Science and Technology Facilities Council (STFC) at the UK Astronomy Technology Centre in Edinburgh (see, https://vltmoons.org/ for more information). Around ~ 100 engineers and 150 scientists from ~ 50 different institutes make possible this large collaboration that will lead to unprecedented science. The principal investigator (P.I.) and co-principal investigators (co-P.I.) per country are:

— **P.I.**: Michele Cirasuolo (ESO)
Co-P.I.:
— Chile: L. Vanzi (AIUC)
— France: H. Flores (GEPI, Paris)
— Italy: E. Oliva (INAF)
— Portugal: J. Afonso (IA)
— Switzerland: M. Carollo (ETHZ) and S. Paltani (Université de Genève)
— UK: O. Gonzalez (UK ATC) and R. Maiolino (Cambridge).

MOONS is part of the new generation of Multi-Object Spectrometers (MOS) like PFS, DESI, WEAVE, 4MOST, being built around the world for different telescopes and aiming at a variety of sciences cases. It will combine the 8 m collecting power of the VLT with optical fibers equipped with robotic positioners. One of the most remarkable features of MOONS differentiating it from other MOS is the IR coverage of the instrument (see Fig. 5.1). The design will allow covering a wavelength region where important spectral features are shifted for high-redshift galaxies opening a new window for extragalactic Astronomy. Also, as compared to previous instruments, MOONS will be located at the Nasmyth port instead of being at its prime focus. In Table 5.1 the main characteristics related to the instrument as presented in Taylor et al. (2018) and Cirasuolo et al. (2020) are summarized.

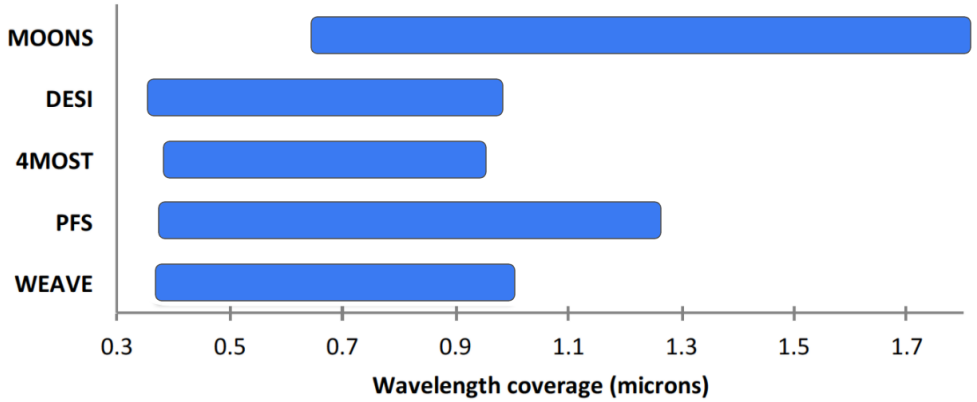

Figure 5.1. – MOONS wavelength coverage. A comparison of the MOONS wavelength coverage to other MOS facilities is shown. This figure is inspired in Figure 1 from Taylor et al. (2018).

Parameter	Value
Telescope	VLT, 8 m
Field of view	25 arcminutes in diameter
Multiplex	1001
On-sky aperture of each fiber	1.2 arcseconds
Field coverage	> 3 fibers can reach any point in the focal plane
# of fibers within a 2-arcminute diameter	7
Minimum fiber separation	10 arcseconds
Spectral channels	*RI, YJ, H* bands observed simultaneously
Resolution modes	Low and high-resolution
Low-res simultaneous spectral coverage	$0.61 - 1.8\mu$m
Low-res spectral resolution	$R_{RI} = 4100$, $R_{YJ} = 4300$, $R_H = 6600$
High-res simultaneous spectral coverage	$\lambda_{RI} = 0.76 - 0.89\mu$m, $\lambda_{YJ} = 0.93 - 1.35\mu$m, $\lambda_H = 1.52 - 1.64\mu$m
High-res spectral resolution	$R_{RI} = 9200$, $R_{YJ} = 4300$, $R_H = 19700$
Throughput	> 30% in low-resolution, > 25% in high-resolution
Sensitivity (point source) in 1 hr integration	See Fig. 5.4 for details
Continuum high res	S/N > 60 at $H_{AB} \sim 17$ and $RI_{AB} \sim 17.5$
Continuum low res	S/N > 5 at mag(AB)~ 23 rebinning to R = 1000 after sky subtraction
Emission lines	S/N > 5 for a line flux of $> 2 \times 10^{-17}$ ergs^{-1}cm^{-2}, FWHM = 200 kms^{-1}
Calibration methods	Daytime flat fields, attached flats as part of observations ThAr lamps for wavelengths
Observing overheads	fiber positioning time < 2 mins Attached flats + 2 mins
Acquisition star limiting mag	V ~ 21 mag (in 30 sec exposure)

Table 5.1. – MOONS instrument characteristics. The most relevant properties in terms of sensitivity, resolution, observation, and sky coverage of the instrument are presented. The table reproduced from Taylor et al. (2018) and Cirasuolo et al. (2020).

As part of the observational strategy, MOONS will be offered to the scientific community as a normal VLT instrument. This guarantees that anyone all over the world can submit a proposal and use the instrument for any science case they plan to target. The observation strategy, path planning, and transmission curves are an essential part of the instrument. Also, the currently available software that is used for the modeling for different teams of the consortium. Let's briefly develop a bit more on these three subjects.

Observing strategies: Observations are divided into Observing Blocks (OBs). They will be made of two different templates, one for the instrument and telescope setup (acquisition) and another for the observations. Fig. 5.2 shows the possible setup options with MOONS. The Fiber Positioning Units (FPUs) will move from the datum position to the science position. In case (A), the OB is a repetition of the observation so FPUs displacement will be minimal then FPUs do not return to the datum until the next observation. In (B), the metrology system is not needed while it is in (C). In (D), an attached flat has been requested by the Astronomer. The time in which (D) can be executed is expected to be around 6 minutes. If fields are close together this time can be much less, then using option (B) can help reduce overheads to a few minutes. In

the stare mode the majority of fibers is allocated to the targets while in the stare+nod all of them will be on the targets. In Xswitch mode every object fiber will have a sky fiber to provide a good sky-subtraction.

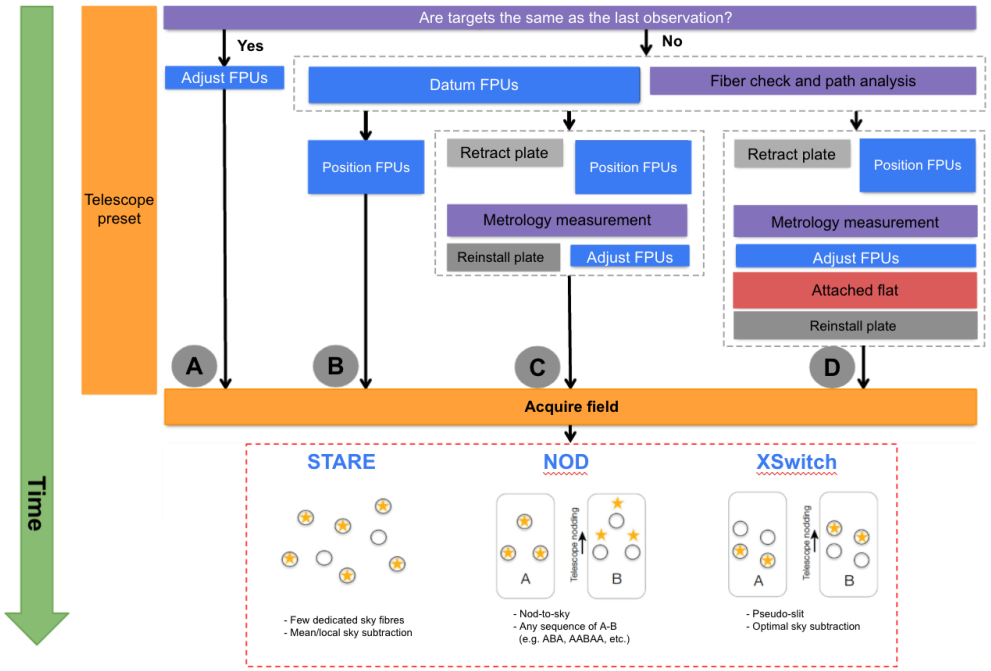

Figure 5.2. – MOONS OB setup. Four different options (i.e., A, B, C, and D) to set up the instrument are presented. Purple and blue boxes represent calculations/measurements and FPU movements, respectively. Telescope operations and on-sky are shown in orange and the red boxes show steps where data is being taken. This is a composite image inspired in figures from Taylor et al. (2018) and Cirasuolo et al. (2020).

Path planning: FPUs have a high chance to collide with each other. Therefore a routine has been created to minimize this risk, taking advantage of a potential field approach where FPUs are attracted to the target locations and repulsed by surrounding FPUs. They will then have the possibility to navigate around each other and avoid broken ones. The two-phase approach implemented by MOONS to get the highest allocation efficiency consists of assigning FPUs to targets avoiding blocking other science targets as possible by the Observation Preparation Software (OPS). This is illustrated in Fig. 5.4. The OPS's output is passed to the path-planning software.

Transmission: the transmission of the instrument is crucial for the observations. The high-resolution modes have a lower transmission when compared to the low-resolution modes. This is due to a combined effect of having two prisms in the optical path and the increased angle of incidence of light onto the dispersive elements. In Fig.

5.4 the current transmission curves are presented.

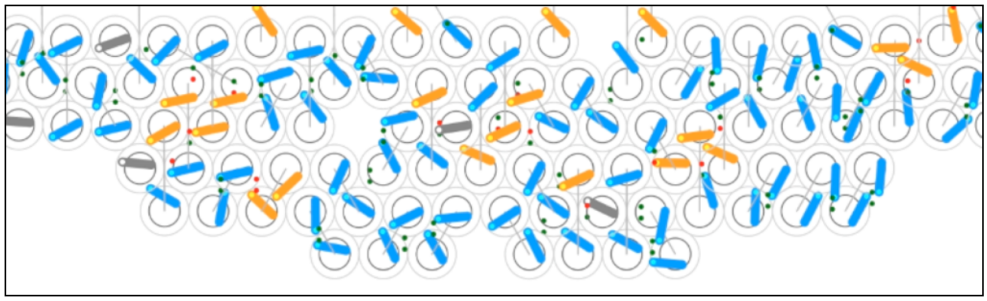

Figure 5.3. – Path planning simulations of the XSwitch observation. FPUs are shown in blue if they reach a target, yellow if they cannot reach the target, and gray if they are not assigned. Targets not being reached are colored in red while those reached by the FPU are in green. Object-sky pairs are connected by a gray line. Gaps in the grid of FPUs correspond to ACs or fiducials. The image is taken from Taylor et al. (2018).

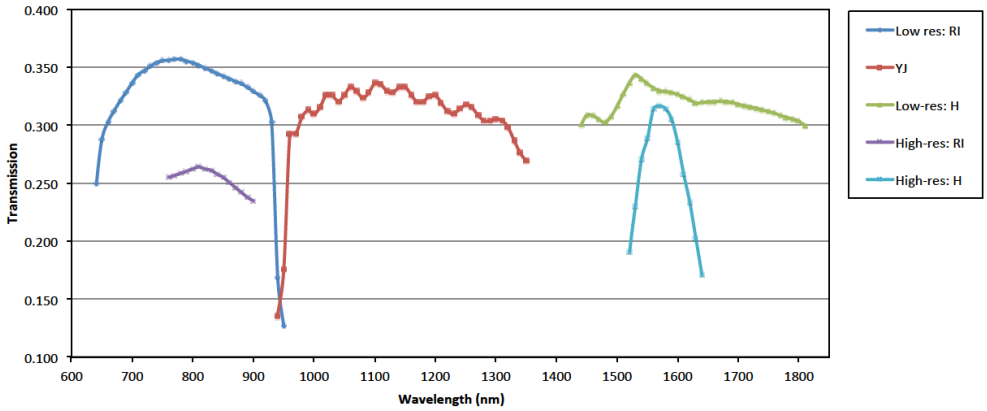

Figure 5.4. – Low and high-resolution predicted transmission for each of the *RI*, *YJ*, and *H* bands. The image is taken from Taylor et al. (2018).

MOONS will provide the scientific community with unprecedented datasets, in particular for the extragalactic Astronomy community. Results from MOONS will be crucial to building spectro-photometric samples that can be tested, for example, with CIGALE as it was presented in Part II of this thesis. In the next sections, I will focus on the MOONS science cases, giving important attention to the extragalactic science case which is relevant to my past and current work.

5.2.1. MOONS science cases

Figure 5.5. – Different science cases of the MOONS galactic and extragalactic surveys. The covered spectral range and the high-resolution of the instrument will be crucial to studying the chemo-dynamical properties of the Milky Way, the Magellanic clouds, and the Sagittarius dwarf galaxy. It will also allow performing spectral diagnostics for galaxies at intermediate-to-high redshift, unveiling the processes of galaxy evolution from the comic dawn to the comic noon. The image is taken from Cirasuolo et al. (2020).

Behind every instrumentation project, carried out by a scientific team, there are critical scientific questions to be answered. For example, the formation and evolution of the universe, and the role played by galaxies in this context. During the last decades, we have learned a lot from local observations (e.g., stars, and nearby galaxies) to larger scales (e.g., high-redshift galaxies and the large-scale structure of the universe) leading to a comprehensive evolutionary scenario of the Universe. Nevertheless, understanding how the large-scale structure of the universe in combination with the physical processes affects the baryonic matter and shapes the formation and evolution of stars and galaxies remains an important question to be answered in Astronomy (Cirasuolo et al., 2020). To answer these questions, we have our galaxy, the Milky Way which

remains an amazing scientific object to be studied in terms of chemical evolution, the orbital motion of stars, stellar populations, among others. The Milky Way observations help us to study the role of galaxies when looking farther away to the young universe in an attempt to understand, for example, the star-formation of the universe, the chemical enrichment, and the mass assembly of galaxies.

MOONS will be targeting different science cases grouped into the galactic and extragalactic surveys. This is depicted in Fig. 5.5. In the galactic survey, MOONS will observe our galaxy and local galaxies like the Magellanic clouds to gain information on their past histories through their Radial velocities, metallicities, and chemical abundances. In the case of extragalactic Astronomy, the instrument will be able to observe spectral features of high-redshift galaxies with high resolution, allowing us to study a large variety of galaxies as never before mapping from the cosmic dawn to the cosmic noon of the Universe. In the next section, I will briefly describe the galactic survey.

5.2.2. Galactic survey

Two main galactic surveys will be targeted by MOONS in the future: *i*) the MOONS REDdened Milky WAY (REDWAY) sampling 3 kpc in the inner disk of the galaxy and other regions affected by extinction in the optical, sampling the chemo-dynamics of the stellar components over 70 nights, and *ii*) the Milky Way Satellites Survey to study the disk/bar region of the Magellanic Clouds and Sagittarius, and its streams sampling their stellar populations over 30 nights. A scheme it is presented in Fig. 5.6.

REDWAY will sample different regions from the galactic bulge and its components to clusters and star-forming regions taking advantage of the high-resolution mode. This survey is expected to observe more than 102000 stars across 120 fields at a SNR $\sim$ 100 in the H-bands including a bright and faint configuration reaching a SNR $>$ 50 and SFR $>$ 15$-$20 in each case and down to $H_{AB} \sim 18.5$. MOONS will provide measurements of radial velocities, [Fe/H], CNO, alpha, and other elements in the bulge covering 15 fields (blue circles in Fig. 5.1 and $\sim$ 13000 red giant stars in the nuclear bulge over a $\sim 50 \times 140$ pc region giving access to radial velocities and stellar parameters.

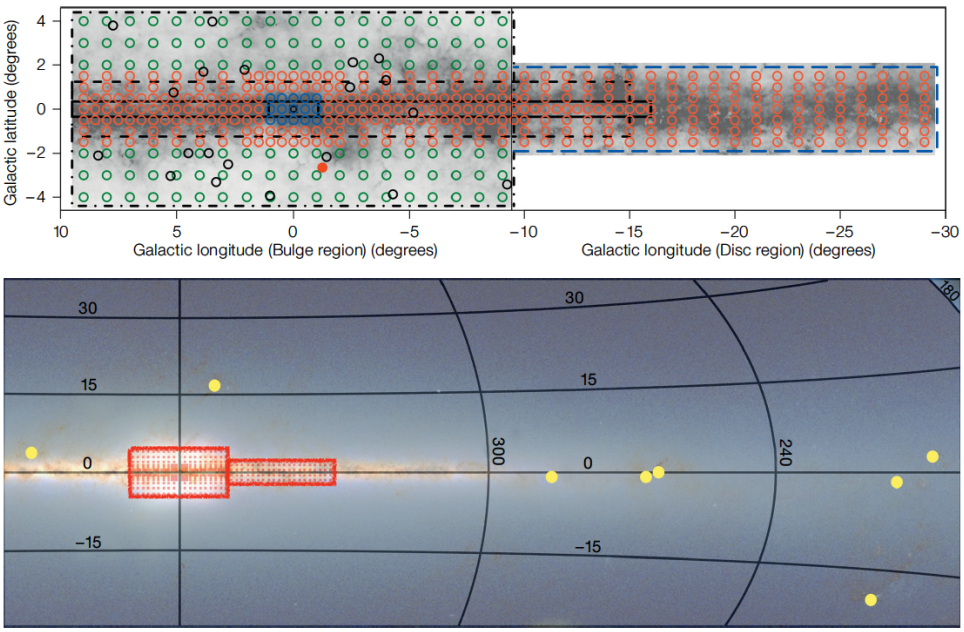

Figure 5.6. – REDWAY MOONS galactic survey scheme. The top panel shows the different fields of the Milky Way to be studied. The nuclear inner bulge is shown in blue, the in-plane bar and inner disc in orange, and the boxy bulge in green. The inner galaxy clusters are colored in black with the bulge deep field in a red-filled dot. The lower panel images correspond to a zoomed-out image showing the star-forming regions and the young clusters that will be observed as yellow dots. The image is taken from Gonzalez et al. (2020).

On the other hand, the second survey will observe the Magellanic clouds and Sagittarius galaxy providing insights on the ongoing star-formation as well as on the streams' interaction with the Milky Way tidal field. The first and second priority MOONS fields for the LMC (left) and the SMC (right) are presented in Fig. 5.9 in red and blue squares, respectively. Element abundances, kinematics information, and stellar parameters will be the outcome of these observations that will enrich our knowledge using around ~ 35000 and ~ 18000 stars in the LMC and SMC, respectively. Thousands of spectra for stars in the thick disc will be also available.

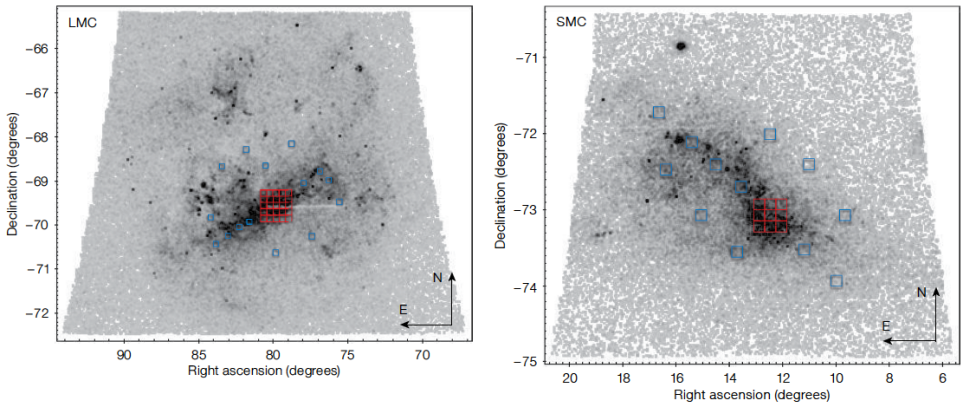

Figure 5.7. – Large Magellanic Cloud (left) and Small Magellanic Cloud (right) giant stars map. In each image, the first and second priority fields for the REDWAY survey are presented as red and blue squares, respectively. The image is taken from Gonzalez et al. (2020).

5.2.3. Extragalactic survey

As part of the extragalactic survey, MOONS will be able to deliver information at high-redshift for hundreds of thousands of galaxies. New insights about the environment where galaxies live will enrich the current galaxy evolution picture we have today. This is possible thanks to the instrument's high sensitivity and high fiber, and broad spectral coverage.

This survey is crucial in terms of the work I am carrying out due to the high quality spectra information that will be delivered, giving us unprecedented material to study absorption and emission features in galaxy spectra as never before. The emission lines are paramount to studying and understanding the underlying physics of galaxies. More precisely, useful emission lines to study star-forming galaxies and AGN like Hα and [OIII]λ5007 will be detected out to z ~ 1.74 and 2.6, while [OII]λ3727 can be accessed from z = 0.7 – 3.8 as presented in Fig. 5.8. As shown in Part II of this thesis, high-quality observations of Hα and [OIII]λ5007 will help us to test our proposed relations in a robust statistical sample and will be giving us access to [NII]6584 and [SII]-doublets to tackle the current discrepancies in the excitation diagrams at intermediate and high redshift. The extragalactic survey will identify a broad range of environments such as clusters of galaxies, filaments, and voids (see, Fig. 5.9), measure spectroscopic redshifts at z ~ 1.5 (i.e., the redshift desert), and allow studying galaxies at high-redshift through the Lyα emission and other transitions in the UV rest-frame (Cirasuolo et al., 2020; Maiolino et al., 2020).

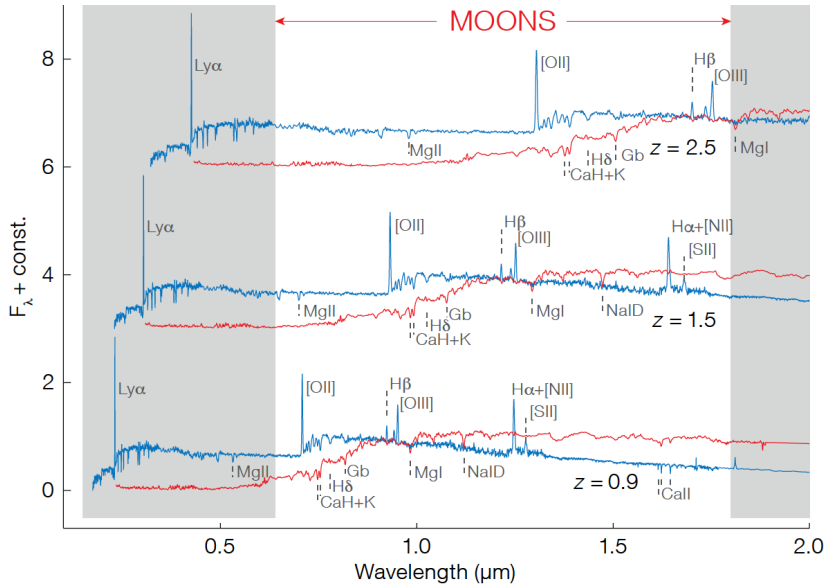

Figure 5.8. – Spectral features to be observed with MOONS at three different redshifts. Three different redshifted spectra are presented at z = 0.9, z = 1.5, and z = 2.5 for passive galaxies in red and star-forming galaxies in blue. Some of the primary rest-frame optical nebular and stellar features are highlighted and described in Table 5.2. The MOONS wavelength range is delimited by the white area. The image is taken from Maiolino et al. (2020).

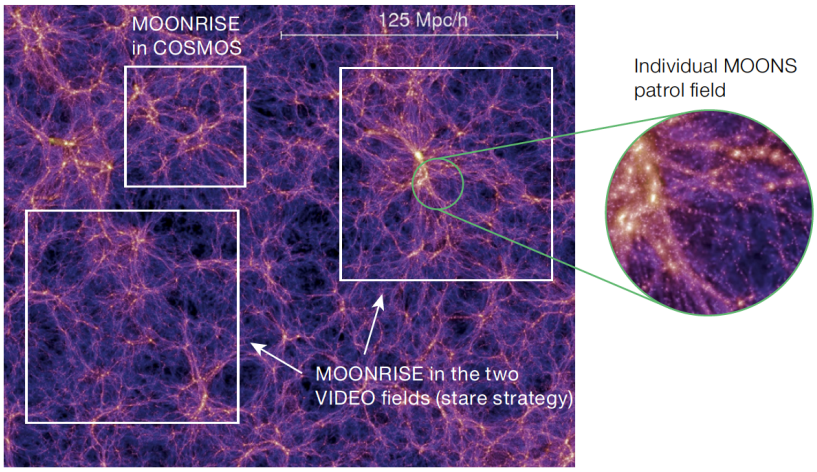

Figure 5.9. – Environments to be observed by the MOONRISE survey. The image corresponds to a slice taken at z = 1.4 from the Millennium simulation (Springel et al., 2005). The MOONRISE strategy for the COSMOS and VIDEO fields are shown as white rectangles with a zoomed-in region representing the individual MOONS patrol field. The image is taken from Maiolino et al. (2020).

A program of 190 observing nights will be dedicated as part of the MOONS Redshift-Intensive Survey Experiment (MOONRISE) survey. The goal is to obtain spectroscopic information for about half a million galaxies at a redshift range of $0.9 < z < 2.6$ and some at the epoch of reionization ($z \sim 6-8$). MOONRISE will allow unprecedented statistics to test assumptions in cosmological simulations. MOONRISE science cases aim to gain information on galaxy kinematics, star formation histories, galaxy transformation, passive galaxies, AGN and black holes, and environment, as well as galaxies at the epoch of reionization. A crucial science case for my work is centered on the metallicity evolution of galaxies and their chemical abundances. A brief explanation on how MOONRISE will address some of these cases is given below focused on what we can learn from the stellar features.

— **Metallicity and chemical abundance:** Obtaining robust measurements of the gas-phase metallicity and abundances are paramount for calibrations in extragalactic Astronomy, for example, in terms of other parameters like SFR and stellar mass. MOONRISE will give access to measurements from multiple nebular transitions as shown in Fig. 5.8 for galaxies spanning over three orders of magnitude in mass and SFR. This allows to test the Fundamental Metallicity Relation (FMR, Mannucci et al., 2010) and evolution of the mass-metallicity relation with redshift (Kashino et al., 2019; Sanders et al., 2021). Dispersion in fundamental relations (see Fig. 5.10) can also be carried out (Maiolino and Mannucci, 2019) as well as test on galaxy evolutionary scenarios from individual measurements (Cullen et al., 2019).

— **AGN and black holes:** Type 2 AGN will be identified by MOONS giving access to excitation diagnostics as the BPT diagram (Baldwin, Phillips, and Terlevich, 1981) as well as type 1 through Hβ and/or Hα broad components. It is paramount to understand the relation of black holes with the star formation, galaxy interactions, and transition to quiescence as well as to measure black hole masses at high-redshift Maiolino et al. (2020).

— **Passive galaxies:** Passive galaxies will be identified at high-redshift taking advantage of the good masking of OH sky lines (see, Fig. 5.11) using nebular emission and stellar continuum. Observations of passive galaxies down to $H_{AB} < 22$ will allow studying star-formation quenching, and age, and SFHs with high SNR stellar continuum (Carnall et al., 2019).

— **Environment and epoch of reionization:** Galaxy evolution and its interaction with the environment will be accessible through the NIR coverage. From voids to clusters, MOONS will explore the galaxies' environment at $z \sim 1-2$, trace filaments, and disentangle galaxies from their satellites (Maiolino et al., 2020). The cosmic dawn will be studied thanks to galaxy spectra at $z \sim 5-10$. Lyα emission along with UV rest-frame lines like CIV, HeII, CIII], and NV are crucial to study neutral gas in the intergalactic medium, the escape fraction of ionizing

photons, ionization parameter, and hardness of the ionizing field. In general, velocity profiles will be also delivered thanks to the excellent resolution of the instrument and high accuracy observations of [OIII]λ5007, Hα, NaDI, among others.

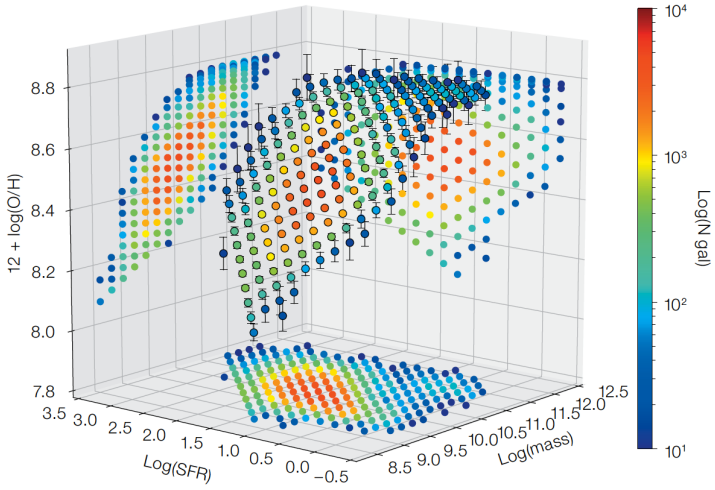

Figure 5.10. – Fundamental metallicity relation (FMR). This figure shows the relation between three main parameters, star-formation rate, stellar mass, and gas-phase metallicity that give shape to the FMR at z ~ 1.5. MOONRISE survey will provide clear information on the dependence of gas-phase metallicity on the galaxys' extensive properties (e.g., SFR, and stellar mass) and the possible evolution of these scaling relations with redshift. The color code in the image corresponds to the number of galaxies in SFR and stellar mass bins. Only galaxies whose gas-phase metallicity can be estimated using two independent indicators are included. The image is taken from Maiolino et al. (2020).

The survey will target three main fields: the Cosmic Evolution Survey field (COSMOS) and two fields XMM-LSS and ECDFS from the VISTA Deep Survey. The idea is to observe 1 deg^2 in COSMOS, and 3 to 6 deg^2 in the VISTA fields. Observation of the COSMOS field will allow our future work to expand and test SED fitting on spectro-photometric samples like the one I presented in Part II of this thesis. The COSMOS field will be crucial in Sect. 6.1 where I present the mock spectra modeling procedure I developed for the MOONS collaboration project. The target selection is based on optical-to-NIR photometry for the photometric redshifts presented in Table 5.2 with available main nebular emission lines and stellar features as presented in Fig. 5.8. Completeness of 80% in the COSMOS field and 70% in the two video fields is expected though it depends on how MOONS will perform the observations. In the Xswitch mode, ~ 400 pairs of fibers will be placed to observe targets and sky for nodding observations. In the Stare mode, ~ 900 pairs will be allocated to targets,

and the sky background will be monitored with a few tens of fibers. In star-forming galaxies, nebular emission lines can be rapidly obtained as compared to the stellar continuum features for passive galaxies (Maiolino et al., 2020). 25% of the allocated fibers will observe for 8 hours passive galaxies while star-forming ones will be observed for 1 or 2 hours at the same time. A total of 38 nights observations in Xswitch mode are allocated to observe ~ 480 passive galaxies and 4350 star-forming galaxies in the COSMOS field. Numbers double if Stare mode is used (Maiolino et al., 2020). At z > 5 with an integration time of 8 hours, observations will lead to study Lyman-break identified galaxies and Lyman-α emitter candidates. The total number of objects observed during the MOONRISE program in Xswitch and Stare modes is shown in Table 5.2.

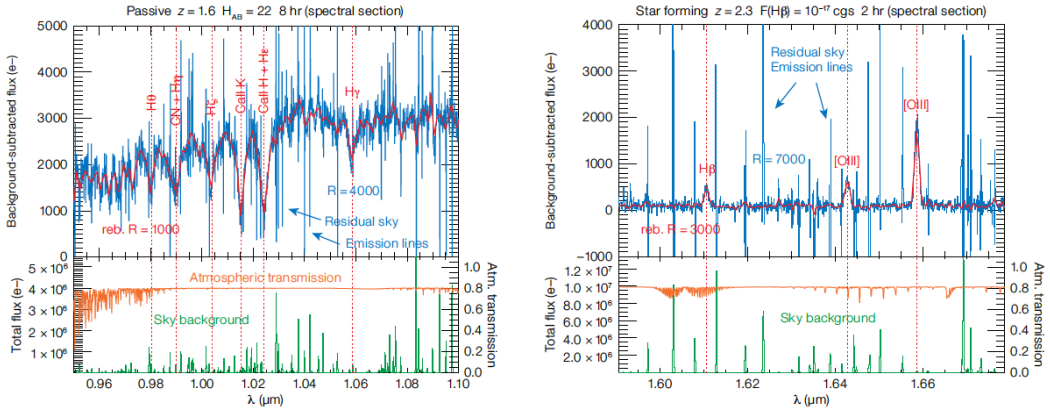

Figure 5.11. – MOONS simulated spectra. The background-subtracted spectrum is presented in blue and rebinned after masking OH emission in red. The atmospheric transmission and the sky background are shown in the lower panel in orange and green, respectively. In the left, the spectrum of a passive galaxy at z = 1.6 and H)AB = 22 as being observed during 8 hours. In the right, a star-forming galaxy at z = 2.5 and H)AB = 23.5 observed during 2 hours. The image is taken from Maiolino et al. (2020).

Crucial nebular emission lines will be observed at intermediate and high redshift providing us with unprecedented data sets to test SED fitting in good quality spectrophotometric samples. This will help us to improve the HII-region modeling for different types of objects sharing information on the underlying physics of galaxies.

Table 5.2. – MOONRISE survey design. The main spectral features for four different redshift ranges are shown. Star-forming and AGN are shown in blue while passive galaxies are colored in red. The table is reproduced as presented in Maiolino et al. (2020).

			Number of galaxies	
Redshift range	Main spectral features	Selection	Xwitch (4 square degrees)	Stare (7 square degrees)
0.9 < z < 1.1	[OII], Hβ, [OIII], Hα, [NII], [SII]	$H_{AB} < 23$ or	33900	75300
	CaH+K, Hδ, Gb, Mgb, NaID, CaII	$\log(M_*) > 9.5$	12900	28500
1.2 < z < 1.7	[OII], Hβ, [OIII], Hα, [NII], [SII]	$H_{AB} < 23.5$ or	88700	197100
	MgII, CaH+K, Hδ, Gb, Mgb, NaIID	$\log(M_*) > 9.5$	13700	30500
2.0 < z < 2.6	[OII], Hβ, [OIII]	$H_{AB} < 24$ or	54500	121100
	MgII, CaH+K, Hδ, Gb, Mgb	$\log(M_*) > 10$	2100	4700
5 < z	Lyα, NV, HeII, CIV, CIII]	$H_{AB} < 26$	2000	4500
Total			**207800**	**461700**

6. Spectra simulation with CIGALE

Contents

6.1. Spectra mock sample simulation

The Laboratoire d'astrophysique de Marseille (LAM [1]) is involved in different MOS projects including MOONS, PFS, and MOSAIC. Researchers in the Galaxie Étoiles et COsmologie (GECO [2]) team like Véronique Buat, Denis Burgarella, and Jorge Villa-Vélez are part of the scientific working (TG-WG7) and technical working group package (C-WG1) of the MOONS collaboration in charge of the redshift and physical parameter determination as well as the end-to-end simulation.

As presented in Sect. 1.2, CIGALE is a code not only oriented to analyze photometry and emission line fluxes from galaxies but also to be used as a simulator. CIGALE gathers a vast number of physical models (see, figures 1.9 and 1.10) at its core which are accessible to the user to reproduce SEDs of galaxies at a given configuration. The idea in a broad way is similar to that of SED fitting but instead of setting the analysis mode inside CIGALE to "sed_analysis" one can set it to "save_fluxes" (see, Boquien et al., 2019). This takes the input configuration of SFH, Single Stellar Population (SSP) models, nebular emission, dust attenuation, and re-emission, and AGN contribution, building a SED and retrieving the fluxes which can be saved to a file. The output corresponds to a simulated spectrum that inherits the characteristics of the stellar libraries implemented. I took advantage of the code's modular structure to create meaningful mock simulated spectra that can be used by the scientific working groups to carry out analysis based on individual object motivated spectra (i.e., module parameters are chosen to cover a wide variety of cases) and realistic motivated (i.e., modules parameters are set to reproduce real data and reproduce accurately the expected spectra of the object) SEDs. The standard process in which CIGALE deals with SFH, attenuation, and emission lines is described in Part I and Part II of this thesis. The inherent resolution of SSPs included in CIGALE puts constraints on mock spectra resolution. I discuss here the choice of the dust attenuation recipes such as Calzetti et al. (2000) or Charlot and Fall (2000) that can be used depending on if one has continuum, or continuum and emission-line information. Simple motivated models can be created using different configurations for the parameters inside these modules. Attention needs to be put when creating models based on real data because the estimated parameters depend strongly on the configuration the user introduces. This will be shown in Sect. 7.2. On the other hand, AGN templates are also available but we do not use this module in our modeling as our work is focused on targetting star-forming and passive galaxies. Nevertheless, if needed, the stellar continuum mock sample can be used to add emission lines produced by AGN separately with a given recipe. The current version of CIGALE's nebular emission module is only adapted for HII-region line emission.

In the next sections, I will explain the different parameters and strategies followed to create mock samples. Information on the HII-region models and the implementation

1. https://www.lam.fr/?lang=en
2. https://www.lam.fr/recherche-14/galaxies-etoiles-et-cosmologie-geco/?lang=en

of MOONS requirements to fully model the spectra appropriately for the multiple collaboration's working groups are also described.

6.2. Stellar continuum and emission line models

The shape of the spectra is modulated by the stellar continuum (i.e., the stellar libraries used to build the SSPs) and the HII-region modeling for the emission lines. Combining different sets of the parameters involved in the SED modeling will change the continuum and line emission to reproduce the different types of objects. As stated before, the continuum is a reflection of the stellar libraries implemented. In our case, this corresponds to the Bruzual and Charlot (2003) models, a collection of low and high-resolution spectra gathered together to reproduce stellar populations. This will be addressed in Sect. 6.2.1. On the other hand, the nebular emission provides line intensities derived from HII-region modeling with CLOUDY where several parameters like the element abundances, depletion factors, gas-phase metallicities, electron densities, ionization parameter among others are set up. This results in a collection of grids in which one can read a line intensity for a particular transition given the parameters described before. The final result is the spectra, a combination of both the stellar continuum and the emission lines which gives us extraordinary information on the ongoing physics of astrophysical objects.

6.2.1. Continuum modeling

The continuum emission in CIGALE can be model based on Bruzual and Charlot (2003), Maraston (2005), Starburst99, and BPASS SSPs. For this particular work, I chose to use the Bruzual and Charlot (2003) templates. These SPPs models have a resolution of 3 Å (i.e., $\lambda/\Delta\lambda \approx 2000$) across a wavelength range spanning over 3200 to 9500 Å. For a larger wavelength range covering from 91 Å to 160 μm low-resolution (i.e., $\lambda/\Delta\lambda \approx 200-500$) spectral evolution is available. The spectral evolution of stellar populations covers ages between 1×10^5 yr and 1×10^{10} yr. The modeling includes thermally-pulsating stars on the asymptotic giant branch being able to reproduce spectra from the Early Data Release (EDR) of the Sloan Digital Sky Survey (SDSS) as well as color-magnitude diagrams in the optical and near-infrared for galactic star clusters of different metallicities and ages. These models were the first to be able to allow accurate studies of absorption-line strengths and reproduce Lick indices that do not depend on element abundance ratios. The different libraries of stellar spectra are presented in Table 6.1. The BaSeL library is used to extend the STELIB and pickles libraries at shorter and longer wavelengths.

6.2.2. Emission line modeling

As presented in Sect. 3.1.2 in previous versions of CIGALE (see, Boquien et al., 2019) the implemented HII-region models were created using CLOUDY for total of

Table 6.1. – Stellar spectra libraries characteristics as reported in Bruzual and Charlot (2003).

Name	Type	Wavelength range	Median resolving power	Metallicity range	Source
BaSeL	theoretical	91 Å to 160 μm	300	$10^{-5}Z_{\odot}$ to $10Z_{\odot}$	Kurucz (1991, priv. comm.) Bassel et al. (1989) Bassel et al. (1991) Fluks et al. (1994) Allard & Hauschildt (1995) Rauch (2002)
STELIB	observational	3200 Å to 9500 Å	2000	$-2.0 <$ [Fe/H] $< +0.50$	Le Borgne et al. (2003)
Pickles	observational	1200 Å to 2.5 μm	500	$Z_{\odot}$	Pickles (1998) Fanelli et al. (1992)

Table 6.2. – HII-region emission line models in CIGALE. These lines are commonly used to derive physical information from galaxies and also for redshift measurements. The wavelengths corresponding to the center of the emission line are given in vacuum. The name of the line is given as it is implemented inside CIGALE.

Name	Wavelength [Å]	Name	Wavelength [Å]	Name	Wavelength [Å]	Name	Wavelength [Å]	Name	Wavelength [Å]
Ly-alpha	1215.67	H-9	3836.47	H-delta	4102.89	HeI-587.6	5877.25	SII-673.1	6732.67
HeII-164.0	1640.42	NeIII-386.9	3870.16	H-gamma	4341.68	OI-630.0	6302.05	ArIII-713.5	7137.80
OIII-166.5	1666.15	HeI-388.9	3889.73	OIII-436.3	4364.44	NII-654.8	6549.85		
CIII-190.9	1908.73	H-8	3890.15	H-beta	4862.64	H-alpha	6564.61		
MgII-279.8	2796.35	NeIII-396.8	3968.91	OIII-495.9	4960.30	NII-658.4	6585.28		
OII-372.7	3727.09	H-epsilon	3971.20	OIII-500.7	5008.24	SII-671.6	6718.29		

124 emission lines (see, Sect. 3.1.2) using an ionization parameter range of $-4.0 < \log U < -1.0$ and six different gas-phase metallicities matching the stellar metallicities $(0.0001, 0.0004, 0.004, 0.008, 0.02, 0.05)$ with a 10 Myr ionizing spectrum based on Bruzual and Charlot (2003) SSPs. For the specific purposes of the mock sample catalog, we decided to create a sub-grid of HII-region models more appropriate to describe different objects based on those models already presented in Sec. 4.1. To develop this task, Patrice Theulé was in charge of producing the HII-region models using CLOUDY. I was in charge of coupling these models to the nebular module inside CIGALE and disconnecting the gas-phase metallicity from the stellar metallicity in the code. Models were cut to cover from the well-known Lyα line at 1215.67 Å to the [ArIII] transition at 7137.80 Å containing a total of 26 emission lines and listed in Table 6.2. This particular set of emission lines was the fruit of an arduous discussion with the different researchers in the MOONS consortium and especially in the TG-WG7. The wavelengths are given in vacuum to be consistent with current instruments such as the Multi-Unit Spectroscopic Explorer (MUSE). Some common lines were treated as singlets instead of doublets (i.e., [OIII]λ1660, [CIII]λ1907, [MgII]λ2803, and [OII]λ3729) while others were not included in the modeling (i.e., [NeIV]λ2422, [NeIV]λ2424, and [NeV]λ3426). Including these lines will be addressed in future versions of the photoionization modeling.

Particularly, Bruzual and Charlot (2003) models needed to be shifted to vacuum

wavelengths to be consistent with the implemented HII-region modeling presented in Sect. 6.2.2 based on current spectroscopic rules for different MOS. These models are given in vacuum wavelengths below 2000 Å and above this limit they are reported in air wavelengths. To be fully consistent, we use the Ciddor (1996) method which is widely implemented in python libraries like Astropy [3] and other Astronomy libraries used in IDL [4] to convert wavelengths 2000 Å to vacuum before producing any mock catalog. The version of CIGALE in which I modified the nebular module is not available to the public yet but in a future release, most of the modifications will be included.

6.3. Simple model spectra for calibrations

As briefly introduced in Sect. 6.1, we produced a simple motivated mock sample using CIGALE. To create this sample, we just focused on three different types of galaxies: i) early-type galaxy, ii) late-type galaxy, and iii) a starburst galaxy. We use a delayed SFH as described in Boquien et al. (2019). Each galaxy is created with a different set of parameters of the age of the main stellar population (i.e., age_{main}) and its e-folding time (i.e., τ_{main}) as well as fraction of the burst, its age, and e-folding time (i.e., f_{burst}, age_{burst}, and τ_{burst}). A brief explanation of the input parameters is listed in Table 6.3.

Table 6.3. – Star-formation history input parameters. Each parameter used to model the SFH using a delayed recipe for the simple mock catalog is presented with a brief explanation.

Symbol	Description
τ_{main}	e-folding time of the main stellar population (Myr). Time it takes to turn M_{gas} into stars.
age_{main}	age of the main stellar population (Myr)
τ_{burst}	e-folding time of the late starburst population (Myr). Time it takes to turn M_{gas} into stars by the late burst model.
age_{burst}	age of the late burst model (Myr)
f_{burst}	mass fraction of the late burst population
IMF	initial mass function
Z_{star}	stellar metallicity from the SSP models (see, Bruzual and Charlot, 2003)
Z_{gas}	gas-phase metallicity
log U	ionization parameter
A^{ISM}	attenuation in the V-band of the inter stellar medium
A^{BC}	attenuation in the V-band of the birth cloud
μ	ratio of the attenuation suffered by ISM, and the ISM+BC (see, Charlot and Fall, 2000)
α	slope of the Dale et al. (2014) IR emission models

First, for the early-type galaxy, we set τ_{main} = 500 Myr and age_{main} = 5000 Myr. The parameters related to the burst are not used for this galaxy to be consistent with early-type galaxies not forming stars nowadays. Secondly, in the case of the spiral-disk galaxy, we set τ_{main} = 10000 Myr, and age_{main} = 5000 Myr where the large tau_main allows the SFH to grow and reach saturation. Finally, for the starburst galaxy we use τ_{main} = 10000 Myr, age_{main} = 5000 Myr similar to the spiral-disk case but we add a burst setting age_{burst} = 50 Myr, $\tau_{burst} = 10^4$ Myr, f_{burst} = 0.1 which major impact is

3. https://www.astropy.org/
4. https://www.l3harrisgeospatial.com/Software-Technology/IDL

to reproduce recent star formation and increase the intensity of the emission lines. The SSPs correspond to those of Bruzual and Charlot (2003) in high-resolution as in CIGALE we have the choice to use the default low-resolution or high-resolution. We set the IMF either to Chabrier or Salpeter at a solar stellar metallicity of 0.02. In CIGALE, we have access to other SPP models such as those of Maraston (2005) and an updated high-resolution version (Maraston and Strömbäck, 2011). I implemented in CIGALE the Maraston and Strömbäck (2011) models aiming to be used for MOONS as we needed a maximum resolution for the models to be downgraded by the pipelines while simulating observations. However, these models are not coupled to the nebular module inside CIGALE because no information on the Lyman continuum photon is provided which is a key ingredient to produce the lines inside the code. Also, Maraston and Strömbäck (2011) models are ELODIE-based covering an age range of 3/55 Myr to 12/15 Gyr over a wavelength range of 0.1/0.39 – 0.68 μm with a sampling of 0.2 Å (i.e., R~ 0.55 Å FWHM). Then the only information we obtain is the stellar continuum which in the particular case of Maraston and Strömbäck (2011) is wavelength limited. Maraston and Strömbäck (2011) were used to make decisions on the modeling strategy for MOONS, and in particular, they were shared with the working group to test outflows by Alice Concas.

The strategy was set to model continuum using Bruzual and Charlot (2003) and nebular emission with the updated HII-region models. The emission lines are modeled fixing the ionization parameter to $\log U = -3.0$ in CIGALE with a line width of 16 kms^{-1} which corresponds to a resolution of 0.7 Å valid for the MOONS wavelength range and resolution. Dust emission is models using Dale et al. (2014) templates with the α parameter fixed to 2.5. In terms of attenuation, we used the Charlot and Fall (2000) recipe in which we set the ratio of the attenuation in the V-band experienced by the young and old stars to $\mu = 0.3$, and the slope of the ISM and BC to -0.7, respectively. The attenuation in the ISM ($\mathrm{Av_{ISM}}$) was set to zero in the case of the early-type galaxy and to three different values $\mathrm{Av_{ISM}} = 0.2$, $\mathrm{Av_{ISM}} = 0.5$, and $\mathrm{Av_{ISM}} = 1.0$ for the spiral-disk and starburst. We refer to these three different attenuated models as low, mid, and high $\mathrm{A_v}$. Different parameters are listed in Table 6.3.

The output spectra from this exercise is the flux density as a function of wavelength presented in Fig. 6.1. It is worth noticing that if CIGALE is used to model spectra, the SFH is normalized such that the total mass of stars formed from the onset of the star formation to the last time step is always $1\mathrm{M}_\odot$. This translates to fluxes being normalized to the total mass. The different models using either high-resolution Bruzual and Charlot (2003) or Maraston and Strömbäck (2011) SSPs for the three types of galaxies with different values of attenuation are shown. The limit in wavelength for each one of the MOONS bands *RI*, *YJ*, and *H* are also presented. This simple mock catalog modeling is useful for test calibrations on how MOONS will perform for typical observations. In general, the models were used to constrain in first place photometric redshift distributions calibrating different $\mathrm{z_{phot}}$ software and methods, as well as setting limits for the magnitude limits for different types of galaxies. As the predictions

are based on idealized models, the outcome can be biased to very optimistic results. Therefore, more complete and robust modeling needs to be implemented, for example, modeling the spectra based on real observations derived from SED fitting (see, Sect. 7.1). This mock catalog is also useful to make decisions on the samples to be used in terms of redshift, stellar mass, magnitude, or any other parameter.

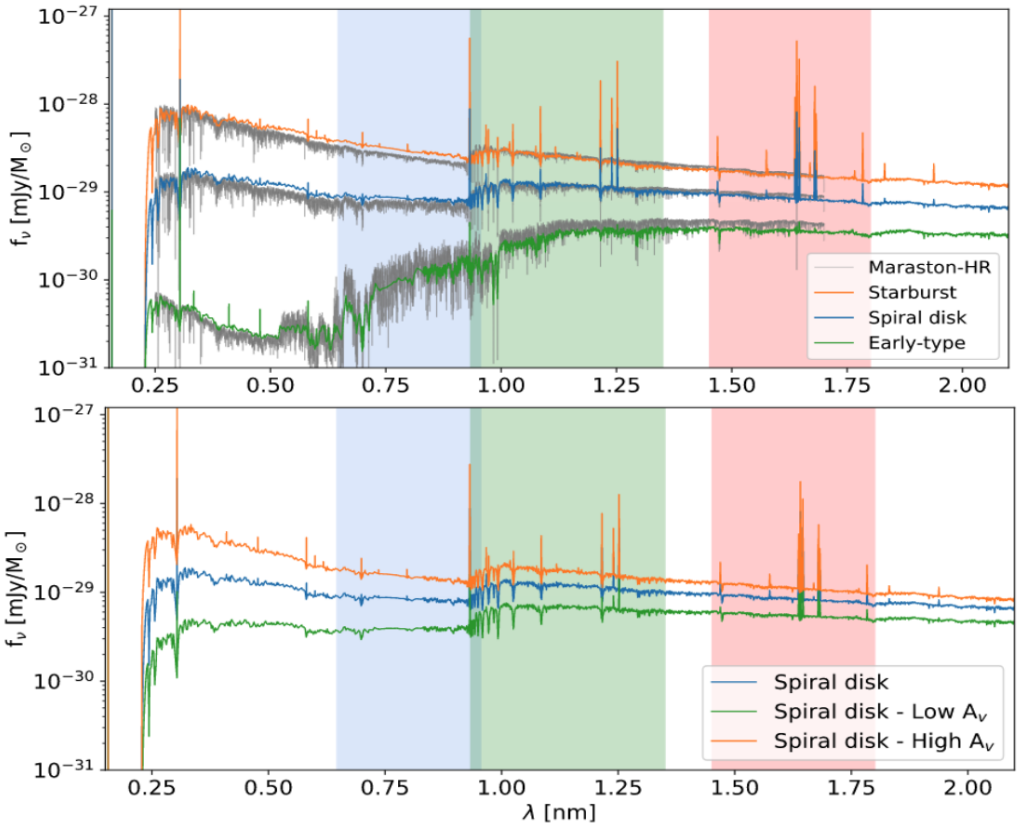

Figure 6.1. – Mock spectra modeled with CIGALE. Two different output data sets for the mock catalog at z = 0 are presented. In the upper panel, the high-resolution spectra for the Maraston and Strömbäck (2011) models are drawn in gray for an early-type, spiral disk and starburst galaxy. The output obtained using high-resolution Bruzual and Charlot (2003) models along with emission lines is shown in green, blue, and orange for the same types of galaxies. The lower panel shows the modeled spectra as obtained using the Bruzual and Charlot (2003) high-resolution models for the spiral disk galaxies with three different values of the attenuation $Av_{ISM-low}$ = 0.2, Av_{ISM} = 0.5, and $Av_{ISM-high}$ = 1.0 in green, blue, and orange respectively. The same output is obtained for the starburst galaxy with three different values but it is not presented in this figure. The blue, green, and red shaded areas correspond to the MOONS bands *RI*, *YJ*, and *H*.

6.4. ETC production of models

The production of mock samples is the first step in the generation of models useful for MOONS. The spectra created with CIGALE need to be translated into 1D-spectra format compatible with MOONS simulators. Currently, there are a couple of simulators whose final goal is to treat the mock/real spectra and generate templates that can be passed through the Exposure Time Calculator (ETC) to obtain accurate simulations on how MOONS observations will look. This tool was developed by Oscar Gonzalez and it remains the official tool for the survey's planning as well as for the exposure calculations. It was updated to the latest performance of the instrument. The VIRTUAL MOONS simulator is a raw simulator created by Gianluca Li Causi which can generate science and raw calibration raw frames. This is used to test the Data Reduction Software (DRS) but also to perform science simulations. The second simulator is the MOONS 1D spectra simulator created by Myriam Rodrigues and Vivienne Wild to generate and reduce science spectra. This is used to test the science pipelines as the spectra are in the MOONS format. These two simulators are in charge of processing the simulated sources produced either from catalogs or from random distributions as I explained in previous sections (cf Sect. 6.1 and Sect. 7.1). The basic scheme flow is presented in Fig. 6.2. The ESO sky model from Noll et al. (2012) is used in the ETC and the Source Simulator. The mock catalog, either modeled with CIGALE or with any other tool can be passed through these simulators to generate templates that can be analyzed for scientific purposes.

The mock spectra simulated with CIGALE are not in the right format for the 1D-spectra simulators. First, we need to interpolate our CIGALE output because the resolution along the wavelength axis varies according to the Bruzual and Charlot (2003) SSPs. The sampling at the MOONS resolution and wavelength range of R = 8000 – 18000 and $\lambda = 0.72 - 1.6$ Å corresponds to 0.23 – 0.35 Å. Then, we interpolate with a spacing of 0.23 Å to guarantee that the spectra are sampled at a good resolution for MOONS using the python library spectrum from *pysynphot* which conserves the flux. The output flux is given in units of erg cm^{-2} s^{-1} Å^{-1} and the wavelength in Å. This output is transformed into a 1D-spectra using the python library pyasl from *PyAstronomy*. The final structure of the file is shown below:

```
header      = {"CODE":'CIGALE / Simulation Code',\
               "MTYPE":'Galaxy',\
               "MNAME": 'Galaxy_Name / Model Name',\
               "R":2200.0,\
               "SAMPLING":0.23,\
               "V_disp":0.0,\
               "TUNIT1":'Angstroms',\
               "TUNIT2":'erg/s/cm2/A',\
               "LAMBDA0":5445.00}
```

Once the mock spectra are translated into the right 1D-spectra format they are ready

to be passed through the simulators, and final templates are created. The results from the simulation process are distributed to the working groups in MOONS to perform analysis on emission line fluxes, spectral fitting, redshift determination, to study outflows, among others. The creation of 1D-spectra is general and can be used to simulate samples for any other instruments besides MOONS if one changes the resolution and adapts the spectra to their simulators. If this is the case, a more general database from real data needs to be included to be used for simulations. This is the subject of the next chapter.

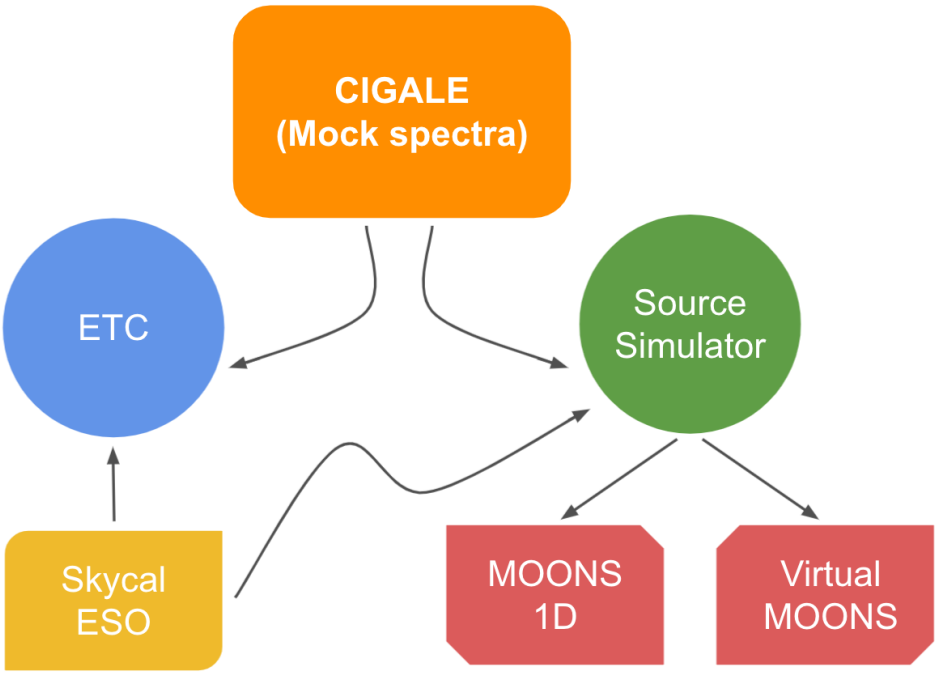

Figure 6.2. – Simulation tools flow chart. The mock spectra created with CIGALE in our case or with any other tool are passed directly to the ETC and the source simulator. Both contain the ESO sky model (Noll et al., 2012). Once the sources are treated by the Source Simulator, they can be used in the MOONS 1D spectra simulator or in Virtual MOONS to obtain final reduced science mock spectra. The figure is inspired by a figure presented by Myriam Rodrigues at the MOONS consortium science meeting.

7. Model spectra of COSMOS sources

Contents

7.1. Mock sample based on COSMOS galaxies

In the last section, I created a mock sample of spectra for canonical galaxies based on a set of ad-hoc values for the SFH, the nebular emission, and dust absorption and re-emission. The goal was to provide a sample of galaxies as reliable as possible to study how the observed spectra with MOONS will look in the future. However, these objects do not faithfully represent the different galaxy types that we can find in the Universe. Due to this, we decided to create mock samples based on observations to build up a more representative catalog, or at least, that traces a real sample of galaxies with reliable distributions of the physical parameters. This catalog is aimed to be used to test scientific cases.

To create this mock catalog based on observations, we chose the COSMOS field because in Part II it was already widely studied, and it also has well-known photometric and spectroscopic information. Additionally, because this field is one of the three main fields MOONS will be observing. The strategy was to fit the SEDs covering UV-to-MIR photometry from the Laigle et al. (2016) COSMOS2015 catalog and retrieve the modeled photometric fluxes and emission lines fluxes. However, producing emission line fluxes is difficult if no emission line is fitted as the ionization parameter and gas-phase metallicity cannot be constrained. The empirical relation of Curti et al. (2020) to obtain the gas-phase metallicity was applied to narrow the possible value range in the same fashion as in Part II to lately perform SED fitting in gas-phase metallicity bins. To constrain the ionization parameter, some tests are explored, either setting the value to a commonly accepted range or fixing it to a single value. I discuss the pros and cons of fixing or leaving free the ionization parameter. I produced the SEDs and derived physical parameters such as the stellar mass and SFRs which can be compared to reported values in COSMOS2015. The photometric fitting of SEDs, the emission line modeling choices, and the production of a final catalog based on real observation are described in the next sections.

7.2. UV-to-MIR continuum fit

The work presented in previous sections (cf. Part II) was carried out to study emission-line galaxies in the COSMOS field. This field is well-known and has information covering multi-wavelength data and spectroscopic information for a large number of sources. To model galaxy spectra (i.e., mock samples) based on real data, we decided to start with the original sample of the COSMOS2015 catalog (Laigle et al., 2016) and the FMOS-COSMOS survey (Kashino et al., 2013; Silverman et al., 2015). This is motivated to have a way to compare the SED fitting results with classical relations used to derive physical parameters such as the SFR in terms of the Hα emission line. The photometry is available for half a million objects, and the emission line fluxes for 5484 sources. The main difference between this sample of galaxies and the one used in Part II relies on the fact that I do not perform any selection based on the

SNR of the emission lines. Also, I do not use the HELP database for the FIR as the goal is to fit only COSMOS2015 UV-to-MIR photometry. Matching the COSMOS2015 and the FMOS-COSMOS survey catalogs leads to a sample of 2508 sources. This sample has a total of 1678 sources with valid Hα measurements with 1552 of them having a SNR > 3. The UV-to-MIR SED fitting process is carried out for the 2508 sources using the photometric redshift reported in the COSMOS2015 catalog. Not including spectroscopic data leads to a larger sample of objects however this is a first step to create a sample to compare the quality of the modeling with CIGALE. The fit of the entire COSMOS2015 catalog will be included in a future analysis to have a more general catalog for the Astronomy community. The spectroscopic fluxes will not be fitted, only the photometry. Be aware that the sample is selected to have emission-lines which can bias the sample to young/active galaxies.

As mentioned before, to fit the UV-to-MIR photometry, and to simulate the continuum and emission lines, we need to constrain the parameters related to the nebular emission (i.e., gas-phase metallicity and ionization parameter). In Part II, I fitted photometry and Hα fluxes in a first run, and after I included the Hβ, and [OIII]λ5007 emission. This puts constraints on the ionization parameter. However, I had to restrict the gas-phase metallicity range as no information on lines sensitive to this parameter was included. Similar assumptions need to be used here as we fit only photometry and this does not put constrains on the quantities governing the ISM physics. In the next sections, I address the different choices on restricting the gas-phase metallicity and the ionization parameter to reliably reproduce the intensity of the emission line in the modeled spectra.

7.2.1. Emission line modeling choices

Modeling spectra with both continuum and nebular emission from real observations need to be carried out carefully. First, the continuum will be based on the broadband photometry used in the SED fitting. Secondly, the nebular emission will depend on the physical parameters of the ISM that we need to be set before the SED fitting. As no emission lines are involved in the SED fitting process, we need to constrain somehow a priori the gas-phase metallicity and ionization parameter to reproduce accurate emission lines for a given object. Currently, there are several relations proposed in the literature to obtain the gas-phase metallicity of an object in terms of the stellar mass and/or the SFR (e.g., Pettini and Pagel, 2004; Mannucci et al., 2010; Andrews and Martini, 2013; Zahid et al., 2017; Sanders et al., 2021; Sanders et al., 2020; Curti et al., 2020) as discussed in Sect. 3.3.1. It is paramount to have good estimates of these parameters to compute properly the gas-phase metallicity. Contrarily, for the ionization parameter, the situation is a bit more complicated because this parameter is hard to measure from observations. A relation proposed by Carton et al. (2017) allows obtaining the ionization parameter in terms of the gas-phase metallicity of the objects. Although Pérez-Montero (2014) does not propose a direct relation, in their work, they explore the dependence of the ionization parameter with oxygen abun-

dance in nearby galaxies finding that the strength of log U increases with decreasing metallicity. These results are confirmed by Topping et al. (2020) in a high-redshift sample which implies that the variation of the ionization parameter with gas-phase metallicity is invariant with redshift. A more complex modeling using the diagrams reported in Pérez-Montero (2014) can be carried out in the future.

Taking into account the current status to obtain the gas-phase metallicity and ionization parameter for a given sample, we decided to use the relation of Curti et al. (2020) to derive gas-phase metallicities based on SFR and stellar mass as done in Part II. For the ionization parameter, we restrict it to a range of values around the one obtained using the relation from Carton et al. (2017). The scheme of the process is presented in Fig. 7.1. I fit the SEDs of galaxies using UV-to-MIR to estimate the SFR and stellar mass. I compute the gas-phase metallicity, restrict the range, and re-fit again, either leaving the ionization parameter free or fixing it to the value derived using Carton et al. (2017) for each metallicity bin. Leaving the ionization parameter to vary in a wide range is not suitable because the only-continuum fit cannot constrain this parameter. Therefore, we introduce a 0.2 dex variation to the value predicted by the Carton et al. (2017) relation just to give some flexibility to the models.

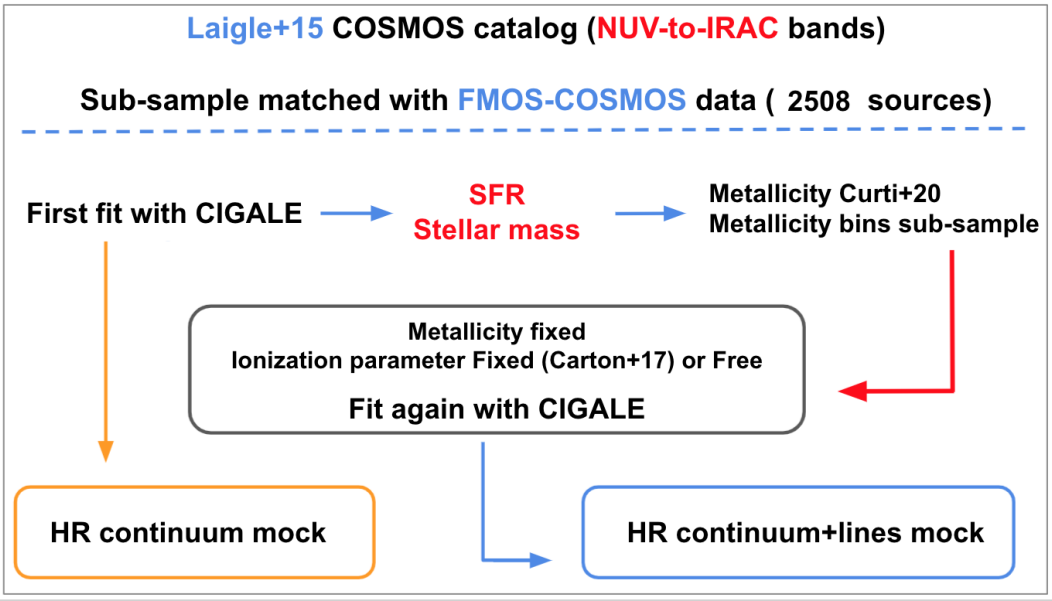

Figure 7.1. – COSMOS field mock catalog. The chart represents the scheme followed to produce the mock catalog from COSMOS field real observations. A sample of 2508 objects is fitted with CIGALE to obtain SFR and stellar mass estimation. These values are used to retrieve the gas-phase metallicity and ionization parameter range based on Curti et al. (2020) and Carton et al. (2017) relations. Two sets of mock catalogs are produced. One mock catalog with continuum emission and the other with continuum+nebular emission. Only photometry is fitted with CIGALE in both cases.

7.2.2. Modeling analysis

The COSMOS2015 catalog provides information on the stellar mass and the SFR of the objects derived using SED fitting. This is useful as I can compare with their values to see how well we can reproduce with CIGALE these parameters before refitting the data set with a fixed metallicity and fixed and/or free ionization parameter (see, Fig. 7.1). The SFR reported in Laigle et al. (2016) given the uncertainty in the template fitting is not recommended to be used so we focus our discussion on the stellar mass estimates. Their SED fitting process was carried out using a combination of exponentially declining and delayed SFHs with two different stellar metallicities (e.g., solar and half solar) for the SSPs and Chabrier (2003) IMF. the Calzetti and $\lambda^{0.9}$ attenuation laws are used to correct for dust effects. Their fits are based on optical photometry. Based on the previous information, we fit our objects' UV-to-MIR photometry with a delayed SFH, Chabrier (2003) IMF at solar metallicity, and Calzetti attenuation curve (i.e., $E_{(B-V)\ \mathrm{factor}} = 0.44$, ratio between the lines and continuum inside CIGALE). The results are presented in Fig. 7.2 where I compare the estimated stellar mass derived with CIGALE to those reported in the COSMOS2015 catalog.

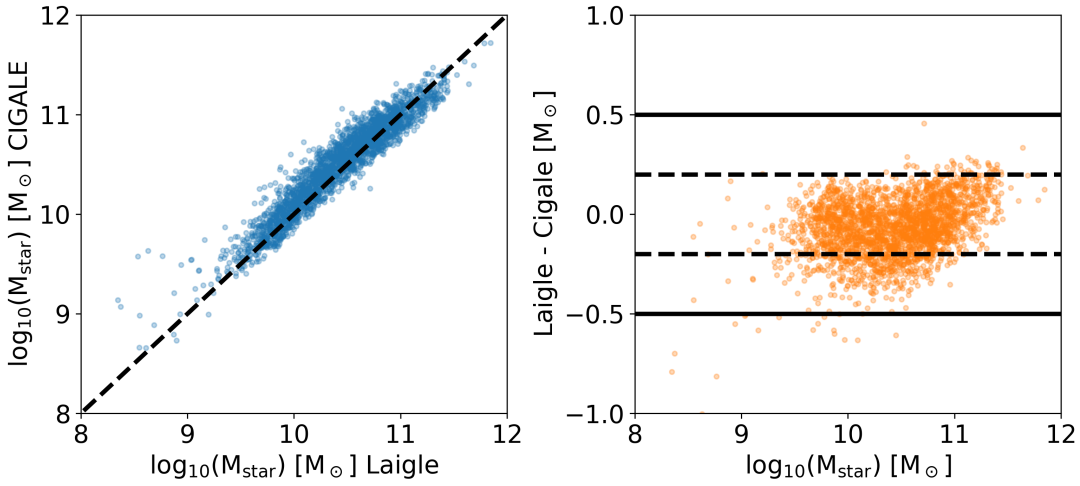

Figure 7.2. – Stellar mass comparison. We compare results from the photometric UV-to-MIR SED fitting with fixed gas-phase metallicity using CIGALE and the values reported from COSMOS2015 catalog of Laigle et al. (2016). The black dashed line represents the 1:1 agreement. In the right panels, the difference between the reported values in the catalog and my fit is shown as a function of CIGALE-derived values. The horizontal lines show 0.2 dex and 0.5 dex difference, respectively.

A good agreement is expected for the stellar mass estimates as this parameter is easily constrained by the broadband photometry. As seen in Fig. 7.2 differences between both estimations are well within 0.2 dex. Our estimation of stellar masses from the SED fitting is in agreement with values presented by Laigle et al. (2016) and

both are correlated. From our fits we obtain also the SFR for our objects. Although it was already stated that the COSMOS2015 reported values should not be used, I will briefly compare these results using the SFR-M_* plane before studying the quality of the our SFR estimates.I showed in Part II of this thesis that including IR information is paramount to derive good estimates of SFR as this parameter is highly affected by dust obscuration. Thus, the quality of the estimated SFR depends on the photometric bands used for the SED fitting. Not including a burst in the delayed recipe and using the Calzetti et al. (2000) recipe as done in Laigle et al. (2016) to correct for dust effects is expected to have also some impact on the results. In Fig 7.3, I present the SFR-M_* plane obtained from Laigle et al. (2016) in the left panel and from our analysis in the right panel. Our objects are more consistent in terms of redshift with the main-sequence of Schreiber et al. (2015) probably because we fit UV-to-MIR continuum photometry and not only the optical bands as in the COSMOS2015 catalog.

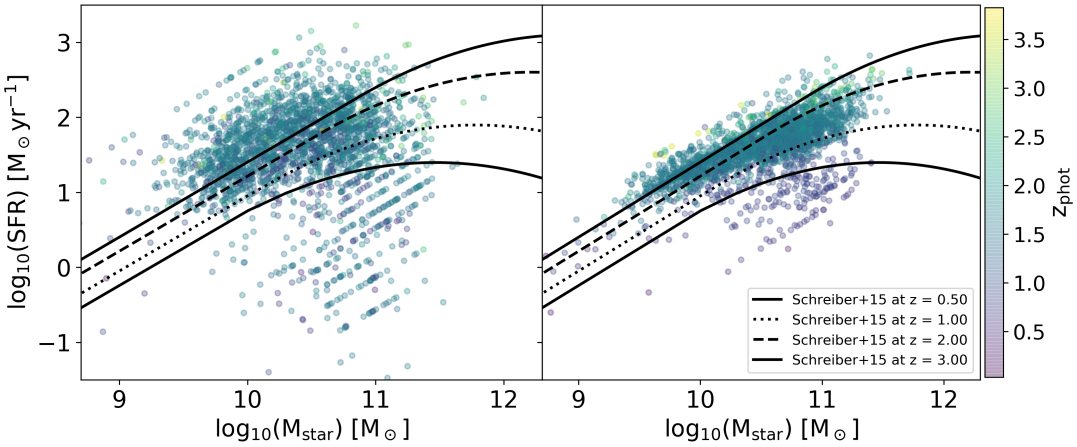

Figure 7.3. – Stellar mass and SFR plane. In the left panel, the stellar mass and SFR plane is presented for the data obtained from Laigle et al. (2016) color-coded by photometric redshift. In the right panel same results are shown for the estimates using CIGALE. The lines correspond to the Schreiber et al. (2015) main-sequence relations evaluated at a given redshift.

To test the reliability of the estimated SFR, we use the observed FMOS-COSMOS Hα flux measurements to compute the SFR(Hα). No cut is performed on the Hα in terms of SNR. In the first place, I verified that correcting the observed line emission using the Calzetti et al. (2000) starburst attenuation curve leads to differences at the high-luminosity because the attenuation is underestimated. In Sect. 3.1.3, it was shown that emission lines cannot be corrected using this curve. Therefore, I correct the observed Hα emission line fluxes using the Cardelli, Clayton, and Mathis (1989) curve and the $E_{(B-V)}$−lines factor derived with CIGALE. Dust-corrected Hα-luminosities are calculated and the SFR is obtained using the Kennicutt (1998) relation. The results are presented in Fig. 7.4 where the SFR rate inferred from Hα-corrected luminosities is compared to the values estimated with CIGALE from the continuum fitting. The

agreement is satisfying and well reproduced for the bulk of the objects.

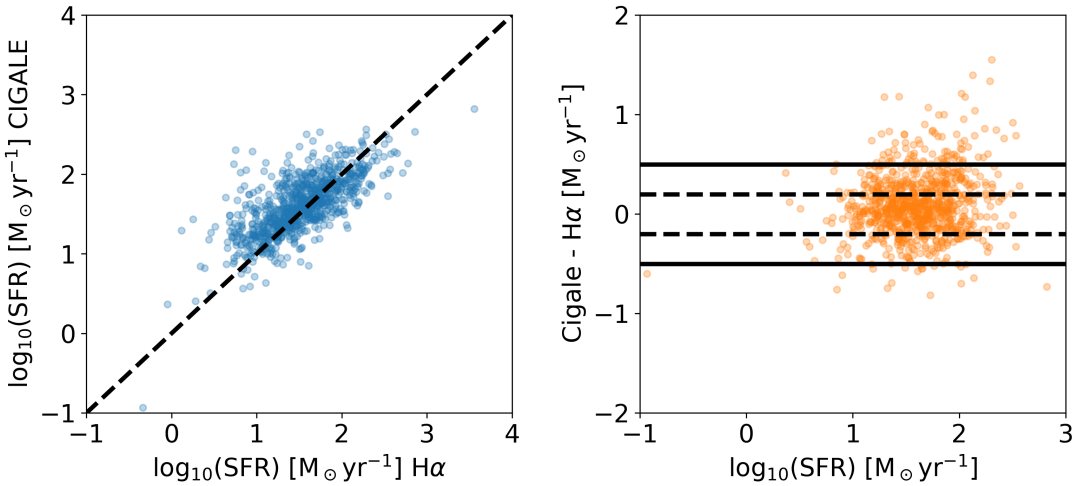

Figure 7.4. – Stellar mass and SFR comparison. SFR inferred using the Hα emission line corrected for dust effects is compared to the values obtained with CIGALE and those reported in Laigle et al. (2016). The dashed line on the left represents the 1:1 relation. The 0.2 dex and 0.5 dex limits are shown in the right-side figures.

Estimated parameters using CIGALE can be trusted as they are in agreement with the stellar mass and SFR plane based on the main-sequence location at each redshift but also because they are consistent with SFR derived using the Hα line. Discrepancies between values reported in COSMOS2015 are expected because in their SED fitting analysis only optical photometry was included. A more detailed study is being carried out to fit a larger sample of galaxies using a delayed SFH with a burst and the Charlot and Fall (2000) recipe to correct emission for dust effects like it was presented in Part II of this thesis. This work is essential and will lead to a better modeled mock spectra sample for the MOONS collaboration in the future and for the entire community as the goal is to create models for the entire COSMOS field.

7.2.3. Excitation diagram checks

Once the strategy is set, we can proceed to predict the emission line fluxes in the SED fitting using UV-to-MIR photometry. We can model any emission line available in the CIGALE database. To do this, the CIGALE file containing the photometry needs to include also column names referring to the emission line and their errors. As they are simple predictions from CIGALE and not actual fits of fluxes, we can set all the values in the column to a default number (i.e., −9999.99) which is not going to be taken into account in the fit but for the outcome of a modeled line. We model a total of 26 emission lines as listed in Table 6.2. I explained before that part of the strategy

is to fix nebular parameters. However, the ionization parameter is not so easy to set. To check the influence of letting the ionization parameter be free or fixed in the SED fitting process I run CIGALE leaving the ionization parameter to vary in a small range around the value predicted from the relation of Carton et al. (2017) and a run fixing it to a standard value of $\log U = -2.0$. The results are shown in Fig. 7.5 where the BPT excitation diagram is presented. The fixed case shown on the right shows a tight distribution as expected because both the ionization parameter and the gas-phase metallicity are fixed not letting the models cover a large region in the parameter space. However, for the case in which we let the ionization parameter vary in a small range as in the left panel, galaxies can occupy a larger zone in the parameter space. The idea in this work is to reproduce as faithfully as possible the expected emission line fluxes for a given population of galaxies. Therefore, leaving the ionization parameter to vary in a small range around the value predicted from the Carton et al. (2017) relation is the best compromise. However, it is important to highlight that one can simply use arbitrary values for both ionization parameter and gas-phase metallicity, and create mock samples covering a determined area of the BPT diagram not necessarily linked to real physical conditions matching the observations.

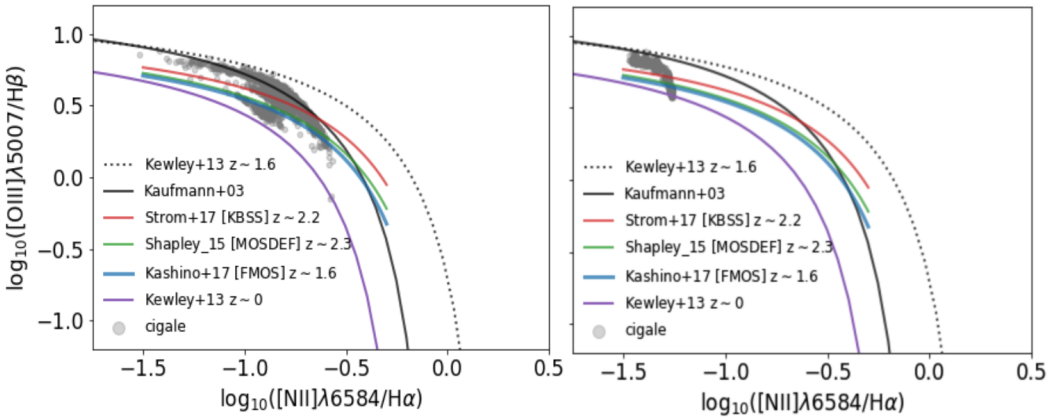

Figure 7.5. – Baldwin–Phillips–Terlevich (BPT) [OIII]λ5007/Hβ versus [NII]λ6584/Hα excitation diagram. The solid black line corresponds to the Kauffmann et al. (2003b) relation and the dashed-black line corresponds to Kewley et al. (2013a) evaluated at z ~ 1.6. The curves of Shapley et al. (2015), Kashino et al. (2017), and Strom et al. (2017) are shown in green, blue, and red, respectively. The purple line represents the local-universe locus of galaxies as shown by Kewley et al. (2013a). The diagram on the left shows the results on the emission line modeling if the ionization parameter is left to vary in a given range of values. The right panel shows the results if the ionization parameter is fixed to a single value.

Although leaving the ionization free to vary in a small range gives us more flexibility, we are aware we cannot constrain this value with SED fitting without information on emission line fluxes. As part of the upcoming work with the CIGALE team and

the MOONS collaboration, we plan to treat this in a more appropriate fashion to choose the correct range of the ionization parameter. Some ideas are to use the Pérez-Montero (2014) relation between the ionization parameter and gas-phase metallicity to model the dispersion in log U based on Monte-Carlo simulations of their reported distributions. This will lead to a more accurate modelization of the intensity and ratio of emission lines.

7.3. Production of spectra

In the last sections, I addressed the main characteristics and assumptions made to model a realistic mock spectra catalog based on COSMOS galaxies. The final results from this modeling are the SEDs (i.e., spectra at the resolution of the SSPs) containing continuum and emission-line information. A similar process to create files in 1D-format suitable for the MOONS ETC and the available simulation software as described in Sect. 6.4 was carried out. In Fig. 7.6 an example for a couple of objects is presented. The upper panel shows the continuum for five different objects spanning over a redshift range of $0.69 \leq z \leq 1.64$. Multiple features for different types of galaxies can be observed in MOONS low-resolution and high-resolution bands shown as colored and gray shaded areas. In the lower panel, the continuum and nebular emission is shown for three different objects covering a redshift range of $1.46 \leq z \leq 1.64$. Although this modeling is performed only on a sample of 2508 objects, the main idea is to fit the vast majority of objects in COSMOS2015 catalog and produce mock samples for continuum-only, and continuum+emission lines for real objects. This can be used to predict how well MOONS will perform in the future, or any other MOS facility.

Two different catalogs are distributed to the MOONS team. A first catalog containing only continuum information which serves as a standard catalog in which every researcher can add on top emission lines using their favorite recipe. This was primarily used to add outflows. The second catalog corresponds to continuum and emission-line information based on HII-region models from CLOUDY included in CIGALE with all the different characteristics described above for the lines. These two catalogs represent a first attempt at producing realistic spectra to help instrument characterization. Future work will lead to the production of a more complete sample that can be freely distributed for scientific purposes.

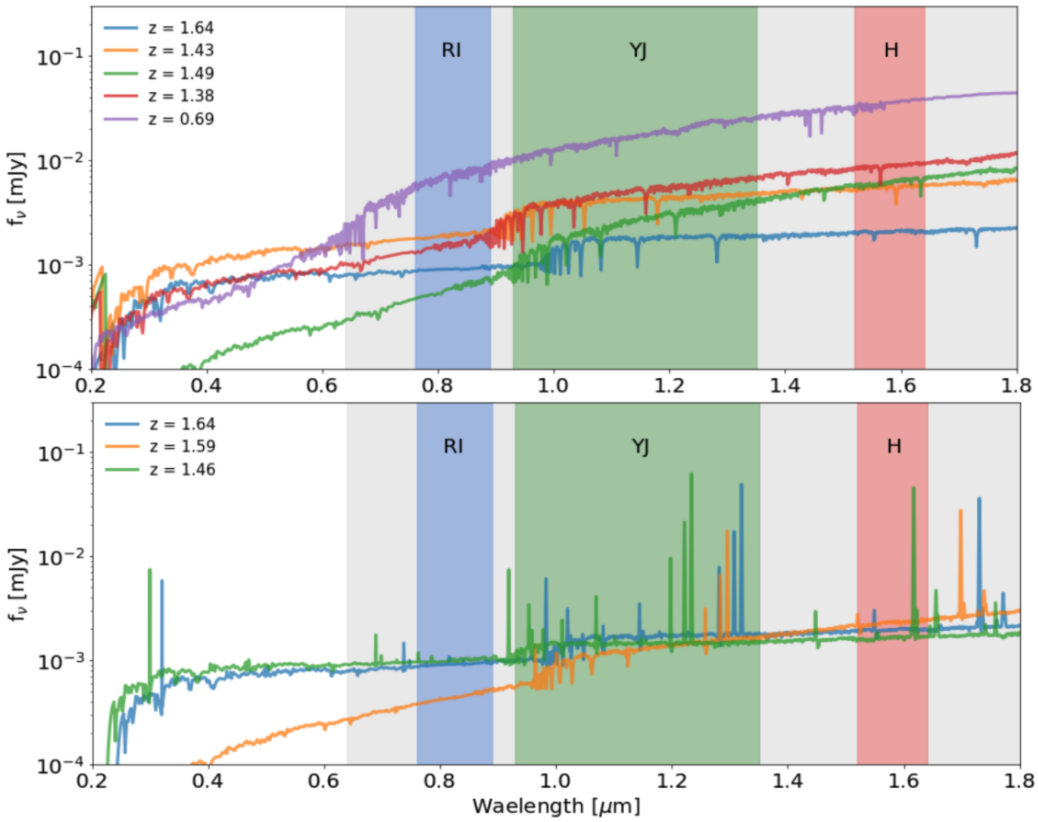

Figure 7.6. – Mock spectra modeled with CIGALE based on real COSMOS field observations. The upper panel shows the stellar continuum model for five different source between $0.69 \leq z \leq 1.64$. The lower panel shows continuum and emission lines for three objects between $1.46 \leq z \leq 1.64$. Fluxes are not normalized to the total mass as in Fig. 6.1. The blue, green, and red shaded areas correspond to the MOONS bands *RI*, *YJ*, and *H* in high-resolution mode while the gray shaded area is the low-resolution model.

7.4. Summary and Conclusions

In this work, I perform spectra modeling using CIGALE to create mock catalogs for the MOONS scientific teams. As part of the science working groups, I created two different types of mock catalogs. A first, simple catalog based on canonical characteristics to create three different types of galaxies (i.e., starburst, late, and early type). These models were used as a first attempt for the collaboration to test the simulation software, and also for redshift determination and magnitude limit calculations. Some work was also done on emission line flux measurements. As a second step, I created mock spectra based on UV-to-MIR photometry SED fitting of 2508 COSMOS observed galaxies using the COSMOS2015 catalog of Laigle et al. (2016). Different assumptions are made in order to constrain the ISM parameters as the gas-phase metallicity (e.g.,

Curti et al., 2020) and ionization parameter (e.g., Carton et al., 2017). This is crucial to model correctly the intensity of the emission lines as well as the respective emission-line ratios.

Although this is still ongoing work, first, we produced catalogs that can be used for the community to test the simulation software. These preliminary results allow the community to have a spectra sample with good resolution to test codes and verify workflow of different pipelines in future instruments like MOONS, but not only as the models are flexible enough to match characteristics of any other instruments. More work will be carried out to complete the creation of models on a larger sample of galaxies using the entire half-million sources reported in the COSMOS2015 catalog and probably in other important fields.

Conclusion and future prospects

Contents

8.1. Overview of results and conclusions

In this thesis work, I showed the results of two different projects I carried out at LAM as part of my doctoral studies. A first work concerning spectro-photometric SED fitting of galaxies investigating emission lines, dust attenuation, and SFRs. A second work on a simulation project using CIGALE to create mock spectra catalogs as part of the MOONS collaboration.

For the spectro-photometric SED fitting work in Part II, I fitted simultaneously photometry and emission-line fluxes with CIGALE in the Cosmic Evolution Survey (COSMOS) field. I used photometry from Laigle et al. (2016) and HELP database, and emission line fluxes from the Fiber Multi-Object Spectrograph (FMOS-COSMOS) survey (Kashino et al., 2013; Silverman et al., 2015). A sample of 183 objects was selected to have flux measurements of both Hα and [OIII]λ5007 at S/N > 3 in the FMOS-COSMOS survey at 1.40 < z < 1.68. In a first run, I performed SED fitting on this sample covering UV-to-FIR continuum emission with 21 broad-band fluxes and Hα emission line fluxes. The conservation of the energy budget by CIGALE allows us to get robust estimates of the amount of dust attenuation as well as the stellar mass and SFR. I propose in Part II of this thesis a relation to obtain the attenuation of the [OIII]λ5007 emission line in terms of the stellar mass. This was motivated because a positive correlation was found between both parameters, and a similar approach already exists for the Hα emission line. Median values of the emission line attenuation $A_{H\alpha} = 1.16 \pm 0.19$ mag and $A_{[OIII]} = 1.41 \pm 0.22$ mag are reported. The relative attenuation affecting different populations is characterized by the μ parameter in the attenuation law. I report a value of $\mu = 0.57 \pm 0.14$ consistent with different works in the literature and twice as large as compared to the original value proposed by Charlot and Fall (2000).

On the other hand, I confirm a positive correlation of the SFR and the dust-corrected [OIII]λ5007-luminosity. I propose two relations, one with a fixed slope and one with a free slope. These results are shown in Sect. 3.3. We measure a slope consistent with unity within the 2σ dispersion of the relation. We estimate a [OIII]λ5007/[OIII] 88 μm ratio of 1.90 for our sample of galaxies and deduce an SFR-[OIII] 88 μm relation in agreement with previous relations that were found at both low and high redshifts, although [OIII]λ5007/[OIII] 88 μm is strongly dependent on electron density and gas-phase metallicity. The SED fitting, including photometry, Hα, Hβ, and [OIII]λ5007 fluxes is also performed with a refined grid of photoionization models and metallicities estimated from the mass-metallicity relation from Curti et al. (2020). The variations of gas-phase metallicity and ionization parameter induce a dispersion in the SFR-$L_{[OIII]\lambda5007}$ relation of 0.24 dex and 1.1 dex, respectively. The lower impact of gas-phase metallicity is likely to be due to the limited range of our sample ($0.006 < Z_{gas} < 0.016$) and our relation of SFR-$L_{[OIII]\lambda5007}$ is expected to be only valid for galaxies of similar gas-phase metallicities as those studied in this work.

In Part III, the mock spectra sample creation using CIGALE as part of the MOONS collaboration was addressed. In the first place, I created a sample of galaxies based on simple assumptions of their SFHs to reproduce starburst, late-type, and early-type galaxies. The main idea was to use this sample to test MOONS simulation tools and to provide the scientific teams with modeled spectra to test the performance of their codes on different data sets. With the team, we decided to create a sample of mock data based on real observations. I chose to work on the COSMOS field because in Part II I already worked on this spectro-photometric sample but also because this is one of the three main fields that will be observed by MOONS. I perform UV-to-MIR SED fitting on a sub-sample of ~ 2000 of COSMOS2015 galaxies. This first attempt to produce realistic mock samples is not performed on the full half a million sources because I cross-matched the FMOS data to have a way to compare SED results with real emission line observations.

Important assumptions need to be made on the ISM parameters if we want to simulate realistic spectra through SED fitting only with photometric data. The ionization parameter cannot be constrained using only broadband emission, therefore some relations in the literature were tested to estimate this parameter based on gas-phase metallicity (see, 7.1). The gas-phase metallicity is also a main parameter that needs to be narrowed down. For this, I implemented the same approach as in Part II using Curti et al. (2020) relation which allows obtaining the gas-phase metallicity based on stellar mass and SFR. The creation of mock spectra data is a complex process in which one needs to be cautious on the assumptions made to be as close as possible to reality. Also because at intermediate and high redshifts there are well-known discrepancies on reproducing emission line fluxes through HII-region modeling.

To conclude, this work proposes novel relations between physical parameters of galaxies at intermediate redshift and the [OIII]λ5007 emission line. The combination of photometric and spectroscopic data in future SED analysis is paramount to put constraints on parameters related to the SFH and the attenuation. Spectroscopic information helps break degeneracies and allows to study galaxies in a more homogeneous fashion using SED fitting. The need of updating SED fitting software in terms of nebular emission models is critical to preparing future datasets from large spectroscopic surveys. Understanding the discrepancies in excitation diagrams at intermediate redshift remains crucial to properly model HII-region emission. This thesis is a first attempt to test how CIGALE performs as a SED spectro-photometric fitter but also as a spectra modeler. The future of SED fitting including emission lines is really promising.

8.2. Future perspectives

The study of galaxies involving multi-wavelength photometry along with spectroscopic information has proved to be a powerful way to derive physical parameters breaking degeneracies affecting results from SED fitting. I first highlight the future

upcoming large spectroscopic surveys such as MOONS, PFS, MOSAIC, and Maunakea Spectroscopic Explorer (MSE), and the role they will play in enriching the knowledge we have on galaxies at intermediate and high redshift. After this, I focus the discussion on the future of SED fitting codes and how they are being transformed to deal more efficiently with the data implementing machine-learning techniques. I address the importance of mock catalog simulations and I highlight which are the crucial parameters one needs to pay attention to carefully to produce reliable samples that can be used to plan future instrument observations.

8.2.1. Future Multi-Object Spectrographs

We are entering an era of large spectroscopic surveys in which frontiers expand towards cosmological realms. Multi-object spectrographs (MOS) on both ground and space missions will lead to unprecedented data sets enriching our perspective of galaxy formation and evolution with hundreds of millions of spectra. In Fig. 8.7, a scheme showing the wavelength coverage of different MOS facilities is presented on the top panel. MOONS, PFS, MSE, and MOSAIC will play an important role in providing information for galaxies at wavelengths larger than 1 μm (Takada et al., 2014; Sugai et al., 2015; Puech et al., 2018; Cirasuolo et al., 2020; Maiolino et al., 2020; Hammer et al., 2021). In particular MOSAIC, MSE and PFS will cover (Tamura et al., 2018; Puech et al., 2018; The MSE Science Team et al., 2019; Tamura and PFS Collaboration, 2021; Hammer et al., 2021) below 0.6 μm an important region known as the redshift desert lying at $1.4 < z < 2.5$. This is paramount to continue the following of this work presented in Part II and Part III, studying galaxies around the cosmic noon (i.e., $z \sim 2$) using emission lines. In particular at $z \sim 1.5$, MOSAIC, MSE, and MOONS will be able to observe the Hβ, [OIII]λ5007 emission lines as well as the Hα and the [NII]-doublet (see, Puech et al., 2018; The MSE Science Team et al., 2019; Tresse, 2019; Maiolino et al., 2020; Cirasuolo et al., 2020; Hammer et al., 2021). At this redshift, PFS will provide only information on the Hβ and [OIII]λ5007 emission lines (Tamura and PFS Collaboration, 2021). Information on the sulfur lines will be crucial to constrain abundances. MOONS is designed to work in the NIR and it will provide good measurements for our future work. This means that we will be able to constrain the ISM parameter of the sample presented in this thesis allows us to better model the HII-regions, potentially solve tensions existing in the excitation diagrams, and fit more emission lines along with photometry.

On the other hand, the multiplexing of an instrument gives a notion of how effective is the instrument to achieve different survey goals. As presented in Puech et al. (2018), MOONS, PFS, and MOSAIC will have around 1000, 2400, and 3500 multiplexes in patrol fields covering 500, 4500, and 5400 armin^2, with incredible high-resolution. The *étendue* of an instrument (telescope's aperture times the field of view) is useful to compare different facilities with the same size telescope's aperture. This parameter can be seen as the maximum beam of the instrument. MOONS, PFS, and MSE will be on 8 – m class telescopes so one can compare them based on their *étendue* as shown

in the lower panel of Fig. 8.7 along with the survey speed. MSE *étendue*/survey speed will be at least 20 (6) times larger/faster than one of the MOONS and 2 (3) times larger/faster than that of PFS (Tresse, 2019). The unprecedented aperture of the ELT gives MOSAIC also an incredible advantage on the survey speed being at least ~ 3 – 4 faster than any NIR ground-based MOS (Puech et al., 2018). The massively multiplexed MOS surveys and the complementary synergies between different instruments will open the door to a new era of NIR spectroscopy.

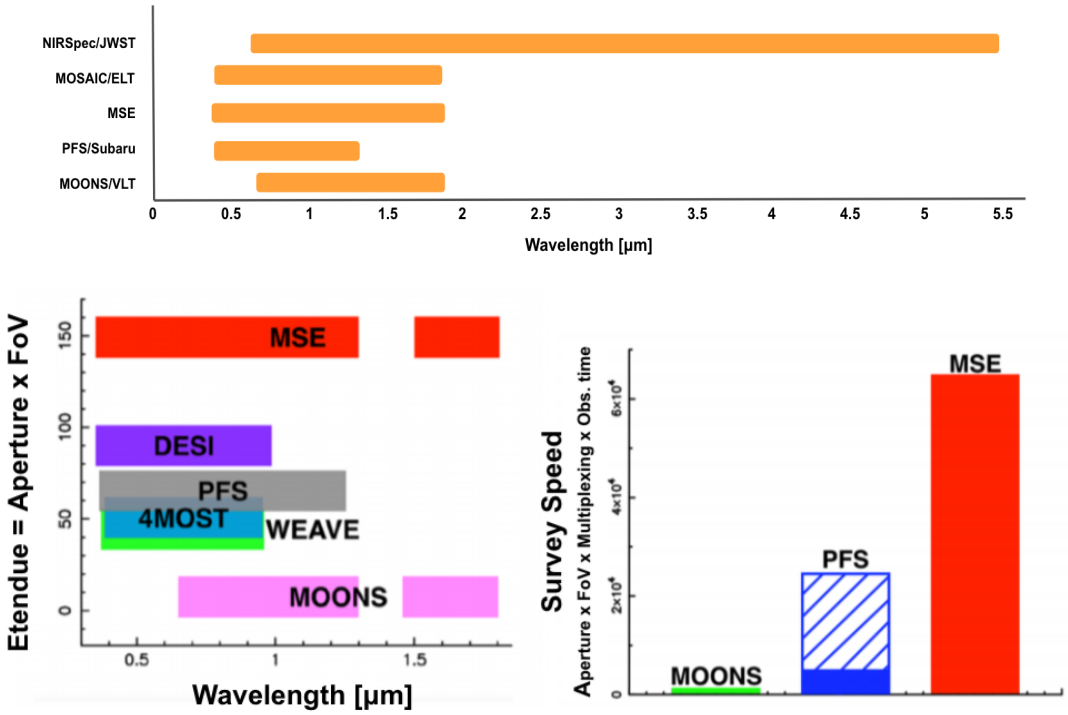

Figure 8.7. – Future MOS comparison. The figure shows the wavelength coverage for MOONS, PFS, MSE, and MOSAIC on the top panel. The lower panel is a figure composite from Tresse (2019) as presented in The MSE Science Team et al. (2019) showing the étendue for several MOS as a function of wavelength and the survey speed for MOONS, PFS and MSE.

This gives the possibility to study multiple emission lines and stellar features which are almost inaccessible nowadays with current instruments as redshift increases. On the other hand, in the case of JWST, it will not only have an outstanding coverage in terms of wavelength, but its sensitive instruments along with the unique observing modes will provide a new full parameter space to be explored for galactic and extragalactic Astronomy. Nowadays, we are extending the knowledge gained with MOS surveys to study nearby galaxies to investigate intermediate and high redshift. These new instruments will allow studying emission lines in the UV rest frame to investigate gas-phase metallicity, ionization origins of the gas, and chemical evolution Maiolino

et al. (2020) through Lyman continuum, Lyα, and CIII emission lines]. Optical emission lines covering from [OII]λ3727 to [SII]λ6716,31 will share valuable information on fundamental relations as the stellar mass-metallicity-SFR and it will allow studies as a function of redshift. As many instruments are pushing towards higher redshifts, this will provide novel datasets to study the Universe at a large scale.

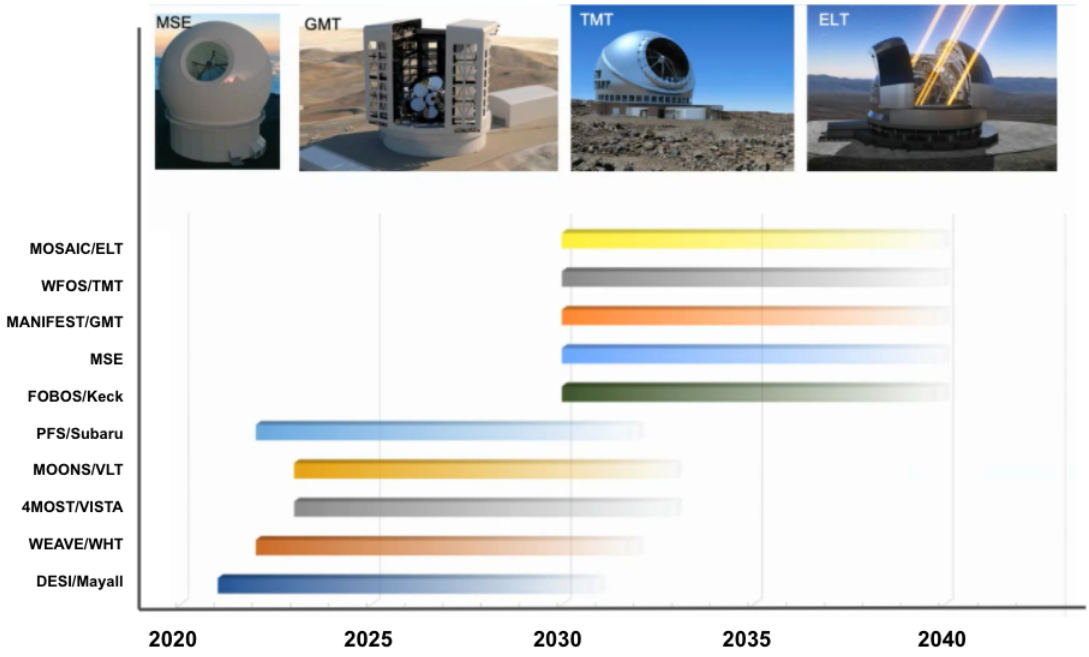

Figure 8.8. – Future MOS planning. The different telescopes where the MOS will be located are presented in this scheme as a function of the year. The image is modified and taken from Michele Cirasuolo's presentation at the Multi-Object Spectroscopy for Statistical Measures of Galaxy Evolution Workshop.

The majority of these MOS facilities are going to be located on ground-based telescopes (e.g., MOONS, PFS, MSE, MOSAIC). In Fig. 8.8, a timeline showing the telescopes under construction and the expected instruments timeline is shown. MOONS and PFS will provide valuable information in the NIR wavelengths before MOSAIC or MSE. This gives an advantage to both instruments respect other ground-based instruments. JWST on the contrary will be launched on the 22nd of December 2021 (previously scheduled to be lunched on the 18th) and will be operating giving the first results in 2022. Interesting science will be available very soon, which means that improving SED fitters to analyze spectro-phometric datasets is paramount. MOONS will provide valuable measurements for the work presented in this thesis. It will allow us to estimate the ISM physical parameters of our galaxies using spectro-photometric SED fitting. It will also help us to understand attenuation in the emission lines and SFR calibrations at cosmic noon.

8.2.2. Future of SED fitting codes

The SED fitting field is rapidly evolving and adapting itself to the current challenges in Astronomy. More precisely, the need of analyzing large datasets faster, including more information like emission line fluxes, automatizing the software including new machine-learning techniques, among others. As presented in Part I, SED fitting has been strongly based on analyzing continuum using photometry but until recent, emission line fluxes are being used along with photometry as current SED fitters (e.g., CIGALE, Bagpipes, BEAGLE, ProSpect, Prospector) implement HII-region model grids. Pacifici et al. (2012) proved how combining low-to-medium resolution spectroscopy along with the photometric data helped to better constrain the physical parameters, in particular, the gas-phase metallicity. Simultaneously fitting photometry and nebular emission allows to break the age-dust degeneracy reducing the uncertainties in dust attenuation and SFR estimates (Pacifici et al., 2012; Pacifici et al., 2015; Fossati et al., 2018; Buat et al., 2018; Corre et al., 2018; Yuan et al., 2019). Then, it is crucial to building accurate HII-region and PDR grids to reproduce the vast differences in nebular emission observed in galaxies at different redshifts.

On the other hand, estimating physical parameters using machine-learning techniques is getting very popular during the last decade. Although nowadays a full SED fitter based on machine-learning techniques is not available, some efforts have been put in investigating how to predict physical properties of galaxies, and how accurate they are as compared to SED fitting (Ball et al., 2008; Hogan, Fairbairn, and Seeburn, 2015; Masters et al., 2015; Sadeh, Abdalla, and Lahav, 2016; Dobbels et al., 2020; Simet et al., 2021). Also on testing new techniques to make current SED runtime faster at the moment of creating models, and comparing them to the observations (Grégoire Aufort's Ph.D. work on CIGALE at LAM). Machine learning can be divided into supervised and unsupervised learning. Supervised means learning from the input datasets and predicting the outcome while unsupervised learns and handles directly the input finding hidden patterns without human intervention. In the recent work of Dobbels et al. (2020), a prediction of IR fluxes for galaxies using the DustPedia and *Herschel*-ATLAS data, and applying supervised machine-learning algorithms showed that a significantly less scatter (e.g., 0.19 dex) can be obtained as compared to the UV-to-MIR energy balance SED fitting approach. Their method is based on neural networks (random forest led to similar results) using 14 UV-to-MIR input layers and obtaining six *Herschel*-target fluxes, and predicting dust luminosity (output layer). Simet et al. (2021) also proved that physical properties as stellar-mass and SFR can be obtained with a competitive degree of accuracy as SED fitting techniques using neural networks. Matching learning techniques can deal with more complicated patterns and incorporate extra information being computationally more efficient as compared to SED fitting once the method is trained (Dobbels et al., 2020; Simet et al., 2021). Nevertheless, although good accuracy can be achieved predicting galaxy properties from noisy simulated data shows that current machine-learning methods are not yet fully competitive (Simet et al., 2021).

CIGALE is joining the machine-learning fever to improve the model analysis computation time. The idea is part of the Ph.D. thesis of Grégoire Aufort as mentioned above. He is working on releasing a more efficient fashion of creating the SFH of galaxies implementing a deep neural network (AIS; Kappen and Ruiz, 2016; Bugallo et al., 2017, Adaptive Importance Sampling) to deal with the SFH and SSPs. At the moment CIGALE computes the SFH using a parametric or a non-parametric form and uses the SSPs in pre-computed files. The approximation of SFH using the AIS technique leads to a code 100 to 10^6 times faster. The deep neural network will be also implemented for the nebular module. At the moment in the official version of Boquien et al. (2019) the nebular models correspond to those of Inoue et al. (2014). The models created by Patrice Theulé and implemented by myself in this thesis work are not available for the public yet. Implementing the emission line database of Vale Asari et al. (2016) along with machine-learning will lead to "DeepCLOUDY", a more efficient and faster way of analyzing the nebular emission grids. This implementation will allow for interpolation between the space parameter of the lines without being restricted to pre-computed grids. Around 200 emission lines will be available. A scheme on where the machine-learning implementation of CIGALE is going to be put in place by Grégoire Aufort is summarized in Fig. 8.9. This will give access to a faster computation and comparison of the physical models to observations when fitting SEDs.

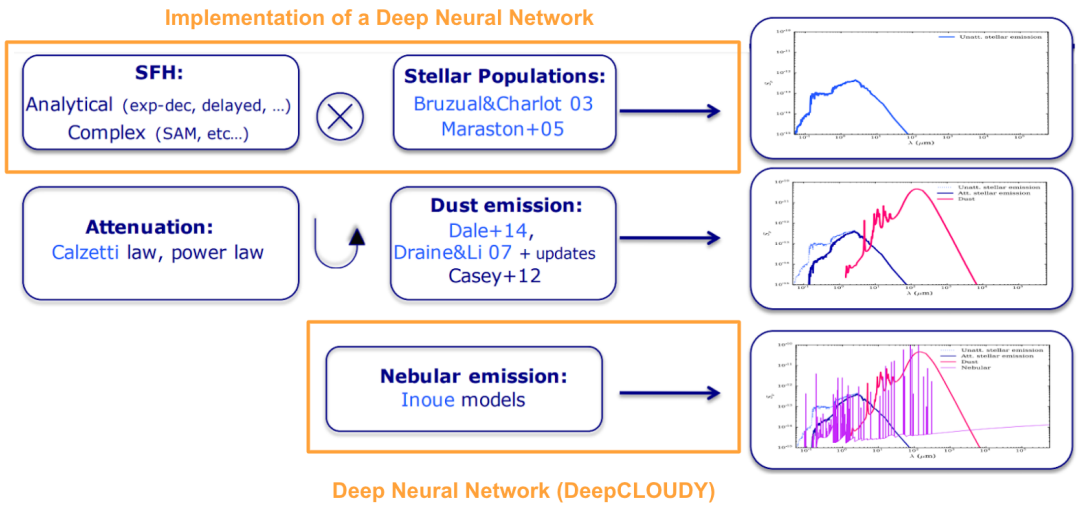

Figure 8.9. – Deep Neural Network implementation in CIGALE. The scheme shows the future implementations of machine-learning techniques in CIGALE to improve the model analysis and speed up the code. This is the Ph.D. work of Grégoire Aufort at LAM. Image credits: Grégoire Aufort.

8.3. Summary

In the future, spectroscopic surveys like MOONS, PFS, JWST, MSE, and MOSAIC will deliver large datasets which will help us to study and understand galaxy formation and evolution in finer detail. In particular, instruments such as MOONS, PFS, and MOSAIC will contribute to populating the NIR wavelengths with high-quality spectra providing new measurements in a zone of high interest for extra-galactic Astronomers. These surveys will provide us with valuable information on the chemical evolution, the orbital motion of stars, stellar populations, among others for the Milky Way and extra-galactic sources. Updating the current SED fitting software available to properly treat emission lines will give us a powerful tool to study the ISM through the gas-phase metallicity, and ionization parameter, independently of the current methods used in the literature based on calibrations. Also, implementing suitable machine-learning recipes will help to analyze these datasets more efficiently, optimize the computation time, and deal with the models in a more effective fashion. Spectroscopic surveys will open a new era in galactic and extragalactic Astronomy and will transform the SED fitting field.

List of publications

2021 Fitting spectral energy distributions of FMOS-COSMOS emission-line galaxies at z∼1.6: Star formation rates, dust attenuation, and [OIII]λ5007 emission-line luminosities, J. A Villa-Vélez, V. Buat, P. Theulé, M. Boquien & D. Burgarella, A&A, 2021, Vol. 654, A153.

2020 A Virgo Environmental Survey Tracing Ionised Gas Emission. VESTIGE VIII. Bridging the cluster-ICM-galaxy evolution at small scales, A. Longobardi, A. Boselli, M. Fossati, J. A. Villa-Vélez, S. Bianchi, V. Casasola, E. Sarpa, F. Combes, G. Hensler, D. Burgarella, C. Schimd, A. Nanni, P. Côté, V. Buat1, P. Amram, L. Ferrarese, J. Braine, G. Trinchieri, S. Boissier, M. Boquien, P. Andreani, S. Gwyn, J. C. Cuillandre, A&A, 2020, Vol. 644, A161.

2019 COSMOS/GOODS-S fields spectro-photometric analysis and the MOONS future perspectives in SED fitting studies, J. A. Villa-Vélez, V. Buat, D. Burgarella, M. Rodrigues, M. Puech, H. Flores, Proceedings of the Annual meeting of the French Society of Astronomy and Astrophysics, 2019, pp.115-119.

Bibliography

Albrecht, A. and P. J. Steinhardt (Apr. 1982). "Cosmology for Grand Unified Theories with Radiatively Induced Symmetry Breaking". In: *Phys. Rev. Lett.* 48.17, pp. 1220–1223. DOI: 10.1103/PhysRevLett.48.1220 (cit. on p. 36).

Allen, Mark G. et al. (Sept. 2008). "The MAPPINGS III Library of Fast Radiative Shock Models". In: *ApJS* 178.1, pp. 20–55. DOI: 10.1086/589652. arXiv: 0805.0204 [astro-ph] (cit. on p. 48).

Alpher, R. A., H. Bethe, and G. Gamow (Apr. 1948). "The Origin of Chemical Elements". In: *Physical Review* 73.7, pp. 803–804. DOI: 10.1103/PhysRev.73.803 (cit. on p. 36).

Alpher, Ralph A. and Robert Herman (Nov. 1948). "Evolution of the Universe". In: *Nature* 162.4124, pp. 774–775. DOI: 10.1038/162774b0 (cit. on p. 36).

Álvarez-Márquez, J. et al. (Oct. 2019). "Rest-frame far-ultraviolet to far-infrared view of Lyman break galaxies at z = 3: Templates and dust attenuation". In: *A&A* 630, A153, A153. DOI: 10.1051/0004-6361/201935719. arXiv: 1907.11463 [astro-ph.GA] (cit. on p. 51).

Andrews, Brett H. and Paul Martini (Mar. 2013). "The Mass-Metallicity Relation with the Direct Method on Stacked Spectra of SDSS Galaxies". In: *ApJ* 765.2, 140, p. 140. DOI: 10.1088/0004-637X/765/2/140. arXiv: 1211.3418 [astro-ph.CO] (cit. on pp. 110–112, 164).

Andrews, S. K. et al. (Feb. 2018). "Modelling the cosmic spectral energy distribution and extragalactic background light over all time". In: *MNRAS* 474.1, pp. 898–916. DOI: 10.1093/mnras/stx2843. arXiv: 1710.11329 [astro-ph.GA] (cit. on p. 49).

Arata, Shohei et al. (Nov. 2020). "Starbursting [O III] emitters and quiescent [C II] emitters in the reionization era". In: *MNRAS* 498.4, pp. 5541–5556. DOI: 10.1093/mnras/staa2809. arXiv: 2001.01853 [astro-ph.GA] (cit. on p. 122).

Arnouts, S. et al. (Dec. 1999). "Measuring and modelling the redshift evolution of clustering: the Hubble Deep Field North". In: *MNRAS* 310.2, pp. 540–556. DOI: 10.1046/j.1365-8711.1999.02978.x. arXiv: astro-ph/9902290 [astro-ph] (cit. on p. 49).

Asplund, Martin et al. (Sept. 2009). "The Chemical Composition of the Sun". In: *ARA&A* 47.1, pp. 481–522. DOI: 10.1146/annurev.astro.46.060407.145222. arXiv: 0909.0948 [astro-ph.SR] (cit. on pp. 69, 126).

Baes, Maarten et al. (Oct. 2011). "Efficient Three-dimensional NLTE Dust Radiative Transfer with SKIRT". In: *ApJS* 196.2, 22, p. 22. DOI: 10.1088/0067-0049/196/2/22. arXiv: 1108.5056 [astro-ph.CO] (cit. on p. 48).

Baldwin, J. A., M. M. Phillips, and R. Terlevich (Feb. 1981). "Classification parameters for the emission-line spectra of extragalactic objects." In: *PASP* 93, pp. 5–19. DOI: 10.1086/130766 (cit. on pp. 71, 125, 128, 149).

Ball, Nicholas M. et al. (Aug. 2008). "Robust Machine Learning Applied to Astronomical Data Sets. III. Probabilistic Photometric Redshifts for Galaxies and Quasars in the SDSS and GALEX". In: *ApJ* 683.1, pp. 12–21. DOI: 10.1086/589646. arXiv: 0804.3413 [astro-ph] (cit. on p. 179).

Barbaro, G. and B. M. Poggianti (Aug. 1997). "The determination of the star formation rate in galaxies." In: *A&A* 324, pp. 490–504. arXiv: astro-ph/9702129 [astro-ph] (cit. on p. 68).

Barnes, D. G. et al. (Apr. 2001). "The HI Parkes All Sky Survey: southern observations, calibration and robust imaging". In: *MNRAS* 322.3, pp. 486–498. DOI: 10.1046/j.1365-8711.2001.04102.x (cit. on p. 41).

Battisti, A. J., D. Calzetti, and R. -R. Chary (Feb. 2016). "Characterizing Dust Attenuation in Local Star-forming Galaxies: UV and Optical Reddening". In: *ApJ* 818.1, 13, p. 13. DOI: 10.3847/0004-637X/818/1/13. arXiv: 1601.00208 [astro-ph.GA] (cit. on pp. 65, 98, 106).

Battisti, A. J. et al. (Sept. 2019). "MAGPHYS+photo-z: Constraining the Physical Properties of Galaxies with Unknown Redshifts". In: *ApJ* 882.1, 61, p. 61. DOI: 10.3847/1538-4357/ab345d. arXiv: 1908.00771 [astro-ph.GA] (cit. on p. 98).

Becker, Robert H., Richard L. White, and David J. Helfand (Sept. 1995). "The FIRST Survey: Faint Images of the Radio Sky at Twenty Centimeters". In: *ApJ* 450, p. 559. DOI: 10.1086/176166 (cit. on p. 41).

Berg, Danielle A. et al. (Aug. 2012). "Direct Oxygen Abundances for Low-luminosity LVL Galaxies". In: *ApJ* 754.2, 98, p. 98. DOI: 10.1088/0004-637X/754/2/98. arXiv: 1205.6782 [astro-ph.CO] (cit. on p. 110).

Bernard-Salas, J. et al. (Feb. 2015). "Spatial variation of the cooling lines in the reflection nebula NGC 7023". In: *A&A* 574, A97, A97. DOI: 10.1051/0004-6361/201423705. arXiv: 1501.07747 [astro-ph.GA] (cit. on p. 45).

Bertelli, G. et al. (Aug. 1994). "Theoretical isochrones from models with new radiative opacities." In: *A&AS* 106, pp. 275–302 (cit. on pp. 48, 52).

Bian, Fuyan et al. (Mar. 2020). "What drives the redshift evolution of strong emission line ratios?" In: *MNRAS* 493.1, pp. 580–585. DOI: 10.1093/mnras/staa259. arXiv: 2002.02976 [astro-ph.GA] (cit. on pp. 72, 129).

Blanc, Guillermo A. et al. (May 2019). "A Characteristic Mass Scale in the Mass-Metallicity Relation of Galaxies". In: *ApJ* 877.1, 6, p. 6. DOI: 10.3847/1538-4357/ab16ec. arXiv: 1904.02721 [astro-ph.GA] (cit. on p. 110).

Boissier, Samuel (Aug. 2017). "A few basic elements concerning the evolution of galaxies". In: *Introduction to Cosmology, Proceedings of the Polish Astronomical Society*. Ed. by Monika Biernacka et al. Vol. 4, pp. 96–115 (cit. on pp. 37, 38, 69).

Bondi, H. and T. Gold (Jan. 1948). "The Steady-State Theory of the Expanding Universe". In: *MNRAS* 108, p. 252. DOI: 10.1093/mnras/108.3.252 (cit. on p. 35).

Boquien, M., V. Buat, and V. Perret (Nov. 2014). "Impact of star formation history on the measurement of star formation rates". In: *A&A* 571, A72, A72. DOI: 10.1051/0004-6361/201424441. arXiv: 1409.5792 [astro-ph.GA] (cit. on pp. 53–55).

Boquien, M. et al. (Feb. 2019). "CIGALE: a python Code Investigating GALaxy Emission". In: *A&A* 622, A103, A103. DOI: 10.1051/0004-6361/201834156. arXiv: 1811.03094

[astro-ph.GA] (cit. on pp. 48, 58, 65, 66, 68, 73, 74, 76, 96, 97, 99, 154, 155, 157, 180).

Boselli, Alessandro (2011). *A Panchromatic View of Galaxies* (cit. on pp. 39, 40, 42, 43, 45, 46, 70, 73).

Bourne, N. et al. (Apr. 2012). "Herschel-ATLAS/GAMA: a census of dust in optically selected galaxies from stacking at submillimetre wavelengths". In: *MNRAS* 421.4, pp. 3027–3059. DOI: 10.1111/j.1365-2966.2012.20528.x. arXiv: 1201.1916 [astro-ph.CO] (cit. on p. 109).

Bouwens, R. J. et al. (Aug. 2012). "UV-continuum Slopes at z ~4-7 from the HUDF09+ERS+CANDELS Observations: Discovery of a Well-defined UV Color-Magnitude Relationship for z >= 4 Star-forming Galaxies". In: *ApJ* 754.2, 83, p. 83. DOI: 10.1088/0004-637X/754/2/83. arXiv: 1109.0994 [astro-ph.CO] (cit. on p. 58).

Bowman, William P. et al. (Apr. 2019). "Galaxies of the z ~ 2 Universe. I. Grism-selected Rest-frame Optical Emission-line Galaxies". In: *ApJ* 875.2, 152, p. 152. DOI: 10.3847/1538-4357/ab108a. arXiv: 1903.07573 [astro-ph.GA] (cit. on p. 113).

Bowman, William P. et al. (Aug. 2020). "MCSED: A Flexible Spectral Energy Distribution Fitting Code and Its Application to z ~ 2 Emission-line Galaxies". In: *ApJ* 899.1, 7, p. 7. DOI: 10.3847/1538-4357/ab9f3c. arXiv: 2006.13245 [astro-ph.GA] (cit. on p. 49).

Brinchmann, J. et al. (July 2004). "The physical properties of star-forming galaxies in the low-redshift Universe". In: *MNRAS* 351.4, pp. 1151–1179. DOI: 10.1111/j.1365-2966.2004.07881.x. arXiv: astro-ph/0311060 [astro-ph] (cit. on pp. 71, 73, 74).

Brinchmann, Jarle, Max Pettini, and Stéphane Charlot (Apr. 2008). "New insights into the stellar content and physical conditions of star-forming galaxies at z = 2-3 from spectral modelling". In: *MNRAS* 385.2, pp. 769–782. DOI: 10.1111/j.1365-2966.2008.12914.x. arXiv: 0801.1678 [astro-ph] (cit. on p. 129).

Bruzual, G. and S. Charlot (Oct. 2003). "Stellar population synthesis at the resolution of 2003". In: *MNRAS* 344, pp. 1000–1028. DOI: 10.1046/j.1365-8711.2003.06897.x. eprint: astro-ph/0309134 (cit. on pp. 52, 81, 97, 99, 126–128, 155–160).

Buat, V. et al. (Sept. 2012). "GOODS-Herschel: dust attenuation properties of UV selected high redshift galaxies". In: *A&A* 545, A141, A141. DOI: 10.1051/0004-6361/201219405. arXiv: 1207.3528 [astro-ph.CO] (cit. on pp. 62, 66).

Buat, V. et al. (Nov. 2018). "Dust attenuation and Hα emission in a sample of galaxies observed with Herschel at 0.6 < z <1.6". In: *A&A* 619, A135, A135. DOI: 10.1051/0004-6361/201833841. arXiv: 1809.00161 [astro-ph.GA] (cit. on pp. 47, 49, 56, 58, 59, 62, 63, 67, 82, 96, 98–100, 103, 107, 108, 179).

Buat, V. et al. (Dec. 2019). "Cold dust and stellar emissions in dust-rich galaxies observed with ALMA: a challenge for SED-fitting techniques". In: *A&A* 632, A79, A79. DOI: 10.1051/0004-6361/201936643 (cit. on p. 97).

Buat, Véronique (Aug. 2017). "Star formation rates measurements: linking stellar and dust emissions". In: *Introduction to Cosmology, Proceedings of the Polish Astronomical Society*. Ed. by Monika Biernacka et al. Vol. 4, pp. 116–124 (cit. on pp. 53, 56).

Bugallo, Monica F. et al. (2017). "Adaptive Importance Sampling: The past, the present, and the future". In: *IEEE Signal Processing Magazine* 34.4, pp. 60–79. DOI: 10.1109/MSP.2017.2699226 (cit. on p. 180).

Burgarella, D., V. Buat, and J. Iglesias-Páramo (July 2005). "Star formation and dust attenuation properties in galaxies from a statistical ultraviolet-to-far-infrared analysis". In: *MNRAS* 360.4, pp. 1413–1425. DOI: 10.1111/j.1365-2966.2005.09131.x. arXiv: astro-ph/0504434 [astro-ph] (cit. on p. 58).

Burgarella, Denis (2021). "Star-Formation Rates from Spectral Energy Distributions of Galaxies". In: *Star-Formation Rates of Galaxies*. Ed. by Andreas Zezas and VéroniqueEditors Buat. Cambridge Astrophysics. Cambridge University Press, pp. 184–203. DOI: 10.1017/9781316875445.011 (cit. on pp. 46, 47, 58, 67, 74, 76, 82).

Burgarella, Denis et al. (Aug. 2017). "The Emission of Galaxies over the Whole Electromagnetic Spectrum". In: *Introduction to Cosmology, Proceedings of the Polish Astronomical Society*. Ed. by Monika Biernacka et al. Vol. 4, pp. 125–131 (cit. on pp. 46, 48, 77).

Byler, Nell et al. (May 2017). "Nebular Continuum and Line Emission in Stellar Population Synthesis Models". In: *ApJ* 840.1, 44, p. 44. DOI: 10.3847/1538-4357/aa6c66. arXiv: 1611.08305 [astro-ph.GA] (cit. on pp. 69, 70, 112).

Calzetti, D. et al. (Apr. 2000). "The Dust Content and Opacity of Actively Star-forming Galaxies". In: *ApJ* 533, pp. 682–695. DOI: 10.1086/308692. eprint: astro-ph/9911459 (cit. on pp. 63, 65, 66, 68, 81, 106, 107, 154, 167).

Calzetti, Daniela (Oct. 2001). "The effects of dust on the spectral energy distribution of star-forming galaxies". In: *New A Rev.* 45.9-10, pp. 601–607. DOI: 10.1016/S1387-6473(01)00144-0. arXiv: astro-ph/0008403 [astro-ph] (cit. on p. 62).

Calzetti, Daniela, Anne L. Kinney, and Thaisa Storchi-Bergmann (July 1994). "Dust Extinction of the Stellar Continua in Starburst Galaxies: The Ultraviolet and Optical Extinction Law". In: *ApJ* 429, p. 582. DOI: 10.1086/174346 (cit. on p. 63).

Capak, Peter et al. (Sept. 2012). *SPLASH: Spitzer Large Area Survey with Hyper-Suprime-Cam*. Spitzer Proposal (cit. on p. 87).

Caplan, J. and L. Deharveng (Feb. 1986). "Extinction and reddening of H II regions in the Large Magellanic Cloud." In: *A&A* 155, pp. 297–313 (cit. on p. 98).

Cardelli, Jason A., Geoffrey C. Clayton, and John S. Mathis (Oct. 1989). "The Relationship between Infrared, Optical, and Ultraviolet Extinction". In: *ApJ* 345, p. 245. DOI: 10.1086/167900 (cit. on pp. 66, 106, 167).

Carnall, A. C. et al. (Nov. 2018). "Inferring the star formation histories of massive quiescent galaxies with BAGPIPES: evidence for multiple quenching mechanisms". In: *MNRAS* 480.4, pp. 4379–4401. DOI: 10.1093/mnras/sty2169. arXiv: 1712.04452 [astro-ph.GA] (cit. on p. 49).

Carnall, Adam C. et al. (Mar. 2019). "How to Measure Galaxy Star Formation Histories. I. Parametric Models". In: *ApJ* 873.1, 44, p. 44. DOI: 10.3847/1538-4357/ab04a2. arXiv: 1811.03635 [astro-ph.GA] (cit. on pp. 54–56, 68, 97, 149).

Carton, David et al. (June 2017). "Inferring gas-phase metallicity gradients of galaxies at the seeing limit: a forward modelling approach". In: *MNRAS* 468.2, pp. 2140–2163.

DOI: 10.1093/mnras/stx545. arXiv: 1703.01090 [astro-ph.GA] (cit. on pp. 164, 165, 169, 172).

Casey, Caitlin M. (Oct. 2012). "Far-infrared spectral energy distribution fitting for galaxies near and far". In: *MNRAS* 425.4, pp. 3094–3103. DOI: 10.1111/j.1365-2966.2012.21455.x. arXiv: 1206.1595 [astro-ph.CO] (cit. on pp. 49, 57, 58).

Chabrier, Gilles (July 2003). "Galactic Stellar and Substellar Initial Mass Function". In: *PASP* 115.809, pp. 763–795. DOI: 10.1086/376392. arXiv: astro-ph/0304382 [astro-ph] (cit. on pp. 53, 97, 127, 128, 166).

Charlot, S. and S. M. Fall (Aug. 2000). "A Simple Model for the Absorption of Starlight by Dust in Galaxies". In: *ApJ* 539, pp. 718–731. DOI: 10.1086/309250. eprint: astro-ph/0003128 (cit. on pp. 3, 48, 56, 63–65, 68, 97–99, 104, 106–108, 136, 154, 157, 158, 168, 174).

Charlot, Stéphane and Marcella Longhetti (May 2001). "Nebular emission from star-forming galaxies". In: *MNRAS* 323.4, pp. 887–903. DOI: 10.1046/j.1365-8711.2001.04260.x. arXiv: astro-ph/0101097 [astro-ph] (cit. on pp. 68, 69).

Chen, Yanping et al. (Dec. 2011). "XSL: The X-Shooter Spectral Library". In: *Journal of Physics Conference Series*. Vol. 328. Journal of Physics Conference Series, p. 012023. DOI: 10.1088/1742-6596/328/1/012023. arXiv: 1112.3651 [astro-ph.GA] (cit. on p. 53).

Chevallard, J. et al. (July 2013). "Insights into the content and spatial distribution of dust from the integrated spectral properties of galaxies". In: *MNRAS* 432.3, pp. 2061–2091. DOI: 10.1093/mnras/stt523. arXiv: 1303.6631 [astro-ph.CO] (cit. on p. 61).

Chevallard, Jacopo and Stéphane Charlot (Oct. 2016). "Modelling and interpreting spectral energy distributions of galaxies with BEAGLE". In: *MNRAS* 462.2, pp. 1415–1443. DOI: 10.1093/mnras/stw1756. arXiv: 1603.03037 [astro-ph.GA] (cit. on pp. 48, 68, 96, 107).

Chevallard, Jacopo et al. (Feb. 2019). "Simulating and interpreting deep observations in the Hubble Ultra Deep Field with the JWST/NIRSpec low-resolution 'prism'". In: *MNRAS* 483.2, pp. 2621–2640. DOI: 10.1093/mnras/sty2426. arXiv: 1711.07481 [astro-ph.GA] (cit. on pp. 51, 97, 98).

Chisholm, J. et al. (Sept. 2019). "Constraining the Metallicities, Ages, Star Formation Histories, and Ionizing Continua of Extragalactic Massive Star Populations". In: *ApJ* 882.2, 182, p. 182. DOI: 10.3847/1538-4357/ab3104. arXiv: 1905.04314 [astro-ph.GA] (cit. on p. 43).

Ciddor, Philip E. (Mar. 1996). "Refractive index of air: new equations for the visible and near infrared". In: *Appl. Opt.* 35.9, p. 1566. DOI: 10.1364/AO.35.001566 (cit. on p. 157).

Ciesla, L., D. Elbaz, and J. Fensch (Dec. 2017). "The SFR-M_* main sequence archetypal star-formation history and analytical models". In: *A&A* 608, A41, A41. DOI: 10.1051/0004-6361/201731036. arXiv: 1706.08531 [astro-ph.GA] (cit. on pp. 96, 103).

Ciesla, L. et al. (Apr. 2015). "Constraining the properties of AGN host galaxies with spectral energy distribution modelling". In: *A&A* 576, A10, A10. DOI: 10.1051/0004-6361/201425252. arXiv: 1501.03672 [astro-ph.GA] (cit. on pp. 54, 56).

Cirasuolo, M. et al. (Sept. 2012). "MOONS: a multi-object optical and near-infrared spectrograph for the VLT". In: *Ground-based and Airborne Instrumentation for Astronomy IV*. Ed. by Ian S. McLean, Suzanne K. Ramsay, and Hideki Takami. Vol. 8446. Society of Photo-Optical Instrumentation Engineers (SPIE) Conference Series, 84460S. DOI: 10.1117/12.925871. arXiv: 1208.5780 [astro-ph.IM] (cit. on p. 139).

Cirasuolo, M. et al. (June 2020). "MOONS: The New Multi-Object Spectrograph for the VLT". In: *The Messenger* 180, pp. 10–17. DOI: 10.18727/0722-6691/5195. arXiv: 2009.00628 [astro-ph.IM] (cit. on pp. 72, 139–142, 144, 147, 176).

Civano, F. et al. (Mar. 2016). "The Chandra Cosmos Legacy Survey: Overview and Point Source Catalog". In: *ApJ* 819, 62, p. 62. DOI: 10.3847/0004-637X/819/1/62. arXiv: 1601.00941 (cit. on p. 94).

Coles, Peter and Francesco Lucchin (2002). *Cosmology: The Origin and Evolution of Cosmic Structure, Second Edition* (cit. on pp. 35, 36).

Colless, Matthew et al. (Dec. 2001). "The 2dF Galaxy Redshift Survey: spectra and redshifts". In: *MNRAS* 328.4, pp. 1039–1063. DOI: 10.1046/j.1365-8711.2001.04902.x. arXiv: astro-ph/0106498 [astro-ph] (cit. on p. 41).

Condon, J. J. et al. (May 1998). "The NRAO VLA Sky Survey". In: *AJ* 115.5, pp. 1693–1716. DOI: 10.1086/300337 (cit. on p. 41).

Conroy, Charlie (Aug. 2013). "Modeling the Panchromatic Spectral Energy Distributions of Galaxies". In: *ARA&A* 51.1, pp. 393–455. DOI: 10.1146/annurev-astro-082812-141017. arXiv: 1301.7095 [astro-ph.CO] (cit. on pp. 52–54, 57–59, 61, 62, 82).

Conroy, Charlie, James E. Gunn, and Martin White (July 2009). "The Propagation of Uncertainties in Stellar Population Synthesis Modeling. I. The Relevance of Uncertain Aspects of Stellar Evolution and the Initial Mass Function to the Derived Physical Properties of Galaxies". In: *ApJ* 699.1, pp. 486–506. DOI: 10.1088/0004-637X/699/1/486. arXiv: 0809.4261 [astro-ph] (cit. on p. 70).

Conroy, Charlie, David Schiminovich, and Michael R. Blanton (July 2010). "Dust Attenuation in Disk-dominated Galaxies: Evidence for the 2175 Å Dust Feature". In: *ApJ* 718.1, pp. 184–198. DOI: 10.1088/0004-637X/718/1/184. arXiv: 1003.2202 [astro-ph.CO] (cit. on pp. 61, 62, 65).

Cordier, Daniel et al. (Feb. 2007). "A Large Stellar Evolution Database for Population Synthesis Studies. III. Inclusion of the Full Asymptotic Giant Branch Phase and Web Tools for Stellar Population Analyses". In: *AJ* 133.2, pp. 468–478. DOI: 10.1086/509870. arXiv: astro-ph/0612669 [astro-ph] (cit. on p. 52).

Corre, D. et al. (Oct. 2018). "Investigation of dust attenuation and star formation activity in galaxies hosting GRBs". In: *A&A* 617, A141, A141. DOI: 10.1051/0004-6361/201832926. arXiv: 1807.00635 [astro-ph.GA] (cit. on pp. 47, 58, 61, 62, 65–67, 97, 179).

Cortese, L. et al. (Apr. 2012). "The dust scaling relations of the Herschel Reference Survey". In: *A&A* 540, A52, A52. DOI: 10.1051/0004-6361/201118499. arXiv: 1201.2762 [astro-ph.CO] (cit. on p. 109).

Cowie, L. L., A. J. Barger, and A. Songaila (Jan. 2016). "Luminosity Dependence and Redshift Evolution of Strong Emission-Line Diagnostics in Star-Forming Galaxies".

In: *ApJ* 817.1, 57, p. 57. DOI: 10.3847/0004-637X/817/1/57. arXiv: 1512.00017 [astro-ph.GA] (cit. on p. 129).

Cresci, G., F. Mannucci, and M. Curti (July 2019). "Fundamental metallicity relation in CALIFA, SDSS-IV MaNGA, and high-z galaxies". In: *A&A* 627, A42, A42. DOI: 10.1051/0004-6361/201834637. arXiv: 1811.06015 [astro-ph.GA] (cit. on p. 110).

Cullen, F. et al. (Aug. 2019). "The VANDELS survey: the stellar metallicities of star-forming galaxies at 2.5 < z < 5.0". In: *MNRAS* 487.2, pp. 2038–2060. DOI: 10.1093/mnras/stz1402. arXiv: 1903.11081 [astro-ph.GA] (cit. on p. 149).

Curti, M. et al. (Feb. 2017). "New fully empirical calibrations of strong-line metallicity indicators in star-forming galaxies". In: *MNRAS* 465.2, pp. 1384–1400. DOI: 10.1093/mnras/stw2766. arXiv: 1610.06939 [astro-ph.GA] (cit. on p. 111).

Curti, Mirko et al. (Jan. 2020). "The mass-metallicity and the fundamental metallicity relation revisited on a fully T_e-based abundance scale for galaxies". In: *MNRAS* 491.1, pp. 944–964. DOI: 10.1093/mnras/stz2910. arXiv: 1910.00597 [astro-ph.GA] (cit. on pp. 5, 81, 110–112, 136, 163–165, 171, 174, 175).

D'Agostino, Joshua J. et al. (June 2019). "Comparison of Theoretical Starburst Photoionization Models for Optical Diagnostics". In: *ApJ* 878.1, 2, p. 2. DOI: 10.3847/1538-4357/ab1d5e. arXiv: 1905.09528 [astro-ph.GA] (cit. on p. 70).

da Cunha, Elisabete, Stéphane Charlot, and David Elbaz (Aug. 2008). "A simple model to interpret the ultraviolet, optical and infrared emission from galaxies". In: *MNRAS* 388.4, pp. 1595–1617. DOI: 10.1111/j.1365-2966.2008.13535.x. arXiv: 0806.1020 [astro-ph] (cit. on pp. 48, 58, 59, 64, 65, 73, 98).

Dale, D. A. et al. (Jan. 2012). "Herschel Far-infrared and Submillimeter Photometry for the KINGFISH Sample of nearby Galaxies". In: *ApJ* 745.1, 95, p. 95. DOI: 10.1088/0004-637X/745/1/95. arXiv: 1112.1093 [astro-ph.CO] (cit. on p. 59).

Dale, Daniel A. et al. (Mar. 2014). "A Two-parameter Model for the Infrared Submillimeter Radio Spectral Energy Distributions of Galaxies and Active Galactic Nuclei". In: *ApJ* 784.1, 83, p. 83. DOI: 10.1088/0004-637X/784/1/83. arXiv: 1402.1495 [astro-ph.GA] (cit. on pp. 49, 57–59, 157, 158).

De Looze, Ilse et al. (Aug. 2014). "The applicability of far-infrared fine-structure lines as star formation rate tracers over wide ranges of metallicities and galaxy types". In: *A&A* 568, A62, A62. DOI: 10.1051/0004-6361/201322489. arXiv: 1402.4075 [astro-ph.GA] (cit. on pp. 121–123).

De Marchi, Guido et al. (Feb. 2016). "Hubble Tarantula Treasury Project - IV. The extinction law". In: *MNRAS* 455.4, pp. 4373–4387. DOI: 10.1093/mnras/stv2528. arXiv: 1510.08436 [astro-ph.SR] (cit. on p. 61).

Dinerstein, H. L. (Jan. 1983). "Infrared emission lines in planetary nebulae." In: *Planetary Nebulae*. Ed. by L. H. Aller. Vol. 103, pp. 79–88 (cit. on pp. 45, 121).

Dobbels, W. et al. (Feb. 2020). "Predicting the global far-infrared SED of galaxies via machine learning techniques". In: *A&A* 634, A57, A57. DOI: 10.1051/0004-6361/201936695. arXiv: 1910.06330 [astro-ph.GA] (cit. on pp. 49, 82, 179).

Donley, J. L. et al. (Apr. 2012). "Identifying Luminous Active Galactic Nuclei in Deep Surveys: Revised IRAC Selection Criteria". In: *ApJ* 748.2, 142, p. 142. DOI: 10.1088/0004-637X/748/2/142. arXiv: 1201.3899 [astro-ph.CO] (cit. on p. 94).

Dopita, Michael A. et al. (Sept. 2013). "New Strong-line Abundance Diagnostics for H II Regions: Effects of κ-distributed Electron Energies and New Atomic Data". In: *ApJS* 208.1, 10, p. 10. DOI: 10.1088/0067-0049/208/1/10. arXiv: 1307.5950 [astro-ph.CO] (cit. on pp. 68, 70, 71, 112).

Dopita, Michael A. et al. (Feb. 2016). "Chemical abundances in high-redshift galaxies: a powerful new emission line diagnostic". In: *Ap&SS* 361, 61, p. 61. DOI: 10.1007/s10509-016-2657-8. arXiv: 1601.01337 [astro-ph.GA] (cit. on pp. 68, 69, 71, 72, 111, 112, 129).

Draine, B. T. (Jan. 2003). "Interstellar Dust Grains". In: *ARA&A* 41, pp. 241–289. DOI: 10.1146/annurev.astro.41.011802.094840. arXiv: astro-ph/0304489 [astro-ph] (cit. on p. 57).

Draine, B. T. and Aigen Li (Mar. 2007). "Infrared Emission from Interstellar Dust. IV. The Silicate-Graphite-PAH Model in the Post-Spitzer Era". In: *ApJ* 657.2, pp. 810–837. DOI: 10.1086/511055. arXiv: astro-ph/0608003 [astro-ph] (cit. on pp. 49, 57–59, 62, 98).

Draine, B. T. et al. (July 2007). "Dust Masses, PAH Abundances, and Starlight Intensities in the SINGS Galaxy Sample". In: *ApJ* 663.2, pp. 866–894. DOI: 10.1086/518306. arXiv: astro-ph/0703213 [astro-ph] (cit. on p. 59).

Draine, B. T. et al. (Jan. 2014). "Andromeda's Dust". In: *ApJ* 780.2, 172, p. 172. DOI: 10.1088/0004-637X/780/2/172. arXiv: 1306.2304 [astro-ph.CO] (cit. on pp. 49, 57–59, 98).

Efstathiou, A. et al. (Dec. 2013). "Active galactic nucleus torus models and the puzzling infrared spectrum of IRAS F10214+4724". In: *MNRAS* 436.2, pp. 1873–1882. DOI: 10.1093/mnras/stt1695. arXiv: 1310.0368 [astro-ph.CO] (cit. on p. 48).

Elbaz, D. et al. (Sept. 2011). "GOODS-Herschel: an infrared main sequence for star-forming galaxies". In: *A&A* 533, A119, A119. DOI: 10.1051/0004-6361/201117239. arXiv: 1105.2537 (cit. on p. 38).

Eldridge, John J. and Elizabeth R. Stanway (Dec. 2009). "Spectral population synthesis including massive binaries". In: *MNRAS* 400.2, pp. 1019–1028. DOI: 10.1111/j.1365-2966.2009.15514.x. arXiv: 0908.1386 [astro-ph.CO] (cit. on p. 48).

Elia, Davide and S. Pezzuto (Sept. 2016). "Remarkable analytic relations among grey-body parameters". In: *MNRAS* 461.2, pp. 1328–1337. DOI: 10.1093/mnras/stw1399. arXiv: 1606.02496 [astro-ph.SR] (cit. on p. 46).

Ellis, Richard S. et al. (Jan. 2017). "The Future of Multi-Object Spectroscopy: a ESO Working Group Report". In: *arXiv e-prints*, arXiv:1701.01976, arXiv:1701.01976. arXiv: 1701.01976 [astro-ph.IM] (cit. on p. 49).

Ellison, Sara L. et al. (Jan. 2008). "Clues to the Origin of the Mass-Metallicity Relation: Dependence on Star Formation Rate and Galaxy Size". In: *ApJ* 672.2, p. L107. DOI: 10.1086/527296. arXiv: 0711.4833 [astro-ph] (cit. on p. 110).

Elvis, Martin et al. (Sept. 2009). "The Chandra COSMOS Survey. I. Overview and Point Source Catalog". In: *ApJS* 184.1, pp. 158–171. DOI: 10.1088/0067-0049/184/1/158. arXiv: 0903.2062 [astro-ph.CO] (cit. on p. 94).

Erb, Dawn K. et al. (Aug. 2010). "Physical Conditions in a Young, Unreddened, Low-metallicity Galaxy at High Redshift". In: *ApJ* 719.2, pp. 1168–1190. DOI: 10.1088/0004-637X/719/2/1168. arXiv: 1006.5456 [astro-ph.CO] (cit. on p. 68).

Evans, I. N. and M. A. Dopita (May 1985). "Theoretical models for H II regions. I. Diagnostic diagrams." In: *ApJS* 58, pp. 125–142. DOI: 10.1086/191032 (cit. on p. 68).

Fabbiano, G. (Feb. 2008). "X-ray observations of galaxies: The importance of deep high-resolution observations". In: *X-rays From Nearby Galaxies*. Ed. by S. Carpano, M. Ehle, and W. Pietsch, pp. 87–92. arXiv: 0711.0764 [astro-ph] (cit. on p. 42).

Fanelli, Michael N., Robert W. O'Connell, and Trinh X. Thuan (Nov. 1988). "Spectral Synthesis in the Ultraviolet. II. Stellar Populations and Star Formation in Blue Compact Galaxies". In: *ApJ* 334, p. 665. DOI: 10.1086/166869 (cit. on p. 63).

Ferkinhoff, C. et al. (May 2010). "First Detection of the [O III] 88 μm Line at High Redshifts: Characterizing the Starburst and Narrow-line Regions in Extreme Luminosity Systems". In: *ApJ* 714.1, pp. L147–L151. DOI: 10.1088/2041-8205/714/1/L147. arXiv: 1003.4296 [astro-ph.CO] (cit. on p. 121).

Ferland, G. J. et al. (Oct. 2017). "The 2017 Release Cloudy". In: *Rev. Mexicana Astron. Astrofis.* 53, pp. 385–438. arXiv: 1705.10877 [astro-ph.GA] (cit. on pp. 48, 69).

Finkelstein, Steven L. et al. (Sept. 2012). "Candels: The Evolution of Galaxy Rest-frame Ultraviolet Colors from z = 8 to 4". In: *ApJ* 756.2, 164, p. 164. DOI: 10.1088/0004-637X/756/2/164. arXiv: 1110.3785 [astro-ph.CO] (cit. on p. 59).

Fitzpatrick, Edward L. (Jan. 1999). "Correcting for the Effects of Interstellar Extinction". In: *PASP* 111.755, pp. 63–75. DOI: 10.1086/316293. arXiv: astro-ph/9809387 [astro-ph] (cit. on p. 66).

Fixsen, D. J. (Dec. 2009). "The Temperature of the Cosmic Microwave Background". In: *ApJ* 707.2, pp. 916–920. DOI: 10.1088/0004-637X/707/2/916. arXiv: 0911.1955 [astro-ph.CO] (cit. on p. 36).

Fontanot, Fabio and Rachel S. Somerville (Oct. 2011). "Evaluating and improving semi-analytic modelling of dust in galaxies based on radiative transfer calculations - II. Dust emission in the infrared". In: *MNRAS* 416.4, pp. 2962–2973. DOI: 10.1111/j.1365-2966.2011.19245.x. arXiv: 1011.0776 [astro-ph.CO] (cit. on p. 63).

Fontanot, Fabio et al. (Jan. 2009). "Evaluating and improving semi-analytic modelling of dust in galaxies based on radiative transfer calculations". In: *MNRAS* 392.2, pp. 553–569. DOI: 10.1111/j.1365-2966.2008.14126.x. arXiv: 0810.3918 [astro-ph] (cit. on p. 63).

Fossati, M. et al. (June 2018). "A Virgo Environmental Survey Tracing Ionised Gas Emission (VESTIGE). II. Constraining the quenching time in the stripped galaxy NGC 4330". In: *A&A* 614, A57, A57. DOI: 10.1051/0004-6361/201732373. arXiv: 1801.09685 [astro-ph.GA] (cit. on pp. 47, 58, 67, 179).

Frampton, P. H. (Dec. 2006). "On Cyclic Universes". In: *arXiv e-prints*, astro-ph/0612243, astro–ph/0612243. arXiv: astro-ph/0612243 [astro-ph] (cit. on p. 35).

Gallagher, J. S., H. Bushouse, and D. A. Hunter (Mar. 1989). "Star Formation Rates and [O II] Emission in Blue Galaxies". In: *AJ* 97, p. 700. DOI: 10.1086/115015 (cit. on p. 67).

Galliano, Frédéric, Eli Dwek, and Pierre Chanial (Jan. 2008). "Stellar Evolutionary Effects on the Abundances of Polycyclic Aromatic Hydrocarbons and Supernova-Condensed Dust in Galaxies". In: *ApJ* 672.1, pp. 214–243. DOI: 10.1086/523621. arXiv: 0708.0790 [astro-ph] (cit. on p. 59).

Galliano, Frédéric, Maud Galametz, and Anthony P. Jones (Sept. 2018). "The Interstellar Dust Properties of Nearby Galaxies". In: *ARA&A* 56, pp. 673–713. DOI: 10.1146/annurev-astro-081817-051900. arXiv: 1711.07434 [astro-ph.GA] (cit. on pp. 45, 52).

Gamow, G. (Oct. 1948a). "The Evolution of the Universe". In: *Nature* 162.4122, pp. 680–682. DOI: 10.1038/162680a0 (cit. on p. 36).

– (Aug. 1948b). "The Origin of Elements and the Separation of Galaxies". In: *Physical Review* 74.4, pp. 505–506. DOI: 10.1103/PhysRev.74.505.2 (cit. on p. 36).

Garcia-Vargas, M. L., A. Bressan, and A. I. Diaz (July 1995). "Predicted emission lines from giant HII regions ionized by aging star clusters." In: *A&AS* 112, p. 35 (cit. on p. 68).

Garn, Timothy and Philip N. Best (Nov. 2010a). "Predicting dust extinction from the stellar mass of a galaxy". In: *MNRAS* 409.1, pp. 421–432. DOI: 10.1111/j.1365-2966.2010.17321.x. arXiv: 1007.1145 [astro-ph.GA] (cit. on pp. 3, 107, 108).

– (Nov. 2010b). "Predicting dust extinction from the stellar mass of a galaxy". In: *MNRAS* 409.1, pp. 421–432. DOI: 10.1111/j.1365-2966.2010.17321.x. arXiv: 1007.1145 [astro-ph.GA] (cit. on p. 107).

Georgi, Howard and S. L. Glashow (Feb. 1974). "Unity of All Elementary-Particle Forces". In: *Phys. Rev. Lett.* 32 (8), pp. 438–441. DOI: 10.1103/PhysRevLett.32.438. URL: https://link.aps.org/doi/10.1103/PhysRevLett.32.438 (cit. on p. 36).

Giavalisco, M. et al. (Jan. 2004). "The Great Observatories Origins Deep Survey: Initial Results from Optical and Near-Infrared Imaging". In: *ApJ* 600.2, pp. L93–L98. DOI: 10.1086/379232. arXiv: astro-ph/0309105 [astro-ph] (cit. on p. 42).

Giovanelli, Riccardo et al. (Dec. 2005). "The Arecibo Legacy Fast ALFA Survey. I. Science Goals, Survey Design, and Strategy". In: *AJ* 130.6, pp. 2598–2612. DOI: 10.1086/497431. arXiv: astro-ph/0508301 [astro-ph] (cit. on p. 41).

Girardi, L. et al. (Feb. 2000). "Evolutionary tracks and isochrones for low- and intermediate-mass stars: From 0.15 to 7 M_{sun}, and from Z=0.0004 to 0.03". In: *A&AS* 141, pp. 371–383. DOI: 10.1051/aas:2000126. arXiv: astro-ph/9910164 [astro-ph] (cit. on pp. 48, 52).

Gonzalez, O. A. et al. (June 2020). "MOONS Surveys of the Milky Way and its Satellites". In: *The Messenger* 180, pp. 18–23. DOI: 10.18727/0722-6691/5196. arXiv: 2009.00635 [astro-ph.GA] (cit. on pp. 146, 147).

Gonzalez-Perez, V. et al. (Feb. 2013). "The ultraviolet colours and dust attenuation of Lyman-break galaxies". In: *MNRAS* 429.2, pp. 1609–1625. DOI: 10.1093/mnras/sts446. arXiv: 1209.2152 [astro-ph.CO] (cit. on p. 63).

Gordon, Karl D., Daniela Calzetti, and Adolf N. Witt (Oct. 1997). "Dust in Starburst Galaxies". In: *ApJ* 487.2, pp. 625–635. DOI: 10.1086/304654. arXiv: astro-ph/9705043 [astro-ph] (cit. on p. 65).

Granato, G. L. et al. (Oct. 2000). "The Infrared Side of Galaxy Formation. I. The Local Universe in the Semianalytical Framework". In: *ApJ* 542.2, pp. 710–730. DOI: 10.1086/317032. arXiv: astro-ph/0001308 [astro-ph] (cit. on p. 63).

Grevesse, N. et al. (July 2010). "The chemical composition of the Sun". In: *Ap&SS* 328.1-2, pp. 179–183. DOI: 10.1007/s10509-010-0288-z (cit. on pp. 112, 126).

Guaita, L. et al. (Mar. 2013). "Magellan/MMIRS near-infrared multi-object spectroscopy of nebular emission from star-forming galaxies at $2 < z < 3$". In: *A&A* 551, A93, A93. DOI: 10.1051/0004-6361/201220013. arXiv: 1301.5600 [astro-ph.CO] (cit. on p. 68).

Gutkin, Julia, Stéphane Charlot, and Gustavo Bruzual (Oct. 2016). "Modelling the nebular emission from primeval to present-day star-forming galaxies". In: *MNRAS* 462.2, pp. 1757–1774. DOI: 10.1093/mnras/stw1716. arXiv: 1607.06086 [astro-ph.GA] (cit. on pp. 68, 112).

Hagen, Lea M. Z. et al. (Apr. 2017). "Swift Ultraviolet Survey of the Magellanic Clouds (SUMaC) - I. Shape of the ultraviolet dust extinction law and recent star formation history of the Small Magellanic Cloud". In: *MNRAS* 466.4, pp. 4540–4557. DOI: 10.1093/mnras/stw2954. arXiv: 1611.00064 [astro-ph.GA] (cit. on pp. 61, 62).

Hainline, Kevin N. et al. (Aug. 2009). "Rest-Frame Optical Spectra of Three Strongly Lensed Galaxies at z ~2". In: *ApJ* 701.1, pp. 52–65. DOI: 10.1088/0004-637X/701/1/52. arXiv: 0906.2197 [astro-ph.CO] (cit. on p. 68).

Hammer, F. et al. (Mar. 2021). "MOSAIC on the ELT: High-multiplex Spectroscopy to Unravel the Physics of Stars and Galaxies from the Dark Ages to the Present Day". In: *The Messenger* 182, pp. 33–37. DOI: 10.18727/0722-6691/5220. arXiv: 2011.03549 [astro-ph.GA] (cit. on p. 176).

Harikane, Yuichi et al. (June 2020). "Large Population of ALMA Galaxies at $z > 6$ with Very High [O iii] 88 μm to [C ii] 158 μm Flux Ratios: Evidence of Extremely High Ionization Parameter or PDR Deficit?" In: *ApJ* 896.2, 93, p. 93. DOI: 10.3847/1538-4357/ab94bd. arXiv: 1910.10927 [astro-ph.GA] (cit. on pp. 121–123).

Harrison, C. M. et al. (Feb. 2018). "AGN outflows and feedback twenty years on". In: *Nature Astronomy* 2, pp. 198–205. DOI: 10.1038/s41550-018-0403-6. arXiv: 1802.10306 [astro-ph.GA] (cit. on p. 43).

Heckman, T. M. (July 1980). "An optical and radio survey of the nuclei of bright galaxies. Activity in normal galactic nuclei." In: *A&A* 500, pp. 187–199 (cit. on p. 71).

Hippelein, H. et al. (Apr. 2003). "Star forming rates between $z = 0.25$ and $z = 1.2$ from the CADIS emission line survey". In: *A&A* 402, pp. 65–78. DOI: 10.1051/0004-6361:20021898. arXiv: astro-ph/0302116 [astro-ph] (cit. on pp. 4, 113, 114, 121).

Ho, Luis C., Alexei V. Filippenko, and Wallace L. W. Sargent (Oct. 1997). "A Search for "Dwarf" Seyfert Nuclei. III. Spectroscopic Parameters and Properties of the Host Galaxies". In: *ApJS* 112.2, pp. 315–390. DOI: 10.1086/313041. arXiv: astro-ph/9704107 [astro-ph] (cit. on p. 71).

Hogan, Robert, Malcolm Fairbairn, and Navin Seeburn (May 2015). "GAz: a genetic algorithm for photometric redshift estimation". In: *MNRAS* 449.2, pp. 2040–2046. DOI: 10.1093/mnras/stv430. arXiv: 1412.5997 [astro-ph.IM] (cit. on p. 179).

Hurley, P. D. et al. (Jan. 2017). "HELP: XID+, the probabilistic de-blender for Herschel SPIRE maps". In: *MNRAS* 464.1, pp. 885–896. DOI: 10.1093/mnras/stw2375. arXiv: 1606.05770 [astro-ph.GA] (cit. on p. 86).

Ibar, E. et al. (Oct. 2013). "Herschel reveals the obscured star formation in HiZELS Hα emitters at z = 1.47". In: *MNRAS* 434.4, pp. 3218–3235. DOI: 10.1093/mnras/stt1258. arXiv: 1307.3556 [astro-ph.CO] (cit. on p. 107).

Ilbert, O. et al. (Oct. 2006). "Accurate photometric redshifts for the CFHT legacy survey calibrated using the VIMOS VLT deep survey". In: *A&A* 457.3, pp. 841–856. DOI: 10.1051/0004-6361:20065138. arXiv: astro-ph/0603217 [astro-ph] (cit. on p. 49).

Inoue, A. K. et al. (Jan. 2014). "ALMA Will Determine the Spectroscopic Redshift z > 8 with FIR [O III] Emission Lines". In: *ApJ* 780.2, L18, p. L18. DOI: 10.1088/2041-8205/780/2/L18. arXiv: 1312.0684 [astro-ph.GA] (cit. on p. 180).

Ivanov, Valentin D. et al. (Sept. 2019). "MUSE library of stellar spectra". In: *A&A* 629, A100, A100. DOI: 10.1051/0004-6361/201936178. arXiv: 1908.02717 [astro-ph.SR] (cit. on p. 48).

Izotov, Yuri I. and Trinh X. Thuan (Feb. 1999). "Heavy-Element Abundances in Blue Compact Galaxies". In: *ApJ* 511.2, pp. 639–659. DOI: 10.1086/306708. arXiv: astro-ph/9811387 [astro-ph] (cit. on p. 68).

Jansen, F. et al. (Jan. 2001). "XMM-Newton observatory. I. The spacecraft and operations". In: *A&A* 365, pp. L1–L6. DOI: 10.1051/0004-6361:20000036 (cit. on p. 40).

Jin, Shuowen et al. (Sept. 2018). ""Super-deblended" Dust Emission in Galaxies. II. Far-IR to (Sub)millimeter Photometry and High-redshift Galaxy Candidates in the Full COSMOS Field". In: *ApJ* 864.1, 56, p. 56. DOI: 10.3847/1538-4357/aad4af. arXiv: 1807.04697 [astro-ph.GA] (cit. on pp. 85–88, 90, 91, 100).

Johnson, Benjamin D. et al. (June 2021). "Stellar Population Inference with Prospector". In: *ApJS* 254.2, 22, p. 22. DOI: 10.3847/1538-4365/abef67. arXiv: 2012.01426 [astro-ph.GA] (cit. on pp. 48, 65).

Jones, A. P. et al. (June 2017). "The global dust modelling framework THEMIS". In: *A&A* 602, A46, A46. DOI: 10.1051/0004-6361/201630225. arXiv: 1703.00775 [astro-ph.GA] (cit. on p. 62).

Jonsson, Patrik et al. (Jan. 2006). "Simulations of Dust in Interacting Galaxies. I. Dust Attenuation". In: *ApJ* 637.1, pp. 255–268. DOI: 10.1086/497567. arXiv: astro-ph/0503135 [astro-ph] (cit. on p. 63).

Kaasinen, Melanie et al. (July 2018). "The ionization parameter of star-forming galaxies evolves with the specific star formation rate". In: *MNRAS* 477.4, pp. 5568–5589. DOI: 10.1093/mnras/sty1012. arXiv: 1804.10621 [astro-ph.GA] (cit. on pp. 132, 135).

Kappen, H. J. and H. C. Ruiz (Mar. 2016). "Adaptive Importance Sampling for Control and Inference". In: *Journal of Statistical Physics* 162.5, pp. 1244–1266. DOI: 10.1007/s10955-016-1446-7. arXiv: 1505.01874 [cs.SY] (cit. on p. 180).

Karim, A. et al. (Apr. 2011). "The Star Formation History of Mass-selected Galaxies in the COSMOS Field". In: *ApJ* 730.2, 61, p. 61. DOI: 10.1088/0004-637X/730/2/61. arXiv: 1011.6370 [astro-ph.CO] (cit. on p. 104).

Kashino, D. et al. (Nov. 2013). "The FMOS-COSMOS Survey of Star-forming Galaxies at z ∼ 1.6. I. Hα-based Star Formation Rates and Dust Extinction". In: *ApJ* 777.1, L8, p. L8. DOI: 10.1088/2041-8205/777/1/L8. arXiv: 1309.4774 [astro-ph.CO] (cit. on pp. 3, 8, 42, 68, 77, 87, 91, 163, 174).

Kashino, D. et al. (Jan. 2017). "The FMOS-COSMOS Survey of Star-forming Galaxies at z ≈ 1.6. IV. Excitation State and Chemical Enrichment of the Interstellar Medium". In: *ApJ* 835.1, 88, p. 88. DOI: 10.3847/1538-4357/835/1/88. arXiv: 1604.06802 [astro-ph.GA] (cit. on pp. 71, 72, 94, 121, 128–131, 169).

Kashino, Daichi et al. (Mar. 2019). "The FMOS-COSMOS Survey of Star-forming Galaxies at z∼1.6. VI. Redshift and Emission-line Catalog and Basic Properties of Star-forming Galaxies". In: *ApJS* 241.1, 10, p. 10. DOI: 10.3847/1538-4365/ab06c4. arXiv: 1812.01529 [astro-ph.GA] (cit. on pp. 69, 91, 92, 149).

Kauffmann, Guinevere et al. (May 2003a). "Stellar masses and star formation histories for 10^5 galaxies from the Sloan Digital Sky Survey". In: *MNRAS* 341.1, pp. 33–53. DOI: 10.1046/j.1365-8711.2003.06291.x. arXiv: astro-ph/0204055 [astro-ph] (cit. on pp. 65, 73, 74).

Kauffmann, Guinevere et al. (Dec. 2003b). "The host galaxies of active galactic nuclei". In: *MNRAS* 346.4, pp. 1055–1077. DOI: 10.1111/j.1365-2966.2003.07154.x. arXiv: astro-ph/0304239 [astro-ph] (cit. on pp. 68, 71, 72, 128–130, 169).

Kennicutt R. C., Jr. (Sept. 1983). "The rate of star formation in normal disk galaxies." In: *ApJ* 272, pp. 54–67. DOI: 10.1086/161261 (cit. on p. 67).

Kennicutt Robert C., Jr. (Apr. 1992). "The Integrated Spectra of Nearby Galaxies: General Properties and Emission-Line Spectra". In: *ApJ* 388, p. 310. DOI: 10.1086/171154 (cit. on pp. 68, 112).

– (Jan. 1998). "Star Formation in Galaxies Along the Hubble Sequence". In: *ARA&A* 36, pp. 189–232. DOI: 10.1146/annurev.astro.36.1.189. arXiv: astro-ph/9807187 [astro-ph] (cit. on pp. 4, 67, 81, 113, 114, 167).

Kennicutt Robert C., Jr. et al. (July 2000). "An Empirical Test and Calibration of H II Region Diagnostics". In: *ApJ* 537.2, pp. 589–612. DOI: 10.1086/309075. arXiv: astro-ph/0002180 [astro-ph] (cit. on p. 112).

Kennicutt, Robert C. and Neal J. Evans (Sept. 2012). "Star Formation in the Milky Way and Nearby Galaxies". In: *ARA&A* 50, pp. 531–608. DOI: 10.1146/annurev-astro-081811-125610. arXiv: 1204.3552 [astro-ph.GA] (cit. on p. 53).

Kewley, L. J. and M. A. Dopita (Sept. 2002). "Using Strong Lines to Estimate Abundances in Extragalactic HII Regions and Starburst Galaxies". In: *ApJS* 142.1, pp. 35–52. DOI: 10.1086/341326. arXiv: astro-ph/0206495 [astro-ph] (cit. on pp. 68, 111).

Kewley, L. J. et al. (July 2001). "Theoretical Modeling of Starburst Galaxies". In: *ApJ* 556.1, pp. 121–140. DOI: 10.1086/321545. arXiv: astro-ph/0106324 [astro-ph] (cit. on pp. 128, 130).

Kewley, Lisa J. and Sara L. Ellison (July 2008). "Metallicity Calibrations and the Mass-Metallicity Relation for Star-forming Galaxies". In: *ApJ* 681.2, pp. 1183–1204. DOI: 10.1086/587500. arXiv: 0801.1849 [astro-ph] (cit. on pp. 68, 110).

Kewley, Lisa J., David C. Nicholls, and Ralph S. Sutherland (Aug. 2019). "Understanding Galaxy Evolution Through Emission Lines". In: *ARA&A* 57, pp. 511–570. DOI: 10.1146/annurev-astro-081817-051832. arXiv: 1910.09730 [astro-ph.GA] (cit. on pp. 71, 72).

Kewley, Lisa J. et al. (Nov. 2006). "The host galaxies and classification of active galactic nuclei". In: *MNRAS* 372.3, pp. 961–976. DOI: 10.1111/j.1365-2966.2006.10859.x. arXiv: astro-ph/0605681 [astro-ph] (cit. on pp. 71, 72).

Kewley, Lisa J. et al. (Sept. 2013a). "The Cosmic BPT Diagram: Confronting Theory with Observations". In: *ApJ* 774.1, L10, p. L10. DOI: 10.1088/2041-8205/774/1/L10. arXiv: 1307.0514 [astro-ph.CO] (cit. on pp. 72, 112, 128–130, 169).

Kewley, Lisa J. et al. (Aug. 2013b). "THEORETICAL EVOLUTION OF OPTICAL STRONG LINES ACROSS COSMIC TIME". In: *The Astrophysical Journal* 774.2, p. 100. DOI: 10.1088/0004-637x/774/2/100. URL: https://doi.org/10.1088%2F0004-637x%2F774%2F2%2F100 (cit. on pp. 71, 112, 129).

Kinney, Anne L. et al. (July 1994). "The Reddening Law outside the Local Group Galaxies: The Case of NGC 7552 and NGC 5236". In: *ApJ* 429, p. 172. DOI: 10.1086/174309 (cit. on p. 63).

Kobulnicky, Henry A., Jr. Kennicutt Robert C., and James L. Pizagno (Apr. 1999). "On Measuring Nebular Chemical Abundances in Distant Galaxies Using Global Emission-Line Spectra". In: *ApJ* 514.2, pp. 544–557. DOI: 10.1086/306987. arXiv: astro-ph/9811006 [astro-ph] (cit. on p. 68).

Kobulnicky, Henry A. and Lisa J. Kewley (Dec. 2004). "Metallicities of $0.3 < z < 1.0$ Galaxies in the GOODS-North Field". In: *ApJ* 617.1, pp. 240–261. DOI: 10.1086/425299. arXiv: astro-ph/0408128 [astro-ph] (cit. on p. 111).

Kojima, Takashi et al. (June 2017). "Evolution of N/O abundance ratios and ionization parameters from z ~ 0 to 2 investigated by the direct temperature method*†". In: *PASJ* 69.3, 44, p. 44. DOI: 10.1093/pasj/psx017. arXiv: 1605.03436 [astro-ph.GA] (cit. on p. 129).

Koyama, Yusei et al. (Jan. 2019). "On the different levels of dust attenuation to nebular and stellar light in star-forming galaxies". In: *PASJ* 71.1, 8, p. 8. DOI: 10.1093/pasj/psy113. arXiv: 1809.03715 [astro-ph.GA] (cit. on p. 107).

Kriek, Mariska and Charlie Conroy (Sept. 2013). "The Dust Attenuation Law in Distant Galaxies: Evidence for Variation with Spectral Type". In: *ApJ* 775.1, L16, p. L16. DOI: 10.1088/2041-8205/775/1/L16. arXiv: 1308.1099 [astro-ph.CO] (cit. on pp. 61, 66).

Kriek, Mariska et al. (Apr. 2008). "A Near-Infrared Spectroscopic Survey of K-Selected Galaxies at z ~2.3: Redshifts and Implications for Broadband Photometric Studies". In: *ApJ* 677.1, pp. 219–237. DOI: 10.1086/528945. arXiv: 0801.1110 [astro-ph] (cit. on p. 58).

Kriek, Mariska et al. (June 2015). "The MOSFIRE Deep Evolution Field (MOSDEF) Survey: Rest-frame Optical Spectroscopy for ~1500 H-selected Galaxies at 1.37 <

z < 3.8". In: *ApJS* 218.2, 15, p. 15. DOI: 10.1088/0067-0049/218/2/15. arXiv: 1412.1835 [astro-ph.GA] (cit. on p. 42).

Kroupa, Pavel (Apr. 2001). "On the variation of the initial mass function". In: *MNRAS* 322.2, pp. 231–246. DOI: 10.1046/j.1365-8711.2001.04022.x. arXiv: astro-ph/0009005 [astro-ph] (cit. on pp. 48, 53).

Kurucz, R. L. (Jan. 1992). "Model Atmospheres for Population Synthesis". In: *The Stellar Populations of Galaxies*. Ed. by Beatriz Barbuy and Alvio Renzini. Vol. 149, p. 225 (cit. on p. 48).

La Mura, Giovanni et al. (Nov. 2017). "Models of Emission-Line Profiles and Spectral Energy Distributions to Characterize the Multi-Frequency Properties of Active Galactic Nuclei". In: *Atoms* 5.4, p. 43. DOI: 10.3390/atoms5040043. arXiv: 1710.10211 [astro-ph.GA] (cit. on p. 70).

Lagos, Claudia del P. et al. (Dec. 2018). "Shark: introducing an open source, free, and flexible semi-analytic model of galaxy formation". In: *MNRAS* 481.3, pp. 3573–3603. DOI: 10.1093/mnras/sty2440. arXiv: 1807.11180 [astro-ph.GA] (cit. on p. 55).

Laigle, C. et al. (June 2016). "The COSMOS2015 Catalog: Exploring the 1 < z < 6 Universe with Half a Million Galaxies". In: *ApJS* 224, 24, p. 24. DOI: 10.3847/0067-0049/224/2/24. arXiv: 1604.02350 (cit. on pp. 3, 8, 83–85, 92, 139, 163, 166–168, 171, 174).

Lang, Robert H. et al. (July 2003). "First results from the HI Jodrell All Sky Survey: inclination-dependent selection effects in a 21-cm blind survey". In: *MNRAS* 342.3, pp. 738–758. DOI: 10.1046/j.1365-8711.2003.06535.x. arXiv: astro-ph/0302317 [astro-ph] (cit. on p. 41).

Lara-López, M. A. et al. (Oct. 2010). "A fundamental plane for field star-forming galaxies". In: *A&A* 521, L53, p. L53. DOI: 10.1051/0004-6361/201014803. arXiv: 1005.0509 [astro-ph.CO] (cit. on p. 110).

Le Borgne, J. -F. et al. (May 2003). "STELIB: A library of stellar spectra at R ~2000". In: *A&A* 402, pp. 433–442. DOI: 10.1051/0004-6361:20030243. arXiv: astro-ph/0302334 [astro-ph] (cit. on pp. 48, 53).

Le Floc'h, Emeric et al. (Sept. 2009). "Deep Spitzer 24 μm COSMOS Imaging. I. The Evolution of Luminous Dusty Galaxies—Confronting the Models". In: *ApJ* 703.1, pp. 222–239. DOI: 10.1088/0004-637X/703/1/222. arXiv: 0909.4303 [astro-ph.CO] (cit. on p. 87).

Lee, Bomee et al. (Feb. 2018). "The Intrinsic Characteristics of Galaxies on the SFR-M$_*$ Plane at 1.2 < z < 4: I. The Correlation between Stellar Age, Central Density, and Position Relative to the Main Sequence". In: *ApJ* 853.2, 131, p. 131. DOI: 10.3847/1538-4357/aaa40f. arXiv: 1706.02311 [astro-ph.GA] (cit. on p. 38).

Lee, Henry et al. (Aug. 2006). "On Extending the Mass-Metallicity Relation of Galaxies by 2.5 Decades in Stellar Mass". In: *ApJ* 647.2, pp. 970–983. DOI: 10.1086/505573. arXiv: astro-ph/0605036 [astro-ph] (cit. on p. 110).

Lehnert, Matthew D. and Timothy M. Heckman (May 1994). "Emission-Line Ratios of the Integrated Spectra of Galaxies: Evidence for a Diffuse Ionized Medium in Other Galaxies?" In: *ApJ* 426, p. L27. DOI: 10.1086/187331 (cit. on p. 68).

Leja, J. et al. (2017). "Deriving Physical Properties from Broadband Photometry with Prospector: Description of the Model and a Demonstration of its Accuracy Using 129 Galaxies in the Local Universe". In: *ApJ* 837, p. 170. DOI: 10.3847/1538-4357/aa5ffe. eprint: 1609.09073 (cit. on pp. 48, 65).

Leja, Joel et al. (May 2019). "How to Measure Galaxy Star Formation Histories. II. Nonparametric Models". In: *ApJ* 876.1, 3, p. 3. DOI: 10.3847/1538-4357/ab133c. arXiv: 1811.03637 [astro-ph.GA] (cit. on pp. 54, 55, 65, 66, 97).

Lejeune, Th., F. Cuisinier, and R. Buser (Oct. 1997). "Standard stellar library for evolutionary synthesis. I. Calibration of theoretical spectra". In: *A&AS* 125, pp. 229–246. DOI: 10.1051/aas:1997373. arXiv: astro-ph/9701019 [astro-ph] (cit. on pp. 43, 44).

Lemaître, G. (Mar. 1931a). "Expansion of the universe, A homogeneous universe of constant mass and increasing radius accounting for the radial velocity of extra-galactic nebulae". In: *MNRAS* 91, pp. 483–490. DOI: 10.1093/mnras/91.5.483 (cit. on p. 35).

– (May 1931b). "The Beginning of the World from the Point of View of Quantum Theory." In: *Nature* 127.3210, p. 706. DOI: 10.1038/127706b0 (cit. on p. 35).

Lequeux, J. et al. (Dec. 1979). "Reprint of 1979A&A....80..155L. Chemical composition and evolution of irregular and blue compact galaxies." In: *A&A* 500, pp. 145–156 (cit. on p. 110).

Lequeux, James (2005). *The Interstellar Medium*. DOI: 10.1007/b137959 (cit. on p. 44).

Levesque, Emily M., Lisa J. Kewley, and Kirsten L. Larson (Feb. 2010). "Theoretical Modeling of Star-Forming Galaxies. I. Emission-Line Diagnostic Grids for Local and Low-Metallicity Galaxies". In: *AJ* 139.2, pp. 712–727. DOI: 10.1088/0004-6256/139/2/712. arXiv: 0908.0460 [astro-ph.GA] (cit. on p. 129).

Linde, A. D. (Feb. 1982). "A new inflationary universe scenario: A possible solution of the horizon, flatness, homogeneity, isotropy and primordial monopole problems". In: *Physics Letters B* 108.6, pp. 389–393. DOI: 10.1016/0370-2693(82)91219-9 (cit. on p. 36).

Liu, Guilin et al. (Dec. 2013). "Extinction and Dust Geometry in M83 H II Regions: An Hubble Space Telescope/WFC3 Study". In: *ApJ* 778.2, L41, p. L41. DOI: 10.1088/2041-8205/778/2/L41. arXiv: 1311.0871 [astro-ph.CO] (cit. on p. 98).

Lo Faro, B. et al. (Dec. 2017). "Characterizing the UV-to-NIR shape of the dust attenuation curve of IR luminous galaxies up to z ~ 2". In: *MNRAS* 472.2, pp. 1372–1391. DOI: 10.1093/mnras/stx1901. arXiv: 1707.09805 [astro-ph.GA] (cit. on pp. 62, 98, 107).

Lodders, Katharina (Jan. 2010). "Solar System Abundances of the Elements". In: *Astrophysics and Space Science Proceedings* 16, p. 379. DOI: 10.1007/978-3-642-10352-0_8. arXiv: 1010.2746 [astro-ph.SR] (cit. on pp. 125, 126).

Lower, Sidney et al. (Nov. 2020). "How Well Can We Measure the Stellar Mass of a Galaxy: The Impact of the Assumed Star Formation History Model in SED Fitting". In: *ApJ* 904.1, 33, p. 33. DOI: 10.3847/1538-4357/abbfa7. arXiv: 2006.03599 [astro-ph.GA] (cit. on p. 54).

Lutz, D. et al. (Aug. 2011). "PACS Evolutionary Probe (PEP) - A Herschel key program". In: *A&A* 532, A90, A90. DOI: 10.1051/0004-6361/201117107. arXiv: 1106.3285 [astro-ph.CO] (cit. on p. 86).

Ly, Chun et al. (Mar. 2007). "The Luminosity Function and Star Formation Rate between Redshifts of 0.07 and 1.47 for Narrowband Emitters in the Subaru Deep Field". In: *ApJ* 657.2, pp. 738–759. DOI: 10.1086/510828. arXiv: astro-ph/0610846 [astro-ph] (cit. on pp. 4, 113, 114, 121).

Ma, Jingzhe et al. (Dec. 2015). "Cold gas and a Milky Way-type 2175-Å bump in a metal-rich and highly depleted absorption system". In: *MNRAS* 454.2, pp. 1751–1766. DOI: 10.1093/mnras/stv2073. arXiv: 1509.01593 [astro-ph.GA] (cit. on p. 61).

Ma, Jingzhe et al. (Dec. 2017). "Quasar 2175 Å dust absorbers - I. Metallicity, depletion pattern and kinematics". In: *MNRAS* 472.2, pp. 2196–2220. DOI: 10.1093/mnras/stx2117. arXiv: 1708.04200 [astro-ph.GA] (cit. on p. 61).

Madau, Piero and Mark Dickinson (Aug. 2014). "Cosmic Star-Formation History". In: *ARA&A* 52, pp. 415–486. DOI: 10.1146/annurev-astro-081811-125615. arXiv: 1403.0007 [astro-ph.CO] (cit. on pp. 53, 55).

Maiolino, R. and F. Mannucci (Feb. 2019). "De re metallica: the cosmic chemical evolution of galaxies". In: *A&A Rev.* 27.1, 3, p. 3. DOI: 10.1007/s00159-018-0112-2. arXiv: 1811.09642 [astro-ph.GA] (cit. on pp. 72, 149).

Maiolino, R. et al. (June 2020). "MOONRISE: The Main MOONS GTO Extragalactic Survey". In: *The Messenger* 180, pp. 24–29. DOI: 10.18727/0722-6691/5197. arXiv: 2009.00644 [astro-ph.GA] (cit. on pp. 72, 147–152, 176, 177).

Małek, K. et al. (Nov. 2018). "HELP: modelling the spectral energy distributions of Herschel detected galaxies in the ELAIS N1 field". In: *A&A* 620, A50, A50. DOI: 10.1051/0004-6361/201833131. arXiv: 1809.00529 [astro-ph.GA] (cit. on pp. 49, 82, 96, 98, 99).

Mannucci, F. et al. (Nov. 2010). "A fundamental relation between mass, star formation rate and metallicity in local and high-redshift galaxies". In: *MNRAS* 408.4, pp. 2115–2127. DOI: 10.1111/j.1365-2966.2010.17291.x. arXiv: 1005.0006 [astro-ph.CO] (cit. on pp. 110–112, 149, 164).

Maraston, C. and G. Strömbäck (Dec. 2011). "Stellar population models at high spectral resolution". In: *MNRAS* 418.4, pp. 2785–2811. DOI: 10.1111/j.1365-2966.2011.19738.x. arXiv: 1109.0543 [astro-ph.CO] (cit. on pp. 52, 158, 159).

Maraston, Claudia (Sept. 2005). "Evolutionary population synthesis: models, analysis of the ingredients and application to high-z galaxies". In: *MNRAS* 362.3, pp. 799–825. DOI: 10.1111/j.1365-2966.2005.09270.x. arXiv: astro-ph/0410207 [astro-ph] (cit. on pp. 52, 155, 158).

Marigo, P. et al. (May 2008). "Evolution of asymptotic giant branch stars. II. Optical to far-infrared isochrones with improved TP-AGB models". In: *A&A* 482.3, pp. 883–905. DOI: 10.1051/0004-6361:20078467. arXiv: 0711.4922 [astro-ph] (cit. on p. 52).

Marino, R. A. et al. (Nov. 2013). "The O3N2 and N2 abundance indicators revisited: improved calibrations based on CALIFA and T_e-based literature data". In: *A&A* 559, A114, A114. DOI: 10.1051/0004-6361/201321956. arXiv: 1307.5316 [astro-ph.CO] (cit. on p. 111).

Martin, D. Christopher et al. (Jan. 2005). "The Galaxy Evolution Explorer: A Space Ultraviolet Survey Mission". In: *ApJ* 619.1, pp. L1–L6. DOI: 10.1086/426387. arXiv: astro-ph/0411302 [astro-ph] (cit. on p. 40).

Maschietto, F. et al. (Sept. 2008). "[OIII] emitters in the field of the MRC0316-257 protocluster". In: *MNRAS* 389.3, pp. 1223–1232. DOI: 10.1111/j.1365-2966.2008.13571.x. arXiv: 0807.0152 [astro-ph] (cit. on p. 113).

Masters, Daniel, Andreas Faisst, and Peter Capak (Sept. 2016). "A Tight Relation between N/O Ratio and Galaxy Stellar Mass Can Explain the Evolution of Strong Emission Line Ratios with Redshift". In: *ApJ* 828.1, 18, p. 18. DOI: 10.3847/0004-637X/828/1/18. arXiv: 1605.04314 [astro-ph.GA] (cit. on p. 129).

Masters, Daniel et al. (Apr. 2014). "Physical Properties of Emission-line Galaxies at z ∼ 2 from Near-infrared Spectroscopy with Magellan FIRE". In: *ApJ* 785.2, 153, p. 153. DOI: 10.1088/0004-637X/785/2/153. arXiv: 1402.0510 [astro-ph.GA] (cit. on p. 129).

Masters, Daniel et al. (Nov. 2015). "Mapping the Galaxy Color-Redshift Relation: Optimal Photometric Redshift Calibration Strategies for Cosmology Surveys". In: *ApJ* 813.1, 53, p. 53. DOI: 10.1088/0004-637X/813/1/53. arXiv: 1509.03318 [astro-ph.CO] (cit. on p. 179).

Mathews, William G. and Fabrizio Brighenti (Jan. 2003). "Hot Gas in and around Elliptical Galaxies". In: *ARA&A* 41, pp. 191–239. DOI: 10.1146/annurev.astro.41.090401.094542. arXiv: astro-ph/0309553 [astro-ph] (cit. on p. 42).

McCracken, H. J. et al. (Aug. 2012). "UltraVISTA: a new ultra-deep near-infrared survey in COSMOS". In: *A&A* 544, A156, A156. DOI: 10.1051/0004-6361/201219507. arXiv: 1204.6586 [astro-ph.CO] (cit. on p. 83).

Meynet, G. and A. Maeder (Sept. 2000). "Stellar evolution with rotation. V. Changes in all the outputs of massive star models". In: *A&A* 361, pp. 101–120. arXiv: astro-ph/0006404 [astro-ph] (cit. on p. 52).

Moriwaki, Kana et al. (Nov. 2018). "The distribution and physical properties of high-redshift [O III] emitters in a cosmological hydrodynamics simulation". In: *MNRAS* 481.1, pp. L84–L88. DOI: 10.1093/mnrasl/sly167. arXiv: 1805.07062 [astro-ph.GA] (cit. on pp. 121, 123).

Moustakas, John, Jr. Kennicutt Robert C., and Christy A. Tremonti (May 2006). "Optical Star Formation Rate Indicators". In: *ApJ* 642.2, pp. 775–796. DOI: 10.1086/500964. arXiv: astro-ph/0511730 [astro-ph] (cit. on p. 113).

Murakami, Hiroshi et al. (Oct. 2007). "The Infrared Astronomical Mission AKARI*". In: *PASJ* 59, S369–S376. DOI: 10.1093/pasj/59.sp2.S369. arXiv: 0708.1796 [astro-ph] (cit. on p. 41).

Nagao, T., R. Maiolino, and A. Marconi (Nov. 2006). "Gas metallicity diagnostics in star-forming galaxies". In: *A&A* 459.1, pp. 85–101. DOI: 10.1051/0004-6361:20065216. arXiv: astro-ph/0603580 [astro-ph] (cit. on p. 68).

Narayanan, Desika et al. (Feb. 2018). "The IRX-β dust attenuation relation in cosmological galaxy formation simulations". In: *MNRAS* 474.2, pp. 1718–1736. DOI: 10.1093/mnras/stx2860. arXiv: 1705.05858 [astro-ph.GA] (cit. on pp. 62, 63, 66).

Natale, Giovanni et al. (May 2015). "Predicting the stellar and non-equilibrium dust emission spectra of high-resolution simulated galaxies with DART-RAY". In: *MNRAS* 449.1, pp. 243–267. DOI: 10.1093/mnras/stv286. arXiv: 1502.03315 [astro-ph.GA] (cit. on p. 63).

Nersesian, A. et al. (Apr. 2019). "Old and young stellar populations in DustPedia galaxies and their role in dust heating". In: *A&A* 624, A80, A80. DOI: 10.1051/0004-6361/201935118. arXiv: 1903.05933 [astro-ph.GA] (cit. on pp. 48, 49, 82).

Nersesian, Angelos et al. (May 2020). "High-resolution, 3D radiative transfer modelling. III. The DustPedia barred galaxies". In: *A&A* 637, A25, A25. DOI: 10.1051/0004-6361/201936176. arXiv: 2004.03616 [astro-ph.GA] (cit. on p. 48).

Neugebauer, G. et al. (Mar. 1984). "The Infrared Astronomical Satellite (IRAS) mission." In: *ApJ* 278, pp. L1–L6. DOI: 10.1086/184209 (cit. on p. 41).

Nicholls, David C. et al. (Apr. 2017). "Abundance scaling in stars, nebulae and galaxies". In: *MNRAS* 466.4, pp. 4403–4422. DOI: 10.1093/mnras/stw3235. arXiv: 1612.03546 [astro-ph.GA] (cit. on pp. 68, 69, 71, 112, 125, 126, 129).

Nieva, M. -F. and N. Przybilla (Mar. 2012). "Present-day cosmic abundances. A comprehensive study of nearby early B-type stars and implications for stellar and Galactic evolution and interstellar dust models". In: *A&A* 539, A143, A143. DOI: 10.1051/0004-6361/201118158. arXiv: 1203.5787 [astro-ph.SR] (cit. on p. 126).

Noeske, K. G. et al. (May 2007). "Star Formation in AEGIS Field Galaxies since z=1.1: The Dominance of Gradually Declining Star Formation, and the Main Sequence of Star-forming Galaxies". In: *ApJ* 660.1, pp. L43–L46. DOI: 10.1086/517926. arXiv: astro-ph/0701924 [astro-ph] (cit. on p. 38).

Noll, S. et al. (Dec. 2009). "Analysis of galaxy spectral energy distributions from far-UV to far-IR with CIGALE: studying a SINGS test sample". In: *A&A* 507.3, pp. 1793–1813. DOI: 10.1051/0004-6361/200912497. arXiv: 0909.5439 [astro-ph.CO] (cit. on pp. 58, 65, 66).

Noll, S. et al. (July 2012). "An atmospheric radiation model for Cerro Paranal. I. The optical spectral range". In: *A&A* 543, A92, A92. DOI: 10.1051/0004-6361/201219040. arXiv: 1205.2003 [astro-ph.IM] (cit. on pp. 160, 161).

O'Donnell, James E. (Feb. 1994). "R v-dependent Optical and Near-Ultraviolet Extinction". In: *ApJ* 422, p. 158. DOI: 10.1086/173713 (cit. on p. 106).

Osterbrock, Donald E. (1989). *Astrophysics of gaseous nebulae and active galactic nuclei*. University Science Books (cit. on p. 106).

Osterbrock, Donald E. and Gary J. Ferland (2006). *Astrophysics of gaseous nebulae and active galactic nuclei* (cit. on p. 43).

Pacifici, Camilla et al. (Apr. 2012). "Relative merits of different types of rest-frame optical observations to constrain galaxy physical parameters". In: *MNRAS* 421.3, pp. 2002–2024. DOI: 10.1111/j.1365-2966.2012.20431.x. arXiv: 1201.0780 [astro-ph.CO] (cit. on p. 179).

Pacifici, Camilla et al. (Feb. 2015). "On the importance of using appropriate spectral models to derive physical properties of galaxies at $0.7 < z < 2.8$". In: *MNRAS* 447.1, pp. 786–805. DOI: 10.1093/mnras/stu2447. arXiv: 1411.5689 [astro-ph.GA] (cit. on p. 179).

Padovani, P. et al. (Aug. 2017). "Active galactic nuclei: what's in a name?" In: *A&A Rev.* 25.1, 2, p. 2. DOI: 10.1007/s00159-017-0102-9. arXiv: 1707.07134 [astro-ph.GA] (cit. on p. 43).

Pagel, Bernard E. J. (1997). *Nucleosynthesis and Chemical Evolution of Galaxies* (cit. on p. 44).

Pannella, M. et al. (July 2015). "GOODS-Herschel: Star Formation, Dust Attenuation, and the FIR-radio Correlation on the Main Sequence of Star-forming Galaxies up to z≈4". In: *ApJ* 807.2, 141, p. 141. DOI: 10.1088/0004-637X/807/2/141. arXiv: 1407.5072 [astro-ph.GA] (cit. on pp. 38, 106).

Panuzzo, P. et al. (Oct. 2003). "Dust and nebular emission. I. Models for normal galaxies". In: *A&A* 409, pp. 99–114. DOI: 10.1051/0004-6361:20031094. arXiv: astro-ph/0307096 [astro-ph] (cit. on p. 68).

Papovich, Casey, Mark Dickinson, and Henry C. Ferguson (Oct. 2001). "The Stellar Populations and Evolution of Lyman Break Galaxies". In: *ApJ* 559.2, pp. 620–653. DOI: 10.1086/322412. arXiv: astro-ph/0105087 [astro-ph] (cit. on p. 58).

Pentericci, L. et al. (Sept. 2018). "The VANDELS ESO public spectroscopic survey: Observations and first data release". In: *A&A* 616, A174, A174. DOI: 10.1051/0004-6361/201833047. arXiv: 1803.07373 [astro-ph.GA] (cit. on p. 42).

Pérez-Montero, E. (July 2014). "Deriving model-based T_e-consistent chemical abundances in ionized gaseous nebulae". In: *MNRAS* 441.3, pp. 2663–2675. DOI: 10.1093/mnras/stu753. arXiv: 1404.3936 [astro-ph.GA] (cit. on pp. 132, 135, 164, 165, 170).

Pettini, Max and Bernard E. J. Pagel (Mar. 2004). "[OIII]/[NII] as an abundance indicator at high redshift". In: *MNRAS* 348.3, pp. L59–L63. DOI: 10.1111/j.1365-2966.2004.07591.x. arXiv: astro-ph/0401128 [astro-ph] (cit. on pp. 68, 111, 112, 164).

Pickles, A. J. (July 1998). "A Stellar Spectral Flux Library: 1150-25000 Å". In: *PASP* 110.749, pp. 863–878. DOI: 10.1086/316197 (cit. on pp. 48, 53).

Pietrinferni, Adriano et al. (Sept. 2004). "A Large Stellar Evolution Database for Population Synthesis Studies. I. Scaled Solar Models and Isochrones". In: *ApJ* 612.1, pp. 168–190. DOI: 10.1086/422498. arXiv: astro-ph/0405193 [astro-ph] (cit. on p. 52).

Pilyugin, Leonid S. and Trinh X. Thuan (Sept. 2005). "Oxygen Abundance Determination in H II Regions: The Strong Line Intensities-Abundance Calibration Revisited". In: *ApJ* 631.1, pp. 231–243. DOI: 10.1086/432408 (cit. on p. 111).

Planck Collaboration et al. (Sept. 2020). "Planck 2018 results. VI. Cosmological parameters". In: *A&A* 641, A6, A6. DOI: 10.1051/0004-6361/201833910. arXiv: 1807.06209 [astro-ph.CO] (cit. on p. 37).

Popescu, C. C. et al. (Oct. 2000). "Modelling the spectral energy distribution of galaxies. I. Radiation fields and grain heating in the edge-on spiral NGC 891". In: *A&A* 362, pp. 138–150. arXiv: astro-ph/0008098 [astro-ph] (cit. on p. 48).

Popping, Gergö, Rachel S. Somerville, and Maud Galametz (Nov. 2017). "The dust content of galaxies from z = 0 to z = 9". In: *MNRAS* 471.3, pp. 3152–3185. DOI: 10.1093/mnras/stx1545. arXiv: 1609.08622 [astro-ph.GA] (cit. on p. 63).

Prugniel, Ph. and C. Soubiran (Apr. 2001). "A database of high and medium-resolution stellar spectra". In: *A&A* 369, pp. 1048–1057. DOI: 10.1051/0004-6361:20010163. arXiv: astro-ph/0101378 [astro-ph] (cit. on p. 53).

Puech, M. et al. (July 2018). "Simulating surveys for ELT-MOSAIC: status of the MOSAIC science case after phase A". In: *Ground-based and Airborne Instrumentation for Astronomy VII*. Ed. by Christopher J. Evans, Luc Simard, and Hideki Takami. Vol. 10702. Society of Photo-Optical Instrumentation Engineers (SPIE) Conference Series, 107028R. DOI: 10.1117/12.2311292. arXiv: 1806.03296 [astro-ph.IM] (cit. on pp. 72, 176, 177).

Puglisi, A. et al. (Feb. 2016). "Dust attenuation in z ~ 1 galaxies from Herschel and 3D-HST Hα measurements". In: *A&A* 586, A83, A83. DOI: 10.1051/0004-6361/201526782. arXiv: 1507.00005 [astro-ph.GA] (cit. on p. 106).

Qin, Jianbo et al. (Nov. 2019). "Understanding the Discrepancy between IRX and Balmer Decrement in Tracing Galaxy Dust Attenuation". In: *ApJ* 886.1, 28, p. 28. DOI: 10.3847/1538-4357/ab4a04. arXiv: 1909.13505 [astro-ph.GA] (cit. on p. 106).

Reddy, Naveen A. et al. (June 2015). "The MOSDEF Survey: Measurements of Balmer Decrements and the Dust Attenuation Curve at Redshifts z ~ 1.4-2.6". In: *ApJ* 806.2, 259, p. 259. DOI: 10.1088/0004-637X/806/2/259. arXiv: 1504.02782 [astro-ph.GA] (cit. on pp. 61, 66, 106).

Renzini, Alvio and Ying-jie Peng (Mar. 2015). "An Objective Definition for the Main Sequence of Star-forming Galaxies". In: *ApJ* 801.2, L29, p. L29. DOI: 10.1088/2041-8205/801/2/L29. arXiv: 1502.01027 [astro-ph.GA] (cit. on p. 38).

Richard, Johan et al. (May 2011). "The emission line properties of gravitationally lensed 1.5 < z < 5 galaxies". In: *MNRAS* 413.1, pp. 643–658. DOI: 10.1111/j.1365-2966.2010.18161.x. arXiv: 1011.6413 [astro-ph.CO] (cit. on p. 68).

Robotham, A. S. G. et al. (June 2020). "ProSpect: generating spectral energy distributions with complex star formation and metallicity histories". In: *MNRAS* 495.1, pp. 905–931. DOI: 10.1093/mnras/staa1116. arXiv: 2002.06980 [astro-ph.GA] (cit. on pp. 48, 55, 68).

Rocha, Miguel et al. (Feb. 2008). "Dust attenuation in hydrodynamic simulations of spiral galaxies". In: *MNRAS* 383.4, pp. 1281–1291. DOI: 10.1111/j.1365-2966.2007.12431.x. arXiv: astro-ph/0702513 [astro-ph] (cit. on p. 63).

Rodighiero, G. et al. (Oct. 2011). "The Lesser Role of Starbursts in Star Formation at z = 2". In: *ApJ* 739.2, L40, p. L40. DOI: 10.1088/2041-8205/739/2/L40. arXiv: 1108.0933 [astro-ph.CO] (cit. on pp. 38, 104).

Roman-Duval, Julia et al. (Feb. 2019). "METAL: The Metal Evolution, Transport, and Abundance in the Large Magellanic Cloud Hubble Program. I. Overview and Initial Results". In: *ApJ* 871.2, 151, p. 151. DOI: 10.3847/1538-4357/aaf8bb. arXiv: 1901.06027 [astro-ph.GA] (cit. on p. 61).

Sabbi, E. et al. (Sept. 2013). "Hubble Tarantula Treasury Project: Unraveling Tarantula's Web. I. Observational Overview and First Results". In: *AJ* 146.3, 53, p. 53. DOI: 10.1088/0004-6256/146/3/53. arXiv: 1304.6747 [astro-ph.GA] (cit. on p. 61).

Sadeh, I., F. B. Abdalla, and O. Lahav (Oct. 2016). "ANNz2: Photometric Redshift and Probability Distribution Function Estimation using Machine Learning". In: *PASP*

128.968, p. 104502. DOI: 10.1088/1538-3873/128/968/104502. arXiv: 1507.00490 [astro-ph.CO] (cit. on p. 179).

Salam, Abdus (1968). "Weak and Electromagnetic Interactions". In: *Conf. Proc. C* 68051, pp. 367–37. DOI: 10.1142/9789812795915_0034 (cit. on p. 36).

Salim, Samir, Médéric Boquien, and Janice C. Lee (May 2018). "Dust Attenuation Curves in the Local Universe: Demographics and New Laws for Star-forming Galaxies and High-redshift Analogs". In: *ApJ* 859.1, 11, p. 11. DOI: 10.3847/1538-4357/aabf3c. arXiv: 1804.05850 [astro-ph.GA] (cit. on pp. 65, 66).

Salim, Samir and Desika Narayanan (Aug. 2020). "The Dust Attenuation Law in Galaxies". In: *ARA&A* 58, pp. 529–575. DOI: 10.1146/annurev-astro-032620-021933. arXiv: 2001.03181 [astro-ph.GA] (cit. on pp. 57, 60–63, 65–67).

Salim, Samir et al. (Jan. 2005). "New Constraints on the Star Formation Histories and Dust Attenuation of Galaxies in the Local Universe from GALEX". In: *ApJ* 619.1, pp. L39–L42. DOI: 10.1086/424800. arXiv: astro-ph/0411354 [astro-ph] (cit. on p. 65).

Salim, Samir et al. (Dec. 2007). "UV Star Formation Rates in the Local Universe". In: *ApJS* 173.2, pp. 267–292. DOI: 10.1086/519218. arXiv: 0704.3611 [astro-ph] (cit. on pp. 60, 61, 65, 73).

Salim, Samir et al. (Nov. 2016). "GALEX-SDSS-WISE Legacy Catalog (GSWLC): Star Formation Rates, Stellar Masses, and Dust Attenuations of 700,000 Low-redshift Galaxies". In: *ApJS* 227.1, 2, p. 2. DOI: 10.3847/0067-0049/227/1/2. arXiv: 1610.00712 [astro-ph.GA] (cit. on p. 61).

Salmon, Brett et al. (Aug. 2016). "Breaking the Curve with CANDELS: A Bayesian Approach to Reveal the Non-Universality of the Dust-Attenuation Law at High Redshift". In: *ApJ* 827.1, 20, p. 20. DOI: 10.3847/0004-637X/827/1/20. arXiv: 1512.05396 [astro-ph.GA] (cit. on pp. 62, 63).

Salpeter, Edwin E. (Jan. 1955). "The Luminosity Function and Stellar Evolution." In: *ApJ* 121, p. 161. DOI: 10.1086/145971 (cit. on p. 53).

Sánchez-Blázquez, P. et al. (Sept. 2006). "Medium-resolution Isaac Newton Telescope library of empirical spectra". In: *MNRAS* 371.2, pp. 703–718. DOI: 10.1111/j.1365-2966.2006.10699.x. arXiv: astro-ph/0607009 [astro-ph] (cit. on p. 53).

Sanders, Ryan L. et al. (Jan. 2016). "The MOSDEF Survey: Electron Density and Ionization Parameter at z~2.3". In: *ApJ* 816.1, 23, p. 23. DOI: 10.3847/0004-637X/816/1/23. arXiv: 1509.03636 [astro-ph.GA] (cit. on p. 129).

Sanders, Ryan L. et al. (Jan. 2020). "The MOSDEF survey: direct-method metallicities and ISM conditions at z ~ 1.5-3.5". In: *MNRAS* 491.1, pp. 1427–1455. DOI: 10.1093/mnras/stz3032. arXiv: 1907.00013 [astro-ph.GA] (cit. on pp. 73, 111, 112, 132, 135, 164).

Sanders, Ryan L. et al. (June 2021). "The MOSDEF Survey: The Evolution of the Mass-Metallicity Relation from $z = 0$ to $z \sim 3.3^{*}$". In: *ApJ* 914.1, p. 19. DOI: 10.3847/1538-4357/abf4c1. arXiv: 2009.07292 [astro-ph.GA]. URL: https://doi.org/10.3847/1538-4357/abf4c1 (cit. on pp. 45, 72, 111, 112, 149, 164).

Santini, P. et al. (Feb. 2014). "The evolution of the dust and gas content in galaxies". In: *A&A* 562, A30, A30. DOI: 10.1051/0004-6361/201322835. arXiv: 1311.3670 [astro-ph.CO] (cit. on p. 109).

Sargent, M. T. et al. (Mar. 2012). "The Contribution of Starbursts and Normal Galaxies to Infrared Luminosity Functions at z < 2". In: *ApJ* 747.2, L31, p. L31. DOI: 10.1088/2041-8205/747/2/L31. arXiv: 1202.0290 [astro-ph.CO] (cit. on pp. 38, 104).

Scalo, J. M. (May 1986). "The Stellar Initial Mass Function". In: *Fund. Cosmic Phys.* 11, pp. 1–278 (cit. on p. 53).

Schaerer, D. and S. de Barros (Aug. 2009). "The impact of nebular emission on the ages of z≈ 6 galaxies". In: *A&A* 502.2, pp. 423–426. DOI: 10.1051/0004-6361/200911781. arXiv: 0905.0866 [astro-ph.CO] (cit. on p. 51).

– (June 2010). "On the physical properties of z ≈ 6-8 galaxies". In: *A&A* 515, A73, A73. DOI: 10.1051/0004-6361/200913946. arXiv: 1002.1090 [astro-ph.CO] (cit. on p. 51).

Schaller, G. et al. (Dec. 1992). "New grids of stellar models from 0.8 to 120 M_solar at Z=0.020 and Z=0.001". In: *A&AS* 96, p. 269 (cit. on p. 52).

Schreiber, C. et al. (Mar. 2015). "The Herschel view of the dominant mode of galaxy growth from z = 4 to the present day". In: *A&A* 575, A74, A74. DOI: 10.1051/0004-6361/201425017. arXiv: 1409.5433 [astro-ph.GA] (cit. on pp. 38, 103, 104, 167).

Schwarz, Gideon (July 1978). "Estimating the Dimension of a Model". In: *Annals of Statistics* 6.2, pp. 461–464 (cit. on p. 103).

Scoville, N. et al. (Sept. 2007). "The Cosmic Evolution Survey (COSMOS): Overview". In: *ApJS* 172, pp. 1–8. DOI: 10.1086/516585. eprint: astro-ph/0612305 (cit. on pp. 42, 83, 84).

Shannon, M. J., D. J. Stock, and E. Peeters (Oct. 2015). "Probing the Ionization States of Polycyclic Aromatic Hydrocarbons via the 15-20 μm Emission Bands". In: *ApJ* 811.2, 153, p. 153. DOI: 10.1088/0004-637X/811/2/153. arXiv: 1508.04766 [astro-ph.GA] (cit. on p. 46).

Shapley, Alice E. et al. (May 2003). "Rest-Frame Ultraviolet Spectra of z~3 Lyman Break Galaxies". In: *ApJ* 588.1, pp. 65–89. DOI: 10.1086/373922. arXiv: astro-ph/0301230 [astro-ph] (cit. on p. 68).

Shapley, Alice E. et al. (Nov. 2006). "The Direct Detection of Lyman Continuum Emission from Star-forming Galaxies at z~3". In: *ApJ* 651.2, pp. 688–703. DOI: 10.1086/507511. arXiv: astro-ph/0606635 [astro-ph] (cit. on p. 58).

Shapley, Alice E. et al. (Mar. 2015). "The MOSDEF Survey: Excitation Properties of z~2.3 Star-forming Galaxies". In: *ApJ* 801.2, 88, p. 88. DOI: 10.1088/0004-637X/801/2/88. arXiv: 1409.7071 [astro-ph.GA] (cit. on pp. 68, 71, 72, 128–130, 169).

Shimakawa, Rhythm et al. (Aug. 2015). "Correlation between star formation activity and electron density of ionized gas at z = 2.5". In: *MNRAS* 451.2, pp. 1284–1289. DOI: 10.1093/mnras/stv915. arXiv: 1411.1408 [astro-ph.CO] (cit. on p. 129).

Shimwell, T. W. et al. (Feb. 2017). "The LOFAR Two-metre Sky Survey. I. Survey description and preliminary data release". In: *A&A* 598, A104, A104. DOI: 10.1051/0004-6361/201629313. arXiv: 1611.02700 [astro-ph.IM] (cit. on p. 41).

Shivaei, Irene et al. (May 2015). "Investigating Hα, UV, and IR Star-formation Rate Diagnostics for a Large Sample of z ~ 2 Galaxies". In: *ApJ* 804.2, 149, p. 149. DOI: 10.1088/0004-637X/804/2/149. arXiv: 1503.03929 [astro-ph.GA] (cit. on p. 61).

Shivaei, Irene et al. (Aug. 2020). "The MOSDEF Survey: The Variation of the Dust Attenuation Curve with Metallicity". In: *ApJ* 899.2, 117, p. 117. DOI: 10.3847/1538-4357/aba35e. arXiv: 2005.01742 [astro-ph.GA] (cit. on pp. 60, 63, 65, 66, 106, 107).

Silva, Laura et al. (Dec. 1998). "Modeling the Effects of Dust on Galactic Spectral Energy Distributions from the Ultraviolet to the Millimeter Band". In: *ApJ* 509.1, pp. 103–117. DOI: 10.1086/306476 (cit. on p. 48).

Silverman, J. D. et al. (Sept. 2015). "The FMOS-COSMOS Survey of Star-forming Galaxies at z~1.6. III. Survey Design, Performance, and Sample Characteristics". In: *ApJS* 220.1, 12, p. 12. DOI: 10.1088/0067-0049/220/1/12. arXiv: 1409.0447 [astro-ph.GA] (cit. on pp. 3, 8, 42, 68, 77, 91, 163, 174).

Simet, Melanie et al. (Feb. 2021). "Comparison of Observed Galaxy Properties with Semianalytic Model Predictions Using Machine Learning". In: *ApJ* 908.1, 47, p. 47. DOI: 10.3847/1538-4357/abd179 (cit. on p. 179).

Skrutskie, M. F. et al. (Feb. 2006). "The Two Micron All Sky Survey (2MASS)". In: *AJ* 131.2, pp. 1163–1183. DOI: 10.1086/498708 (cit. on p. 41).

Smith, D. J. B. et al. (Nov. 2012). "Herschel-ATLAS: multi-wavelength SEDs and physical properties of 250 μm selected galaxies at z < 0.5". In: *MNRAS* 427.1, pp. 703–727. DOI: 10.1111/j.1365-2966.2012.21930.x. arXiv: 1208.3079 [astro-ph.CO] (cit. on pp. 49, 82).

Sobral, David et al. (Aug. 2015). "Evidence for PopIII-like Stellar Populations in the Most Luminous Lyman-α Emitters at the Epoch of Reionization: Spectroscopic Confirmation". In: *ApJ* 808.2, 139, p. 139. DOI: 10.1088/0004-637X/808/2/139. arXiv: 1504.01734 [astro-ph.GA] (cit. on p. 68).

Springel, Volker et al. (June 2005). "Simulations of the formation, evolution and clustering of galaxies and quasars". In: *Nature* 435.7042, pp. 629–636. DOI: 10.1038/nature03597. arXiv: astro-ph/0504097 [astro-ph] (cit. on p. 148).

Stacey, G. J. et al. (Dec. 2010). "A 158 μm [C II] Line Survey of Galaxies at z ~1-2: An Indicator of Star Formation in the Early Universe". In: *ApJ* 724.2, pp. 957–974. DOI: 10.1088/0004-637X/724/2/957. arXiv: 1009.4216 [astro-ph.CO] (cit. on p. 121).

Stalevski, Marko et al. (Mar. 2012). "3D radiative transfer modelling of the dusty tori around active galactic nuclei as a clumpy two-phase medium". In: *MNRAS* 420.4, pp. 2756–2772. DOI: 10.1111/j.1365-2966.2011.19775.x. arXiv: 1109.1286 [astro-ph.CO] (cit. on p. 49).

Stalevski, Marko et al. (May 2016). "The dust covering factor in active galactic nuclei". In: *MNRAS* 458.3, pp. 2288–2302. DOI: 10.1093/mnras/stw444. arXiv: 1602.06954 [astro-ph.GA] (cit. on p. 49).

Stark, Daniel P. et al. (Feb. 2013). "Keck Spectroscopy of 3 < z < 7 Faint Lyman Break Galaxies: The Importance of Nebular Emission in Understanding the Specific Star

Formation Rate and Stellar Mass Density". In: *ApJ* 763.2, 129, p. 129. DOI: 10.1088/0004-637X/763/2/129. arXiv: 1208.3529 [astro-ph.CO] (cit. on p. 51).

Stark, Daniel P. et al. (Dec. 2014). "Ultraviolet emission lines in young low-mass galaxies at z ~ 2: physical properties and implications for studies at z > 7". In: *MNRAS* 445.3, pp. 3200–3220. DOI: 10.1093/mnras/stu1618. arXiv: 1408.1420 [astro-ph.GA] (cit. on p. 68).

Stark, Daniel P. et al. (Dec. 2015a). "Spectroscopic detection of C IV λ1548 in a galaxy at z = 7.045: implications for the ionizing spectra of reionization-era galaxies". In: *MNRAS* 454.2, pp. 1393–1403. DOI: 10.1093/mnras/stv1907. arXiv: 1504.06881 [astro-ph.GA] (cit. on p. 68).

Stark, Daniel P. et al. (June 2015b). "Spectroscopic detections of C III] λ1909 Å at z ~ 6 – 7: a new probe of early star-forming galaxies and cosmic reionization". In: *MNRAS* 450.2, pp. 1846–1855. DOI: 10.1093/mnras/stv688. arXiv: 1408.3649 [astro-ph.GA] (cit. on p. 68).

Stark, Daniel P. et al. (Jan. 2017). "Lyα and C III] emission in z = 7-9 Galaxies: accelerated reionization around luminous star-forming systems?" In: *MNRAS* 464.1, pp. 469–479. DOI: 10.1093/mnras/stw2233. arXiv: 1606.01304 [astro-ph.GA] (cit. on p. 68).

Stasińska, Grazyna and Claus Leitherer (Dec. 1996). "H II Galaxies versus Photoionization Models for Evolving Starbursts". In: *ApJS* 107, p. 661. DOI: 10.1086/192377 (cit. on p. 68).

Stebbins, Joel, C. M. Huffer, and A. E. Whitford (Sept. 1939). "Space Reddening in the Galaxy." In: *ApJ* 90, p. 209. DOI: 10.1086/144099 (cit. on p. 61).

Steidel, Charles C. et al. (Nov. 2014). "Strong Nebular Line Ratios in the Spectra of z ≈ 2-3 Star Forming Galaxies: First Results from KBSS-MOSFIRE". In: *ApJ* 795.2, 165, p. 165. DOI: 10.1088/0004-637X/795/2/165. arXiv: 1405.5473 [astro-ph.GA] (cit. on pp. 68, 72, 112, 129).

Steidel, Charles C. et al. (Aug. 2016). "Reconciling the Stellar and Nebular Spectra of High-redshift Galaxies". In: *ApJ* 826.2, 159, p. 159. DOI: 10.3847/0004-637X/826/2/159. arXiv: 1605.07186 [astro-ph.GA] (cit. on pp. 72, 129).

Straughn, Amber N. et al. (Oct. 2009). "Emission-Line Galaxies from the Hubble Space Telescope Probing Evolution and Reionization Spectroscopically (PEARS) Grism Survey. I. The South Fields". In: *AJ* 138.4, pp. 1022–1031. DOI: 10.1088/0004-6256/138/4/1022. arXiv: 0907.2254 [astro-ph.CO] (cit. on pp. 4, 113, 114).

Strom, Allison L. et al. (Feb. 2017). "Nebular Emission Line Ratios in z~2-3 Star-forming Galaxies with KBSS-MOSFIRE: Exploring the Impact of Ionization, Excitation, and Nitrogen-to-Oxygen Ratio". In: *ApJ* 836.2, 164, p. 164. DOI: 10.3847/1538-4357/836/2/164. arXiv: 1608.02587 [astro-ph.GA] (cit. on pp. 71, 72, 128–130, 169).

Sugai, Hajime et al. (July 2015). "Prime Focus Spectrograph for the Subaru telescope: massively multiplexed optical and near-infrared fiber spectrograph". In: *Journal of Astronomical Telescopes, Instruments, and Systems* 1, 035001, p. 035001. DOI: 10.1117/1.JATIS.1.3.035001. arXiv: 1507.00725 [astro-ph.IM] (cit. on p. 176).

Sutherland, Ralph et al. (July 2018). *MAPPINGS V: Astrophysical plasma modeling code*. ascl: 1807.005 (cit. on p. 69).

Takada, Masahiro et al. (Feb. 2014). "Extragalactic science, cosmology, and Galactic archaeology with the Subaru Prime Focus Spectrograph". In: *PASJ* 66.1, R1, R1. DOI: 10.1093/pasj/pst019. arXiv: 1206.0737 [astro-ph.CO] (cit. on p. 176).

Tamura, N. and PFS Collaboration (Jan. 2021). "Prime Focus Spectrograph: Next Generation Subaru Telescope Facility Instrument Coming to First Light". In: *American Astronomical Society Meeting Abstracts*. Vol. 53. American Astronomical Society Meeting Abstracts, p. 502.03 (cit. on p. 176).

Tamura, Naoyuki et al. (July 2018). "Prime Focus Spectrograph (PFS) for the Subaru telescope: ongoing integration and future plans". In: *Ground-based and Airborne Instrumentation for Astronomy VII*. Ed. by Christopher J. Evans, Luc Simard, and Hideki Takami. Vol. 10702. Society of Photo-Optical Instrumentation Engineers (SPIE) Conference Series, p. 107021C. DOI: 10.1117/12.2311871 (cit. on p. 176).

Tang, Mengtao et al. (Mar. 2021). "Rest-frame UV spectroscopy of extreme [O III] emitters at $1.3 < z < 3.7$: toward a high-redshift UV reference sample for JWST". In: *MNRAS* 501.3, pp. 3238–3257. DOI: 10.1093/mnras/staa3454. arXiv: 2007.12197 [astro-ph.GA] (cit. on p. 51).

Taylor, Edward N. et al. (Dec. 2011). "Galaxy And Mass Assembly (GAMA): stellar mass estimates". In: *MNRAS* 418.3, pp. 1587–1620. DOI: 10.1111/j.1365-2966.2011.19536.x. arXiv: 1108.0635 [astro-ph.CO] (cit. on p. 58).

Taylor, William et al. (July 2018). "Rising MOONS: an update on the VLT's next multi-object spectrograph as it begins to grow". In: *Ground-based and Airborne Instrumentation for Astronomy VII*. Ed. by Christopher J. Evans, Luc Simard, and Hideki Takami. Vol. 10702. Society of Photo-Optical Instrumentation Engineers (SPIE) Conference Series, 107021G. DOI: 10.1117/12.2313403 (cit. on pp. 139–143).

Teplitz, Harry I. et al. (Oct. 2000). "Measurement of [O III] Emission in Lyman-Break Galaxies". In: *ApJ* 542.1, pp. 18–26. DOI: 10.1086/309539. arXiv: astro-ph/0005254 [astro-ph] (cit. on p. 113).

The MSE Science Team et al. (Apr. 2019). "The Detailed Science Case for the Maunakea Spectroscopic Explorer, 2019 edition". In: *arXiv e-prints*, arXiv:1904.04907, arXiv:1904.04907. arXiv: 1904.04907 [astro-ph.IM] (cit. on pp. 176, 177).

Theios, Rachel L. et al. (Jan. 2019). "Dust Attenuation, Star Formation, and Metallicity in $z \sim 2$-3 Galaxies from KBSS-MOSFIRE". In: *ApJ* 871.1, 128, p. 128. DOI: 10.3847/1538-4357/aaf386. arXiv: 1805.00016 [astro-ph.GA] (cit. on p. 106).

Thorne, Jessica E. et al. (July 2021). "Deep Extragalactic VIsible Legacy Survey (DEVILS): SED fitting in the D10-COSMOS field and the evolution of the stellar mass function and SFR-$M_\star$ relation". In: *MNRAS* 505.1, pp. 540–567. DOI: 10.1093/mnras/stab1294. arXiv: 2011.13605 [astro-ph.GA] (cit. on pp. 46, 47, 49–51, 54).

Tomczak, Adam R. et al. (Feb. 2016). "The SFR-M* Relation and Empirical Star-Formation Histories from ZFOURGE* at $0.5 < z < 4$". In: *ApJ* 817.2, 118, p. 118. DOI: 10.3847/0004-637X/817/2/118. arXiv: 1510.06072 [astro-ph.GA] (cit. on p. 38).

Topping, Michael W. et al. (Dec. 2020). "The MOSDEF-LRIS Survey: The connection between massive stars and ionized gas in individual galaxies at $z \sim 2$". In: *MNRAS* 499.2, pp. 1652–1665. DOI: 10.1093/mnras/staa2941. arXiv: 2008.02282 [astro-ph.GA] (cit. on pp. 132, 135, 165).

Trayford, James W. et al. (Jan. 2020). "Fade to grey: systematic variation of galaxy attenuation curves with galaxy properties in the EAGLE simulations". In: *MNRAS* 491.3, pp. 3937–3951. DOI: 10.1093/mnras/stz3234. arXiv: 1908.08956 [astro-ph.GA] (cit. on pp. 48, 62, 63).

Tremonti, Christy A. et al. (Oct. 2004). "The Origin of the Mass-Metallicity Relation: Insights from 53,000 Star-forming Galaxies in the Sloan Digital Sky Survey". In: *ApJ* 613.2, pp. 898–913. DOI: 10.1086/423264. arXiv: astro-ph/0405537 [astro-ph] (cit. on pp. 110, 111).

Tresse, L. (Dec. 2019). "Evolution and formation of galaxies with the Maunakea Spectroscopic Explorer facility". In: *SF2A-2019: Proceedings of the Annual meeting of the French Society of Astronomy and Astrophysics*. Ed. by P. Di Matteo et al., p. Di (cit. on pp. 176, 177).

Vale Asari, N. et al. (Aug. 2016). "BOND: Bayesian Oxygen and Nitrogen abundance Determinations in giant H II regions using strong and semistrong lines". In: *MNRAS* 460.2, pp. 1739–1757. DOI: 10.1093/mnras/stw971. arXiv: 1605.01057 [astro-ph.GA] (cit. on p. 180).

Veilleux, Sylvain and Donald E. Osterbrock (Feb. 1987). "Spectral Classification of Emission-Line Galaxies". In: *ApJS* 63, p. 295. DOI: 10.1086/191166 (cit. on pp. 71, 128).

Vila-Costas, M. B. and M. G. Edmunds (Nov. 1993). "The nitrogen-to-oxygen ratio in galaxies and its implications for the origin of nitrogen." In: *MNRAS* 265, pp. 199–212. DOI: 10.1093/mnras/265.1.199 (cit. on pp. 69, 125, 129).

Voges, W. et al. (Sept. 1999). "The ROSAT all-sky survey bright source catalogue". In: *A&A* 349, pp. 389–405. arXiv: astro-ph/9909315 [astro-ph] (cit. on p. 40).

Walcher, C. J. et al. (Dec. 2008). "The VVDS-SWIRE-GALEX-CFHTLS surveys: physical properties of galaxies at z below 1.2 from photometric data". In: *A&A* 491.3, pp. 713–730. DOI: 10.1051/0004-6361:200810704. arXiv: 0807.4636 [astro-ph] (cit. on pp. 73, 74).

Walcher, Jakob et al. (Jan. 2011). "Fitting the integrated spectral energy distributions of galaxies". In: *Ap&SS* 331, pp. 1–52. DOI: 10.1007/s10509-010-0458-z. arXiv: 1008.0395 [astro-ph.CO] (cit. on pp. 73, 74).

Weaver, J. R. et al. (Jan. 2021). "COSMOS2020: A next-generation catalog to explore the 1 < z < 8 universe". In: *American Astronomical Society Meeting Abstracts*. Vol. 53. American Astronomical Society Meeting Abstracts, p. 215.06 (cit. on p. 83).

Weinberg, Steven (Nov. 1967). "A Model of Leptons". In: *Phys. Rev. Lett.* 19.21, pp. 1264–1266. DOI: 10.1103/PhysRevLett.19.1264 (cit. on p. 36).

Weingartner, Joseph C. and B. T. Draine (Feb. 2001). "Dust Grain-Size Distributions and Extinction in the Milky Way, Large Magellanic Cloud, and Small Magellanic Cloud". In: *ApJ* 548.1, pp. 296–309. DOI: 10.1086/318651. arXiv: astro-ph/0008146 [astro-ph] (cit. on pp. 57, 60).

Weisskopf, Martin C. et al. (July 2000). "Chandra X-ray Observatory (CXO): overview". In: *X-Ray Optics, Instruments, and Missions III*. Ed. by Joachim E. Truemper and Bernd Aschenbach. Vol. 4012. Society of Photo-Optical Instrumentation Engineers

(SPIE) Conference Series, pp. 2–16. DOI: 10.1117/12.391545. arXiv: astro-ph/0004127 [astro-ph] (cit. on p. 40).

Wells, Martyn et al. (July 2015). "The Mid-Infrared Instrument for the James Webb Space Telescope, VI: The Medium Resolution Spectrometer". In: *PASP* 127.953, p. 646. DOI: 10.1086/682281. arXiv: 1508.03070 [astro-ph.IM] (cit. on p. 51).

Whitaker, Katherine E. et al. (Feb. 2012). "A Large Population of Massive Compact Post-starburst Galaxies at z > 1: Implications for the Size Evolution and Quenching Mechanism of Quiescent Galaxies". In: *ApJ* 745.2, 179, p. 179. DOI: 10.1088/0004-637X/745/2/179. arXiv: 1112.0313 [astro-ph.CO] (cit. on p. 38).

Wild, Vivienne et al. (Oct. 2007). "Bursty stellar populations and obscured active galactic nuclei in galaxy bulges". In: *MNRAS* 381.2, pp. 543–572. DOI: 10.1111/j.1365-2966.2007.12256.x. arXiv: 0706.3113 [astro-ph] (cit. on p. 98).

Wild, Vivienne et al. (Nov. 2011). "Empirical determination of the shape of dust attenuation curves in star-forming galaxies". In: *MNRAS* 417.3, pp. 1760–1786. DOI: 10.1111/j.1365-2966.2011.19367.x. arXiv: 1106.1646 [astro-ph.CO] (cit. on pp. 62, 63, 65).

Wilkins, Stephen M. et al. (Aug. 2012). "Predictions for the intrinsic UV continuum properties of star-forming galaxies and the implications for inferring dust extinction". In: *MNRAS* 424.2, pp. 1522–1529. DOI: 10.1111/j.1365-2966.2012.21344.x. arXiv: 1206.2732 [astro-ph.CO] (cit. on p. 63).

Witt, Adolf N. and Karl D. Gordon (June 1996). "Multiple Scattering in Clumpy Media. I. Escape of Stellar Radiation from a Clumpy Scattering Environment". In: *ApJ* 463, p. 681. DOI: 10.1086/177282 (cit. on p. 65).

– (Jan. 2000). "Multiple Scattering in Clumpy Media. II. Galactic Environments". In: *ApJ* 528.2, pp. 799–816. DOI: 10.1086/308197. arXiv: astro-ph/9907342 [astro-ph] (cit. on p. 65).

Wright, G. S. et al. (July 2015). "The Mid-Infrared Instrument for the James Webb Space Telescope, II: Design and Build". In: *PASP* 127.953, p. 595. DOI: 10.1086/682253. arXiv: 1508.02333 [astro-ph.IM] (cit. on p. 51).

Yabe, Kiyoto et al. (Dec. 2015). "The Subaru FMOS Galaxy Redshift Survey (FastSound). III. The mass-metallicity relation and the fundamental metallicity relation at z ~ 1.4*". In: *PASJ* 67.6, 102, p. 102. DOI: 10.1093/pasj/psv079. arXiv: 1508.01512 [astro-ph.GA] (cit. on p. 129).

Yanchulova Merica-Jones, Petia et al. (Oct. 2017). "The Small Magellanic Cloud Investigation of Dust and Gas Evolution (SMIDGE): The Dust Extinction Curve from Red Clump Stars". In: *ApJ* 847.2, 102, p. 102. DOI: 10.3847/1538-4357/aa8a67. arXiv: 1709.01093 [astro-ph.GA] (cit. on p. 61).

Yang, G. et al. (Jan. 2020). "X-CIGALE: Fitting AGN/galaxy SEDs from X-ray to infrared". In: *MNRAS* 491.1, pp. 740–757. DOI: 10.1093/mnras/stz3001. arXiv: 2001.08263 [astro-ph.GA] (cit. on pp. 42, 49).

Yates, Robert M., Guinevere Kauffmann, and Qi Guo (May 2012). "The relation between metallicity, stellar mass and star formation in galaxies: an analysis of observational and model data". In: *MNRAS* 422.1, pp. 215–231. DOI: 10.1111/j.1365-2966.2012.20595.x. arXiv: 1107.3145 [astro-ph.CO] (cit. on p. 110).

York, Donald G. et al. (Sept. 2000). "The Sloan Digital Sky Survey: Technical Summary". In: *AJ* 120.3, pp. 1579–1587. DOI: 10.1086/301513. arXiv: astro-ph/0006396 [astro-ph] (cit. on p. 41).

Yuan, Fang-Ting et al. (Nov. 2019). "Properties of LBGs with [OIII] detection at z ≈ 3.5. The importance of including nebular emission data in SED fitting". In: *A&A* 631, A123, A123. DOI: 10.1051/0004-6361/201935975. arXiv: 1910.03235 [astro-ph.GA] (cit. on pp. 47, 58, 67, 179).

Zackrisson, E. et al. (Sept. 2001). "A model of spectral galaxy evolution including the effects of nebular emission". In: *A&A* 375, pp. 814–826. DOI: 10.1051/0004-6361:20010912. arXiv: astro-ph/0107139 [astro-ph] (cit. on p. 68).

Zahid, H. Jabran et al. (Sept. 2017). "Stellar Absorption Line Analysis of Local Star-forming Galaxies: The Relation between Stellar Mass, Metallicity, Dust Attenuation, and Star Formation Rate". In: *ApJ* 847.1, 18, p. 18. DOI: 10.3847/1538-4357/aa88ae. arXiv: 1708.07107 [astro-ph.GA] (cit. on pp. 107, 111, 112, 164).

Zezas, Andreas (2021). "High-Energy Star-Formation Rate Indicators". In: *Star-Formation Rates of Galaxies*. Ed. by Andreas Zezas and VéroniqueEditors Buat. Cambridge Astrophysics. Cambridge University Press, pp. 243–278. DOI: 10.1017/9781316875445.014 (cit. on p. 42).